Comprehensive Analytical Modeling of Laser Powder-Bed/Fed Additive Manufacturing Processes and an Associated Magnetic Focusing Module

By

Yuze Huang

A thesis
presented to the University of Waterloo
in fulfilment of the
thesis requirement for the degree of
Doctor of Philosophy
in
Mechanical Engineering

Waterloo, Ontario, Canada, 2019

Examining Committee Membership

The following served on the Examining Committee for this thesis. The decision of the Examining Committee is made by majority vote.

External Examiner: Yu Zou, Assistant Professor
Dept. of Materials Science & Engineering
University of Toronto

Supervisor: Ehsan Toyserkani, Professor
Dept. of Mechanical and Mechatronics Engineering
University of Waterloo

Supervisor: Mir Behrad Khamesee, Professor
Dept. of Mechanical and Mechatronics Engineering
University of Waterloo

Internal Member: Norman Zhou, Professor
Dept. of Mechanical and Mechatronics Engineering
University of Waterloo

Internal Member: Mohammad Kohandel, Associate Professor
Dept. of Applied Mathematics
University of Waterloo

Internal Member: Mihaela Vlasea, Assistant Professor
Dept. of Mechanical and Mechatronics Engineering
University of Waterloo

Author's Declaration

This thesis consists of materials all of which I authored or co-authored: See the section of Statement of Contributions. This is a true copy of the thesis, including any required final revisions, as accepted by my examiners. I understand that my thesis may be made electronically available to the public.

Statement of Contributions

I would like to acknowledge my co-authors who contributed to the research described in this thesis:

Prof. Ehsan Toyserkani: Supervision of the research, providing original idea for the current thesis in the additive manufacturing field, editing papers and providing lab facilities.

Prof. Mir Behrad Khamesee: Supervision of the research, providing original idea for the current thesis in the electromagnetism, editing papers and providing lab facilities.

Dr. Hamed Asgari: Polishing, etching the Stainless Steel 17-4PH cuboid samples, running the SEM measurement and editing paper.

Zhang Zhidong: Co-designing part of the LPB-AM experiments with Stainless Steel 17-4PH powder, polishing and etching the samples.

Mohammad Ansari: Running the thin-wall structure experiments with robotic LPF-AM DMD®-IC106 system, polishing, etching the Inconel 625 samples and editing paper.

Abstract

State-of-the-art metal additive manufacturing (AM), mainly laser powder-fed AM (LPF-AM) and laser powder-bed AM (LPB-AM), has been used to produce high-quality, complex-shaped, and end-user metallic parts. To achieve desirable dimensional, microstructural and mechanical features of as-built components through fast process optimization or feedback-control-based adaptive processing adjustment, a high fidelity and calculation-efficient processing model is urgently needed. The thesis research has been motivated by the need for time-efficient process models of both LPF-AM and LPB-AM. To this end, comprehensive accelerated models for these processes have been built and experimentally verified.

The comprehensive process model of LPF-AM was built by an innovative analytical approach. Firstly, a mathematical module that couples laser heat flux and powder mass flow was developed, while considering the attenuated laser intensity distribution and the heated powder spatial distribution. Correspondingly, a powder catchment module was built in terms of a three-dimensional (3D) melt pool shape and powder stream spatial distribution. Integrating these physical modules into the thermal modeling, a coupled heat and mass comprehensive model of the LPF-AM process was achieved. Experimental depositions of Inconel 625 proves the model's high accuracy in predicting as-built deposits' geometry (a maximum error of ~6.2% for clad width, ~7.8% for clad height) and powder catchment efficiency (maximum error of less than ~6.8%). It was found that the predicted real-time melt pool peak temperatures match well with the experimental results in Stainless Steel (SS) 316L deposition. The calculated micro-hardness has a maximum prediction error of ~16.2% compared with the measured results. The predicted microstructural evolutions show reasonable agreement with the experimental observations for both SS 316L and Inconel 625 depositions. Moreover, sensitivity analysis shows that the powder feed rate has the largest positive effect on the clad height.

The time-efficient process model of LPB-AM was achieved by a novel analytical approach that couples the critical physics of the process, while considering the volume shrinkage and the melting regime. The proposed model can perform a time-efficient prediction of the localized-transient thermal field, melt pool temperature distribution, and multi-track overlapping dimension. The powder bed was treated as a homogeneous medium with effective

thermophysical properties derived from the randomly packed rain model. In addition, different melting regimes of the LPB-AM process were considered in the built model. A 3D heat source model with variant penetration depths, together with the varying melting regimes, was utilized to solve the transient thermal field. Moreover, the density and top surface roughness of the final parts were empirically modeled using response surface regression under a Box-Behnken design. Subsequently, the mechanical properties of the part and the in-situ build rates were simultaneously optimized by combining the built analytical models and empirical models with employing a multi-objective genetic algorithm. Experimental results with SS 17-4PH show that the predicted melt pool dimensions have a high degree of accuracy under steady melting regimes, with a maximum of ~14% error for the width prediction and ~15% error for the depth calculation. Furthermore, an optimized parameter solution set was provided based on the built 3D Pareto fronts.

The built models' calculation time for the localized-transient characteristics for LPF-AM and LPB-AM are ~4 ms and ~1.2 ms, respectively. These findings confirm the great potential of the present research to be used for fast process optimization and in-situ process control.

In addition, a new magnetic concentration approach designed with various configurations was explored. This approach is designed to focus the diverging metal particles in the gas-powder stream of LPF-AM, thereby improving powder catchment and deposition accuracy. It was shown that the proposed permanent-magnet-based configurations may not be suitable for concentrating submillimeter-sized particles. However, an additional development, a doublet-electromagnet-quadrupoles-based configuration with high frequency, may be capable of concentrating the non-ferrous metallic particles (e.g., aluminum particle) with a radius of $r_p \geq 150\ \mu m$.

Acknowledgements

I would like to express my deepest gratitude to my two supervisors, Prof. Ehsan Toyserkani and Prof. Mir Behrad Khamesee for their support, patience, caring and guidance through the years of my research studies. They have been strong and supportive advisors with persistent help in my whole graduate studies. I really appreciate their encouragement that help me to overcome the difficulties in my research.

I would also like to express my sincere gratitude to my committee members, Professor Yu Zou, Professor Norman Zhou, Professor Mohammad Kohandel and Professor Mihaela Vlasea. Their comments and suggestions are very helpful.

I would like to acknowledge all my colleagues at Multi-Scale Additive Manufacturing Lab and Maglev Micro-robotics Lab for their friendship and assistance. I especially have to acknowledge Xiaodong Zhang for his endless patience, inspiring discussion, suggestion and excellent knowledge in the magnetic field. Very special thanks to Dr. Mohammad Hossein Farshidianfar for his training in the house-developed laser powder-fed additive manufacturing systems. Thank to my co-authors Zhidong Zhang, Mohammad Ansari, Dr. Hamed Asgari, Dr. Mohammad Hossein Farshidianfar and Dr. Dyuti Sarker for their fruitful cooperation. I have to acknowledge Dr. Allan Rogalsky for the powder bed density measurement support, Dr. Ehsan Marzbanrad for the scanning electron microscope support, Dr. Usman Ali for the CT scanning image processing support and Jerry Li for the randomly packed powder bed rain model coding.

Thanks to all my friends in University of Waterloo. With their company, the life in Waterloo become more interesting and colorful. I will treasure the cheerful moments and days enshrined in my memory forever.

Finally and most importantly, I would like to thank all my family members. I would like to thank my parents for their support and encouragement in the past years. I would also like to thank my wife, Han Shasha, for her understanding and love. She devotes all her love to our baby, Heju. With her thoughtfulness and encouragement, I overcame the obstacles in my PhD study.

This study is dedicated to my

parents, Zhixia and Xianwen,

my daughter Heju and my wife, Shasha

Table of Contents

List of Figures

List of Tables

List of Abbreviations

3D	Three dimensional
AM	Additive manufacturing
CAD	Computer aided design
CNC	Computer numerical control
DED	Direct energy deposition
DMLS	Direct metal laser sintering
ECS	Eddy Current Separation
FGM	Functionally graded materials
FLC	Freeform laser consolidation
HAZ	Heat affected zone
LDC	Laser direct casting
LC	Laser cladding
LDED	Laser-based direct energy deposition
LENS	Laser engineered net shaping
LPB-AM	Laser powder-bed additive manufacturing
LPB-AM	Laser powder-bed fusion
LPF-AM	Laser powder-fed additive manufacturing
STL	Standard tessellation language
SLM	Selective laser melting
SLS	Selective laser sintering

List of Symbols

A_S	Melt pool effective projection area	a	Dynamic contact angle
$\boldsymbol{B}$	Magnetic field intensity	B_R	Process build rate in LPB-AM
c_p	Specific heat capacity	D	Laser spot diameter in LPF-AM
d_l	Laser spot diameter in LPB-AM	d_p	Melt pool depth
E	Specific energy	$\boldsymbol{F}$	Magnetic force
$\boldsymbol{g}$	Acceleration of gravity	H	Nozzle height
h	Clad/deposit height	h_s	Hatch space
h_t	Layer thickness	i, j	Track/layer scanning index
I	Laser beam intensity	k	Thermal conductivity
L	Track length	l	Melt pool length
$\boldsymbol{M}$	Magnetic moment	m	Particle mass
$\dot{m}$	Powder feed rate	N	Particle number
P_L	Laser power	q	Heat source
R_{0L}	Laser beam waist radius	r_0	Nozzle internal radius
r_p	Particle radius	S	Melt pool inclined surface
T	Temperature	t^s, t^f	Deposition starting/ending time
V_B	Powder bed volume	v	Process/scanning speed
v_p	Particle velocity	w, w_l	Melt pool width
w_s	Stripe width	z_0	Laser beam waist position
α	Thermal diffusivity	α_w	Brewster effect coefficient
β	Laser absorptivity	γ_{SV}, γ_{LS}	Interfacial tension/energy
δ	Skin depth (eddy current)	ε	Hoffman-Voinov-Tanner constant
θ	Powder stream divergence angle	$\emptyset$	Melt pool inclination angle
Ω	Simulation domain	λ	Laser wavelength
σ	Electrical conductivity	ρ	Density
φ	Nozzle angle	μ	Magnetic permeability
(x, y, z)	Moving Cartesian coordinates	(ξ, η, ζ)	Fixed Cartesian coordinates

Chapter 1. Introduction

1.1. Overview

In recent years, due to the fast development of high-energy heat sources, low-cost metal powder feedstock, high-performance computers equipped with advanced computer-aided design (CAD) and topology optimization modules, metal additive manufacturing (AM) is no longer limited to rapid prototyping. Instead, it has been explored for the possibility of manufacturing high-quality, complex, end-user metallic parts according to a state-of-the-discipline report [1] from the U.S. National Aeronautics and Space Administration. As the AM process has a high cooling rate and low solid-liquid interfacial free energy as well as a small nucleus critical radius for promoting heterogeneous nucleation [2], AM fabricated parts will typically exhibit finer grains than those processed by traditional manufacturing processes (e.g., casting), resulting in better mechanical properties. Furthermore, the AM process has the unique ability to create complex metallic components that are difficult or impossible to manufacture by conventional processes.

The metal AM process deposits metallic powder, wire or sheets onto the substrate/object surface, where they are melted due to a high-energy source (i.e., laser, electron beam, electron arc and ultrasonic vibration), then solidify to form new features in a layer-by-layer approach [3]. The two most commonly used laser-based metal AM processes, laser powder-fed AM (LPF-AM) and laser powder-bed AM (LPB-AM), also termed as directed energy deposition (DED) and powder bed fusion (PBF) by ASTM Standard F2792 [4], respectively, have shown great potential for producing complex, customized and high quality parts from single or multiple metallic materials.

Both the LPF-AM and LPB-AM processes begin with CAD models that are stored in Standard Tessellation Language (STL) file format, generate the scanning path based on numerically sliced cross-section dimensions from the CAD model, utilize a laser source to melt the metallic powder, and finally produce three-dimensional (3D) parts. LPF-AM utilizes a carrier gas (e.g., argon) to deliver the powder onto the build surface through a nozzle, whereas the LPB-AM loads the powder layer across the whole powder bed by means of a recoater/roller. The details of LPF-AM and LPB-AM are compared in Table 1-1.

Table 1-1. LPF-AM and LPB-AM comparison. (The build rate, surface roughness and fabrication dimension are cited from reference [5]).

Features	LPF-AM	LPB-AM
Alias	Laser engineered net shaping (LENS^{TM}); Laser cladding (LC); Laser direct casting (LDC); Laser-based direct energy deposition (LDED); Freeform laser consolidation (FLC)	Direct metal laser sintering (DMLS); Selective laser sintering (SLS); Selective laser melting (SLM); Laser powder bed fusion (LPB-AM)
Laser beam diameter	$1\sim3\ mm$	$50\sim200\ \mu m$
Multi-material	Yes	No
Build rate	Up to $70\ cm^3/h$	$5\sim20\ cm^3/h$
Layer thickness	$0.1\sim2\ mm$	$20\sim90\ \mu m$
Surface roughness	Ra $\geq 7\sim20\ \mu m$	Ra $\geq 4\sim10\ \mu m$
Max. fabrication dimension	$2000\ mm \times 1500\ mm \times 750\ mm$	$500\ mm \times 280\ mm \times 325\ mm$
Major application	Repair worn parts; Add new features on built parts; Direct manufacturing of parts;	Rapid prototyping; Direct manufacturing of parts

Efforts are underway to deepen our understanding of both the LPF-AM and LPB-AM processes through modeling. Numerous models have been developed to build the relations between the process, microstructure and properties, and may be roughly categorized as numerical, analytical and empirical/statistical. Although process modeling has attracted considerable academic attention, it has still been outpaced by the growth of AM technology [6]. Improved comprehensive and time-efficient process models are urgently needed for both the LPF-AM and LPB-AM processes, so as to optimize the processing parameters and to achieve real-time process control. By building the comprehensive and time-efficient process models, the LPF-AM process and LPB-AM process may finally become automatic operations governed by real-time diagnostics and feedback control, producing desirable parts with tailored mechanical properties.

1.2. Motivation

To date, the low-level reliability and repeatability of both LPF-AM and LPB-AM are still the major barriers for their industrial application [7,8]. Fabricated components' mechanical properties, dimensional accuracies and surface finishes are quite inconsistent and are susceptible to overly complex process parameters. Numerous defects, i.e., cracks, pores, and lack of fusion may be induced due to improper parameter settings, and significantly increase unnecessary follow-up costs. By contrast, full-density and high-performance parts can be fabricated based on optimized process parameters for both LPF-AM [9] and LPB-AM [10].

In addition, both the LPF-AM and LPB-AM processes have a high sensitivity to process perturbation and external disturbances [11,12]. A small change of process parameters (e.g., laser absorptivity, scanning speed) or processing surroundings (ambient temperature, oxygen level) may induce significant variations in the transient temperature field, heating/cooling rate, and the overall melt pool shape, eventually influencing process stability and fabricated parts' properties. Moreover, up-to-date multi-physics models (e.g., the finite element method based numerical model) are rarely adopted for process optimization or real-time control due to the extremely high computational cost, complexity and lack of testing. The developed simple and fast analytical process models are challenged by low prediction accuracy due to the omission of the major physical mechanisms in the process. The developed empirical models can be time efficient, but their statistical nature limits their application and accuracy.

To address these challenges, accelerated process modeling with improved fidelity as an alternative method has gained increasing attention from both academia and industry. Process modeling is a classic way of understanding the unfamiliar aspects of a process. More specifically, accelerated process modeling can serve as a bridge to link the process parameters to the target properties of the fabricated components, thus regulating the LPF-AM and LPB-AM processes to reduce the defects and achieve high fabrication quality. Additionally, a time-efficient process model is essential to provide process-fluctuation prediction and acts as a benchmark reference generator inside the structure of closed-loop control systems, providing a sound platform for the real-time control of LPF-AM and LPB-AM and significantly improving process reliability and stability.

Additionally, the LPF-AM process has been troubled by low catchment efficiency. With the widespread use of compressed carrier gas for powder feeding (known as blown-powder feeding) in LPF-AM, the low powder catchment induced by the diverging powder stream is increasingly apparent. Research shows that higher catchment efficiency can be achieved when most powder strikes the center of the laser beam [13]. Efforts are underway to concentrate diverging powder stream but have gained limited application due to the involved complex systems (e.g., aerodynamic focusing [14]) and the reduction of powder feed rate (cyclone nozzle system [10]). With the development of magnetic focusing techniques, powder stream may be concentrated in a fast and non-contact way by external magnetic force.

Motivated by these research gaps, accelerated process modeling that incorporates major process physics is conducted for the two most commonly used laser metal AM processes: LPF-AM and LPB-AM. In addition, a new electrodynamic concentration approach for focusing the non-ferrous metallic particles in blown powder feeding of LPF-AM is investigated.

1.3. Objectives

The thesis mainly aims to develop time-efficient process models for both LPF-AM and LPB-AM. The desired calculation times of the target models should be at least three times smaller than those of the conventional models (e.g., $8\sim23\ ms$ [15,16] for LPF-AM, $10\sim20\ ms$ [17,18] for LPB-AM), to achieve the fast process optimization and fulfill the lower bound requirement for the response times ($100\ ms$ [19] for LPF-AM, $0.1\ ms$ [20] for LPB-AM) of the thermal feedback control systems in LPF-AM and LPB-AM. Another goal is to explore a magnetic non-contact approach to focusing the diverging particles in the gas-powder stream of LPF-AM so as to improve powder catchment. To achieve these goals, the following objectives will be pursued:

- Developing a coupled laser beam and powder stream interaction module in LPF-AM while considering associated spatial distribution and attenuation.
- Developing a powder catchment module in LPF-AM while considering powder mass distribution and the geometry variation of the molten pool.
- Exploring a magnetic focusing approach to concentrating the diverging particles (conducting non-ferrous particle) in the blown-powder feeding of LPF-AM.

- Designing and fabricating a strong permanent magnet source, based on a Halbach array, with which to test the proposed concentration generator.
- Developing time-efficient process-thermal models for both LPF-AM and LPB-AM, incorporating the major physics mechanism in the processes.
- Characterizing the mechanical properties of the parts fabricated via LPF-AM and LPB-AM.
- Multi-objective optimizing of LPB-AM to improve the build rate and simultaneously optimize fabrication quality.

1.4. Thesis Outline

The thesis includes ten chapters, laid out as Figure 1-1. Chapter 1 presents an overview of the background, motivation and objectives of the research. Chapter 2 reviews on the state-of-the-art metallic additive manufacturing with both LPF-AM and LPB-AM. Chapter 3 presents a module for coupling powder stream and laser beam in the LPF-AM process. In Chapter 4, a new magnetic concentration approach for conducting metal particles in the gas-powder stream of LPF-AM is investigated and the associated concentration module is built. Chapter 5 and Chapter 6 systematically elaborate on the modeling for the LPF-AM and LPB-AM processes, respectively. In Chapter 7, the built process model of LPF-AM is utilized to predict the real-time thermal characteristics, solidification parameters and microstructure. Chapter 8 presents the application of the built LPF-AM model in estimating the thermal cycles and layer-wise hardness for thin-wall structures. In Chapter 9, a multi-objective optimization of the LPB-AM process is conducted using the built model to achieve the maximum real-time build rate while maintaining high fabrication quality. Chapter 10 presents the major conclusions of this research in modeling of LPF-AM and LPB-AM and powder stream focusing. Based on these conclusions, possible future work is briefly introduced.

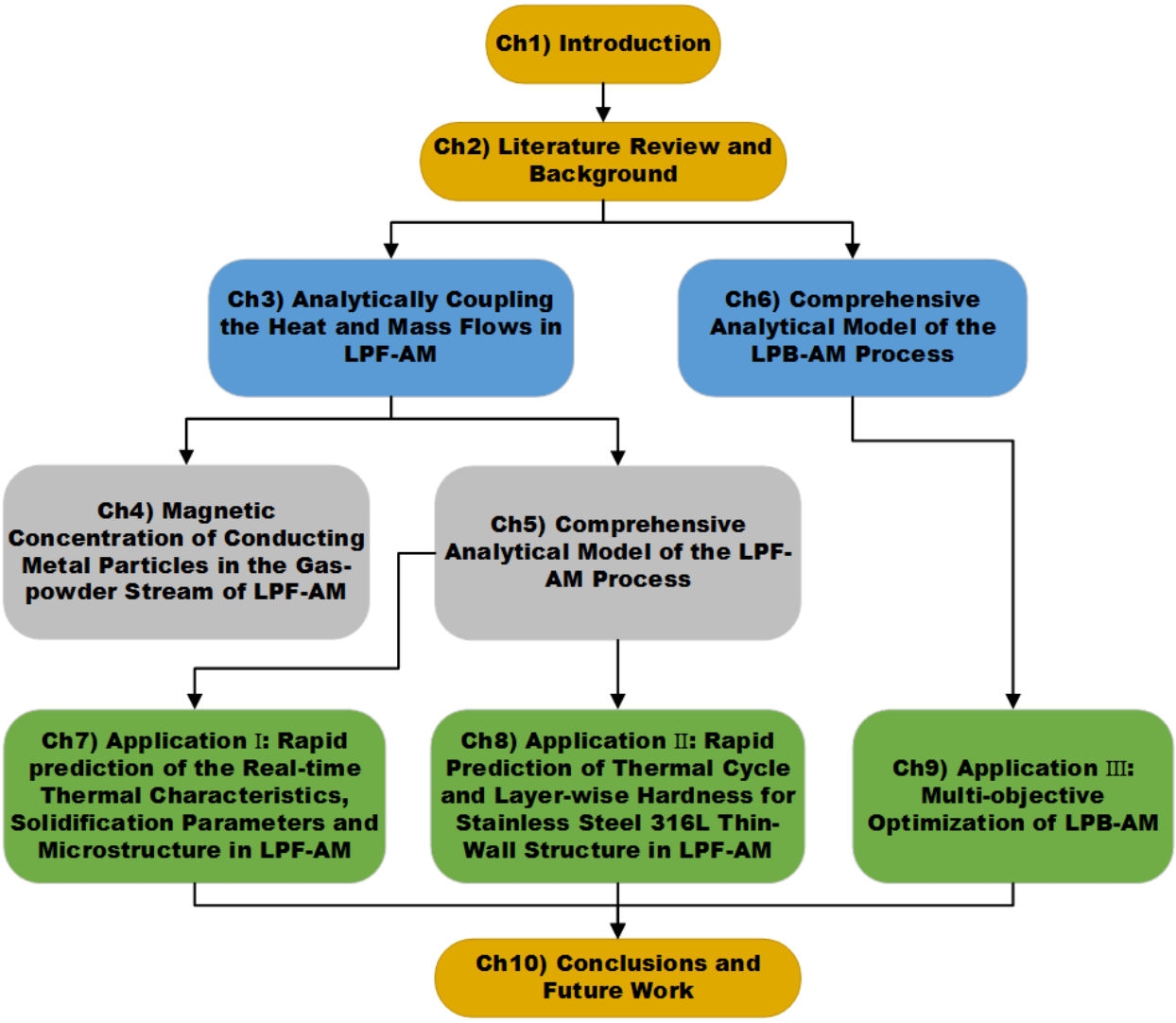

Figure 1-1. Thesis outline

Chapters 3-9 are adapted from author's published, submitted or will be submitted work as following:

Chapter 3

- Huang, Yuze, Mir Behrad Khamesee, and Ehsan Toyserkani. A Comprehensive Analytical Model for Laser Powder-fed Additive Manufacturing. Additive Manufacturing 12 (2016): 90-99. https://doi.org/10.1016/j.addma.2016.07.001

Chapter 4

- Huang Yuze, Mir Behrad Khamesee and Ehsan Toyserkani. Electrodynamic Concentration of Non-ferrous Metallic Particles in the Moving Gas-powder Stream:

Mathematical Modeling and Analysis. International Journal of Magnetics and Electromagnetism. 5, (2019):019.

Chapter 5

- Huang, Yuze, Mir Behrad Khamesee, and Ehsan Toyserkani. A New Physics-based Model for Laser Directed Energy Deposition (Powder-fed Additive Manufacturing): From Single-track to Multi-track and Multi-layer. Optics & Laser Technology 109 (2019): 584-599.https://doi.org/10.1016/j.optlastec.2018.08.015

Chapter 6 and Chapter 9

- Huang Yuze, Hamed Asgari, Zhang Zhidong, Mohammad Ansari, Mir Behrad Khamesee, Ehsan Toyserkani. Process Modeling and Optimization of Laser Powder-bed Fusion Additive Manufacturing: Formulation, Verification and Multi-Objective Optimization. The manuscript will be submitted for publication.

Chapter 7

- Huang Yuze, Mohammad Ansari, Hamed Asgari, Mohammad Hossein Farshidianfar, Dyuti Sarker, Mir Behrad Khamesee, Ehsan Toyserkani. Rapid Prediction of Real-time Thermal Characteristics, Solidification Parameters and Microstructure in Laser Directed Energy Deposition (Powder-fed Additive Manufacturing). Submitted to Journal of Materials Processing Technology (Under review).

Chapter 8

- Huang Yuze, Mohammad Ansari, Hamed Asgari, Mir Behrad Khamesee, Ehsan Toyserkani. Rapid Prediction of Thermal Cycle and Layer-wise Hardness for Stainless Steel 316L Thin-Wall Structure in Laser Directed Energy Deposition (Powder-fed Additive Manufacturing). The manuscript will be submitted for publication.

Similar versions of these published, submitted or will be submitted work have been modified to fit the content of the thesis. The corresponding license agreements are provided in the section of Letter of Copyright Permission.

Chapter 2. Literature Review and Background

This chapter primarily addresses major aspects and characteristics of both LPF-AM and LPB-AM, including the physical aspects, process parameters, application and challenges. Critical governing equations and corresponding boundary conditions for heat conduction equations are also presented in this chapter. Additionally, major magnetic techniques for particle manipulation are summarized.

2.1. LPF-AM Process

LPF-AM setup typically consists of a high-energy laser system, a powder-feeding module, a displacement system with computer numerical control (CNC) and a worktable as illustrated in Figure 2-1. In the LPF-AM process, the metal powder is delivered through a carrier inert gas stream onto the substrate/object surface, which is melt immediately by a high-energy laser source and solidified as the laser passes away. According to the predefined scanning pattern, further powder is deposited, melted and solidifies to form new features on an existing substrate/object in a layer-by-layer approach.

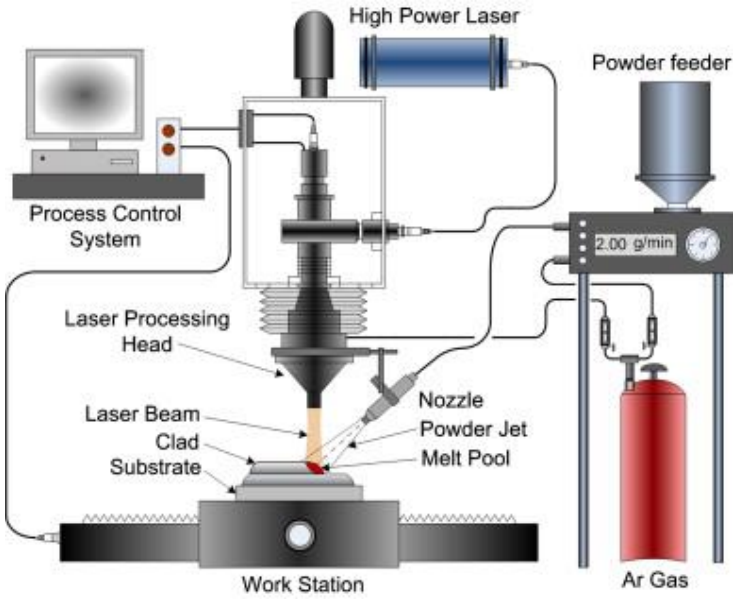

Figure 2-1. Schematic of the lateral LPF-AM setup. Reproduced with permission from [21]. Copyright © 2009 Elsevier Ltd.

Generally, LPF-AM can be classified as two main types, depending on the configuration of the powder feeding: lateral powder feeding and coaxial powder feeding as shown in Figure 2-2.

Lateral powder feeding (Figure 2-2 (a)) holds a higher powder catchment, whereas coaxial powder feeding (Figure 2-2 (b)) possesses more degrees of freedom that enables the coaxial feeding to be more specifically suited for complex-shaped parts fabrication.

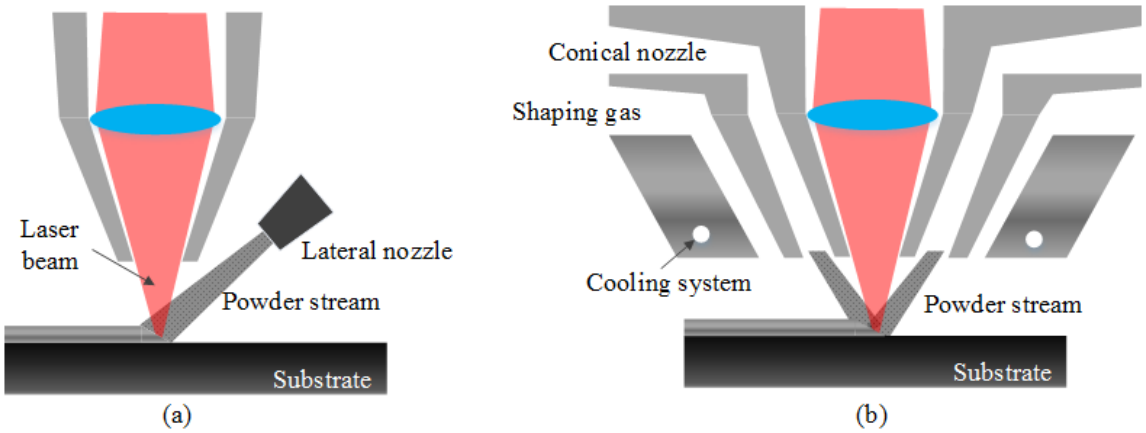

Figure 2-2. Schematic of (a) lateral powder feeding and (b) coaxial powder feeding of LPF-AM.

2.1.1. Physical Aspects and Process Parameters of LPF-AM

From the instant melting and solidification of the powder material in the small melt pool, to the final large parts fabrication, a great number of physical phenomena (e.g., heat conduction, heat radiation, melting, convection, solidification and wetting) occur during the LPF-AM process. Additionally, these physical phenomena play a significant effect on final parts' quality and they are governed by the process parameters. Therefore, understanding these physical events and their relations to the process parameters are crucial to achieve desirable fabrication quality.

The important physical events and the associated governing process parameters are illustrated in Figure 2-3 by following the heat and mass transfer path in LPF-AM. As seen, the LPF-AM process mainly include two steps: the first step is heat and mass delivery; the second step is heat and mass interaction. The physical events in these two steps mainly include laser source ignition, gas-powder delivery, powder stream and laser beam interaction, melt pool formation by heat conduction, heat loss by radiation and convection, melt pool fluid dynamics, liquid melt pool wetting, contact angle variation, rapid solidification and final shrinkage as the solidified metal cools to ambient temperature. All these events and their corresponding sub-events are controlled by the associated process parameters as listed in Figure 2-3.

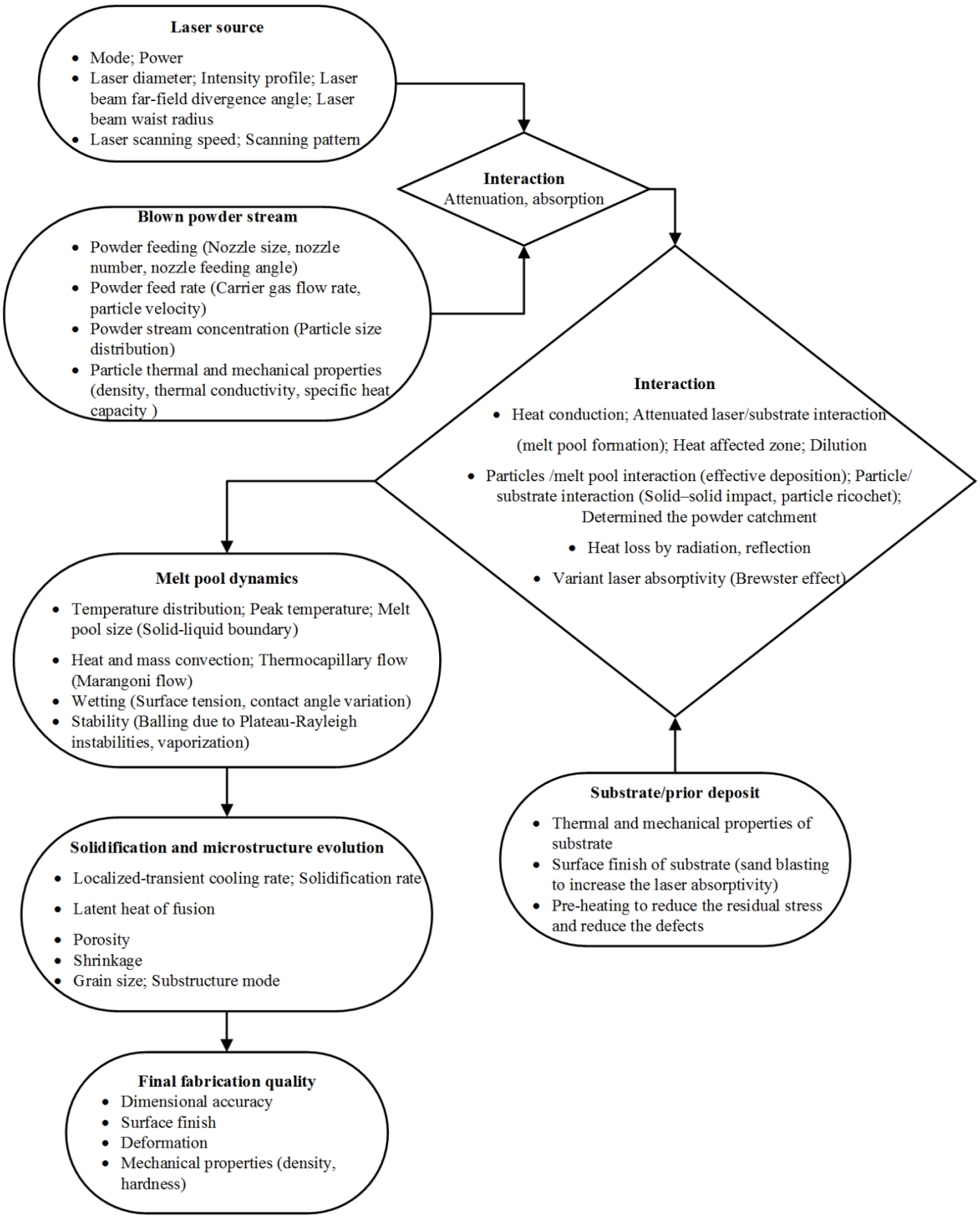

Figure 2-3. Major physical events and the main process parameters in the LPF-AM process

In addition, some of the physical events are sensitive to the external disturbances. For instance, the increased oxygen level in the fabrication environment may induce severe oxidation of a deposited layer, which may deteriorate the melt pool wetting and affect the following layers adhesion with the prior deposits. Moreover, the interaction effects of the process parameters play significant roles on some physical phenomena. For instance, the melt pool size and its thermal distribution are mainly governed by the combination effect of the powder feed rate, scanning speed and laser powder. Therefore, the processing parameters should be optimized under an overall consideration of the processing parameters.

2.1.2. Application and Challenge of LPF-AM

The LPF-AM process holds many advantages over the conventional coating and manufacturing processes, i.e., arc welding, plasma spraying and casting, due to the adoption of fine laser heat source and its layer-upon-layer material adding nature. LPF-AM can produce 3D parts or additional features with minor heat affected zone (HAZ), fair fabrication accuracy, small dilution (percentage of surface layer composed by melting the substrate) by direct depositing metallic materials on the subject surface in a one-step process. Subsequently, LPF-AM eliminates the intermediate manufacturing process (e.g., side cutting, holes drilling) and reduces overall weight (e.g., less number of joints/fasteners) and fabrication time. Moreover, LPF-AM is able to achieve the production of functional-grading composites [22,23].

The functionality of LPF-AM has attracted multiple industries to embrace its features for 3D parts fabrication [24], surface coating [25], and worn out components repair [26] from single to multiple materials. Nowadays, the LPF-AM repaired/fabricated complex-shaped parts have been widely used for aircraft components [27,28], automobile parts [29,30], biomedical implants [31]. For instance, repaired turbine blade by LPF-AM as shown in Figure 2-4 (a) that was previously regarded as non-repairable by conventional processes. Additionally, the complex-shaped blades can also be directly fabricated by LPF-AM as illustrated in Figure 2-4 (b).

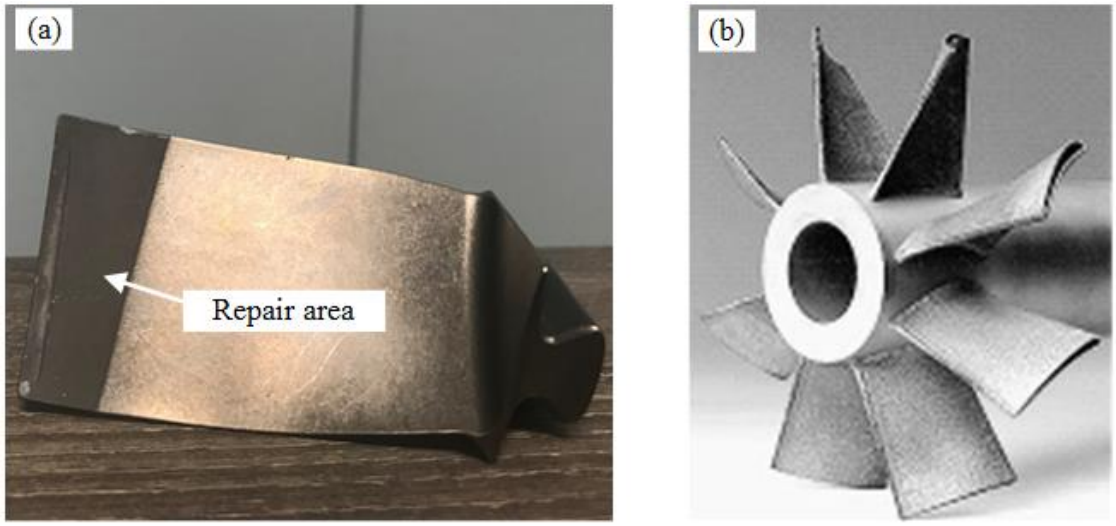

Figure 2-4. Application examples of LPF-AM. (a) Damaged blade repair. (Source: Courtesy of Multi-Scale Additive Manufacturing Laboratory, University of Waterloo). (b) Manufactured blades by LPF-AM. Reproduced with permission from [32]. Copyright © Springer-Verlag Berlin Heidelberg 2013.

Although LPF-AM has been successfully used for metal parts repair and complex-shaped components fabrication, the LPF-AM process still faces significant challenges that hinders its wider adoption by industry.

(1). Powder catchment. The powder catchment efficiency can remain quite low in the LPF-AM process (less than 20% for coaxial powder feeding [33] and less than 50% for lateral powder feeding [34]). Even if the un-melted particles can be collected and reused, the whole cost of the process is significantly increased due to the low catchment efficiency.

(2). Energy efficiency. As per the prior study of Gedda et al. for the LPF-AM process with a CO_2 laser source [35], only 40% of the laser energy is used to melt the powder and the substrate. Roughly, 60% of the laser power is wasted.

(3). Process optimization. The current process optimization is primarily conducted by the trial-and-error experimental approach, which is highly expensive and time costly to run numerous experiments for achieving the optimal process parameters of each new type material. Moreover, experiment-based optimization results may be different for various LPF-AM systems even with same deposition material due to variant configurations.

(4). Surface finish. Component fabrication accuracy for LPF-AM is of $0.02\sim0.4\,mm$ as reported by Mazumder et al. [36]. The surface roughness of the fabricated parts by LPF-AM is reported as $Ra = 7\sim20\,\mu m$ [5]. However, high surface finish is necessary for

most industry application. For instance, tooling parts generally requires a surface finish in the order of 1 μm [37]. Therefore, post-processing is recommended for those applications that further increase the cost.

(5). Process control. As reported by Tang [38], utilization of constant processing parameters may result in thermal distortion, excessive dilution and cracking. Furthermore, the LPF-AM process has a highly localized and dynamic thermal behavior. This may result in undesirable microstructural features and inconsistent mechanical properties of the fabricated parts due to the change of local processing conditions (e.g., accumulated heat may persist in the previous layers that increases the localized temperature) [39]. Therefore, achieving the adaptive and time-variant processing adjustment by in-situ feedback and control response is highly needed. However, the current real-time monitoring systems are limited to the in-situ thermal/dimensional measurement (e.g., melt pool temperature, deposition height) by thermal/optical sensors, very limited characterization tools is applicable for on-line microstructure monitoring. Moreover, interaction effect between process parameters is significant for the fabrication quality; different combinations may result in variant microstructures. Accordingly, process parameters should be adjusted with reference to other parameters [40]. Nevertheless, time-efficient process models that are capable to provide the on-line process fluctuation prediction and optimize the parameters combinations inside the closed-loop control systems are very limited.

(6). Functionally graded materials (FGM) parts manufacturing. FGM parts are featured by heterogeneous material composition and microstructure that change gradually over the whole part [41], which is capable to adjust the distribution of properties for achieving designed functions [42]. However, to achieve successful FGM deposition, the real-time processing needs to consider both the material-based aspects and their interaction effect for choosing proper parameters and the associated deposition path. Therefore, real-time control of the process is necessary. However, it would be very challenging to measure the real-time features due to the variant emittance of each material [33]. In addition, time-efficient process models that incorporate multi-material properties for in-situ control are very limited.

2.2. LPB-AM process

LPB-AM setup typically consists of a high-energy laser source, scanning mirror module (control the scanning position), powder supply system (automatic dispenser powder bed with a feed piston, a build piston and a recoater) and an inert gas filled machining chamber as shown in Figure 2-5. In the LPB-AM process, the laser beam is guided to melt the thin layer metallic powder ($20\sim100\ \mu m$ [43]) based on the predefined scanning patterns in a layer-by-layer approach. Once a layer scanning is done, the build platform will be lowered down by one-layer thickness. Subsequently, a fresh powder layer will be spread evenly on the top build surface by means of a recoater/roller and the process will repeat itself until the whole part is completed. Generally, fiber lasers with $1.06\sim1.08\ \mu m$ wavelengths and hundreds of watts power are used in the LPF-AM process [44]. Inert gas, i.e., nitrogen and argon, is utilized to fill the internal chamber to avoid oxidation. To reduce the residual stress and fabrication defects (e.g., cracks), the internal chamber is generally preheated to a fixed temperature of roughly 353 K.

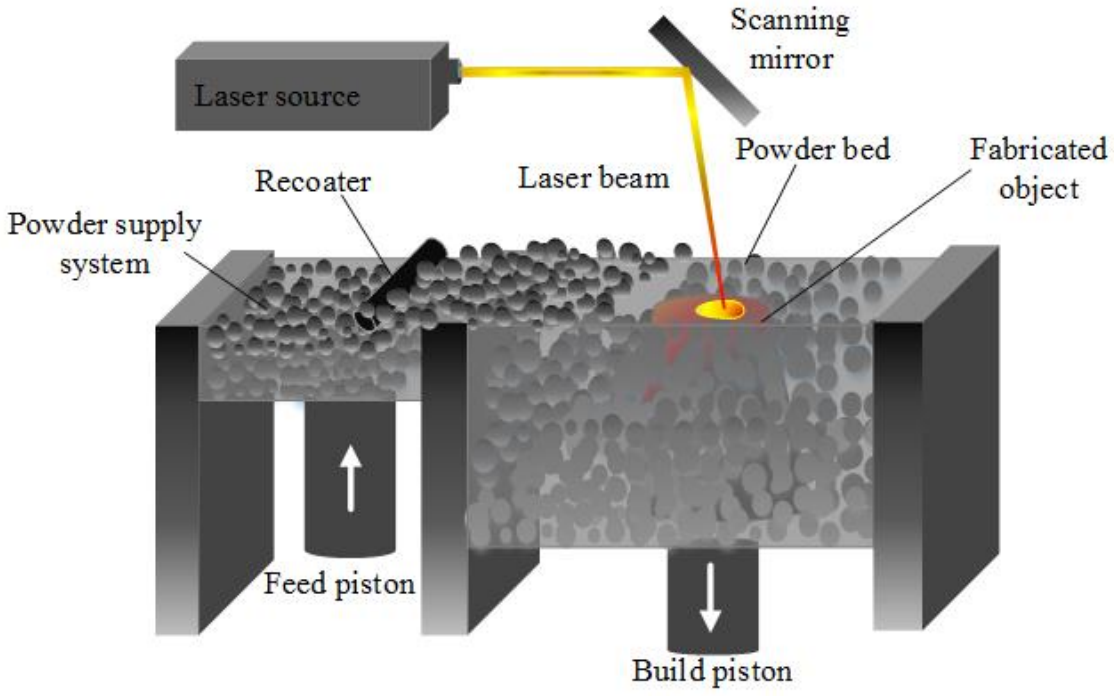

Figure 2-5. Schematic of LPB-AM setup.

LPB-AM can be roughly clarified as partial melting (binder material is liquefied while the structural material remains solid) and full melting with reference to the nature of the fusion process. The former one is also named as selective laser sintering (SLS) and the later one is

called selective laser melting (SLM). Driven by the high mechanical property requirement of the fabricated components from industry, this thesis focuses on the full melting process of LPB-AM, which can generally produce near full dense parts.

2.2.1. Physical Aspects and Process Parameters of LPB-AM

The LPB-AM process includes a sequential heating and melting of the powder material and a fast solidification of the melted powder. This process involves a number of physical phenomena that happen on quite different length and time scales. For the length scale spanning, phenomena are ranging from centimeters of the final parts shrinkage to the micrometers of the laser beam and particle interaction (e.g., absorption, scattering). In the time scale scanning, the phenomena cover hours of overall thermal cycles during the fabrication to the milliseconds of melt pool formation and solidification [45]. Understanding these physical phenomena and identifying their interplay and relations with the governing process parameters are crucial for successful part fabrication.

Major physical phenomena and the corresponding process parameters are shown in Figure 2-6 by following the general process chain of the LPB-AM process. As seen, the physical events mainly occur in the laser beam and powder bed interaction stage, including laser absorption, laser penetration, scattering, thermal radiation, thermal convection, evaporation and rapid solidification. Some of these phenomena are related with each other and are affected by the process parameters. For instance, the amount of laser absorptivity was affected by the laser penetration depth, which is further governed by the process parameters, i.e., particle size, powder bed porosity and laser wavelength [46].

In addition, to achieve a higher degree of fabrication quality, variant processing parameters are widely used for different fabrication zones in the LPB-AM process. Taking the EOS machine system as an example, the major body of the fabricated parts may be set with the hatching parameters, while the edge part may be applied with the contouring parameters that typically has a lower laser power and smaller scanning speed compared to the hatching parameters.

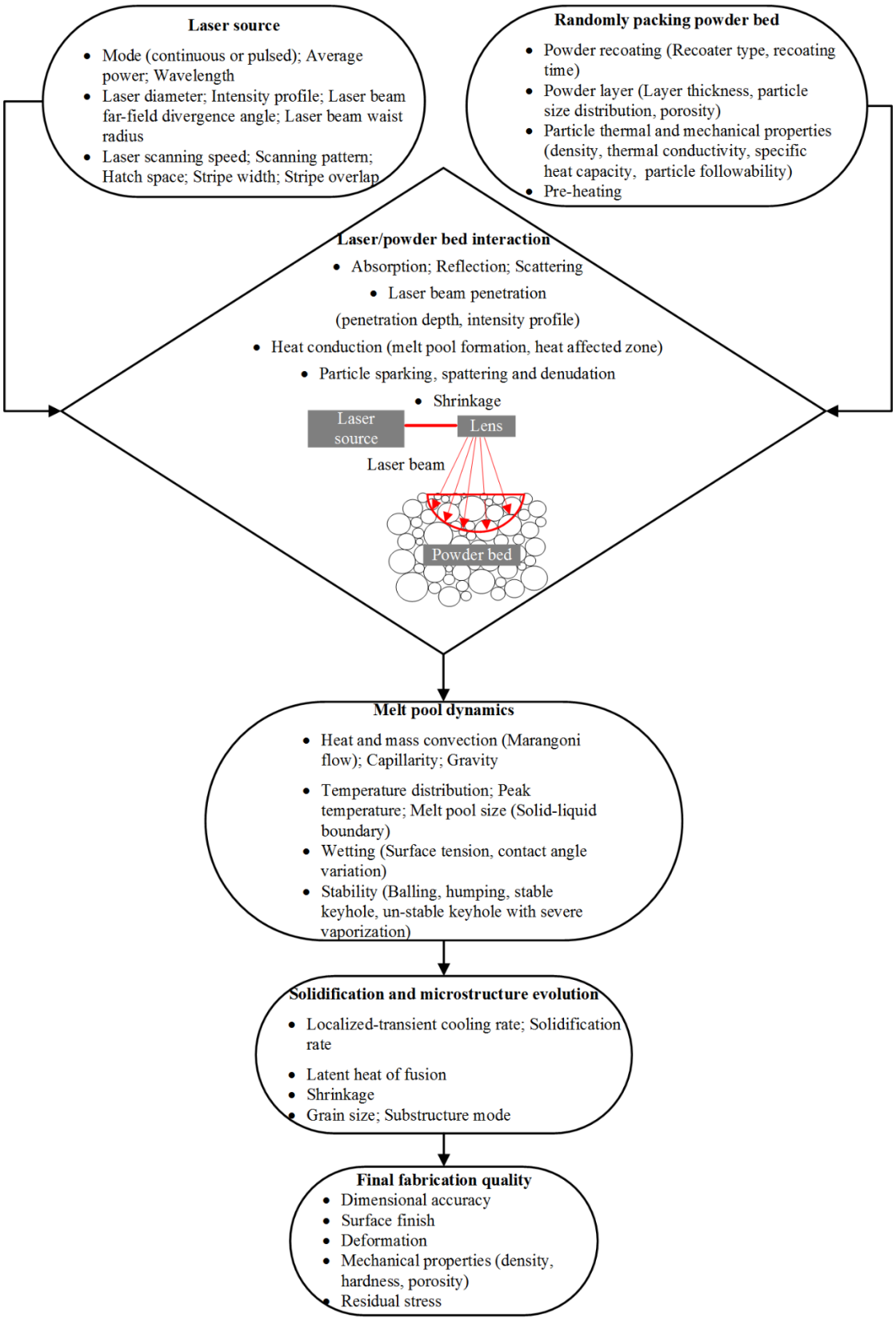

Figure 2-6. Major physical phenomena and the main process parameters in the LPB-AM process

2.2.2. Application and Challenges of LPB-AM

LPB-AM is finding critical applications in multidisciplinary areas, i.e. dental sector, aerospace and automotive industries [47], making full-density complex-shaped metal parts. Especially, the extremely high cooling rate (10^4~10^6 K/s) of the LPB-AM process can lead to much finer grain size and superior strength of the fabricated parts as compared with traditionally manufactured counterparts [48]. However, the cost to run the LPB-AM process is typically much higher than that of the conventional manufacturing processes. Therefore, the LPB-AM is currently limited to the fabrication of high-value parts.

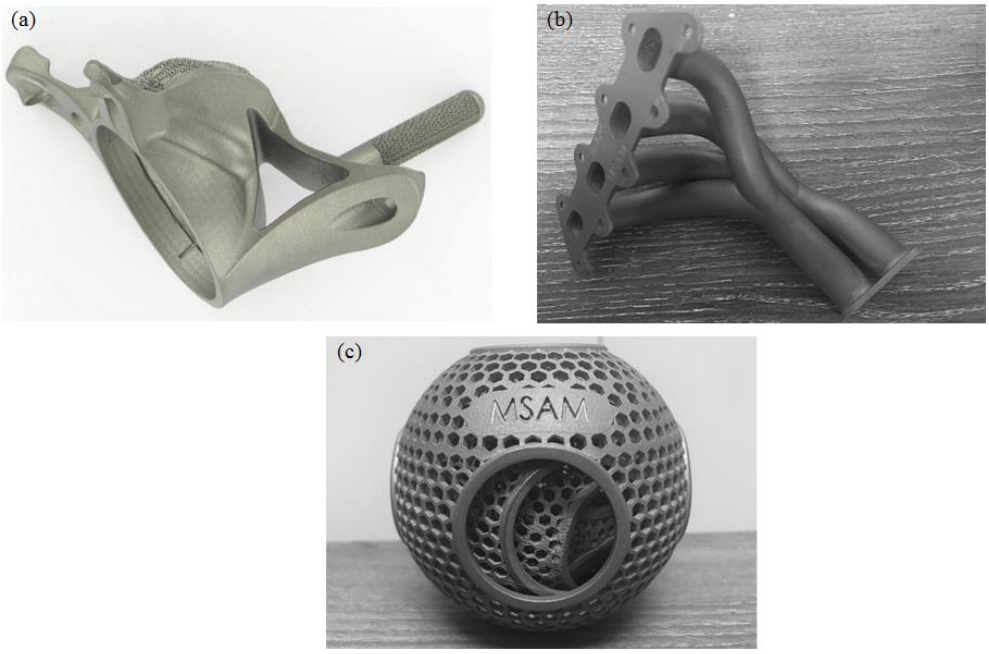

Figure 2-7. Application examples of LPB-AM. (a) Partial hip replacement. Reproduced with permission from [49]. Copyright © 2017 Elsevier Ltd. (b) Complex-shaped tubes (Source: Courtesy of Multi-Scale Additive Manufacturing Laboratory, University of Waterloo). (c) Cellular lattice structures (Source: Courtesy of Multi-Scale Additive Manufacturing Laboratory, University of Waterloo)

As summarized by Yap et al. [50], LPB-AM has been utilized for dental prostheses [51] and body implants [52], which can be customized to meet the customers' individual requirement. In addition, LPB-AM has been used to produce the cooling channels [53] and complex-shaped tubes owing to the high freedom of design advantage. Moreover, LPB-AM has been expanded to make complex lattice structures (e.g., cellular lattice structures [54]) for weight reduction. The

examples of the fabricated parts for the application of body implants, complex-shaped tubes and complex lattice structures are presented in Figure 2-7 (a), (b) and (c), respectively.

Although the LPB-AM process has been widely used for producing full dense and near net-shape metal parts, there are still many challenges for LPB-AM to be fully adopted by the industry.

(1). Cost of powder material. The size, shape and surface finish of the metallic particle play significant roles in the mechanical property (e.g., density) of the fabricated components by LPB-AM [55]. However, the cost for the metallic powder with proper morphology and dimension is relatively high. The spheroidized titanium powder may range in the price from $260 to $450 per kilogram, other powder material such as Niobium is even higher, roughly $1200 per kilogram [56]. Despite the fact that un-melted powder can be reused, some particles among the un-melted feedstock may be partially sintered, creating non-spherical or satellite-like particles. In addition, oxides and soot may be formed that further propagate chemical impurities in the feedstock. All these phenomena may induce porosity and increase the surface roughness of the fabricated components [57,58].

(2). Process optimization. Similar to the LPF-AM process, the current process optimization is predominantly conducted by the trial-and-error experimental approach in the LPB-AM process. However, as reported by Yadroitsev [5], there are more than 130 parameters could affect the fabrication quality in LPB-AM. Therefore, it might be highly expensive to run the experiments for achieving the optimal process parameters for each new type of material. Moreover, the large dimensional and time mismatches between the fabrication features (laser beam and layer thickness are in the order of $\sim 10\ \mu m$, scanning speed is of $\sim 1\ m/s$ [59]) and the final fabricated parts ($> 1\ cm^3$ in dimension and $> 1\ hour$ fabrication time) significantly increase the computational cost of the LPB-AM models. Especially for the high fidelity and multi-physics models, the extremely high computational cost bans their application for process optimization.

(3). Build volume and build rate. Owing to the limited volume of both powder supply systems (e.g., powder bed) and inner fabrication chambers, the maximum part size of LPB-AM fabrication is reported as $500\ mm \times 280\ mm \times 325\ mm$ [5]. In addition, as laser beams have a relatively small spot size ($50\sim200\ \mu m$ in diameter) and layer thicknesses are generally set in the small range of $20\sim60\ \mu m$, the processing rate of the LPB-AM

process is relatively low. Moreover, to avoid inter-layer or inter-track porosities, additional re-melting of adjacent tracks/layers will be required in the LPB-AM process. Therefore, conservative process parameters are adopted that further lower down the build rate. The build rate of LPB-AM is around $5{\sim}20\ cm^3/h$ [5] and it typically takes hours or days for large-sized component fabrication by LPB-AM.

(4). Energy efficiency. As per to the case study of Mishra [60], the energy efficiency of a 180W laser beam ranges from 5% to 11% for stainless steel powder fabrication in the LPB-AM process. Depending on processing parameters and powder materials, energy efficiencies of the LPB-AM process are around 2% ~ 20%. The reflection loss is around 50% ~ 60% for metallic powder material; roughly, 20% ~ 30% energy is utilized for the re-melting of surrounding layers and heating of the substrate.

(5). Multi-material manufacturing. Currently, LPB-AM is limited for single-material processing that hinders its application in FGM parts manufacturing. Unlike the blown powder feeding in the LPF-AM process, the LPB-AM process utilizes the dispenser-like powder bed to feed the powder in a layer-by-layer approach. It will be a great challenge for the present recoater to uniformly allocate the multi-materials powder mixture to form a homogenous layer. Furthermore, the current powder recycling system is not adaptable for multi-material powder mixtures. Nevertheless, research for redesigning the whole process chain of LPB-AM to achieve the multi-material processing is ongoing [61].

(6). In-process sensing and control. In-situ process monitoring and robust control are highly needed for the LPB-AM process to improve the part quality and reproducibility. However, a large number of difficulties exist for in-process sensing and control in the LPB-AM process. Current predominant in-process sensing approaches are limited to monitor the in-situ electromagnetic signatures (e.g., electromagnetic emission) of the melt pool and the surrounding HAZ, which are challenged by the data management [44]. With reference to the fast laser scanning speed ($\sim 1\ m/s$) and the laser focusing area ($50{\sim}200\ \mu m$ in diameter), sensors should have a high sampling frequency and resolution, which significantly increases the cost of the sensor system. In addition, the computational efficiency of the existing models allows for off-line optimization or feedforward control only [62], prohibiting the feedback control application. While off-line optimizations and feedforward controls can promote the fabrication quality, these methods may not

guarantee a defect-free fabrication due to the unpredictable process perturbations. Advanced model-based feedback control allows for intelligent alterations of processing parameters with reference to the measured in-situ process signatures, providing process perturbations to improve process reliability and repeatability [20]. However, time-efficient process models of LPB-AM are very limited.

2.3. Process Modeling

Process modeling has been a quite active research field for both LPF-AM and LPB-AM, ranging from local physical events modeling of the regional domain (e.g., laser and powder stream interaction in LPF-AM, laser beam penetration over the powder bed under LPB-AM) to the whole process modeling throughout the whole process physical domain. Roughly, the process modeling can be categorized as numerical, analytical and empirical/statistical.

2.3.1. Process Modeling of LPF-AM

In the LPF-AM process, the laser beam is attenuated by the powder streams and interacts with substrate/prior layers to form melt pools. Meanwhile, the heated powder will be deposited into the melt pool and the liquid melt pool will solidify rapidly and form new features over the substrate/prior layers. All these physical events will affect the molten pool temperature distribution, solidification characteristics and the dimension accuracy of the layer deposits, leading to a quite unstable production in both fabrication quality and dimensional accuracy. Therefore, these process attributes should be controlled and optimized for a steady process production.

Numerical modeling has been proven to accurately simulate the powder flux distribution [63], laser particle interaction process [64], melt pool formation [65], clad layer geometry [66,67], temperature, velocity and thermal stress fields distribution over the LPF-AM process [68,69]. However, the model accuracy of such numerical models generally relies on the fine discretization or moving mesh, significantly increasing the complexity of process modeling and the computational cost.

Empirical/statistical models developed based on the experimental data have been extensively used for process optimization and control in LPF-AM. Fathi et al. [70] developed a sliding mode

controller for closed-loop control based on a parametric Hammerstein model. Lijun [71] built a generalized predictive controller based on a state space model for predictive control of the melt pool temperature. Jin et al. [72] achieved offline shape deformation control by extending the established Bayesian models from Qiang et al. [73]. Despite these excellent successes, the accuracy of the empirical-statistical models will be directly affected by the corresponding evaluation approaches or experimental conditions, and the models may provide broadly similar but not exactly equal results [6]. In addition, only limited numbers of process variables are taken into consideration in these models, but research from Qi and Mazumder [74] shows that the fabricated part characteristics may be strongly affected by around 12 different factors in the LPF-AM process.

Analytical modeling is a classic way for understanding the physics of the process [6] and has been utilized for process optimization and process control in LPF-AM. Picasso et al. [75] established a simple but realistic analytical model for LPF-AM. Powder attenuation effect for the laser beam was accounted with simple geometry intersecting ratio. Heated powder energy was added together with laser beam energy as the heat source to calculate the substrate temperature field. With the relative simplicity, their model can produce immediate results about scanning speed, powder feed rate and catchment efficiency. Fathi et al. [76] developed a mathematical model of LPF-AM to predict the melt pool depth, dilution and the temperature field with given values of clad height and clad width. They built the mathematical top surface of the melt pool with parabolic equation and solved the heat conduction in substrate to predict the temperature field based on an infinite moving point heat source. Shengfeng et al. [77] proposed a similar analytical model to predict the cladding height and catchment efficiency with assuming the melt pool to be a flat plane on substrate. Experimental results show that the catchment efficiency has the same varying trend with the nozzle angle. Xinyong et al. [78] developed a mathematical model to estimate the catchment efficiency based on mass conservation and kinematic equations, but no consideration was paid to the interaction effect between the laser beam and the particles. Kaplan and Groboth [79] developed an analytical process model to estimate the substrate temperature and the clad geometry based on the process mass and energy balances. It was pointed out that the process powder catchment and laser energy distribution are influenced by the powder flux distribution. Doumanidis and Kwak [80] established an analytical model for clad geometry and melt pool temperature estimation by sequentially solving the mass and energy

balance and the thermal conduction in the substrate. The built model is successfully incorporated into the on-line closed-loop control. Tan et al. [81] established an analytical model to estimate the clad layer geometry based on the on-line temperature measurements. The melt pool was fitted as an ellipse and the powder catchment efficiency was calculated directly as melt pool and the powder stream area ratio. They also considered the powder flux distribution in clad height prediction and indicate that the model can be potentially used for on-line feedback control. Qian et al. [82] developed a multivariable analytical model to predict the steady state melt pool temperature and the single-track dimension. Based on the developed model, a feedback linearization control for the melt pool height and temperature was achieved. More recently, Jianyi et al. [83] extended the above single-track model built by Qian et al. [82] to a multi-layer model by considering the residual heat from the prior layers, where the varying initial temperature model for the following layers was solved by the quasi-steady-state Rosenthal's solution with a dummy moving heat point source.

2.3.2. Process Modeling of LPB-AM

Currently, the majority of the LPB-AM process modeling is focused on the multi-scale modeling [45] that couples the multi-physics of the process through a variety of numerical methods (such as Finite-Element-Method (FEM)) [84]. Nevertheless, there is a considerable dimensional mismatch between the fabrication features (i.e. the dimension of powder particles as tens of micrometers) and the fabricated part (tens to hundreds of millimeters). This dimensional mismatch demands an extremely fine discretization of the processing domain to enable the calculation convergence of the highly dynamic multi-physics by numerical methods. Consequently, extremely high computational cost is required for these numerical models, inhibiting their application in process optimization and online control. For example, the calculation for a 90 μm length simulation by ANSYS software with a 3.2GHz and 8GB of RAM computer took 3763 hours in total [85].

The calculation time is extremely high for the realistic multi-physics and multi-scale modeling of the LPB-AM process. Therefore, recent research works have been focused on the computational reduction models, ranging from effective approximation numerical modeling, empirical/statistical modeling to analytical or semi-analytical modeling. For the effective approximation numerical modeling, the layer-uniformed or track/vector-uniformed heat source

reduction model is widely utilized to replace the localized laser heat source. Loucas *et al.* [86] examined the predicted shape distortions of the fabricated parts by using localized laser heat source, track-uniformed heat source and layer-uniformed heat source. It was observed that a good correlation was reached for the predicted shape distortion of these three heat sources. Peng *et al*. [87] developed a novel thermal circuit network (TCN) model to predict the thermal distortion using a layer-uniformed heat input. The thermal calculation time for each super layer was reduced from 14 hours for the standard FEM model to 2 minutes for their TCN model while sacrificing 15% of accuracy. It should be mentioned, however, that the thermal and dimensional features of the melt pool may not be constant in the entire scanning process. The increments of the melt pool size of adjacent scan tracks were clearly observed in the study of Luis *et al.* [88]. Even these heat source reduction models can provide relatively accurate estimations for the final part-scale shape distortion, large prediction errors may be inevitable for the prediction of localized thermal and mechanical features. Therefore, these models may be competent for process optimization of part-scale characteristics, but might not be qualitied for the prediction of localized features (e.g., melt pool size, in-situ localized temperature and cooling rate). However, the transient-localized thermal and mechanical features provide the vital information that needed for process control.

Empirical/statistical modeling of the LPB-AM process has attracted researchers' attention due to difficulties for mathematically modeling the stochastic physical phenomena (e.g., stochastic powder bed, denudation and spatter) that occur in the LPB-AM process. The data-driven predictive modeling techniques (e.g., artificial neural networks, genetic algorithm and logistic regression) has been widely applied in the empirical/statistical modeling. Park and Nguyen [89] *et al.* built an artificial neural network to optimize the process parameters for achieving desirable density and surface roughness. Luke *et al.* [90] built the regression model of the LPB-AM process using response surface method and further optimized the process by the genetic algorithm to produce void free parts. In addition, Gustavo *et al.* [91] and Chandrika [92] utilized the Gaussian process-based surrogate modeling with data-mining techniques to reduce model computational cost and optimize the process. However, owing to the experiment-data-based nature, these empirical/statistical models may have limitations for variant LPB-AM machine systems as well as various type of metallic powder material. Moreover, these models may not be

applicable for real-time localized thermal features (e.g., in-situ temperature, cooling rate) prediction.

Research on analytical modeling of the LPB-AM process has been increasing due to its relatively low computational cost. Mohanty and Hattel [18] built a pseudo-analytical model to estimate the thermal field. They utilized several existing modeling techniques to accelerate the model calculation in an innovative way. The convective melt pool dynamics were replaced by a high equivalent thermal conductivity and only heat conduction was considered in their model. Equivalent boundary temperature was used for each domain by averaging the temperature of adjacent domains. The temperature at the center discontinuous domain was solved with the analytical Rosenthal's solution. It was found that the calculation time for the thermal solution phase was improved from 18 to 4 seconds by their pseudo-analytical model compared to the FEM-based model with the same 400 elements. The calculation time for each finite element cell was around $10\ ms$. Forslund *et al.* [17] provided a time-efficient thermal field solution for the LPB-AM process with piecewise constant parameters. The thermal solution was calculated analytically by the quadrature scheme, in which a pre-calculated lookup table was utilized for solving the heat conduction equations. For a $20 \times 4\ mm^2$ domain scanning with 32481 nodes, their research showed a total of 683 seconds for the thermal field calculation, which is roughly a calculation time of $20\ ms$ for each node. Yang *et al.* [93] developed a semi-analytical thermal model for the LPB-AM process. Numerical discretization was utilized to decompose the thermal boundary domain. The laser beam area with a steep thermal gradient was solved by the analytical Green's function, while the complimentary domains were solved by finite differences with a coarse discretization. Subsequently, the thermal solution was calculated by summing up the transient temperature solutions of the point sources based on the superposition principle. It was shown that the computational time for 20 tracks scanning in a domain ($2 \times 2 \times 2\ mm^3$, with cell size $0.5\ mm$) is 16.5 seconds, which is about $250\ ms$ for each single cell.

In a recent study, Steuben *et al.* [62] enriched the analytical heat conduction solution of Green's function with temperature-dependent material property and realistic domain geometry. This showed comparable results to those of solved by numerical methods (e.g., FEM) but with six orders of lower computational cost. Their research showed that the temperature calculation time for single point is around 100 μs using an Intel-i7 quad-core based computer platform, with great

potential to be utilized for the in-situ thermal feedback control of LPB-AM. Nevertheless, some crucial physical factors (e.g. powder bed porosity, laser absorptivity) and dimensional features were not considered in their calculations.

2.3.3. Governing equations and boundary conditions of analytical thermal modeling

To achieve the objective of time-efficient process modeling for both the LPF-AM and LPB-AM process, the thesis focuses on the analytical modeling that can be utilized for fast process optimization and potentially be used for real-time process control.

According to the Fourier's second law [94], the heat transfer in both the LPF-AM and LPB-AM process can be expressed as,

$$k\nabla^2 T - \rho c_p v \nabla T = \rho c_p \frac{\partial T}{\partial t} - Q \tag{2-1}$$

where k is the thermal conductivity, T the temperature, ρ the density, c_p the thermal capacity, v the scanning speed, t the time and Q is the generated heat per unit volume. In both the LPF-AM and LPB-AM process, the majority of the laser energy is absorbed by the substrate/prior layers to form the melt pool through heat conduction. The volume heat Q can be ignored while neglecting the heat dissipation or phase transformation [62]. Accordingly, Equation (2-1) can be simplified as the heat conduction equation [95],

$$\frac{\partial}{\partial x}\left(k\frac{\partial T}{\partial x}\right) + \frac{\partial}{\partial y}\left(k\frac{\partial T}{\partial y}\right) + \frac{\partial}{\partial z}\left(k\frac{\partial T}{\partial z}\right) = \rho c_p \frac{\partial T}{\partial t} \tag{2-2}$$

Here a homogeneous thermal conductivity $k_x = k_y = k_z = k$ is assumed. Therefore, for an instantaneous heat source $q(X,t)$ over the semi-infinite homogeneous $\Omega = \mathbb{R}^2 \times \mathbb{R}^-$ space domain, the transient temperature rise $\Delta T(X,t)$ of point X= (x, y, z) for time moment t can be solved as [95]:

$$\Delta T(X,t) = 2\int_{\tau=0}^{\tau=t}\iiint_{\Omega} G(x-x',y-y',z-z',t-\tau)\frac{q(x',y',z',\tau)}{\rho c_p}dx'dy'dz'\,d\tau$$
$$G(X,t) = \left(\frac{1}{4\pi\alpha t}\right)^{3/2} exp\left(-\frac{|X|^2}{4\alpha t}\right) \tag{2-3}$$

where $\alpha = k/\rho c_p$ is the thermal diffusivity and $G(X,t)$ is the Green's solution. The boundary condition for above Equation (2-3) is:

$$\frac{\partial T(X,t)}{\partial x} = \frac{\partial T(X,t)}{\partial y} = \frac{\partial T(X,t)}{\partial z} = 0, on\ \Omega\ \text{boundary} \tag{2-4}$$

2.4. Particle concentration techniques

Currently, the highly active techniques for small-size particle concentration or separation might be clarified as (1) aerodynamics concentration [14], (2) acoustic concentration [96] or separation [97], and (3) magnetic concentration (e.g., ferromagnetic nanoparticles [98,99]) or magnetic separation (e.g., ferromagnetic particle [100,101] and nonmagnetic particles [102]). Magnetic techniques have been attracting the attention of researchers due to its fast response and non-contact nature.

To the best of author's knowledge, none of the developed magnetic techniques has been utilized for the relatively large-sized (submillimeter) particle concentration as used in the LPF-AM process. However, one of the magnetic separation technique, the eddy current separation (ECS) [103], has been successfully applied for nonmagnetic large-sized (ranging from submillimeter [104] to millimeter [105]) particle separation. Basically, ECS utilizes the induced circulating eddy currents to exert the magnetic force on the conducting particles [106]. The generated magnetic force has a specific direction that deflects the particles towards to the magnetic field strength decreasing direction. Instead of being used for particle separation, the induced magnetic force may be utilized for particle concentration by using a proper magnetic system setup. A possible realization of this idea is to build a magnetic concentration generator, which can provide a non-uniform magnetic field with high radial gradient by a coaxial arrangement. Once particles travel through the concentration generator, the motion of the particle will be driven by radial magnetic force towards to the powder stream center axis.

However, relatively little is known regarding the development of this kind of magnetic concentration generator. In principle, ECS devices that have been used to separate particles with the repulsive magnetic force may be good references. The developed magnetic devices for particle separation are summarized in Table 2-1. These devices are categorized as three types based on the corresponding magnetic sources. With considering continuous powder flows in the

feeding process of LPF-AM, the pulsed electromagnet source may not be applicable for powder stream concentration. Therefore, this thesis explores the particle concentration with both the other two magnetic sources: permanent magnet and high frequency electromagnet sources.

Table 2-1. Developed eddy current separation systems

Magnetic source	Developed systems	Features
Permanent magnet	Vertical eddy current separator [107], Rotating disc [103] or drum [102] separator	Simple construction with economic operation; Particle size range $2\sim5mm$ in diameter.
High frequency electromagnet	Electrodynamic sorting [105]	Complex construction with high energy consumption; Particle size range$1\sim8mm$ in diameter.
Pulsed electromagnet	Pulsed electrodynamic separation [104]	Complex construction with high energy consumption; Potentially applicable for particle with size as small as $200\mu m$ in diameter.

2.5. Summary

The review in this chapter shows that both the LPF-AM and LPB-AM processes have attracted multiple industries to embrace their features for metallic parts fabrication. However, significant challenges still exist that hinder their wider adoption by industry. As summarized, the LPF-AM process is challenged by low powder catchment, low energy efficiency, time-consuming and highly cost process optimization, low surface finish, limited process control and un-reliable FGM parts fabrication. Likewise, the LPB-AM process is troubled by the high cost of powder material, time-consuming and highly cost process optimization, limited build volume, low build rate, low energy efficiency, hardly achievable multi-material manufacturing and the limited in-situ sensing and control.

To accelerate process optimization and improve process reliability through process control, a time-efficient process model is highly needed. Nevertheless, the majority of current developed numerical models tends to utilize the fine discretization or expensive moving mesh refinement, leading to an extremely high computational cost. By contrast, the built empirical/statistical models can be time efficient. However, the statistical nature limits their application for various AM systems and powder materials.

Analytical modeling does not require a fine mesh and can be easily used to integrate or lump major physical phenomena into whole process modeling by building their relationships in a time-efficient approach, which is more specifically suitable for time-efficient process optimization and real-time process control. However, based on the review work, most of the built analytical models for the LPF-AM process have decoupled the mass and energy flows, ignored the changes of the laser power absorptivity due to the varying of clad geometry (Brewster effect), and calculated the molten pool limits only based upon laser power source. As a result, those models may have different prediction accuracy. In addition, the developed analytical models are limited for single-track modeling and ignored the heat accumulation effect during the multi-track and multi-layer scanning. The accumulated heat from the prior layers/tracks may not be completely dissipated by heat conduction before the next layer/track applied due to the high scanning rate. Therefore, the following layers/tracks may form on a locally preheated zone with a higher initial temperature compared with that of the prior layers/tracks, leading to non-uniform melt pool geometries and different wetting conditions.

Likewise, few of the developed analytical models of the LPB-AM process have considered the different melting regimes (e.g., heat conduction, keyhole and balling) in the LPB-AM process, which are accompanied by various physics phenomena. It was reported by Jingjing et al. [108] that the mechanical and microstructural properties of LPB-AM fabricated parts depend highly on the melting mode. The microstructure of the Ti-6Al-4V samples consisted of acicular α' phase and a typical hierarchical structure of martensite under conduction mode, while α' and α lamellae were the main constituent phases in keyhole regime. The experimental study of Ting et al. [109] showed that the fabricated AL7050 samples were characterized with varying surface morphology, defects and microstructure under different melting modes. Therefore, the melting regime as a key factor should be taken into consideration in the LPB-AM process modelling.

Moreover, to narrow down the powder stream divergence and improve powder catchment in the LPF-AM process, general particle concentration techniques were summarized as aerodynamics concentration, acoustic concentration and magnetic concentration. To utilize the non-contact magnetic technique for particle concentration of the diverging powder stream in LPF-AM, the proper magnetic system setup, namely the magnetic concentration generator, should be explored.

As outlined in the review, the permanent magnet and the high frequency electromagnet may work as the magnetic source in the proposed concentration generator.

Chapter 3. Analytically Coupling the Heat and Mass Flows in LPF-AM*

3.1. Introduction

In the LPF-AM process, powder streams interact with laser beams and attenuate the beam intensity, while the heated powder particles impinge into the melt pool adding mass and energy to melt pool and form effective deposition. All these interactions affect melt pool temperature distribution and the final shape of the as-built deposits. This chapter addresses a mathematical module that analytically couples the moving laser beam with Gaussian energy distribution, the powder stream and the semi-infinite substrate together, while considering the attenuated laser power intensity distribution, the heated powder spatial distribution and the melt pool 3D shape variation. The particles concentration on transverse plane is modeled with Gaussian distribution based on optical measurement. Subsequently, a powder catchment module is developed with considering both the 3D melt pool shape and the powder stream spatial distribution.

3.2. Theory

A mathematical module for coupling the heat and mass flows in the LPF-AM process has been developed in this chapter with the following assumptions:

(1) Lateral nozzle has a perfect circular outlet.

(2) Gas-powder flow is assumed as a steady state flow and the effect of the gravity and drag force are considered negligible. Therefore, the powder stream is induced with a uniform velocity in transverse direction which is assumed to be the same as the gas velocity near the nozzle outlet.

(3) Convection and radiation losses in the powder stream was not considered and particles are assumed as isothermal with spherical geometry [110].

(4) Powder particles, impinging onto the molten pool, are considered effectively added to and mixed with the liquid flow on melt pool surface. It is required that the adhesion force F_{ad}

---

* A similar version of this chapter was published as:

Huang, Yuze, Mir Behrad Khamesee, and Ehsan Toyserkani. A Comprehensive Analytical Model for Laser Powder-fed Additive Manufacturing. Additive Manufacturing 12 (2016): 90-99. https://doi.org/10.1016/j.addma.2016.07.001

is bigger than the repelling force F_r ($F_{ad}/F_r > 1$) between the melt pool surface and the impinging particle. Lin [111] calculated the ratio of F_{ad} / F_r =100 for stainless steel in coaxial LPF-AM, which testifies that the powder is effectively melted and attached onto the molten pool surface. The liquid phases will then be rapidly mixed and become homogeneous due to the strong convection currents generated by the thermal gradients on melt pool surface (Marangoni convection/effect) [11,112].

(5) Thermo-physical properties for both powder and substrate are considered to be temperature independent. Average values over the temperature variation were assumed in the model.

3.2.1. Powder spatial distribution

The schematic of the LPF-AM process is shown in Figure 3-1. The laser beam scans in the positive y-direction with the process velocity v. Origin of coordinates is fixed at the center of laser beam spot on a substrate. Feeding nozzle has an inclined angle φ and distance H with respect to the substrate plane. Laser beams and powder streams interact with each other after point P.

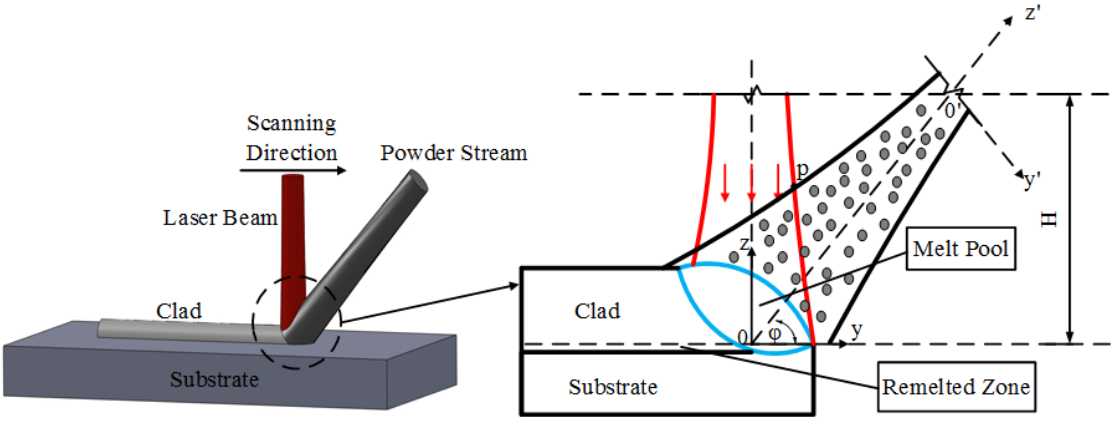

Figure 3-1. Schematic diagram for laser powder-fed additive manufacturing

Powder concentration mode in transverse direction was identified with Gaussian distribution by Lin [113] with both optical techniques and the theory of particles diffusion and convection in gaseous medium based on Fuchs's aerosols laminar flow. Optical luminance experimental analysis of Pinkerton's research [114] verified that the particles stream have Gaussian concentration profiles in the transverse plane. Yang [115] and Gangxian [116] also built the powder stream concentration with a Gaussian model and the model predicted values were

consistent with the experimental results. In this chapter, the powder concentration distributions in the transverse plane were expressed by the powder stream luminance distributions. Based on Mie theory [112,117], the luminance of the powder stream is proportional to particles concentration. Therefore, the luminance distribution in the image expresses the particles concentration distribution within the powder stream. The powder stream images were taken by a Canon EOS 60D camera (Canon, Ōita, Japan) with a Pentacon $135\ mm$ f/2.8 lens (Pentacon, Dresden, Germany). The powder stream luminance was measured by grayscale intensity with MATLAB Image-Processing Software, in which the RGB images were converted to grayscale images. As the Inconel 625 powder stream grayscale image shown in Figure 3-2, the powder concentration has Gaussian distribution in transverse plane under various distances from the nozzle outlet.

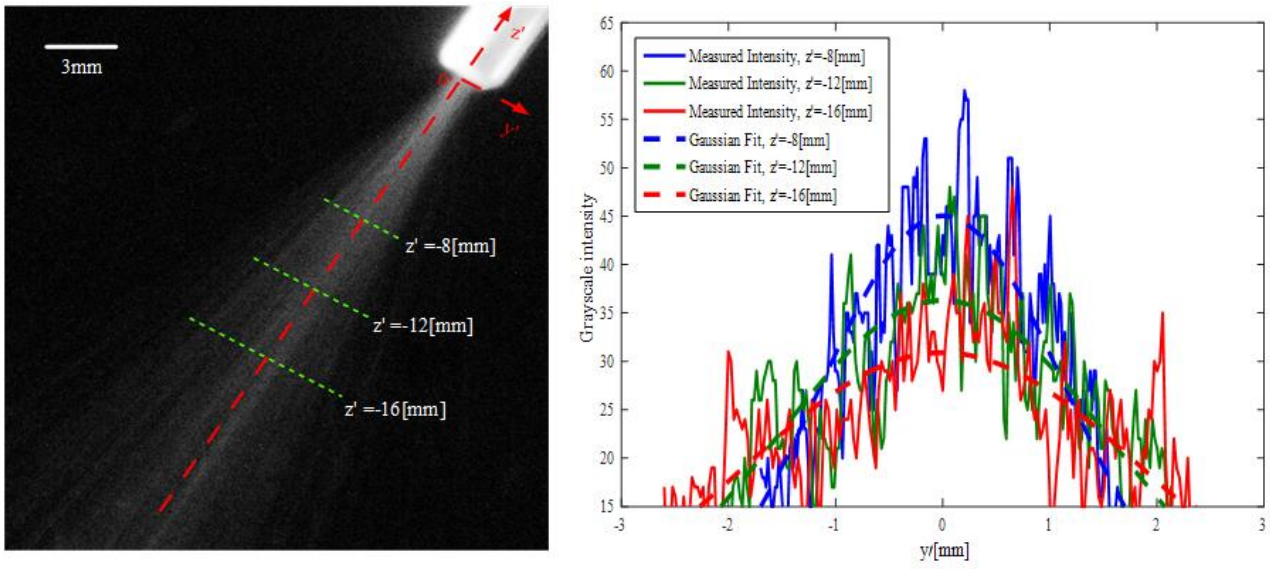

Figure 3-2. Inconel 625 powder stream grayscale intensity distribution measurement (a) Grayscale image with transversal lines (b) Measured grayscale intensity distribution with Gaussian fitting results on transversal lines. $\dot{m} = 5\ (g/min)$, $\varphi = 60^{\circ}$, $\dot{g} = 2.5\ (dL/min)$, $r_0 = 0.7\ (mm)$.

Thereafter, powder spatial mass concentration $\rho(x', y', z')$ and number concentration $n(x', y', z')$ can be derived as,

$$\rho(\mathrm{x}', \mathrm{y}', \mathrm{z}') = \frac{2\dot{m}}{v_p \pi r^2(\mathrm{z}')} \exp\left[-\frac{2(x'^2 + y'^2)}{r^2(\mathrm{z}')}\right] \tag{3-1}$$

$$n(\mathrm{x}',\mathrm{y}',\mathrm{z}') = \frac{2\dot{m}}{v_p m_p \pi r^2(\mathrm{z}')} \exp\left[-\frac{2(x'^2+y'^2)}{r^2(\mathrm{z}')}\right] \tag{3-2}$$

where $\dot{m}$ is the powder feed rate, m_p the average mass for each particle, $v_p = \dot{g}/\pi r_0^2$ the average powder velocity (based on assumption 2), $\dot{g}$ the gas flow rate, r_0 the nozzle internal radius and $r(z')$ is the effective radius of powder stream reaching $1/e^2$ of the peak concentration value of the powder stream center [116]. Based on the measurements and derivations elaborated in Appendix A, the effective radius of powder stream can be expressed as,

$$r(\mathrm{z}') = r_0 - z'\tan\theta, \quad z' < 0 \tag{3-3}$$

where θ is the effective divergence angle. Considering the coordinates transformation from $x'y'z'$ to xyz,

$$\begin{aligned} x' &= x \\ y' &= (\mathrm{y} - H/\tan\varphi)\sin\varphi - (z-H)\cos\varphi \\ z' &= (\mathrm{y} - H/\tan\varphi)\cos\varphi + (z-H)\sin\varphi \end{aligned} \tag{3-4}$$

Accordingly, the powder mass concentration in xyz coordinates will be derived as

$$\begin{aligned} \rho(\mathrm{x},\mathrm{y},\mathrm{z}) &= \frac{2\dot{m}}{v_p \pi r^2(\mathrm{z})} \exp\left[-\frac{2\left[x^2 + [(\mathrm{y} - H/\tan\varphi)\sin\varphi - (z-H)\cos\varphi]^2\right]}{r^2(\mathrm{z})}\right], \\ r(z) &= -\left[(\mathrm{y} - H/\tan\varphi)\cos\varphi + (z-H)\sin\varphi\right]\tan\theta + r_0 \end{aligned} \tag{3-5}$$

3.2.2. Laser beam and powder stream interaction

The laser beam and consequently its power intensity is attenuated by the powder stream during their interaction [110,112]. The total attenuation is a sum effect of scattering and absorption, which is also named as extinction. This chapter uses a Gaussian TEM_{00} mode laser power with intensity distribution as [11],

$$I(x,\mathrm{y},\mathrm{z}) = \frac{2P_L}{\pi R_L^2(z)} exp\left(-\frac{2(x^2+y^2)}{R_L^2(z)}\right) \tag{3-6}$$

where P_L is the laser power, $R_L(z)$ is the effective radius of the laser beam at a distance $\Delta z = z_0 - z$ from the beam waist position z_0 with R_{0L} radius for the laser beam and far-field divergence angle θ_L. $R_L(z)$ is expressed as [11],

$$R_L(z) = \sqrt{R_{0L}^2 + 4\theta_L^2(z_0 - z)^2} \tag{3-7}$$

The laser power intensity that is attenuated by powder stream with dz distance could be calculated based on Mie' theory [112,117],

$$dI = -\sigma I(x,y,z)n(x,y,z)dz \tag{3-8}$$

where $I(x,y,z)$ is the laser intensity at point (x,y,z), σ the extinction cross section of a sphere particle ($\sigma = Q_{ext}\pi r_p^2$), Q_{ext} the extinct coefficient, and r_p is the mean radius of the particles. $n(x,y,z)$ can be calculated by,

$$n(\mathrm{x,y,z}) = \frac{2\dot{m}}{v_p m_p \pi r^2(\mathrm{z})} \exp\left[-\frac{2\left[x^2 + \left[(\mathrm{y} - H/\tan\varphi)\sin\varphi - (z-H)\cos\varphi \right]^2 \right]}{r^2(\mathrm{z})} \right] \tag{3-9}$$

In the LPF-AM process, as the particle size is much bigger than the laser wavelength, it is reasonable to assume that the extinction coefficient $Q_{ext} = 1$ [112,118] and most of the attenuated laser energy is absorbed by the particle. Equation (3-8) is derived from the first-order approximation of Mie's theory, which calculates the total attenuation or extinction power for the laser beam travels through the powder stream and is valid when $2\pi r_p/\lambda_L < 300$ [112]. In this study, the average particle radius is $r_p = 42\ \mu m$, laser wavelength is $\lambda_L = 1.06\ \mu m$. Therefore, the condition of the first-order approximation of Mie's theory is satisfied. We should point out that this criterion is only considered when the scattering is included for total attenuated power calculation. But in the LPF-AM process, r_p is normally much larger than λ_L, the powder absorption is the predominant attenuation type. Therefore, Equation (3-8) can be directly used based on Lambert-Beer law without considering this condition [68,113,114].

As shown in Figure 3-1, the powder stream and laser beam will be interacted with each other after point *P*. The attenuated laser beam intensity $I_A(x,\mathrm{y},\mathrm{z})$ may be calculated with the integration of Equation (3-8) over the interaction length in z-axis as,

$$I_A(x,y,z) = I(x,y,\mathrm{z}) \exp\left[-\sigma \int_{z}^{z_p(x,y)} \mathrm{n(x,y,z)\,dz} \right] \tag{3-10}$$

where $z_p(x,\mathrm{y})$is the upper surface of the powder stream, which is approximated with the powder stream top boundary line $z_p(\mathrm{y})$,

$$\mathrm{z}_p(\mathrm{y}) = K + (y - K/\tan\varphi)\cdot\tan(\varphi-\theta),\ \ (K = H + r_0\sin\varphi/\tan\theta,\ \ \varphi > 0) \tag{3-11}$$

The powder absorbs energy from the laser beam during their interaction, and the absorbed energy increases the particles temperature. Based on assumption 3, the temperature increment ΔT for time interval $\Delta t = d_z / v_p sin\varphi$ follows the energy balance equation,

$$\beta I_A(\mathrm{x,y,z})\pi r_P^2 \Delta t = c_p \rho_p \frac{4}{3}\pi r_P^3 \Delta T \tag{3-12}$$

where β is the powder laser absorptivity, c_p the material specific heat capacity, and ρ_P is the average particle density. Integrating Equation (3-12) over the interaction length in *z*-axis allows the particle temperature $T_p(x,y,z)$ to be calculated as,

$$T_p(x,y,z) = T_0 + \frac{3\beta}{4\sin\varphi v_p c_p \rho_p r_P}\left|\int_z^{\bar{z}_p(y)} I_A(\mathrm{x,y,z})\,\mathrm{dz}\right| \tag{3-13}$$

where $\bar{z}_p(y) = z_p(-y)$ is the symmetrical line of $z_p(y)$ about *z*-axis, and T_0 is the ambient temperature. The path of integration from *z* to $\bar{z}_p(y)$ is used to approximate the particle traveling distance component in the laser beam transverse direction.

As particles impinge onto the melt pool, they draw energy to increase their enthalpy to that of the melt pool in a short time [118]. Therefore, the heated powder energy intensity $I_p(x,\mathrm{y,z})$ is expressed as a negative energy source. It should be noted that the heated particles do add positive energy to the melt pool. Therefore, the negative energy source defining here is used to couple the powder mass flow with the melt pool under the consideration of melt pool energy variation due to the added powder.

$$I_p(x,\mathrm{y,z}) = c_p v_p sin\varphi \rho(x,y,z)\left[T_p(x,y,z) - T_m\right] \tag{3-14}$$

3.2.3. Thermal conduction on substrate

On substrate surface, the coming energy from the attenuated laser beam $I_A(x,\mathrm{y,z})$ and heated powder flux $I_p(x,\mathrm{y,z})$ are summed up and treated as a bulk heating source. Thus, the resultant energy source intensity $I_{net}(x,\mathrm{y,z})$,

$$I_{net}(x,\mathrm{y,z}) = I_A(x,\mathrm{y,z}) + I_p(x,\mathrm{y,z}) \tag{3-15}$$

For a moving heat source on a semi-infinite work-piece surface, the temperature field $T(x,\mathrm{y,z})$ could be expressed based on Rosenthal's equation [94],

$$T(\mathrm{x},\mathrm{y},\mathrm{z})-T_0=\frac{P_L}{2\pi k}\frac{e^{-\nu(\mathrm{x}+R)/2\alpha}}{R},\qquad R=\sqrt{x^2+y^2+z^2} \tag{3-16}$$

where P_L is the laser beam power, k the thermal conductivity, α the thermal diffusivity, and v is the process velocity. While considering the resultant energy intensity distribution, the temperature field in substrate is derived by integrating Equation (3-16) over the laser beam area based on superposition principle.

$$\begin{aligned}T(\mathrm{x},\mathrm{y},z)-T_0=&\frac{1}{2\pi k}\int_{\xi=-r_L(z)}^{\xi=r_L(z)}\int_{\eta=-\sqrt{r_L^2(z)-\zeta^2}}^{\eta=\sqrt{r_L^2(z)-\zeta^2}}\left[\beta_w I_A(\xi,\eta,z)+c_p\rho(\xi,\eta,z)(T_p(\xi,\eta,z)-T_m)\right]\\&\times\frac{\exp\left[-\nu(\mathrm{y}-\eta+\mathrm{R})/2\alpha\right]}{\mathrm{R}}d\eta d\xi,\qquad \mathrm{R}=\sqrt{(\mathrm{x}-\xi)^2+(\mathrm{y}-\eta)^2+z^2}\end{aligned} \tag{3-17}$$

where β_w is the process laser power absorptivity.

To approach the reality, the latent heat of fusion, thermo-capillary phenomena (Marangoni effect) and the varying laser power absorptivity (Brewster effect) are taking into consideration with the following approximations.

The effect of latent heat of fusion L_f on thermal field is considered with increasing the specific heat as,

$$c_p^*=\frac{L_f}{T_l-T_\mathrm{s}}+c_p,\qquad T>T_s \tag{3-18}$$

where the T_l and T_s are the liquidus and solidus temperature, respectively. In the case that $T_l=T_\mathrm{s}$, the temperature averaged c_p is used. The Brewster effect that describes the plane inclination angle effect on the absorption of polarized laser power is presented by [94],

$$\beta_w(\emptyset)=\beta(0)[1+a_w\emptyset] \tag{3-19}$$

where $\emptyset$ is the inclination angle, $\beta(0)$ the laser power absorptivity for a flat plane and a_w is the Brewster effect coefficient depends on the material. For the sake of simplification, the inclination angle is approximated based on the clad height h and laser beam diameter D as,

$$\emptyset=tan^{-1}(h/D) \tag{3-20}$$

The Marangoni flow is counted by modifying the thermal conductivity with a correction factor μ_M as [67],

$$k^*(T) = \mu_M k(T_m), \quad T > T_m \tag{3-21}$$

3.2.4. Molten pool geometry

Molten pool projection limits on substrate surface is approximated by the solid-liquid line. Equation (3-17) is simplified as,

$$T(x, y, z) - T_0 = \Gamma(x, y, z) \tag{3-22}$$

As shown in Figure 3-3, points *A*, *B*, *C* and *D* are located on the boundary of the molten pool, according to Equation (3-22), the coordinate values can be calculated as,

$$\begin{cases} \Gamma(\mathrm{y}_A, 0, 0) = T_m - T_0, \mathrm{y}_A > 0 \\ \Gamma(\mathrm{y}_B, 0, 0) = T_m - T_0, \mathrm{y}_B < 0 \\ \Gamma(0, \mathrm{x}_D, 0) = T_m - T_0, \mathrm{x}_D > 0 \\ \Gamma(0, \mathrm{x}_C, 0) = T_m - T_0, \mathrm{x}_C < 0 \end{cases} \tag{3-23}$$

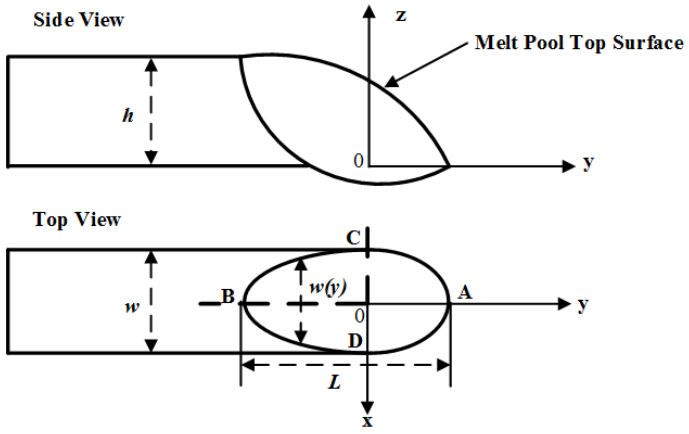

Figure 3-3. Schematic diagram for melt pool geometry

The projection of the melt pool on substrate plane has the boundary Ω,

$$\Omega = \{y_B \le y \le y_A, x_C \le x \le x_D\}, \quad l = y_A - y_B, \quad w = |x_C| = |x_D| \tag{3-24}$$

where l and w are the melt pool length and width for boundary Ω, respectively. The boundary of the melt pool is approximated by two half ellipses with same minor semi-axis of $w/2$ (The left part has a major semi-axis of $|y_B|$ and the right part has major semi-axis of $|y_A|$). While considering the melt pool top surface boundary as a parabolic curve, the melt pool top surface is expressed as [76],

$$z(\mathrm{x},\mathrm{y})=\left[-h\frac{(\mathrm{y}-y_B)^2}{(\mathrm{y}_A-y_B)^2}+h\right]\cdot(1-\frac{4x^2}{w^2(\mathrm{y})}),\qquad \left(\mathrm{x}\in[\mathrm{x}_C,\mathrm{x}_D],\mathrm{y}\in[y_B,\mathrm{y}_A]\right) \tag{3-25}$$

The width of the melt pool $w(y)$ can be expressed as,

$$w(\mathrm{y})=\begin{cases} w\times\sqrt{(1-\frac{y^2}{y_A{}^2})},\mathrm{y}\geq 0 \\ w\times\sqrt{(1-\frac{y^2}{y_B{}^2})},\mathrm{y}<0 \end{cases} \tag{3-26}$$

3.2.5. Clad geometry

Dividing the substrate surface into small elemental patches dS, each patch is so small that the powder flow density over it is essentially uniform, the powder mass dm that impinged onto dS in an elemental elapsed time can be approximated as,

$$dm=\rho(x,y,0)\cdot dS\cdot v_p sin\varphi \tag{3-27}$$

The clad height on dS area can be calculated based on the sum of the powder impinging onto it during the dwelling time as,

$$h_{dS}=\frac{1}{\rho_P dS}\int_0^{\mathrm{D}/v} dmdt \tag{3-28}$$

Then, for any point within the melt pool boundary, the clad height can be derived as,

$$h(x,y)=\lim_{\delta\to 0}h_{dS}=\frac{2\sin\varphi D\dot{m}}{v\rho_P\pi r^2(\mathrm{z}=0)}\exp\left[-\frac{2\left[x^2+\left[(\mathrm{y}-H/\tan\varphi)\sin\varphi+H\cos\varphi\right]^2\right]}{r^2(\mathrm{z}=0)}\right], \tag{3-29}$$

$$(x,y)\in\Omega$$

where δ is the largest diameter of patch dS. Based on Equation (3-29), the original clad height h_0 is estimated with an average value over the laser beam spot boundary and the process clad height h (along the laser scanning direction) is calculated over the melt pool boundary Ω. The clad width is approximated with the melt pool width $w(y)$ as expressed by Equation (3-26).

3.2.6. Catchment efficiency

To calculate the melt pool effective area in the coming powder stream, the melt pool is approximated by an inclined surface S_1, which is then projected to powder transverse planes S_2

and S_3 that cut through the highest and lowest point of the melt pool top surface, respectively (see Appendix B). The particles number probability density for per unit time per unit area on powder stream transverse plane can be expressed as,

$$f(\mathrm{x}',\mathrm{y}',\mathrm{z}') = \frac{n(\mathrm{x}',\mathrm{y}',\mathrm{z}')}{\int_{-\infty}^{+\infty}\int_{-\infty}^{+\infty} n(\mathrm{x}',\mathrm{y}',\mathrm{z}')d_{x'}d_{y'}} = \frac{2}{\pi {r_p}^2(\mathrm{z}')}\exp\left[-\frac{2(x'^2+y'^2)}{{r_p}^2(\mathrm{z}')}\right] \tag{3-30}$$

Subsequently, the catchment efficiency can be derived as the integration of the particle number probability over the melt pool projection area on the powder transverse plane. By integrating Equation (3-30) over the effective projection area A_{S_2} and A_{S_3}, the overall catchment efficiency is derived as,

$$\eta = \frac{\iint_{A_{S_2}} f(\mathrm{x}',\mathrm{y}',\mathrm{z}')dx'dy' + \iint_{A_{S_3}} f(\mathrm{x}',\mathrm{y}',\mathrm{z}')dx'dy'}{2} \tag{3-31}$$

3.3. Numerical analysis

Attenuated laser beam intensity and the associated temperature contour on substrate surface, calculated based on Equations (3-14) - (3-21), were simulated by MATLAB software with parameters listed in Section 3.4. Figure 3-4 (a) shows the original laser beam intensity distribution with maximum intensity $660\ (J/mm^2)$. The simulation results for Inconel 625 powder stream attenuation is shown in Figure 3-4 (b). As seen, the largest attenuated laser intensity loss is around $28\ (J/mm^2)$. Compared the largest attenuation intensity loss with the original maximum laser intensity, a maximum laser beam attenuation percentage can be determined as ~4%.

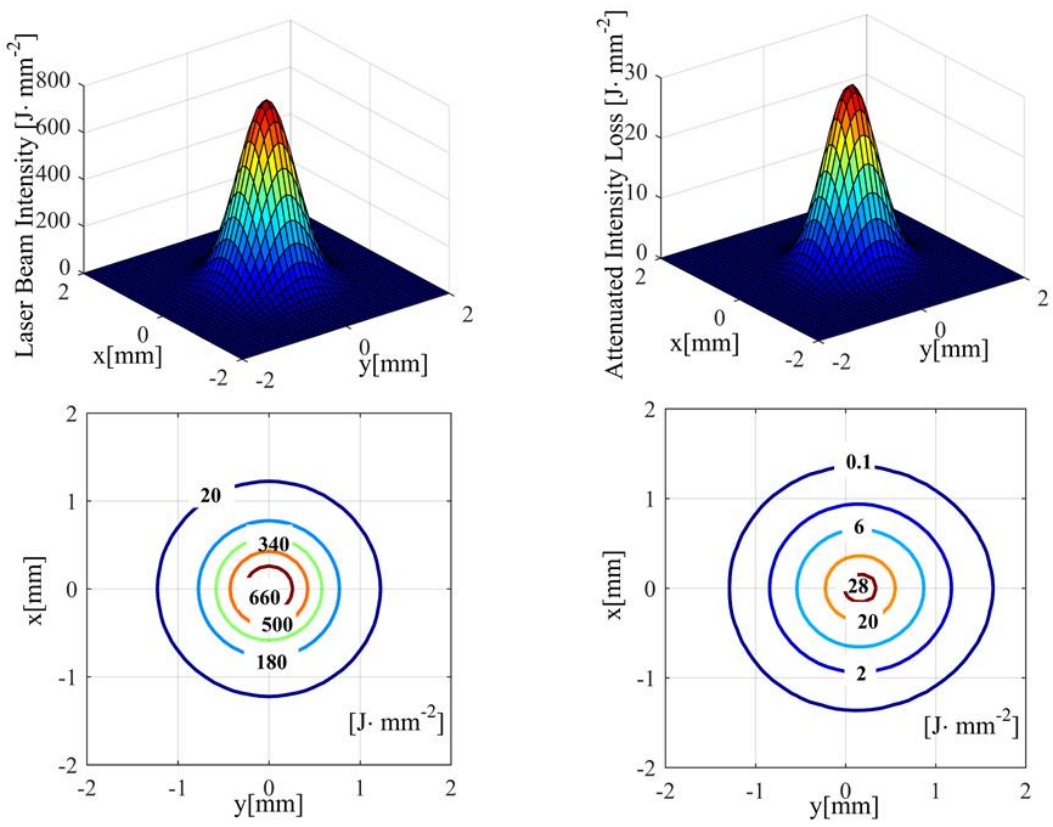

(a) (b)

Figure 3-4. Laser beam intensity distribution on the substrate surface (a) Without attenuation (b) Attenuated laser intensity loss by the powder. $\dot{m} = 7\ (g/min)$, $P_L = 1000$ (W), $\dot{g} = 2.5\ (dL/min)$, $r_0 = 0.7\ (mm)$.

With coupling the attenuated laser beam and the heated powder stream as the resultant moving heat source, the temperature field on substrate surface is calculated and shown in Figure 3-5. Melt pool projection geometry on the substrate surface is approximated with two half-ellipses (the dash line shown in Figure 3-5), which fits well with the calculated melt pool temperature 1563 *K* that identifying the solid-liquid interface.

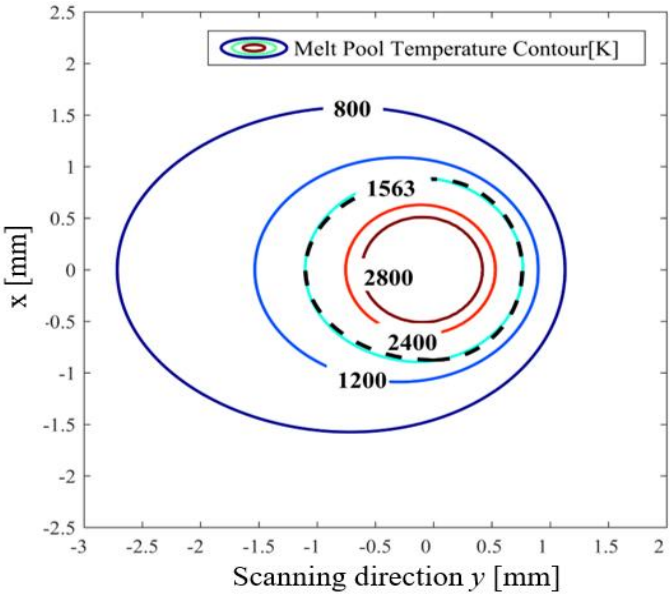

Figure 3-5. Molten pool temperature distribution on the Inconel 625 substrate surface. $\dot{m} = 5\ (g/min)$, $v = 7.5\ (mm/s)$. $P_L = 1000$ (W), $\dot{g} = 2.5\ (dL/min)$, $r_0 = 0.7\ (mm)$.

3.4. Experimental verification

Inconel 625 powder (Carpenter, Bridgeville, Pennsylvania, USA). Ni60.82%, Cr 21.4%, Mo 8.76%, Nb 3.31%, Fe 4.72%, Si 0.58% and Mn 0.41%, wt%) with particle size 45-125 μm (Gaussian distribution) was deposited on Inconel 625 plates (McMaster-Carr, Aurora, Ohio, USA) by a LPF-AM setup developed in-house. This setup includes a continuous IPG photonics fiber laser with the maximum power of 1100 W installed in a Fadal CNC machine. The powder feeder purchased from Sulzer Metco was used to feed materials through a lateral nozzle. The Inconel 625 plates had the dimensions of 75×15×5 (mm3). For both the clad and the substrate, the thermo-physical properties of Inconel 625 are considered to be temperature independent, and the thermal parameters are calculated based on the mean values over the temperature range as listed in Table 3-1. Single layer deposition experiments were done to test the model with varying process velocity and powder feed rate. Each group experiment was repeated five times and the process parameters are listed in Table 3-2.

To measure the LPF-AM powder catchment, the attached powder was evaluated by weighing the substrate before and after deposition, the total ejected powder was calculated with the product of the powder feed rate and deposition time. Then the experimental catchment efficiency was

evaluated as the ratio of that attached powder weight divided by ejected powder weight. The clad width and clad height were measured by optical microscopy.

Table 3-1. Inconel 625 thermo-physical properties [119]

Density ρ_P [Kg/m3]	Thermal conductivity k [W $m^{-1}K^{-1}$]	Specific heat capacity C [J $kg^{-1}K^{-1}$]	Melting temperature T_m [K]
8440	9.8(21℃)-25.6 (1000℃)	410(21℃) - 670 (1090℃)	1563(1290℃)

Table 3-2. Laser metal direct deposition process parameters

Parameters	Values	Parameters	Values
Scanning velocity	1000 (mm/s)	Laser power	1000 (W)
Laser wavelength	1.06 (μm)	Latent heat of fusion	204500 (J/kg)[120]
Beam waist radius	0.43(mm)	Far-field divergence angle	0.02 (rad)
Beam waist position	19.8 (mm)	Argon gas feed rate	2.5 (dL/min)
Nozzle height	7(mm)	Nozzle angle	60°
Nozzle internal radius	0.7 (mm)	Laser spot diameter	1.8 (mm)
Nozzle tube thickness	0.8 (mm)	Brewster effect coefficient	0.0196
Correction factor	2.5		

In this research, a combined parameter specific energy $E = P_L/vD$ [11], which describes the energy delivered by the laser power per unit feed rate area of the laser track, was used to address the process and validate the analytical model with comparing the modeled and measured clad dimension and catchment efficiency. Figure 3-6 shows the single layer deposition profiles of Inconel 625 at different specific energy. As seen, the layer profiles keep smooth with a higher specific energy ((a), (b) and (c)). Both the clad width and height increase with the increasing of specific energy.

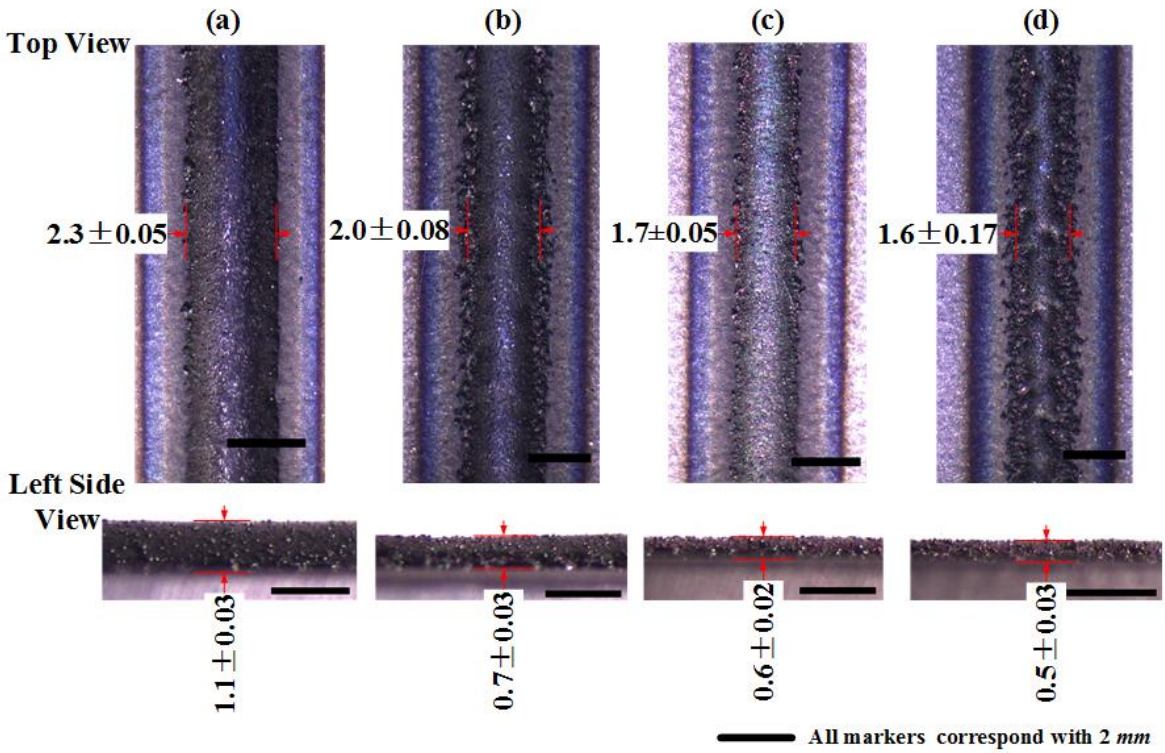

Figure 3-6. Inconel 625 single layer deposition profile by LPF-AM. $\dot{m} = 7\ (g/min)$. (a) $E = 185.2\ (J/mm^2)$, (b) $E = 123.5\ (J/mm^2)$, (c) $E = 92.6\ (J/mm^2)$, (d) (b) $E = 74.1\ (J/mm^2)$

Figure 3-7 shows that the built model successfully predicts the experimentally observed trend of that catchment efficiency increasing with increasing specific energy. However, it was also noticed that there will be great gaps between the predicted and the measured catchment value if the laser power absorptivity is set to a stable value (30%, 40%, 50% or 60%). On the contrary, as the Brewster effect describes, the results match well by using varying laser power absorptivity. In this chapter, an average Brewster effect coefficient α_w was calculated by adjusting the laser power absorptivity $\beta_w(\emptyset)$ to match the measured catchment efficiency based on Equations (3-19) and (3-20).

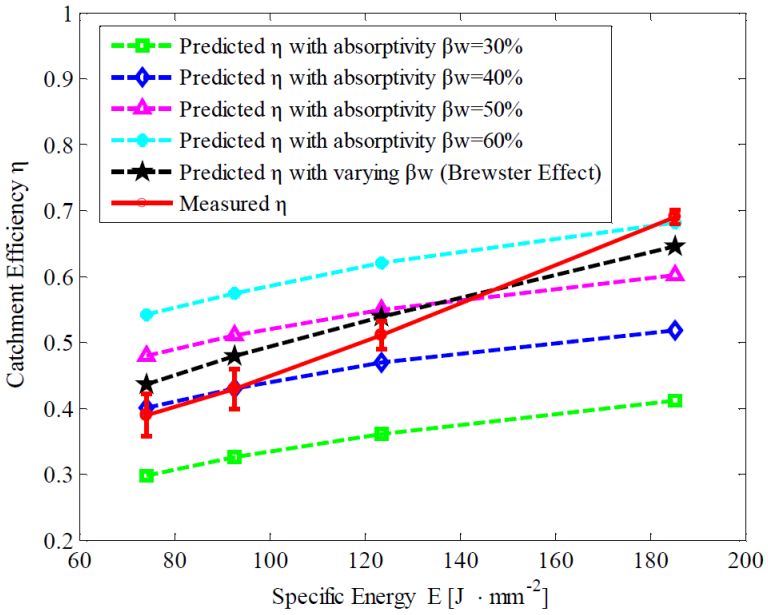

Figure 3-7. Model predicted and measured catchment efficiency. $\dot{m} = 5\ (g/min)$.

Figure 3-8 compares the modeled and measured clad widths, clad heights and catchment efficiencies with varying specific energy and powder feed rate. The experimental results have low standard deviation values, indicating an excellent repeatability and precision. The model matches well with the experimental results. With increasing specific energy, the clad width, melt pool length, clad height and catchment efficiency increase as well, which is consistent with the results in references [81][77]. For a given condition in the LPF-AM process, the higher specific energy means there is more laser power at per unit area of laser track, which enlarges the melt pool area as well as the powder catchment.

From Figure 3-8 (a), (c) and (d), it can be seen that for a given powder feed rate ($\dot{m} = 5\ (g/min)$), the predicted clad width, clad height and catchment efficiency are bigger than the measured results. However, with an increase of the specific energy, the difference gap is smaller or disappear. The higher specific energy increases the powder catchment as well as the clad height and its non-planar geometrical features. With an elevated clad height at a relatively fixed width, the wetting angle increases thus the laser power absorptivity increased due to Brewster effect. The model uses an average Brewster effect coefficient to compensate the increasing absorptivity, which is smaller than the real time-varying laser power absorptivity. This may be one of the reasons for the disagreement of the measured and predicted clad height shown in Figure 3-8 (c) for a higher powder feed rate ($\dot{m} = 7\ (g/min)$.

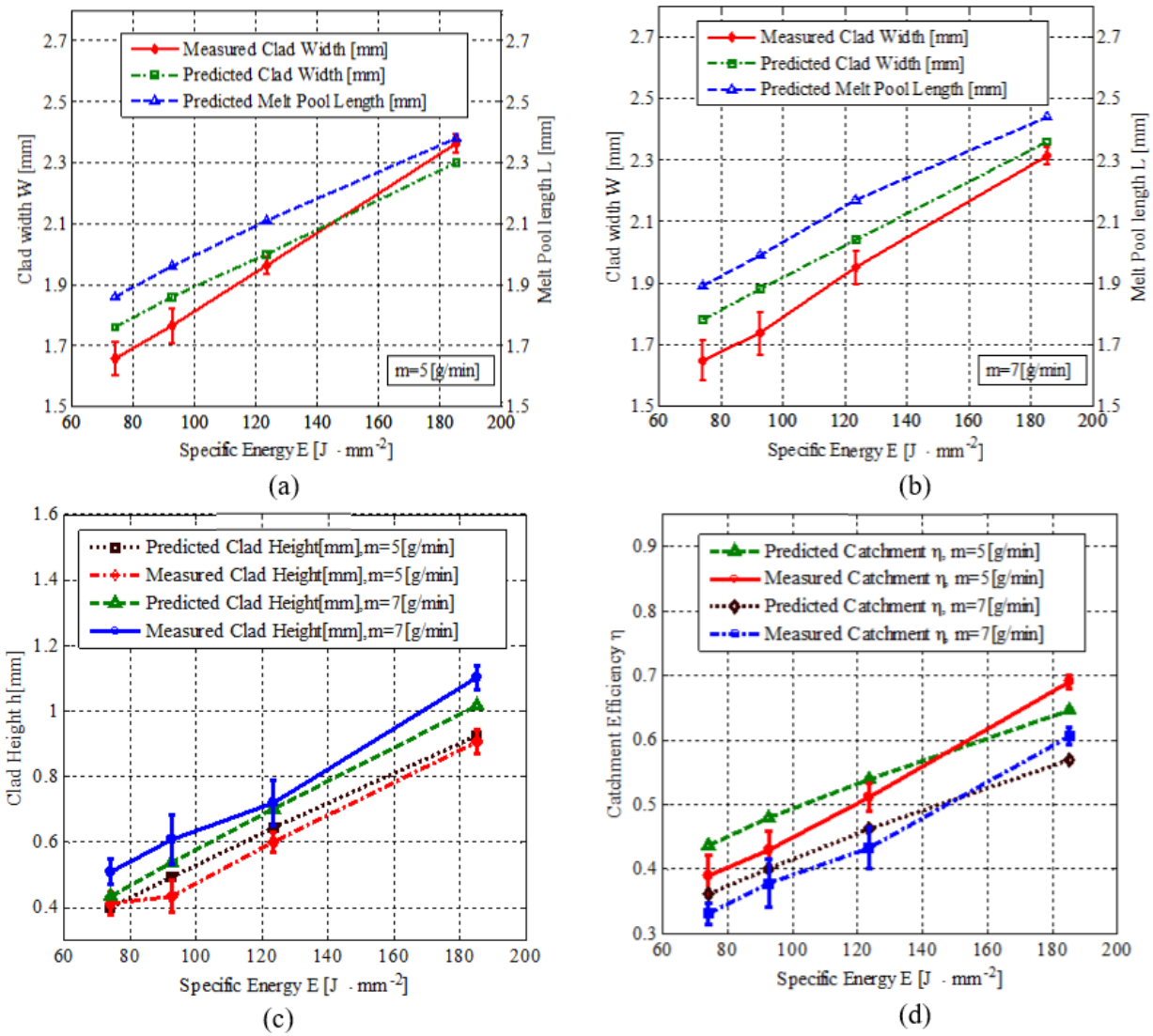

Figure 3-8. Experimental and model predicted results comparison, (a)-(c) clad geometry, (d) catchment efficiency

For the specific energy values in the range of ($100\sim190\,J/mm^2$), the maximum percentage difference for the model predicted and experimental results are 6.2% for the clad width, 7.8% for the clad height and 6.8% for the catchment efficiency. These results validate the accuracy of the model. The developed model has the potential to effectively be used for designing comprehensive controllers for the process by incorporating into high speed hardware platform. The model can also be expanded to multi-nozzle LPF-AM setups (e.g., LENS technology from Optomec) by combining each single powder stream as shown in references [16, 25].

3.5. Summary

This chapter addresses a comprehensive module that analytically couples the laser beam, the powder stream and the semi-infinite substrate. The powder stream concentration over the transverse plane was measured in terms of the powder feed rate, carrier gas feed rate and the associated feeding nozzle set up. Thereafter, a Gaussian function was built to describe the powder stream concentration. A powder catchment module was also derived according to the 3D dimension of the melt pool and the powder stream concentration. Experimental validation through the deposition of Inconel 625 proves the model can accurately predict the clad geometry and catchment efficiency in the range of specific energy that is corresponding to high clad quality (maximum percentage difference is 6.2% for clad width, 7.8% for clad height and 6.8% for catchment efficiency).

Chapter 4. Magnetic Concentration of Non-ferrous Metallic Particles in the Gas-powder Stream of LPF-AM: Mathematical Modeling and Analysis*

4.1. Introduction

A major challenge in blown powder-feeding of the LPF-AM process is to deliver powder to precise spatial point to satisfy geometric precision. However, the current powder-feeding methods generally lead to a wide and divergent powder stream, resulting in low powder catchment as well as undesirable geometric accuracy. As shown in Figure 4-1 (a) and (b) of a lateral LPF-AM, where the powder stream spreads much wider than the laser beam, and the particles that do not impinge into the laser beam area might not be effectively deposited by a solid-solid surface impact ricochet [111]. Therefore, it is desirable to narrow down the powder stream for improving the fabrication precision and powder catchment as shown in Figure 4-1 (c) and (f).

Currently, eddy current separation (ECS) has been successfully used for metallic conducting particle deflection with a high response efficiency. Basically, ECS utilizes the induced circulating currents in conducting particles to react back on external applied magnetic fields by a magnetic force [106,121]. The generated magnetic force has a specific direction that deflects the particles towards to the magnetic field strength decreasing direction. In addition, the generated magnetic force has been shown to be capable of deflecting the particles with size ranging from submillimeter [104] to millimeter [105]. Therefore, with a proper magnetic system setup (e.g., high radial magnetic field gradient), the induced magnetic force may be utilized for particle concentration.

A large number of eddy current separation models have been built to explore this complex ECS process. In the recent review work, Smith et al. [121] summarized theoretical models for magnetic force calculation. Based on their work, the force models can be roughly categorized as

---

* A similar version of this chapter was published as:

Huang Yuze, Mir Behrad Khamesee and Ehsan Toyserkani. Electrodynamic Concentration of Non-ferrous Metallic Particles in the Moving Gas-powder Stream: Mathematical Modeling and Analysis. International Journal of Magnetics and Electromagnetism. 5, (2019):019.

numerical and analytical. For the numerical models, Faraday's law was first utilized to solve the induced electrical field by the external magnetic field $\boldsymbol{B}$ (All vectors are set as bold font in this chapter). Ohm's law was then used to dictate the generated eddy current $\boldsymbol{J}$. Thereafter, magnetic force $\boldsymbol{F}$ over the particle volume V_p can be calculated as $\boldsymbol{F} = \int(\boldsymbol{J} \times \boldsymbol{B})dV_p$ by Finite Element Method with applying fine domain discretization or mesh. For instance, Fengjie et al. [122] built a new numerical model of the magnetic force by a joint simulation of COMSOL and MATLAB, leading to an efficient calculation for the particle deflection distance. By contrast, a closed form analytical solution of the magnetic force can be achieved under the linear magnetic field case. The force can be approximated by the magnetic dipole moment model ($\boldsymbol{F} = \nabla(\boldsymbol{M} \cdot \boldsymbol{B})$ [123]), where the magnetic dipole moment $\boldsymbol{M}$ is analytically solved. Ray et al.[124] and Nagel [125] reported that the analytical models possess a high accuracy in force calculation for systems equipped with the time-variant electromagnetic field or the permanent magnet source.

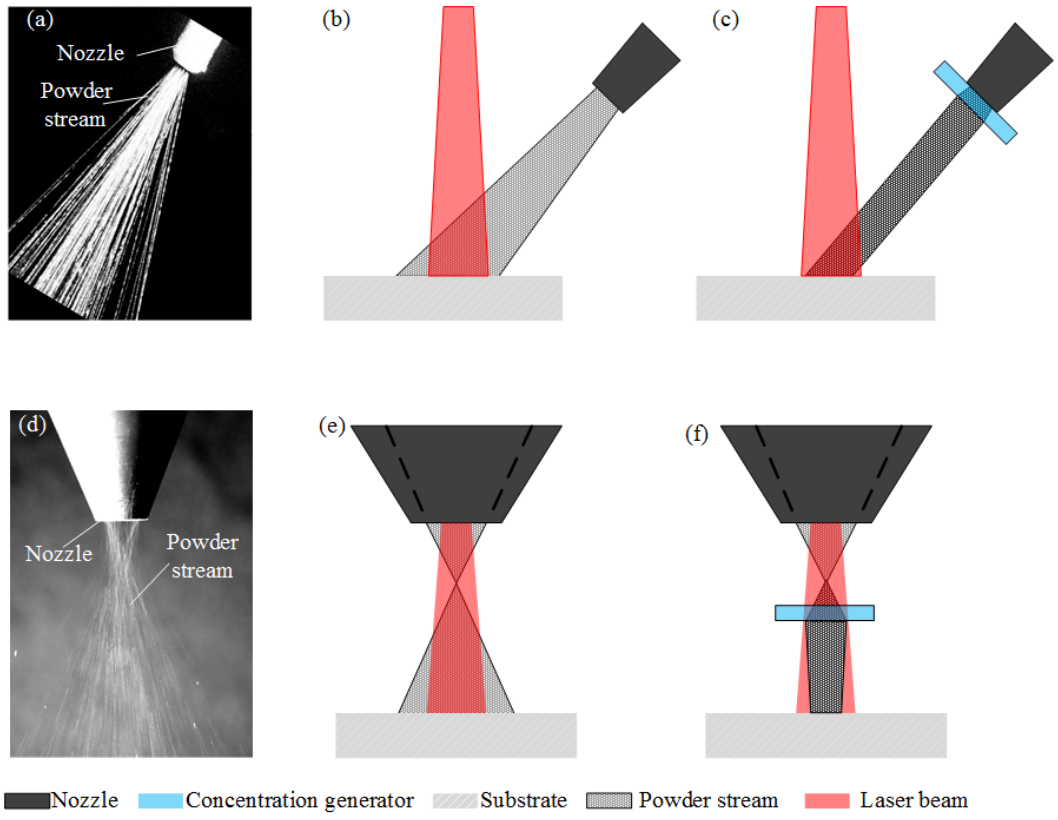

Figure 4-1. Powder stream of the lateral (a, b, c) and coaxial (d, e, f) LPF-AM process. (a), (d) Diverging powder stream image. (b), (e) Schematic of the divergent powder stream and laser beam. (c), (f) Schematic of the concentrated powder stream and laser beam.

Inspired by ECS technique and the associated magnetic force models, this chapter proposed and theoretically tested a new magnetic concentration approach for submillimeter-sized non-ferrous metallic particle focusing in LPF-AM. This innovative approach has a potential application to generate a tightly focused powder stream in the LPF-AM process, improving the powder catchment and fabrication precision. Analytical models for the effective magnetic concentration force as well as the particle concentration angle were developed with considering the skin effect. Conceptual design of the concentration generator was proposed with three different configurations: the doublet Halbach permanent magnet quadrupoles (doublet-Halbach-PMQs), the doublet electromagnet quadrupoles (doublet-EMQs), and the linear Halbach permanent magnet arrays (linear-Halbach-PM). Numerical simulations of the concentration angle for the proposed concentration generators were conducted for pure aluminum particles with a radius of $50 < r_p < 500\mu m$.

4.2. Mathematical modeling

A few ideal conditions should be assumed here to conduct this research. First, as the particles travel through the concentration generator, the powder stream will thin out (e.g. larger diameter $2\sim3\ mm$) and the particles will not be substantially impeded by the presence of other particles. Second, the particle rotation angle tends to be zero during the induced magnetic force action time, which can be explained by the fact that the response time of the eddy current ($\sim0.05\ \mu s$, calculated based on reference [126]) is quite small compared with that of the particle rotation period. Third, the effect of the gas drag force on the particles' movement can be omitted. The drag force on the moving particles were calculated based on the fluid mechanics [127] as elaborated in Appendix C. It was found that the magnitude of the drag force is insignificant as it is roughly $0.2\%\sim2\%$ to that of the effective magnetic force.

4.2.1. Principle of the magnetic concentration approach

The schematic diagram for the proposed concentration approach is shown in Figure 4-2. The concentration generator was designed with an annulus shape. This special arrangement provides a magnetic field with high radial gradient that the field intensity decreased significantly from the outer circumferential layer to the inner center region in the transverse cross-section.

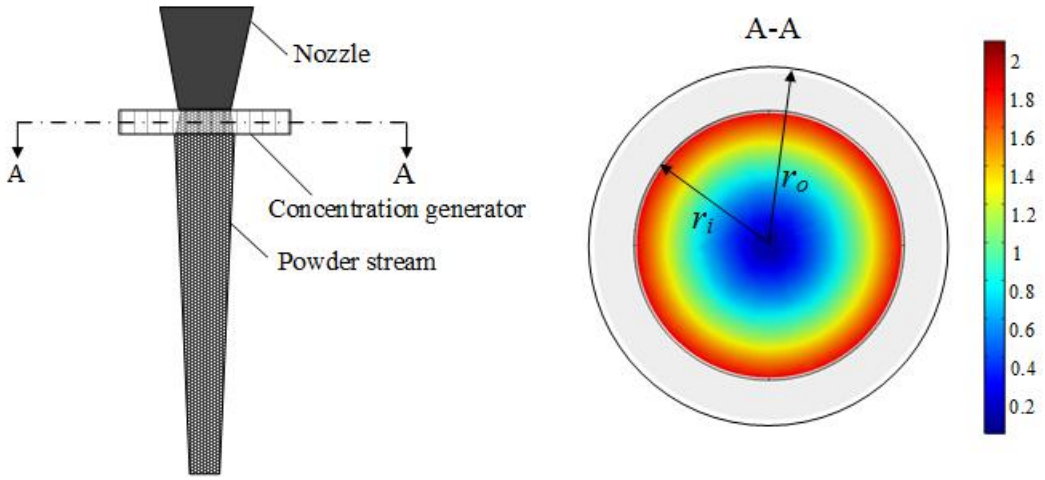

Figure 4-2. Schematic diagram for the proposed magnetic concentration approach. The magnitude of the field intensity in the transverse cross-section were marked with the color bar (the scale bar shows the relative values), decreasing from the circumferential region towards to the center region from red color to blue color. Inner radius r_i and outer radius r_o.

According to the Faraday's law of induction, eddy current may be induced in the conducting particles as the particles travel through the alternating magnetic field $\boldsymbol{B}$ of the concentration generator. Subsequently, the induced eddy current will react back to the applied field $\boldsymbol{B}$ by generating a magnetic force that drags the particles toward to the field intensity decreasing direction. Therefore, the outer-layer particles may be driven by the radial magnetic force to the inner region of the powder stream.

4.2.2. Magnetic force

As the conducting particles travel through the magnetic field of the concentration generator as shown in Figure 4-3, the dominant term of the magnetic force $\boldsymbol{F}$ exerted on the particle can be expressed as [123],

$$\boldsymbol{F} = \nabla(\boldsymbol{M}\cdot\boldsymbol{B}) = (\boldsymbol{M}\cdot\nabla)\boldsymbol{B} + \boldsymbol{M}\times(\nabla\times\boldsymbol{B}) = [M_\tau \quad M_r \quad M_z]\begin{bmatrix} \frac{\partial B_\tau}{\partial\tau} & \frac{\partial B_r}{\partial\tau} & \frac{\partial B_z}{\partial\tau} \\ \frac{\partial B_\tau}{\partial r} & \frac{\partial B_r}{\partial r} & \frac{\partial B_z}{\partial r} \\ \frac{\partial B_\tau}{\partial z} & \frac{\partial B_r}{\partial z} & \frac{\partial B_z}{\partial z} \end{bmatrix} \quad (4\text{-}1)$$

where z, r and τ are the coordinates in the axial-radial-tangential coordinate system. Here should be noted that the displacement current is assumed as zero in the present research, accordingly, $\nabla \times \boldsymbol{B} = 0$ in the above Equation (4-1).

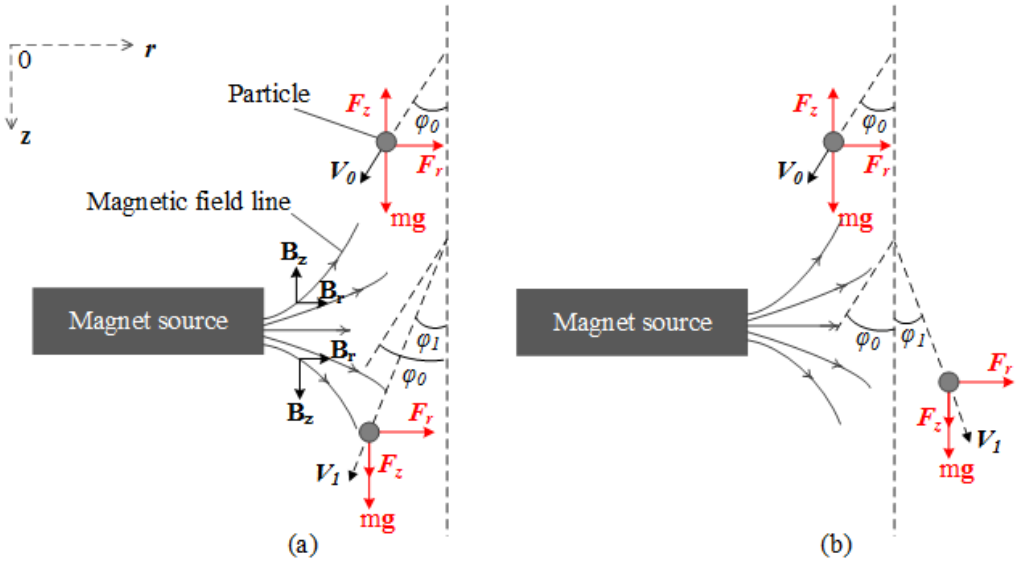

Figure 4-3. Force analysis of the moving particle in the longitudinal cross-section when the particle travels through the proposed concentration generator. (a) Radial velocity of the particle keeps centrifugal direction. (b) Radial velocity of the particle changes to centripetal direction. Initial velocity V_0 and divergence angle φ_0. Final velocity V_1 and divergence angle φ_1.

The effective magnetic moment can be derived as [128],

$$\boldsymbol{M} = -\frac{3}{8\pi\mu}\alpha_m V_p \boldsymbol{B} \tag{4-2}$$

where α_m the magnetic polarization coefficient, μ the magnetic permeability and $V_p = \frac{4}{3}\pi r_p^3$ is the particle volume with radius r_p.

The coefficient α is a complex variable and can be calculated as [129],

$$\begin{cases} \alpha_m = a_{m1} + a_{m2}i \\ a_{m1} = \dfrac{3}{2q}\left[\dfrac{\sinh(2q) - \sin(2q)}{\cosh(2q) - \cos(2q)}\right] - 1 \\ a_{m2} = \dfrac{3}{2q}\left[\dfrac{\sinh(2q) + \sin(2q)}{\cosh(2q) - \cos(2q)} - \dfrac{1}{q}\right] \end{cases} \tag{4-3}$$

where $q = r_p/\delta_e$ is a coefficient and δ_e is the effective skin depth. The induced eddy current has a non-uniform distribution in depth direction (known as skin effect). The skin depth here

describes the distance from the surface that the current density reduces to $1/e$ of the surface value. The conventional skin depth can be calculated as,

$$\delta = \frac{1}{\sqrt{\pi f \mu \sigma}} \tag{4-4}$$

where σ is the electrical conductivity and f is the magnetic field frequency. With considering the particle's small thickness (thickness $th = 2r_p$), the effective skin depth δ_e may be expressed as [130],

$$\delta_e = \begin{cases} \delta, & th > 5\delta \\ \delta\,[1 - \exp(-th/\delta)], & th \leq 5\delta \end{cases} \tag{4-5}$$

Therefore, the transient magnetic force on the particle can be calculated as,

$$\begin{cases} \boldsymbol{F_t} = \boldsymbol{0} \\ \boldsymbol{F_r} = -\dfrac{3}{8\pi\mu_0}\alpha_m V_p B_r \dfrac{\partial B_r}{\partial r} \\ \boldsymbol{F_z} = -\dfrac{3}{8\pi\mu_0}\alpha_m V_p B_r \dfrac{\partial B_z}{\partial r} \end{cases} \tag{4-6}$$

Based on the above Equations ((4-3)- (4-6)), the magnetic force component $\boldsymbol{F_z}$ changes direction as the particle passing through the magnetic field as shown in Figure 4-3. Consequently, the time-averaged vertical force F_{zavg} will be equal to zero. In addition, when the magnetic field frequency is relatively low that the skin depth δ is comparable with the particle size, the magnetic polarization coefficient α will be nearly imaginary. Subsequently, the phase of the induced magnetic moment $\boldsymbol{M}$ will approximately lag the magnetic field $\boldsymbol{B}$ by $\pi/2$ and the time-averaged magnetic force applied on the particle will be equal to zero. Therefore, the time-averaged radial magnetic force applied on the particle might be approximated as,

$$F_{ravg} = \begin{cases} 0, & a_{m1} \ll a_{m2} \\ -\dfrac{3}{16\pi\mu_0} k V_p B_r \dfrac{\partial B_r}{\partial r}, & a_{m1} \approx a_{m2} \\ -\dfrac{3}{16\pi\mu_0} a_{m1} V_p B_r \dfrac{\partial B_r}{\partial r}, & a_{m1} \gg a_{m2} \end{cases} \tag{4-7}$$

where $k = cos\theta_d \sqrt{a_{m1}^2 + a_{m2}^2}$ is the couple coefficient. The couple coefficient k is derived based on the phase delay angle $\theta_d = tan^{-1}(a_{m2}/a_{m1})$ between the magnetic moment and the external magnetic field.

4.2.3. Concentration angle

According to the force derivation elaborated in the above Section 4.2.1, it is reasonable to assume that the particle will be only affected by the gravity force ($m\boldsymbol{g}$, $\boldsymbol{g}$ is the gravitational acceleration) and the concentration force ($\boldsymbol{F_{ravg}}$) as it travels through the concentration generator. Here the particle mass is calculated as $m = \rho_p V_p$ and ρ_p is the particle density. Then the particle acceleration time t for the concentration system with length L can be expressed as,

$$t = \frac{-V_0 cos\varphi_0 + \sqrt{(V_0 cos\varphi_0)^2 + 2gL}}{g} \tag{4-8}$$

where V_0 and φ_0 are the initial velocity and initial divergence angle (shown in Figure 4-3) when the particle enters the concentration generator, respectively. Correspondingly, the final divergence angle and final velocity when the particle exits the concentration generator are represented by φ_1 and V_1, respectively. According to the momentum theorem, simultaneous equations can be derived as,

$$\begin{cases} m(\boldsymbol{V_0} sin\varphi_0 + \boldsymbol{V_1} sin\varphi_1) = \boldsymbol{F_{ravg}}\, t \\ m(\boldsymbol{V_0} cos\varphi_0 + \boldsymbol{V_1} cos\varphi_1) = m\boldsymbol{g}\, t \end{cases} \tag{4-9}$$

Subsequently, the concentration angle $\Delta\varphi$ as the particle travelling through the magnetic field can be solved as,

$$\Delta\varphi = \begin{cases} \varphi_0 + \varphi_1, & V_0 sin\varphi_0 m / F_{cavg} \le t \\ \varphi_0 - \varphi_1, & V_0 sin\varphi_0 m / F_{cavg} > t \end{cases} \tag{4-10}$$

4.3. Conceptual design of the concentration generator

To achieve the magnetization configuration of the designed annulus-shaped concentration generator as discussed in Section 4.2.1, two possible quadrupole-based configuration systems are sketched out in Figure 4-4 (a) and (b), in which the PM and EM are used as the magnetic sources, respectively. The permanent-magnet-based quadrupoles (PMQs) can access to high gradient fields, which can reach up to $200\ T/m$ in a typical $10\ mm$ bore diameter structure [131]. By contrast, conventional electromagnetic quadrupole setups can only achieve a field gradient that is as high as 50 T/m due to the comparably large aperture requirement [132]. In addition, extremely high gradient fields can be achieved for the PMQs under a Halbach array configuration [133], which can produce over $600\ T/m$ with a $5\ mm$ bore diameter arrangement [134]. To fully

explore the Halbach array configuration, a linear Halbach PM array setup was also investigated in this research.

The Halbach PMQs array is consisted by 16 sections of PM with magnetization orients 0°, $\pm 90^{\circ}$, 180° in transverse plane as shown in Figure 4-4 (c, e). The linear Halbach PM array is composed by 12 sections of PM with magnetization orients 0°, $\pm 90^{\circ}$ in longitudinal plane as shown in Figure 4-4 (d, f). As can be seen from Figure 4-4 (e, f), both Halbach PMQs and linear Halbach PM arrays generate magnetic fields that the field intensity decreases rapidly in radial direction.

In addition, it is noticed that the magnitude of radial field intensity $\boldsymbol{B_r}$ of the Halbach PMQs array is not a constant in the same radial layer as shown in Figure 4-4 (g). By contrast, the linear Halbach PM array produces a nearly constant magnitude of $\boldsymbol{B_r}$ for a certain radial layer as shown in Figure 4-4 (h). However, the Halbach PMQs array can easily be extended to an alternately N–S and S–N magnetization configuration in the z-axis direction by changing the magnetization of each PMQs array. Accordingly, a relatively small magnet period with a high field variation rate can be achieved. Moreover, the inconsistent $\boldsymbol{B_r}$ over the radial layers in the cylinder Halbach PMQs array may be ameliorated by a specific doublet Halbach PMQs arrangement, where the second Halbach PMQs is set with a 45° angle difference magnetization compared to that of the first Halbach PMQs.

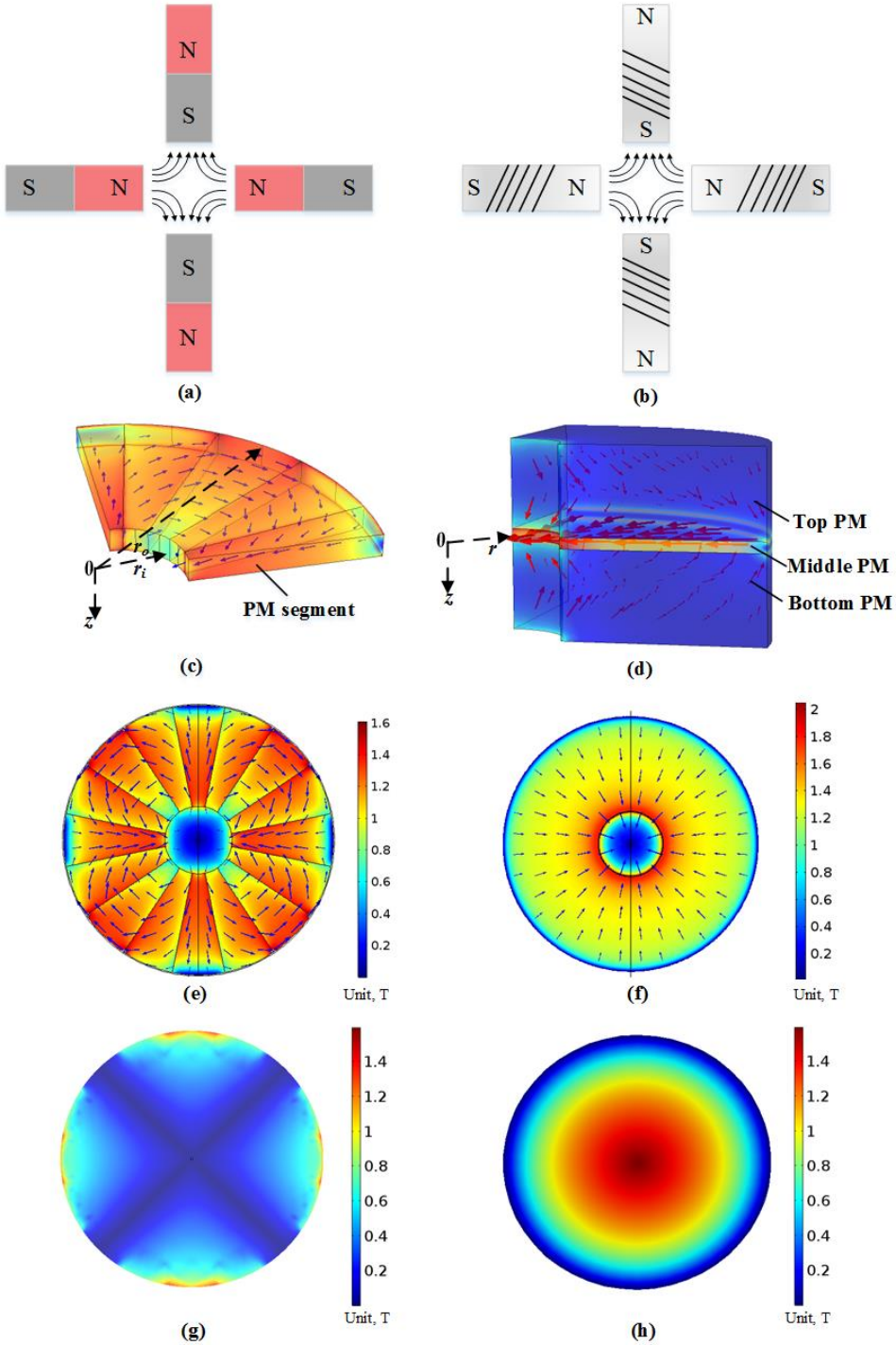

Figure 4-4. Schematic illustration of the proposed magnetic concentration systems. (a) Permanent-magnet-based quadrupoles. (b) Electromagnet-based quadrupoles. 3D view of the quarter segment (c), magnetic intensity norm (e) and inner region ($r \leq r_i$) radial intensity distribution (g) of Halbach PMQs array. 3D view of the quarter segment (d), magnetic intensity norm (f) and inner region ($r \leq r_i$) radial magnetic intensity distribution (h) of linear Halbach PM array. The blue and red arrows represent the magnetic field direction.

In sum, the magnetic concentration generator may be built with these three configurations: the doublet Halbach permanent magnet quadrupoles (doublet-Halbach-PMQs), the doublet electromagnet quadrupoles (doublet- EMQs) and the linear Halbach permanent magnet arrays (linear-Halbach-PM). The doublet-Halbach-PMQs are arranged with alternately N–S and S–N magnetization configuration in z-axis direction and the magnetization of quadrupoles orients with 45°angle difference in horizontal plane within each pair of the doublet quadrupoles.

4.4. Numerical results and discussion

The available neodymium N52 magnets with residual magnetic flux density 1.45 T are incorporated into the designed doublet-Halbach-PMQs. As the nozzle diameter of the powder feeding process is typically smaller than $2mm$ [34], the Halbach PMQs is built with inner radius $r_i = 2mm$, outer radius $r_o = 10mm$ and thickness $H = 1mm$. Thereafter, the period λ of the designed doublet-Halbach-PMQs may be evaluated by $\lambda = 2H$, and field frequency f can be calculated as $f = V/\lambda$ when the particle passing the system with velocity V. The magnetic field distribution of the proposed Halbach-PMQs was simulated by COMSOL Multiphysics® software and the averaged flux density ($B_r = 0.8\text{T}$) and gradient ($\partial B_r/\partial r = 700\ \text{T}/m$) over the radius zone ($1mm \leq r \leq 2mm$) were used to evaluate the concentration angle. A strong field intensity of 0.5 T and high gradient of 50 T/m [132] were assumed for the EM-quadrupole configuration. Process parameters of the numerical calculation for the designed doublet-Halbach-PMQs and EM-quadrupoles are listed as Group 1 and Group 2 in Table 4-1, respectively. Spherical aluminum particles were used in the numerical calculation and the material properties are listed in Table 4-2.

Table 4-1. Process parameters

No	Concentration system length *L* (mm)	Initial velocity $\boldsymbol{V_0}$ (m/s)	Initial divergence angle $\boldsymbol{\varphi_0}$ (degree)
Group 1	6	2	10
Group 2	6	2	10

Table 4-2. Material properties of the aluminum particle [107]

Electrical conductivity (S/m)	Density (Kg/m^3)	Permeability (H/m)
3.5E+7	2700	1.256665E−6

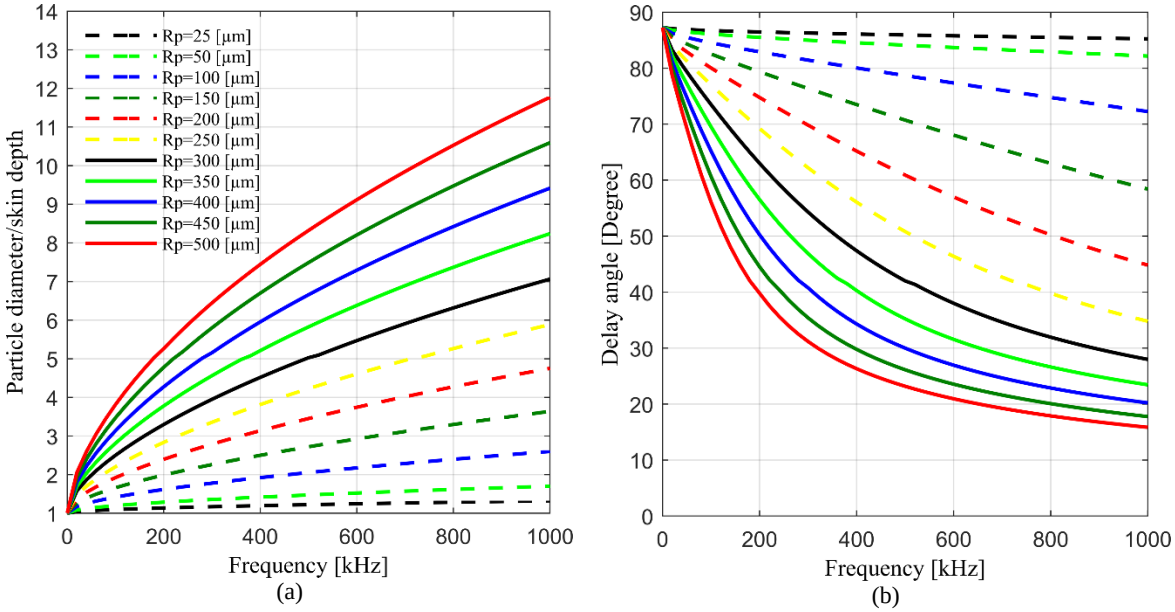

Figure 4-5. Particle size effect simulation with the dependence of the magnetic field frequency (a) Ratio of particle diameter to skin depth and (b) Phase delay angle.

Figure 4-5 (a) shows the ratio of particle diameter to the skin depth increases with the increasing of the magnetic field frequency as well as the particle size. Based on the physical model developed in Section 4.2, low ratios of particle diameter to the skin depth lead to high phase delay angles, which is clearly observed in Figure 4-5 (b). As seen, the delay angle is approximately equal to $\pi/2$ at the low field frequency case and decreases with the increasing of the field frequency as well as the particle size.

Figure 4-6 further explains the calculation results shown in Figure 4-5. As can be seen in Figure 4-5, with the increasing of the magnetic field frequency, the magnitude of polarization coefficient real part a_1 increases and the magnitude of imaginary part a_2 increases first and then decreases. Accordingly, the phase delay angle decreases (Figure 4-5 (b)) and the corresponding couple coefficient increases with an increase of the field frequency. Therefore, the magnetic force rises with the increasing of the magnetic field frequency. However, for the small-size particles with radius $r_p \leq 100\mu m$, the magnetic force will be quite weak even with an extremely high frequency (e.g., 1MHz), which is due to the fact that the small-size particles will lead to a low ratio of particle diameter to skin depth and a large phase delay angle (shown in Figure 4-5). This phenomenon may also be explained by the theory that the induced eddy currents are restricted by the lack of space or high resistivity [135].

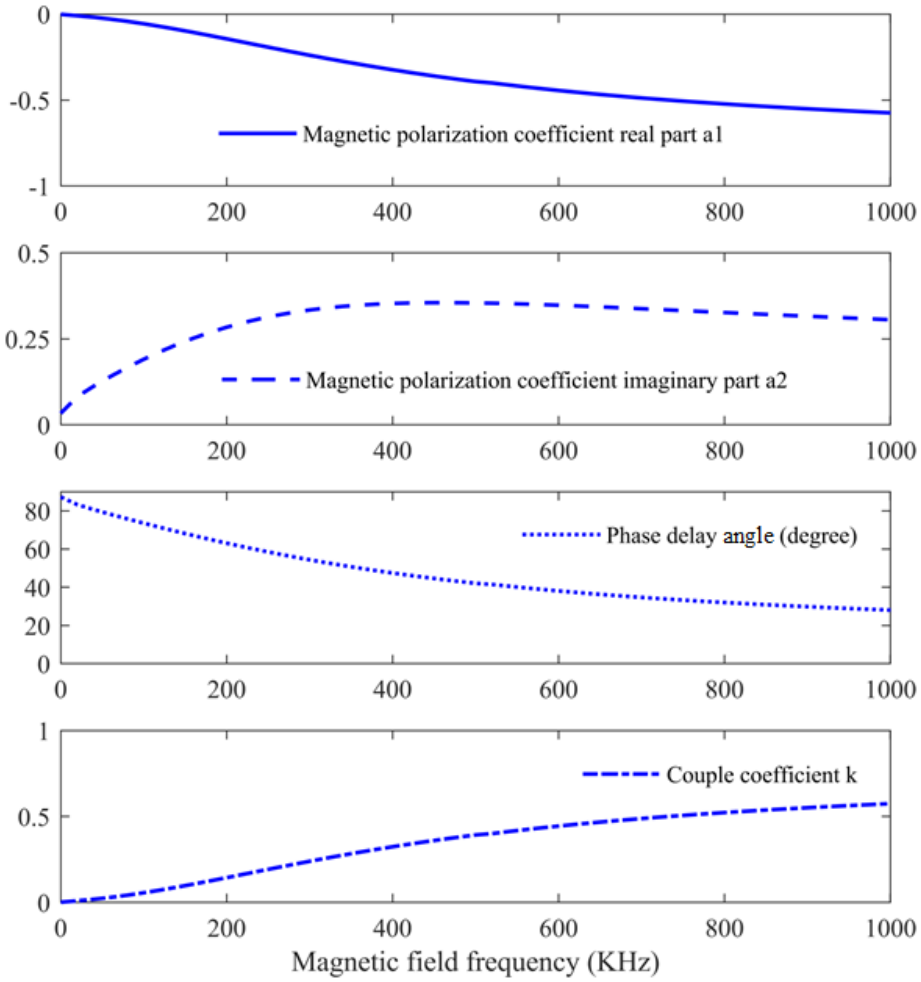

Figure 4-6. Polarization coefficients, phase delay angles and couple coefficients for aluminum particles over the magnetic field frequency. $r_p = 300\mu m$.

According to the results as shown in Figure 4-5 and Figure 4-6, it is reasonable to derive that the effective magnetic force will be very small for the linear-Halbach-PM configuration due to the relatively low field frequency. Therefore, the powder stream may not be effectively deflected/concentrated by the linear-Halbach-PM configuration. An experimental case study (shown in Appendix D) was also conducted to verify this conclusion. In the following part of this research, the concentration angles for the configurations with doublet-Halbach-PMQs and EM-quadrupoles were calculated under a wide range of magnetic field frequency.

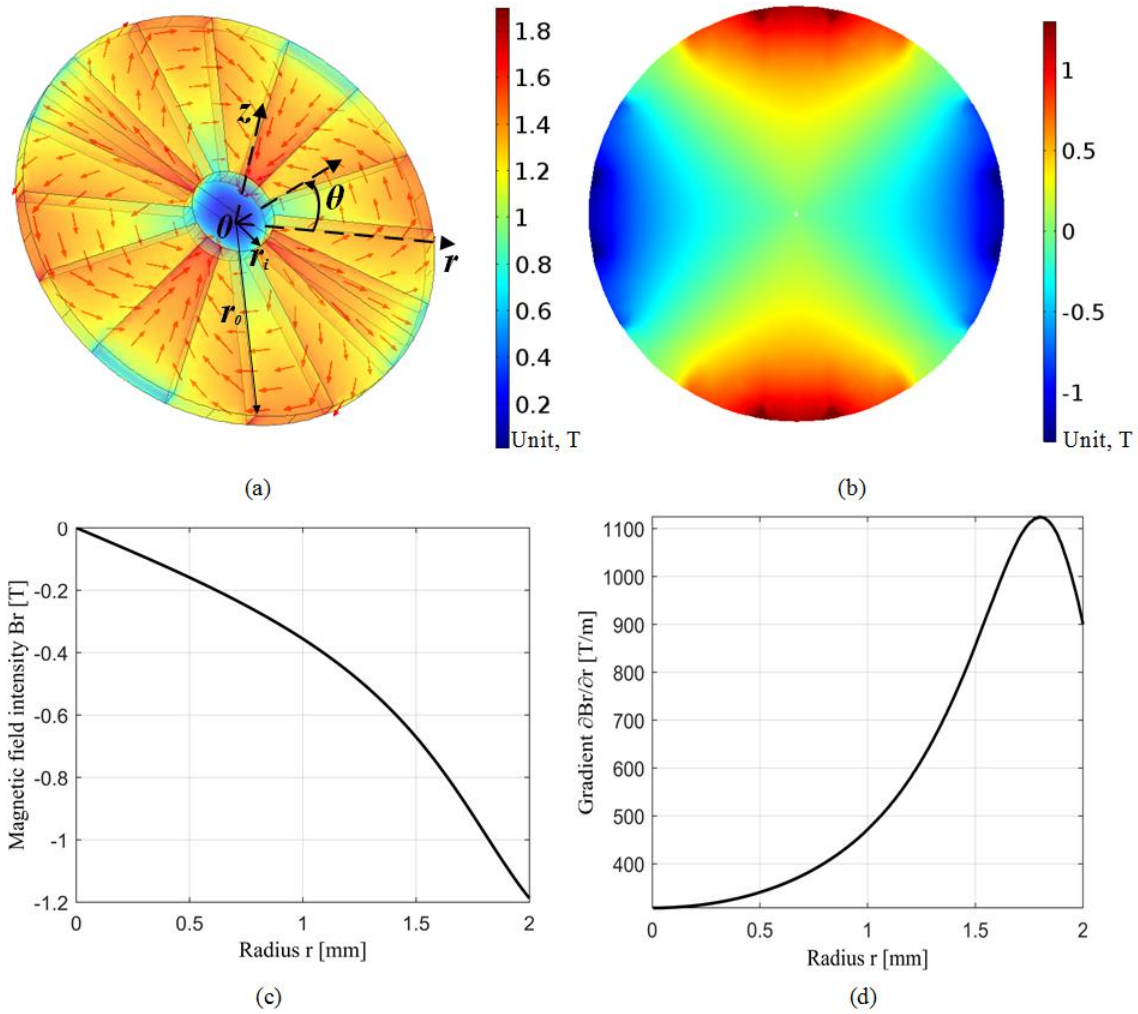

Figure 4-7. Magnetic field simulation of the concentration generator under Halbach-PMQs configuration. (a) Magnetization configuration 3D view with magnetic field intensity norm (T), the red arrows represent the magnetic field direction. (b) Magnetic field intensity $\boldsymbol{B_r}$ 2D distribution in the transverse cross-section ($z = 0$). (c) Magnetic field intensity $\boldsymbol{B_r}$ variation along $\theta = 0^{\circ}$ and $z = 0$. (d) Magnetic field gradient $\partial B_r/\partial r$ variation along $\theta = 0^{\circ}$ and $z = 0$. Inner radius $r_i = 2\ mm$, outer radius $r_o = 10\ mm$.

Figure 4-7 shows the simulated magnetic field for the proposed annulus-shaped Halbach-PMQs by COMSOL Multiphysics® software. The magnetization configuration is clearly shown in Figure 4-7 (a) and the induced radial flux intensity $\boldsymbol{B_r}$ within the inner region ($r \leq r_i$) of the Halbach PMQs is shown in Figure 4-7 (b). As seen, the radial magnetic field intensity increases from the center layer to the circumferential layer within the Halbach PMQs inner region. Figure 4-7 (c) and Figure 4-7 (d) show the magnitude of $\boldsymbol{B_r}$ and gradient $\partial B_r/\partial r$ rise towards to the outer circumference along the radius, respectively. Therefore, it can be derived that the magnetic

concentration force will be much larger for the particles in the outer layer of the powder stream than that in the inner layer. This is a desirable force distribution pattern since the outer layer particles have a large divergence and are expected to be exerted a high magnetic concentration force.

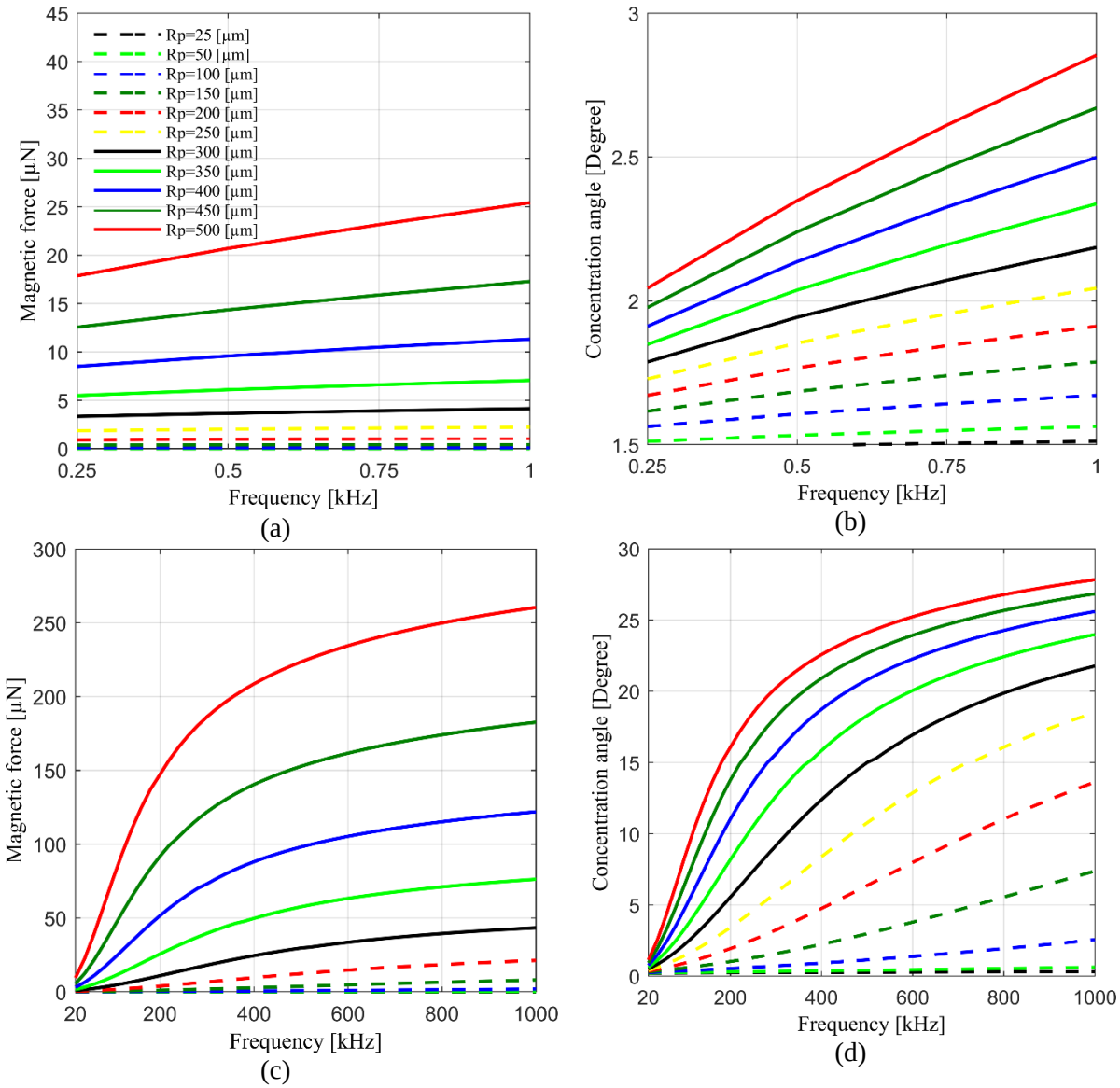

Figure 4-8. Simulated (a) force and (b) concentration angle of the concentration generator with doublet-Halbach-PMQs configuration, calculated (c) force and (d) concentration angle of the concentration generator with doublet- EMQs configuration.

Figure 4-8 presents the calculated magnetic forces and the concentration angles over a wide range of particle size for the proposed concentration generators. All simulation results shown in Figure 4-8 (a-d) indicate that the effective magnetic force and the concentration angle increase

with the enlarging of the field frequency as well as the increasing of the particle size. From Figure 4-8 (a-b), it can be seen that the doublet-Halbach-PMQs configuration cannot be effectively used for small-size particle ($25 < R_p < 350\,\mu m$) concentration, and the maximum concentration angle is smaller than 3° for large-size particles ($350 < R_p < 500\,\mu m$). The reason may be attributed to the relatively low field frequency that the induced skin depth is comparable with respect to the particle size. Based on the process parameters listed in Table 4-1, the equivalent magnetic field frequency of the doublet-Halbach-PMQs configuration is calculated as small as $1\,kHz$. By contrast, the EM-quadrupole configuration can be easily set with a high-level frequency, which is capable to deliver large magnetic force and concentration angles as shown in Figure 4-8 (c-d). A numerical simulation for magnetic forces on an aluminum particle with a radius of $R_p = 300\,\mu m$ was run in the ANSYS Maxwell V16 software as elaborated in Appendix E. An averaged magnetic force of $60\,\mu N$ was achieved under the frequency of $1\,MHz$. This result is approximate to the analytical calculation as shown in Figure 4-8 (c). However, for particles with a radius of $R_p \leq 100\,\mu m$, the magnetic force will be insufficient under high frequency (e.g., 1 MHz) as illustrated in Figure 4-8 (c). The reason may be explained by the fact that the small-size particles will lead to a low ratio of diameter/skin depth and a large phase delay angle as shown in in Figure 4-5.

4.5. Summary

In this chapter, a new magnetic approach that utilizes the induced magnetic force for non-ferrous metallic particles concentration in the gas-powder stream of LPF-AM was investigated. The effective magnetic concentration forces in the proposed configurations were explored and an analytical concentration angle model was developed with considering the skin effect. Three different conceptual designs of the proposed concentration generator were analyzed. It was found that the particle size has a strong effect on the effective concentration force as well as the concentration angle. For a specific particle size, the magnetic field frequency should be large enough that the induced skin depth is much smaller than the particle size to achieve an effective concentration.

Both the numerical calculation and the experimental case study show that the proposed PM-based configurations (doublet-Halbach-PMQs and linear-Halbach-PM) cannot be effectively

used to concentrate the aluminum particles with diameter $50\sim1000\ \mu m$ due to the low induced magnetic field variation frequency. But the numerical calculation shows that the proposed doublet- EMQs concentration with high frequency is capable to concentrate particles with a radius of $r_p \geq 150\mu m$. It was found that particles with r_p of 300 μm can be concentrated with more than 15° angle variation at the frequency of 600 *kHz*.

Chapter 5. Comprehensive Analytical Model of the LPF-AM Process*

5.1. Introduction

In this chapter, a new comprehensive modeling of the LPF-AM process that ranges from single-track to multi-track and multi-layer deposition is built. For the multi-track and multi-layer scanning, the accumulated temperature field is added to the initial temperature field of the following layers/tracks to quantitatively describe the accumulated heat effect. Subsequently, a dynamic thermal field of the multi-track and multi-layer deposition can be built and the corresponding heating/cooling rate and geometry profile can be estimated. In addition, powder mass distribution is incorporated into the transient thermal field module based on the built heat and mass flow coupling model developed in Chapter 3. Additionally, the model considers the melt pool shape variation as the liquid melt pool bead spreading on the solid surface, in which an isothermal wetting case is assumed and a dynamic contact angle is solved based on the Hoffman-Voinov-Tanner law [136].

5.2. Model formulation

5.2.1. Thermal field

In the single-track deposition of the LPF-AM process, each point along the laser scanning path will experience a thermal cycle, in which the transient temperature may range from the ambient temperature to a high temperature (e.g., melting temperature) and then cooling down. To quantify this thermal cycle mathematically, the temperature distribution in time and space domain should be solved. The solution for the temperature rise of an instantaneous point heat source in the semi-infinite homogeneous solid with temperature independent properties has been presented in Equation (2-3). The solution is derived from Green's function with the absence of convective and radiative heat flow, which has been validated in the context of additive manufacturing process modeling and shows a good agreement with the experiment

* A similar version of this chapter was published as:

Huang, Yuze, Mir Behrad Khamesee, and Ehsan Toyserkani. A New Physics-based Model for Laser Directed Energy Deposition (Powder-fed Additive Manufacturing): From Single-track to Multi-track and Multi-layer. Optics & Laser Technology 109 (2019): 584-599.https://doi.org/10.1016/j.optlastec.2018.08.015

[17,76,93,137]. Research studies [35,138] showed that the heat lost amount by radiation and convection is negligible in the comparison to that of the heat conduction. Thus, the heat radiation and convection effects are not considered in this chapter.

Based on Equation (2-3), for a moving heat source (moving speed v_x, v_y) with an arbitrary power intensity distribution that is released at $q(t)$ ($q(t) = dQ/dt$) from time $\tau = 0$ to $\tau = t$, the temperature rise of the interest point $X = (x, y, z)$ in the moving heat source coordinate may be derived with summing up the integration of the instantaneous point source over the whole specific heat source zone as,

$$\Delta T(X,t) = \int_{\tau=0}^{\tau=t} \left\{ \iiint \frac{q(\xi,\eta,\zeta,\tau)}{4\rho_p c_p [\pi\alpha_P (t-\tau)]^{3/2}} exp\left[-\frac{R^2}{4\alpha(t-\tau)}\right] d\xi d\eta d\zeta \right\} d\tau, \qquad \text{R} = \sqrt{(x - v_x\tau)^2 + \left(y - v_y\tau\right)^2 + \text{z}^2} \tag{5-1}$$

where ξ, η, ζ are the coordinates in the moving coordinate system.

In the multi-track and multi-layer deposition, the residual heat from prior layers/tracks may induce a higher initial temperature for the following layers/tracks. To count for the heat accumulation effect, the accumulated temperature field from prior layers/tracks are added to an adaptive initial temperature field for the following layers/tracks. The accumulated temperature field may be estimated based on the cooling effect of prior layers/tracks. As the residual heat still acts on the prior layers/tracks for some time, the input heat source cannot be switched off for the cooling effect simulation when the laser beam moves to the following layers/tracks [139]. Thus, the imaginary moving heat source theory [83,137,139] may be adopted to approximate the cooling effect of prior layers/tracks, in which the prior layers/tracks cooling patterns are extended on the time domain by assuming the corresponding imaginary heat sources (q_1) still move continuously in prior layers/tracks with their initial power ($q_1 = q_0$) and original direction after the deposition ending time (t^f) as shown in Figure 5-1.

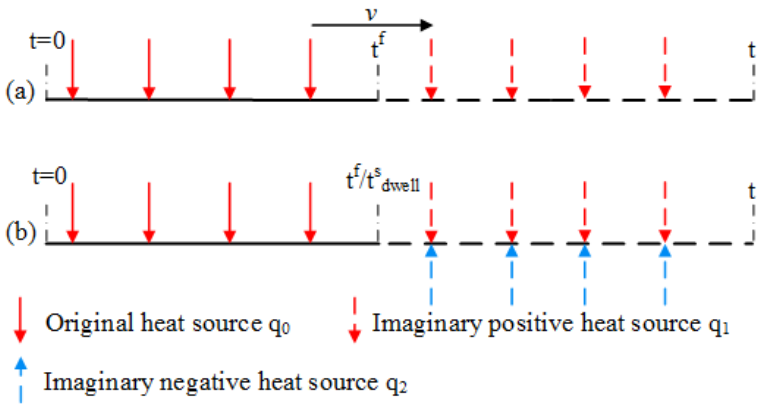

Figure 5-1. Schematic diagram for the cooling effect simulation by using the imaginary moving heat sources. (a) Active heat source q_0 and q_1, (b) Active heat source q_0, q_1 and q_2.

Similarly, in the case that the laser beam is turned off for a dwell time and then runs successively on the following layers/tracks, the transient cooling solutions of prior layers/tracks may be estimated by activating the imaginary negative heat sources (q_2) at the dwell starting time t^s_{dwell} (shown in Figure 5-2 (b)). Here has to be noted that the magnitude of the heat sources are equal to each other $q_0 = q_1 = q_2$ and the dwell starting time is the same time moment of the deposition ending time $t^s_{dwell} = t^f$. Therefore, the adaptive initial temperature T_{AI} of the interest point $X = (x, y, z)$ at time moment t may be estimated as,

$$T_{AI}(X,t) = \Delta T(X, t - t^s) - \Delta T(X, t - t^s_{dwell}) + T_0 \qquad (5\text{-}2)$$

where T_0 is the initial temperature. In the case that the laser beam isn't turned off between lasers/tracks and runs successively on the following layers/tracks (it is recommended in the LPF-AM process to improve the process efficiency), the adaptive initial temperature of following layers/tracks can be easily calculated based on the Equation (5-2) by setting the second term $\Delta T(X, t - t^s_{dwell}) = 0$.

In the multi-layer and multi-track deposition as shown in Figure 5-2 (track hatch space H_c, layer thickness h_c and track length L), a left-handed coordinate $(x, \mathrm{y}, \mathrm{z})$ is built to be moving together with the laser heat source with its origin located at the laser beam center. The laser is switched on at time t^s and moving with a speed v along the y-axis. Under the lateral feeding case, the powder feeding nozzle is assumed to rotate 180 degrees at each time that the laser beam changes

scanning direction. Thus, the adaptive initial temperature $T_{AI,nm}$ for the interest point $X = (x, \mathrm{y}, \mathrm{z})$ of nth track and mth layer at time moment t may be derived as,

$$
\begin{aligned}
&T_{AI,nm}(X,t)\\
&=\begin{cases}
T_0, \qquad n_{Total}=1, m_{Total}=1\\
\sum_{i=1,j=1}^{i=n-1,j=1}\left\{\begin{matrix}\Delta T_{ij}\left(X,t-t_{ij}^{s}\right)\\ -\Delta T_{ij}\left(X,t-t_{ij,dwell}^{s}\right)\end{matrix}\right|X=[x-(n-i)H_c,y,z]\Bigg\}+T_0,\\
1<n\le n_{Total}, m=m_{Total}=1\\
\sum_{i=1,j=1}^{i=1,m-1}\left\{\begin{matrix}\Delta T_{ij}\left(X,\ t-t_{ij}^{s}\right)\\ -\Delta T_{ij}\left(X,t-t_{ij,dwell}^{s}\right)\end{matrix}\right|X=[x,\mathrm{y},\mathrm{z}-(m-j)h_c]\Bigg\}+T_0,\\
n=n_{Total}=1, 1<m\le m_{Total}\\
\sum_{j=2}^{j=m-1}\left\{\begin{matrix}\sum_{i=1}^{i=n_{Total}}\Delta T_{ij}\left(X,t-t_{ij}^{s}\right)\\ -\Delta T_{ij}\left(X,t-t_{ij,dwell}^{s}\right)\end{matrix}\right|X=[x-|n-i|H_c,\mathrm{y},\mathrm{z}-(j-1)h_c]\Bigg\}\\
+\sum_{i=1,j=m}^{i=n-1,j=m}\left\{\begin{matrix}\Delta T_{ij}\left(X,\ t-t_{ij}^{s}\right)\\ -\Delta T_{ij}\left(X,t-t_{ij,dwell}^{s}\right)\end{matrix}\right|X=[x-(n-i)H_c,y,z]\Bigg\}+T_0,\\
1<n\le n_{Total}, 1<m\le\ m_{Total}
\end{cases}
\end{aligned}
\tag{5-3}
$$

where i and j denote the track and layer scanning index, respectively, t_{ij}^{s} the deposition starting time of the ith track and jth layer, $t_{ij,dwell}^{s}=t_{ij}^{s}+L_i/v_i$ the starting dwell time of the ith track and jth layer, n_{Total} the total track number in each deposition layer and the m_{Total} is the total layer number during the multi-track and multi-layer deposition.

With considering the high cooling rate of the LPF-AM process, two aspects should be improved for the calculation of the above adaptive initial temperature $T_{AI,nm}$. On one hand, the residual heat amount of the prior layers/tracks may decrease to a very tiny value as the laser beam scans over the following layers/tracks, it might be desirable to discard such small accumulated temperature calculation for some prior layers/tracks with respect to the setting tolerance ($\Delta T_{ij} < TOL_{dT}$). On the other hand, the transient temperature value at the time moment $t = R_L/v$ that the heat source scans over one laser beam radius R_L might be set as the saturation temperature $T_{AI,S}$. Thus, the adaptive initial temperature $T_{AI,nm}$ can be expressed as,

$$
T_{AI,nm}=\begin{cases}T_{AI,nm}, T_{AI,nm}\le T_{AI,S}\\ T_{AI,S}, T_{AI,nm}>T_{AI,S}\end{cases}, \qquad T_{AI,S}=\Delta T(X,R_L/v)+T_0 \tag{5-4}
$$

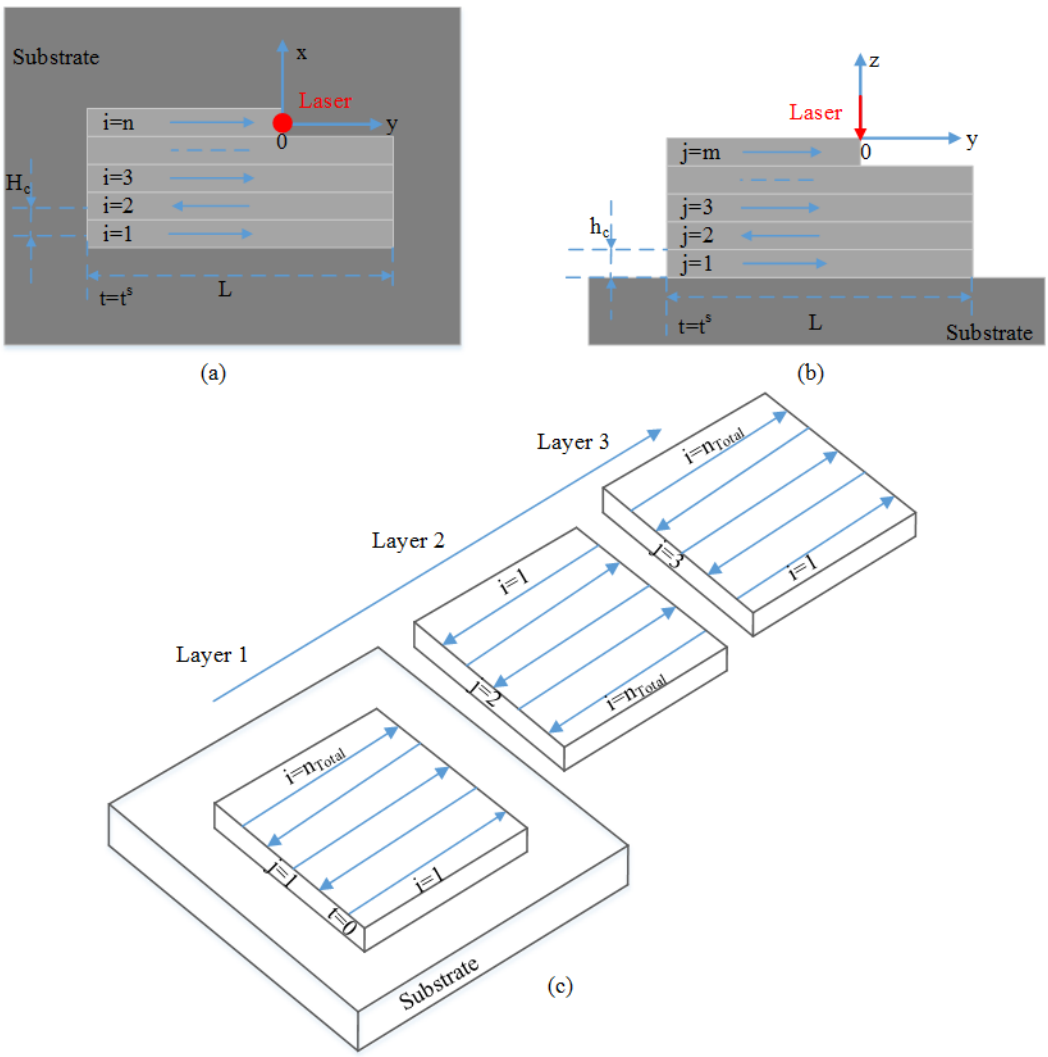

Figure 5-2. Schematic diagram for multi-track and multi-layer deposition. (a) Top view, (b) Side-view, (c) Laser scanning pattern. $(x, \mathrm{y}, \mathrm{z})$ left-handed coordinate.

The laser beam with Gaussian TEM_{00} mode is used in the research and its intensity distribution $I(x, \mathrm{y}, \mathrm{z})$ is described in Equations (3-6) and (3-7). In the LPF-AM process, the laser beam will be attenuated by the powder stream before it reaches the substrate surface, and the powder that impinges into the melt pool will draw energy immediately from the melt pool to increase its enthalpy. As the attenuated laser power were mainly used for heating the powder stream, the total energy that added into the melt pool may be approximated by the sum of the energy of the original laser beam and the unheated powder stream. The enthalpy exchange for the particles that strikes the melt pool may be considered as a local surface process [118], and hence the mass source of the powder stream might be expressed as a negative heat source,

$$I_p(x,\mathrm{y},\mathrm{z}) = c_p v_p sin\varphi \rho(x,y,z)(T_0 - T_m) \tag{5-5}$$

where $\rho(x,y,z)$ the powder stream concentration, $v_p = \dot{g}/\pi r_0^2$ the particle velocity ($\dot{g}$ is the powder carrying gas feed rate and r_0 is the nozzle inner radius) and φ is the nozzle inclination angle. The derivation for $\rho(x,y,z)$ are elaborated in Section 3.2.1, which are formulated with considering the powder stream properties (powder feed rate $\dot{m}$, powder divergence angle θ and feeding nozzle height H_N).

Accordingly, the mass and heat flows of the process might be analytically coupled together with the equivalent resultant heat flux $I_R(x,\mathrm{y},\mathrm{z}) = I(x,\mathrm{y},\mathrm{z}) + I_p(x,\mathrm{y},\mathrm{z})$. Thereafter, the temperature rise may be calculated by the following integration based on Equation (5-1),

$$\Delta T(X,t) = \int_{\tau=0}^{\tau=t} \int_{\xi=-\infty}^{\xi=+\infty} \int_{\eta=-\infty}^{\eta=+\infty} \frac{I_R(\xi,\eta,z)}{4\rho_p c_p [\pi\alpha_P(t-\tau)]^{3/2}} exp\left[-\frac{R^2}{4\alpha(t-\tau)}\right] d\xi d\eta d\tau\,, \tag{5-6}$$

$$R = \sqrt{(x-\xi)^2 + (y - v\tau - \eta)^2 + \mathrm{z}^2}$$

Equation (5-6) can be further simplified as below and the derivation is given in Appendix F,

$$\Delta T(X,t) = \frac{2}{\rho_p c_p \pi\sqrt{\pi\alpha_P}} \int_{\tau=0}^{\tau=t} d\tau \left\{ \frac{\beta_w P_L/\sqrt{(t-\tau)}}{R_L^2 + 8\alpha_P(t-\tau)} exp\left[-\frac{2[x^2 + (y-v\tau)^2]}{R_L^2 + 8\alpha_P(t-\tau)} - \frac{z^2}{4\alpha_P(t-\tau)}\right] \right. \tag{5-7}$$
$$\left. + \frac{c_p \dot{m}(T_0 - T_m)/\sqrt{(t-\tau)}}{[r_{avg}^2 + 8\alpha_P(t-\tau)]} exp\left[-\frac{2[x^2 + [(y-v\tau)/sin\varphi]^2]}{r_{avg}^2 + 8\alpha_P(t-\tau)} - \frac{z^2}{4\alpha_P(t-\tau)}\right] \right\}$$

In consequence, the temperature field for the nth track and mth layer at time moment t may be derived as,

$$T_{nm}(X,\mathrm{t}) = \Delta T(X, t - t_{nm}^s) + T_{AI,nm}(X,t) \tag{5-8}$$

To improve the model fidelity, the effect of latent heat of fusion, Brewster effect on the process laser absorptivity and the Marangoni flow effect were considered as described in Equations (3-18)-(3-21).

5.2.2. Clad geometry

The integral in Equation (5-7) does not have a closed-form solution. However, it can be easily solved with numerical calculation. Then the melt pool dimension (e.g., width w_p, length l_p and depth d_p) is estimated based on the solid-liquid interface boundary. Accordingly, the clad width w_0 is estimated by the melt pool width, and the clad height h_0 is derived based on the mass balance over the melt pool area. Experimental results of the research [140] show that the shape of the clad track can be approximated by the parabolic function with a high accuracy. With assuming the cross-section boundary of the clad to be a parabolic shape, the clad height can be derived as,

$$h_0 = \frac{3v_p sin\varphi}{2w_0 v\rho_P} \iint_S \rho(x,y,z)dS \tag{5-9}$$

where S is the melt pool projection area on the substrate plane. However, the shape of the liquid melt pool will be varied as it is spreading on the solid surface before the contact line is settled. The surface tension will act on the phase triple point to move the phase line in such a way that the dynamic contact angle α tends to a final wetting angle α_w as shown in Figure 5-3.

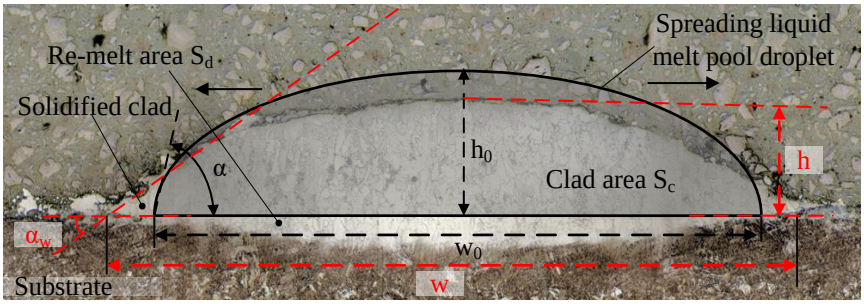

Figure 5-3. Schematic diagram for the dynamic contact angle variation

The original droplet contact angle can be estimated as $\alpha_0 = tan^{-1}(4h_0/w_0)$. With the isothermal spreading assumption, the spreading behavior of the liquid droplet before contact line being arrested can be expressed based on Hoffman-Voinov-Tanner law [136,141]

$$\frac{\mu v_c(t)}{\gamma_{LV}} = \varepsilon[\alpha^3(t) - \alpha_e^3] \tag{5-10}$$

where μ the liquid metal viscosity, v_c the contact line spreading velocity, γ_{LV} the liquid-vapor interfacial tension and ε is usually approximated as a universal constant with a value of 0.013

[141]. Although the realistic molten metal droplet wetting is a non-isothermal configuration [142], the isothermal wetting assumption here may not spoil the validity of the proposed model since the temperature variation may be negligible during the tiny time of liquid bead spreading.

Based on Young's equation, the equilibrium angle α_e can be derived as [136],

$$cos\alpha_e = \frac{\gamma_{SV} - \gamma_{LS}}{\gamma_{LV}} \tag{5-11}$$

in which γ_{SV} and γ_{LS} represent the solid-vapor and solid-liquid interfacial energy, respectively. In the LPF-AM process, the composition of the clad material and the substrate are almost the same or be very similar to each other. Thus, the interfacial energy between the clad nucleus and the solid substrate or prior layer will have the relationship as $\gamma_{LS} \approx 0$ while the interfacial energies $\gamma_{SV} \approx \gamma_{LV}$ [2]. Therefore, the equilibrium wetting angle should tend to zero ($\alpha_e \to 0$). As the radially outward motion of the contact line is driven by the uncompensated Young's force, the contact line acceleration may be approximated as,

$$A(t) = \frac{4\gamma_{LV}[cos\alpha_e - cos\alpha(t)]}{\rho_P w_0^2} \tag{5-12}$$

With combing Equations (5-10) and (5-11) to Equation (5-12), the dynamic contact angle can be derived as,

$$\alpha(t) = -2\sqrt{3}\tanh\left[\frac{\sqrt{3}\mu t}{9\varepsilon\rho_P w_0^2} - tanh^{-1}\left(\sqrt{3}\alpha_0/6\right)\right] \tag{5-13}$$

As proposed by Stefano and Ain [141], the contact line will be settled less than $3t_{osc}$, in which $t_{osc} = \sqrt{\rho_P(w_0/2)^3/\gamma_{LV}}$ is the inertial oscillation time scale. Therefore, the final wetting angle α_w may be approximated by Equation (5-13) with $t = 3t_{osc}$. With assuming the liquid clad S_c has a parabolic boundary at the beginning and then forms a parabolic section as the contact line is settled,, an area conservation function can be derived as,

$$S_c = \frac{2}{3}w_0 h_0 = \frac{2}{3}wh \tag{5-14}$$

where w and h are the final clad width and height, respectively. Based on Eqs. (18-19), the final clad width and height can be calculated as,

$$\begin{cases} h = \dfrac{\sqrt{w_0 h_0 tan\alpha_w}}{2} \\ w = 2\sqrt{\dfrac{w_0 h_0}{tan\alpha_w}} \end{cases} \tag{5-15}$$

With assuming the re-melt zone on the substrate has a parabolic geometry with area $S_d = 2w_0 d_p/3$, then the geometry dilution may be estimated by the ratio of the clad area to the re-melt area in the cross-section plane as,

$$dilution = \frac{d_p}{h_0 + d_p} \tag{5-16}$$

The single track shape may be estimated by the parabolic function as $f(x,y) = a(y)x^2 + b(y)x + c(y)$ with the coefficients $a(y) = -4h/w^2$, $b(y) = 0$ and $c(y) = h$, which can be calculated based on Equation (5-15). It should be noted that the clad width w and height h were calculated based on the transient thermal field in the moving laser coordinate as shown in Figure 5-2 and thus they should be a function of the time t or position $y = vt$.

For the multi-track deposition, the overlapping tracks will be deposited successively with an overlapping ratio $OR = (D_L - H_c)/D_L$ that is defined based on the hatch space. As the surface tension will lead to different cladding angles for the following tracks, the multi-track overlapping profile cannot be directly predicted based on the addition of each individual profiles [140]. Also, the residual heat from the prior tracks deposition may still keep a relatively high value during the following tracks deposition, the thermal patterns of the following tracks will not stay constant. Therefore, the following tracks geometry (e.g., width, height) cannot be assumed as a constant value. Inspired by the recursive overlapping profile model proposed by V. Ocelík et al. [140], a new dynamic multi-track profile model was developed based on the transient temperature field presented in Section 2.1.

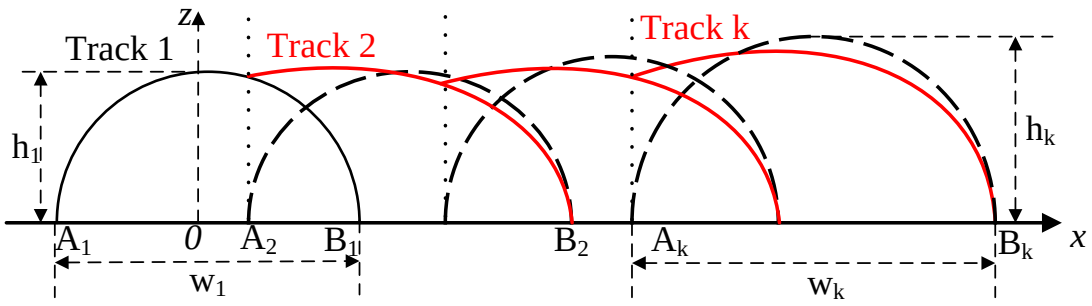

Figure 5-4. Schematic diagram for the derivation of the dynamic multi-track profile model

As shown in Figure 5-4, the k_{th} track shape may be calculated with the parabolic function $f_k = a_k x^2 + b_k x + c_k$ and the coefficients a_k, b_k, c_k may be derived by solving the following equations,

$$\begin{cases} f_k(A_k) = f_{k-1}(A_k) \\ f_k(B_k) = 0 \\ \int_{A_k}^{B_k} f_k dx = \int_{A_k}^{B_{k-1}} f_{k-1} dx + \dfrac{2w_k h_k}{3} \end{cases} \tag{5-17}$$

The above multi-track shape model may also be easily extended to simulate the multi-layer and multi-track profile with assuming the new layer is deposited on the top surface of the first track by moving a hatch space distance.

5.3. Materials and experimental procedure

In this study, the water atomized pure iron powder (Rio Tinto, Melbourne, Australia) was deposited on the sandblasted cold rolled 1018 steel substrate (75 × 15 × 5mm^3) by a LPF-AM setup developed in-house. This setup includes a continuous IPG photonics fiber laser with the maximum power of 1100 W that is installed in a Fadal CNC machine. The powder feeder purchased from Sulzer Metco is used to feed materials through a lateral nozzle. The particle morphology was measured by the scanning electron microscope and is shown in Figure 5-5 (a). The powder size distribution was measured by the CAMSIZER X2 (Retsch Technology, Haan, Germany) and is illustrated in Figure 5-5 (b). As can be seen, the particle has an average size of 30 μm in diameter. The thermo-physical properties of the iron powder are considered to be temperature independent, and the thermal parameters are averaged over the temperature range as shown in Table 5-1. Experiments were done to test the built model with single-tack, multi-layer

thin wall structure and multi-layer/multi-track structure with the same track length of 30 mm. The experimental process parameters are listed in Table 5-2.

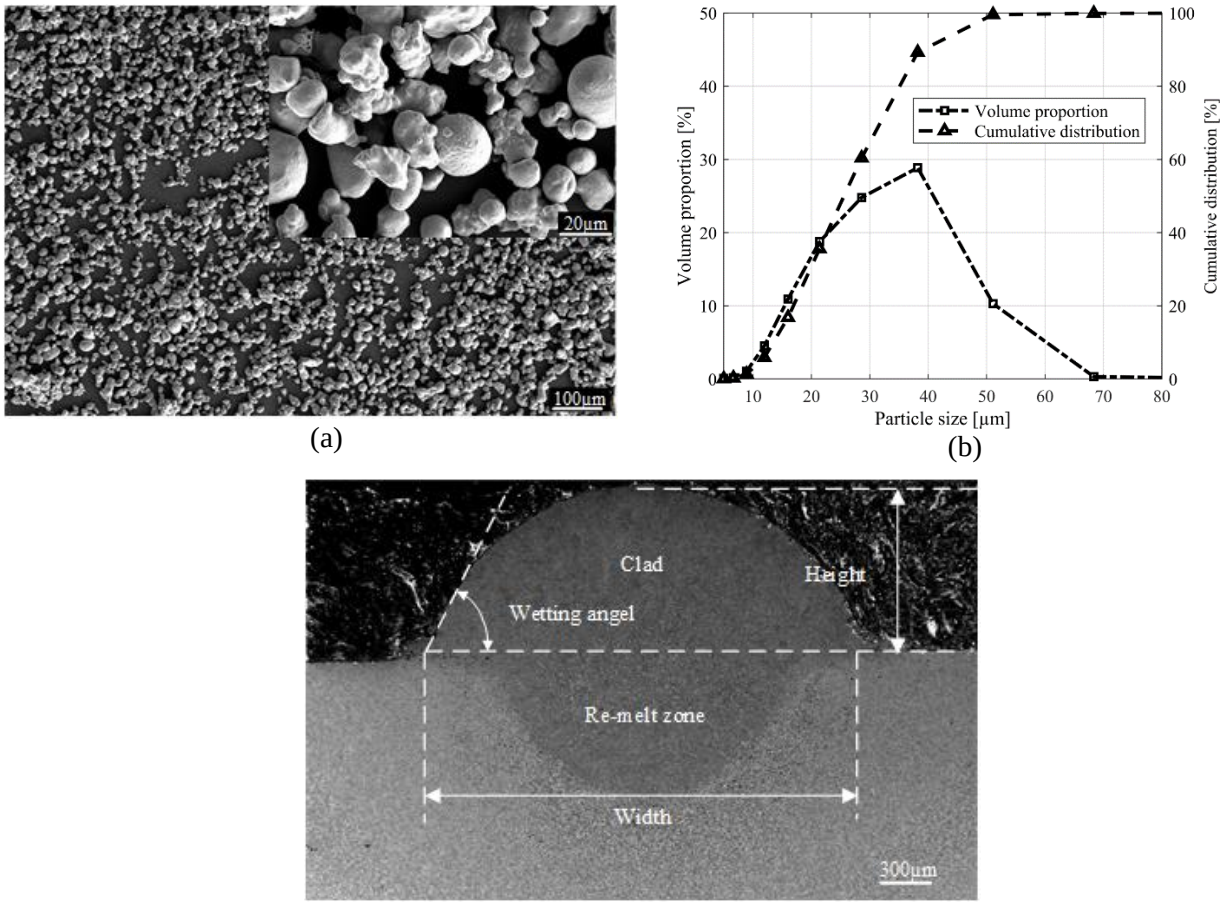

Figure 5-5. Pure iron powder characteristics and single-track transverse cross-section view. (a) Powder morphology, (b) Particle size distribution, (c) Transverse cross-section with large dilution.

The samples of the single-track deposition were cross-sectioned, mounted, polished and etched with nitric/hydrochloric solutions (2% Nital). Then the clad width, height, re-melt area and wetting angle were measured by a laser microscope VK-X250K (Keyence, Itasca, USA) as shown in Figure 5-5 (c) with a transverse cross-section view. The clad heights of the thin-wall structures and the 3D profiles of the deposited multi-track and multi-layer structures were measured by a 3D optical scanner (AICON, Meersburg, Germany).

Table 5-1. Particle thermal- physical parameters [143]

Melting Temperature T_m $[K]$	Density ρ $[Kg/m^3]$	Thermal conductivity k $[W/(m \cdot K)]$	Specific heat c_p $[J/(Kg \cdot K)]$
1811 (1538 ℃)	7870 (25 ℃)-7035 (1538℃)	80.4 (25℃)-34.6 (1538℃)	447.31 (25℃)-822.1 (1538℃)

Table 5-2. Process parameters for iron powder deposition by LPF-AM. (The viscosity and the surface tension were cited from reference [143])

Parameters	Values	Parameters	Values
Process speed, v	2, 3 $[mm/s]$	Laser power, P_L	420-900 $[W]$
Far-field angle, θ_L	0.02 $[rad]$	Brewster effect coefficient, a_w	0.0196
Beam waist radius, R_{0L}	0.43 $[mm]$	Laser absorptivity of iron, β	0.6
Beam waist position, Z_0	13.81 $[mm]$	Carrying gas feed rate, $\dot{g}$	2.5 $[dL/min]$
Nozzle height, H_N	8, 10 $[mm]$	Nozzle angle, φ	50°
Nozzle internal radius, r_0	0.7 $[mm]$	Track length, L	30 $[mm]$
Correction factor, μ_M	2.5 [67]	Track hatch space, H_c	0.58 $[mm]$
Viscosity, μ	0.0058 $[kg/(m \cdot s)]$	Deposition thickness, h_c	0.3 $[mm]$
Powder feed rate, $\dot{m}$	2, 4 [g/min]	Powder divergence angle, θ	5.8°
Ambient temperature, T_0	298 $[K]$	Surface tension, γ_{LV}	1.88 [N/m]

5.4. Results and discussion

In this section, sufficient details are provided to use the proposed model for thermal field, heating/cooling rates, melt pool dimensions, multi-layer/track initial temperature and clad geometry prediction. The model was verified using the measurements of different builds, including single-track, multi-layer thin-wall structures and multi-tack/multi-layer patch structures.

5.4.1. Thermal field prediction

Figure 5-6 shows the temperature calculation results for different points (illustrated in Figure 5-6 (a)) along the laser scanning path of a single-track. The thermal cycle patterns of the points along the laser beam scanning path are clearly shown in Figure 5-6 (b) and Figure 5-6 (c) when different process speeds are used for simulation.

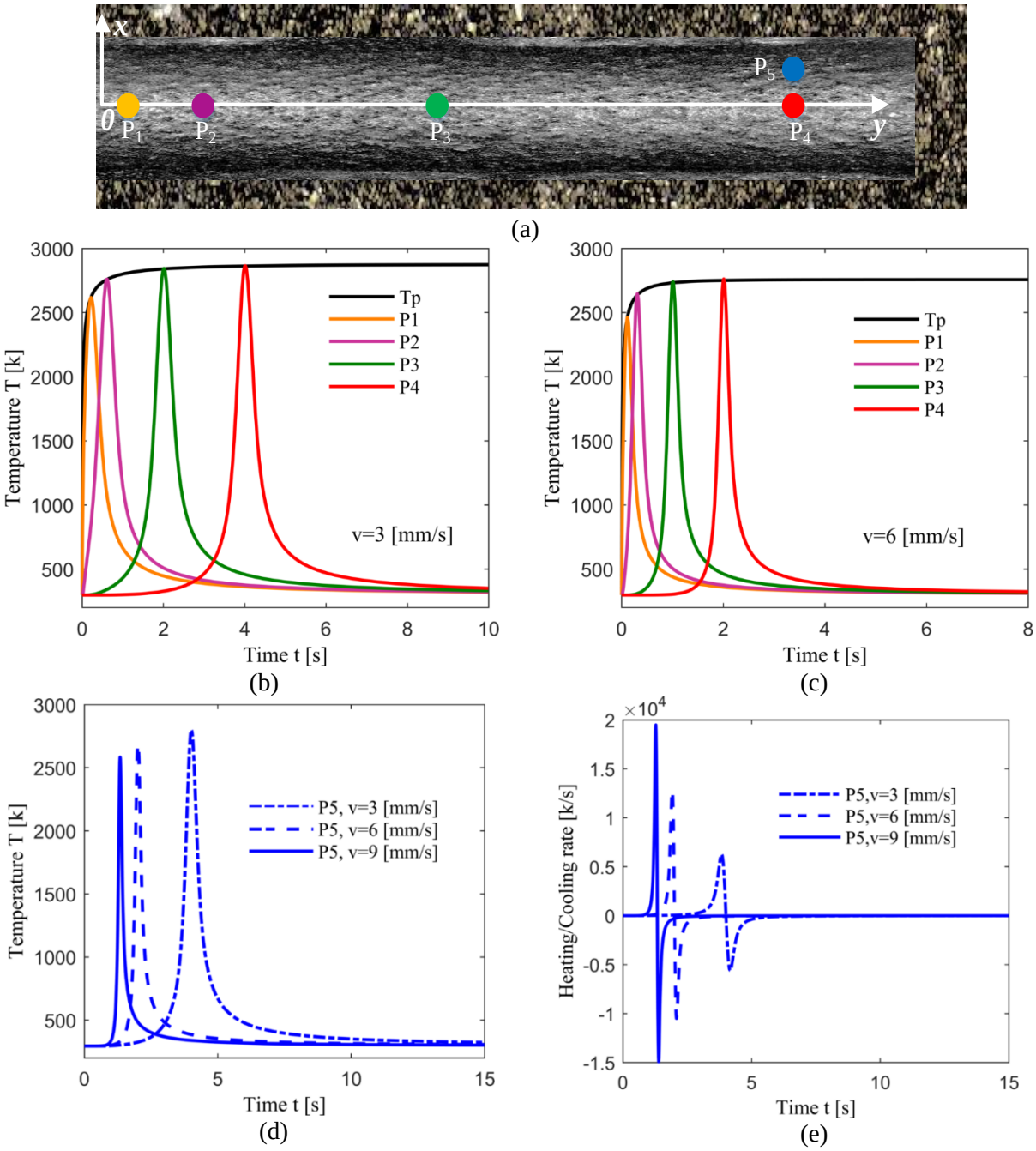

Figure 5-6. Transient temperature and heating/cooling rate of a single-track scanning. (a) Schematic diagram of the interest points on the single track, left-handed coordinate. (b), (c) Transient thermal cycle for points (0, y_{pi}, z=0.2) and peak temperature T_p (black solid line) for the moving points (0, y, z=0.2) that just under the laser beam, $y = vt$. (d) Transient thermal cycle for point P_5 (0.2, 12, z=0.2). (e) Heating/cooling rate for point P_5 (0.2, 12, z=0.2). Laser power 700 W, powder feed rate 2 g/min, nozzle height 10 mm and y_{p1}=0.6, y_{p2}=1.8, y_{p3}=6, y_{p4}=12. Length unit is mm.

As it can be seen, the peak temperatures for the rest of the points along the scanning path reach a steady state just after the laser source onset, which may be explained with the energy balance that the energy input rate is equal to the energy dissipation rate. Figure 5-6 (d) illustrates that the peak temperature decreases with increasing process speed, which may be attributed to the fact that energy input per unit time decreases with the increasing of the scanning speed. Figure 5-6 (e) shows the heating/cooling rates with different process speeds. According to Figure 5-6 (e), at a constant laser power and powder feed rate, the maximum of heating/cooling rates increases with the increasing of the process speed, which is consistent with the results in the literature [144,145]. As the thermal field (e.g., cooling rate) has a strong effect on the microstructure formation [146,147] and residual stresses [148], this developed model may be used to control the mechanical properties by predicting the thermal field based on the process parameters.

Figure 5-7 (a) and Figure 5-7 (b) show the schematic diagram for the adaptive initial temperature calculation in the multi-layer single-track and the single-layer multi-tack deposition process, respectively. The scanning path follows the parallel pattern that is shown in Figure 5-2. As illustrated in the model theory of Section 2, the initial adaptive temperature of the following layers/tracks may be computed by summing up the accumulated temperature field from prior layers/tracks with a distance of layer thickness h_c or hatch space hatch space H_c in each iterative computation. The predicted adaptive initial temperatures for the multi-layer thin-wall structure deposition along the track length are shown in Figure 5-7 (c, d, e, i, k) and the anticipated initial temperature for the multi-track single layer deposition are illustrated in Figure 5-7 (f, g, h, j). As the laser scanning start point of the second layer/track is the end point of the first layer/track, the initial temperature of the second layer/track rises up instantly and gradually decreases as the laser beam passed, which is in accordance with the quasi-steady-state Rosenthal's temperature solution in [83].

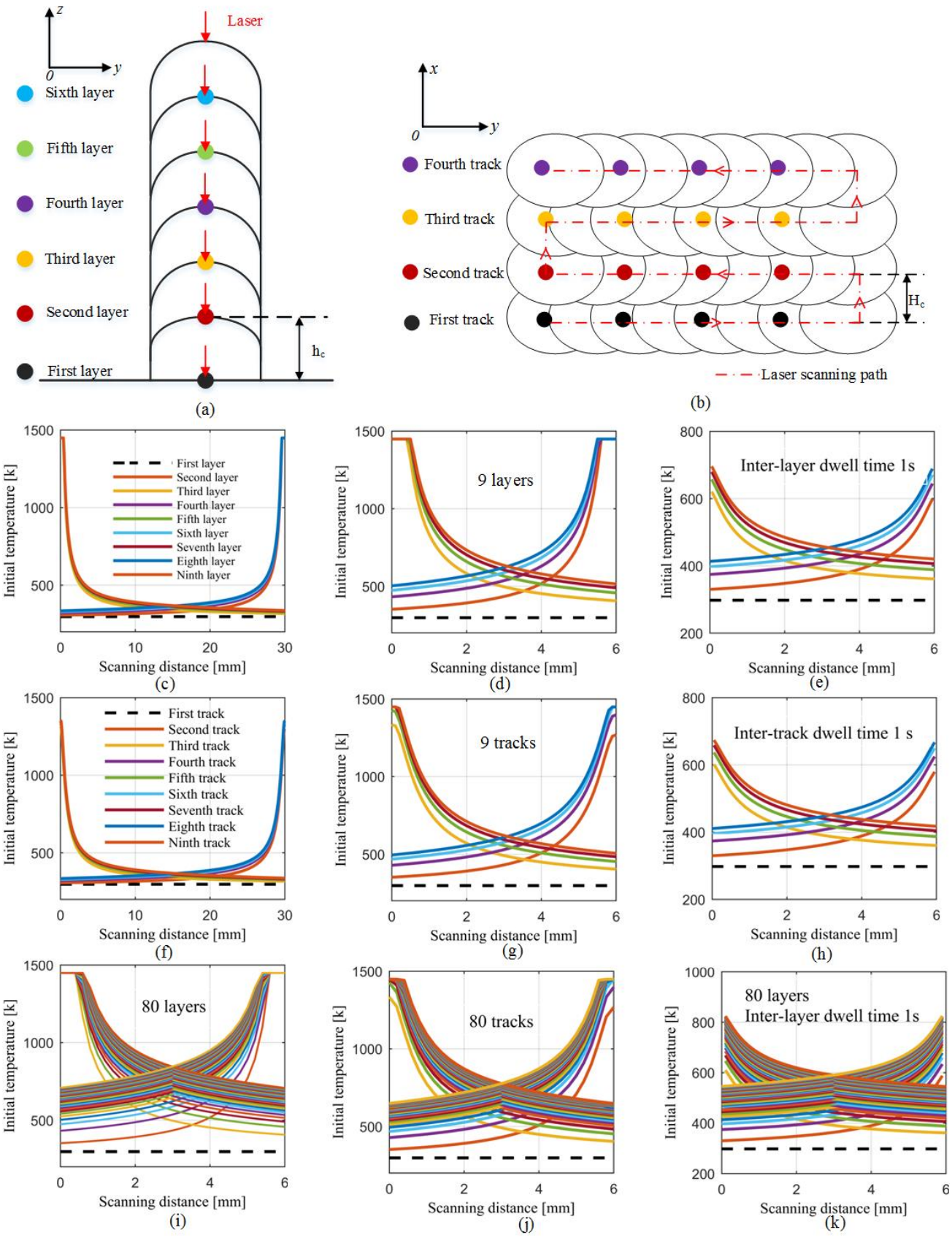
Laser
z
y
0
Sixth layer
Fifth layer
Fourth layer
Third layer
Second layer
First layer
h_c
(a)
x
y
0
Fourth track
Third track
Second track
First track
H_c
Laser scanning path
(b)
Initial temperature [k]
Scanning distance [mm]
First layer
Second layer
Third layer
Fourth layer
Fifth layer
Sixth layer
Seventh layer
Eighth layer
Ninth layer
(c)
9 layers
(d)
Inter-layer dwell time 1s
(e)
First track
Second track
Third track
Fourth track
Fifth track
Sixth track
Seventh track
Eighth track
Ninth track
(f)
9 tracks
(g)
Inter-track dwell time 1 s
(h)
80 layers
(i)
80 tracks
(j)
80 layers
Inter-layer dwell time 1s
(k)

Figure 5-7. Adaptive initial temperature simulation for multi-layer/track deposition. Schematic diagrams for the adaptive initial temperature calculation of (a) single-track and multi-layer thin-wall structure and (b) single-layer and multi-track structure. Calculated adaptive initial temperature of (c, d, e, i, k) thin-wall structure and (f, g, h, j) single-layer and multi-track structure. Layer thickness 0.31 mm, hatch space 0.98 mm with 30% overlapping ratio, laser power 650 W, scanning speed 3 mm/s, powder feed rate 2 g/min, nozzle height 8 mm and track length 30 mm. The points position that were used for the initial temperature calculation of multi-layer ($X = (0, y, z + mh_c)$) and multi-track ($X = (x + nH_c, y, 0)$) were marked with color balls in (a) and (b), respectively.

Compare Figure 5-7 (c) with Figure 5-7 (d), it can be seen that a larger adaptive initial temperature will be achieved for a shorter track length (scanning distance) in the single-track and multi-layer deposition. And the initial temperature will be reduced with adding an inter-layer dwell time (shown in Figure 5-7 (e)). The results in Figure 5-7 (f, g, h) show a same trend in the single-layer and multi-track deposition with that of the multi-layer deposition. The reason may be attributed to the fact that larger scanning path or inter-layer/track dwell time will increase the cooling time of the prior layers/tracks before the next heat loading comes and lead to a slighter retained heat. By increasing the layers/tracks numbers, a larger initial temperature will be achieved as shown in Figure 5-7 (i, j, k) due to a higher amount of heat loading. And one solution to lessen the accumulated heat effect is to add an inter-layer/track dwell time as exhibited in Figure 5-7 (e, h, k).

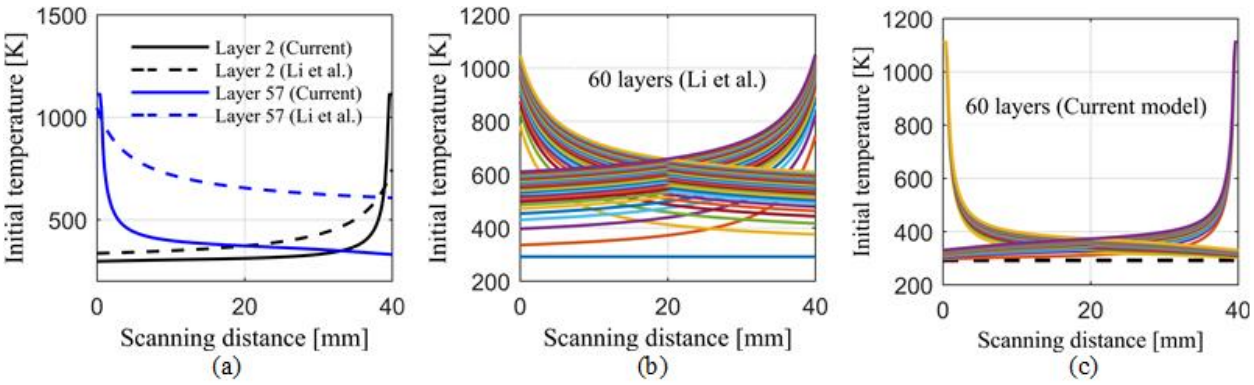

Figure 5-8 A comparison of the model calculated multi-layer initial temperatures in current research and prior research of Li et al. [83].(a) Calculated initial temperatures of layer 2 and layer 57. (b) Reference model results with 60 layers. (c) Current research model results with 60 layers. The thermal-mechanical properties of the powder material and the associated process parameters were based on the LPF-AM deposition of Ti–6AL–4V in the research work of Li et al. [83].

Figure 5-8 compares the initial temperatures that were calculated by the current model with that predicted by the model of Li et al. [83]. As observed from Figure 5-8 (a)-(c), the predicted initial temperatures of current research show higher temperature values and larger cooling rates than that calculated by the model of Li et al. The major reason may be caused by the fact that a quasi-steady-state Rosenthal's solution was used in the model of Li et al., which only presents the steady thermal feature at time $t \to +\infty$. By contrast, a transient Green's thermal solution was applied in the current research, being able to calculate the transient thermal variations in the LPF-AM process. Another factor that may contribute these differences is the omission of the feeding powder and their associated concentration distribution in the built model of Li et al.

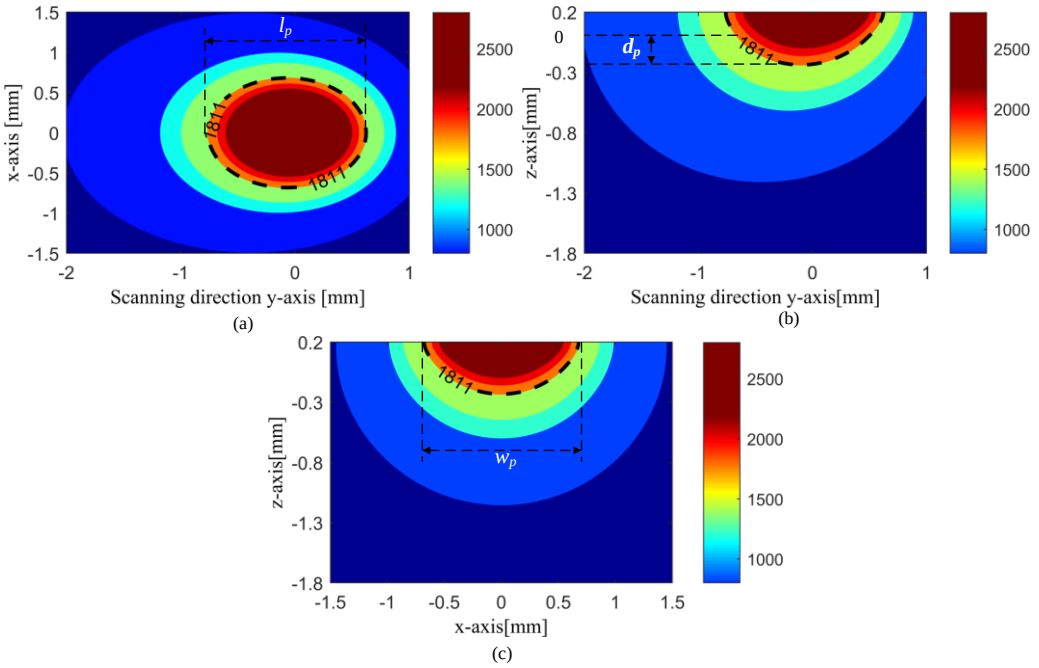

Figure 5-9. Melt pool thermal field distribution at the time moment ($t = L/2v$) that the laser beam moves to a half-track length. (a) Peak temperature field in xy plane (substrate surface plane), (b) Temperature field in yz plane (longitudinal cross-section), (c) Temperature field in xz plane (transverse cross-section). Process speed 6 mm/s, track length 30 mm, laser power 600 W, powder feed rate 2 g/min, nozzle height 10 mm. The melt pool boundary is indicated by the black dash line (T=1811 k).

Figure 5-9 illustrates the calculated melt pool temperature distribution. The melt pool boundary is identified with the liquid-solid isotherm and the melt pool dimension is labeled with width w_p, length l_p and depth d_p. Up to now, it is still challenging for any sensing technology to measure the temperature field in the melt pool depth direction, thus the real-time melt pool depth cannot

easily be measured or validated. By contrast, the built model can efficiently be used to predict the temperature field in the transverse cross-section (Figure 5-9 (c)) and longitudinal cross-section (Figure 5-9 (b)) for estimating the melt pool depth during the LPF-AM process.

5.4.2. Clad geometry verification

Figure 5-10 shows the calculated powder stream concentration based on reference [34] and the corresponding predicted single-track profile. As shown in Figure 5-10 (a), the powder concentration is not distributed evenly over the substrate surface, instead, it is denser in the center of the powder stream and inclines toward the powder feeding direction, resulting in a non-uniform clad height distribution over the melt pool. Therefore, it is essential to consider the powder concentration distribution in clad geometry prediction. Figure 5-10 (b) shows that the predicted single-track height varies over the transverse cross-section, which is in consistent with the measured track profile as shown in Figure 5-10 (c).

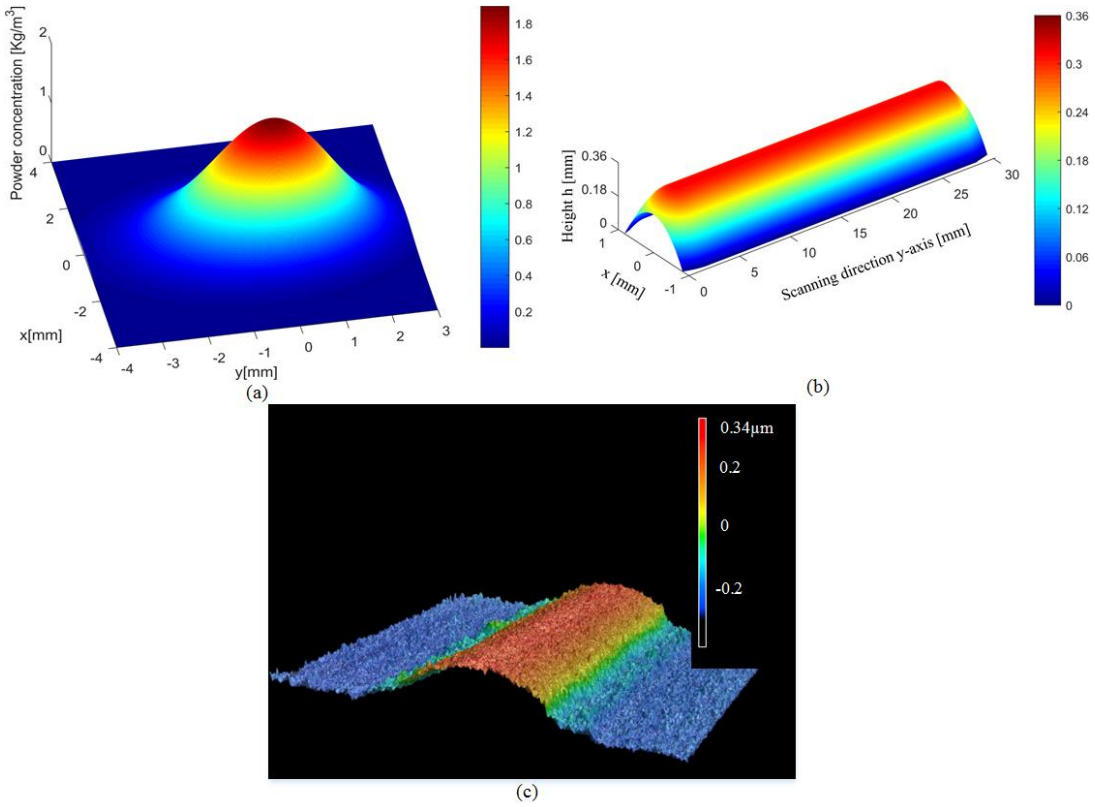

Figure 5-10. Powder stream concentration and single-track profile. (a) Powder stream concentration, (b) Predicted single-track profile, (c) Measured single-track profile. Process speed 2 mm/s, powder feed rate 2 g/min, nozzle height 10 mm and laser power 550 W.

Figure 5-11 compares the model predicted clad width, height, dilution and wetting angle with that of the experimental measurements. Two combined specific energy balance terms $E_c = P_L/vD_0$ and $E_m = P_L/\dot{m}D_0$ were used to address the process and compare the modeled and measured clad dimension and dilution. The energy term E_C represents the energy limit for continuous laser deposition and E_M describes the energy limit needed to melt the powder [94], which are two important energy limits for building the proper process parameters window. As seen, the model predicted results match well with that of the experiments, and the model prediction accuracy is extensively improved with considering the liquid melt pool spreading theory 2.

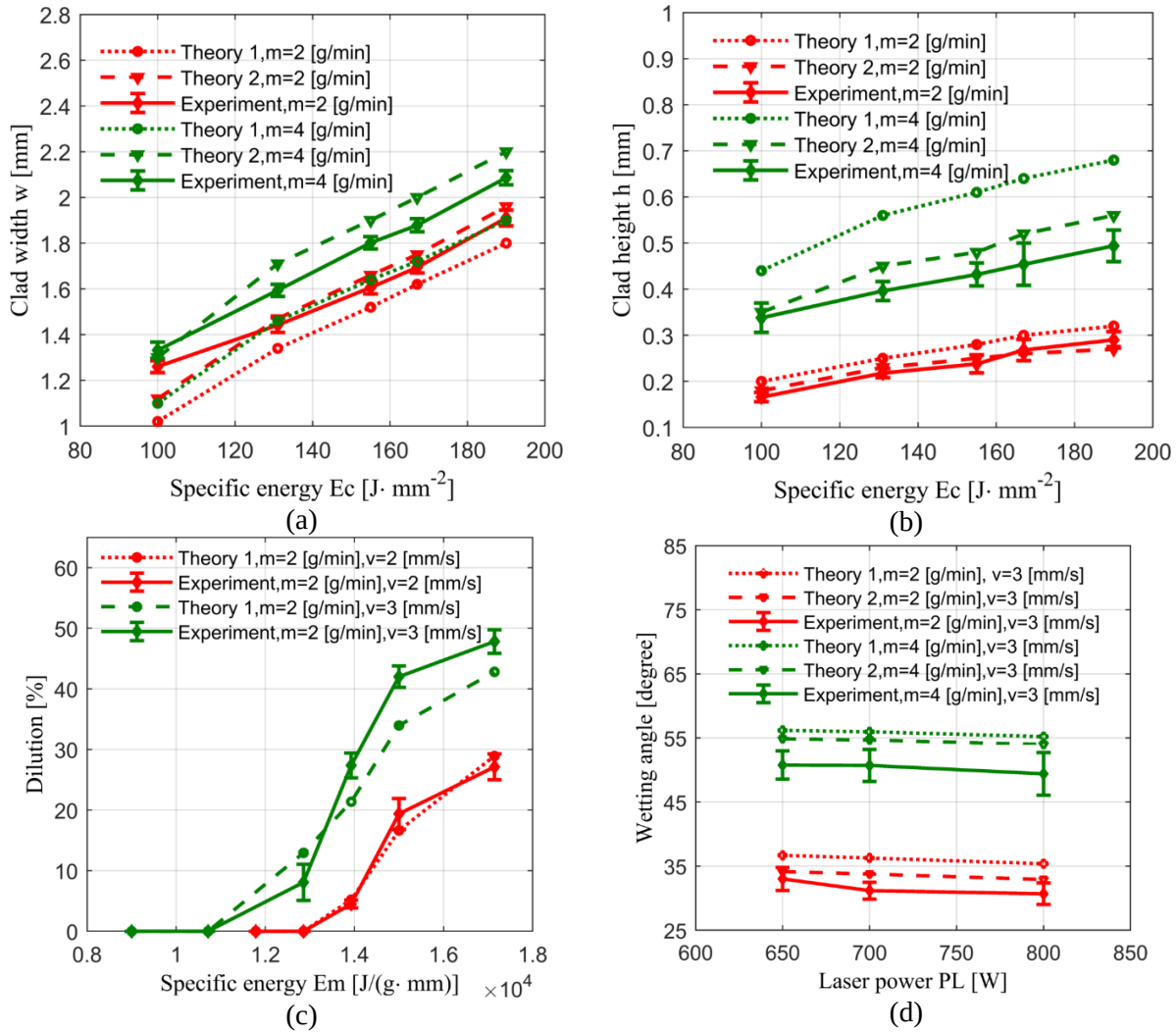

Figure 5-11. Single-track dimension and dilution. (a) Clad width, (b) Clad height, (c) Dilution, (d) Wetting angle. Theory 1 and theory 2 represents the calculation without and with considering the liquid melt pool spreading, respectively.

Figure 5-11 (a, b) show that the clad width and height increase with increasing E_C, which may be explained by the fact that the energy input at per unit area of laser track is intensified as increasing E_C, thus the melt pool area as well as the powder catchment are magnified. It can also be seen that at a constant E_C, the clad width and clad height increase with enlarging the powder feed rate. The slight increase of the clad width is quite interesting. One reason may be attributed to the fact that the process laser absorptivity rises up due to the Brewster effect when a higher powder feed rate is employed.

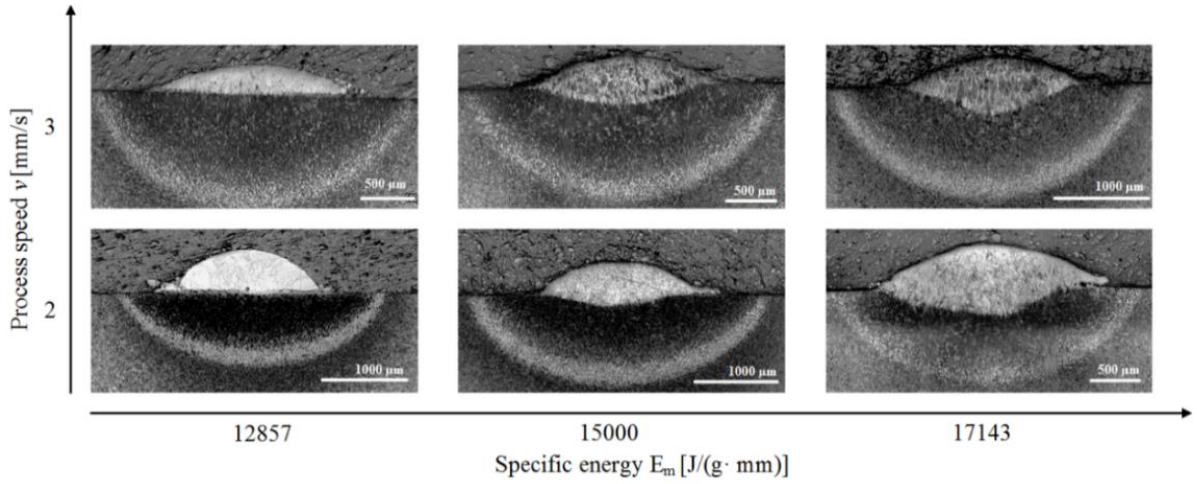

Figure 5-12. Transverse cross-section view for dilution variation with varying specific energy balance E_m. Powder feed rate 2 g/min and nozzle height 10 mm.

Figure 5-11 (c) and Figure 5-12 both show that the dilution percentage rises with enlarging E_m, which is in accordance with the truth that a higher E_M represents a greater energy level for larger amount of powder melting. As shown in Figure 5-12, the higher E_m is characterized by a larger re-melt zone and therefore induced a higher value of dilution. Besides, a threshold exists for the E_m before dilution occurs, which is consistent with the reference [94]. Therefore, the energy balance term E_m may be used as a reference threshold for dilution control or prediction. Figure 5-11 (c) and Figure 5-12 also indicate that the dilution rises with the increasing of the process speed at a constant E_M value, but the dilution increasing rate decreases with the enlarging of the process speed, which is in agreement with the experimental results in [76]. Since the dilution is an extremely important quality index that indicating the level of the inter-layer bonding and composition [149], a proper dilution percentage should be kept (normally between 10%-30%) to ensure good layer integrity and pore free deposition [150]. It would be beneficial to use the

proposed model for the dilution prediction and control. Figure 5-11 (d) shows the laser power has a mildly negative effect on the clad wetting angle, whereas the powder feed rate has a large positive effect on the wetting angle, which agrees well with the conclusions in the literature [150,151].

Figure 5-13 compares the model predicted height with the experimental measurement of a multi-layer thin-wall build. The model height is calculated by accumulating all the prior single-layers' height. It can be observed from Figure 5-13 (b) that the measured and forecasted height along the track length match well with each other, especially at the two ends of the track. Both the measured and predicted results show that the clad height is larger at the two end points than that of the rest points along the track. This two humps phenomenon agrees with the experimental results in reference [83] and may be attributed to the higher initial temperature at the beginning points of each layer than that of rest points along the track, which can be clearly seen in Figure 5-7 (c) and Figure 5-7 (d).

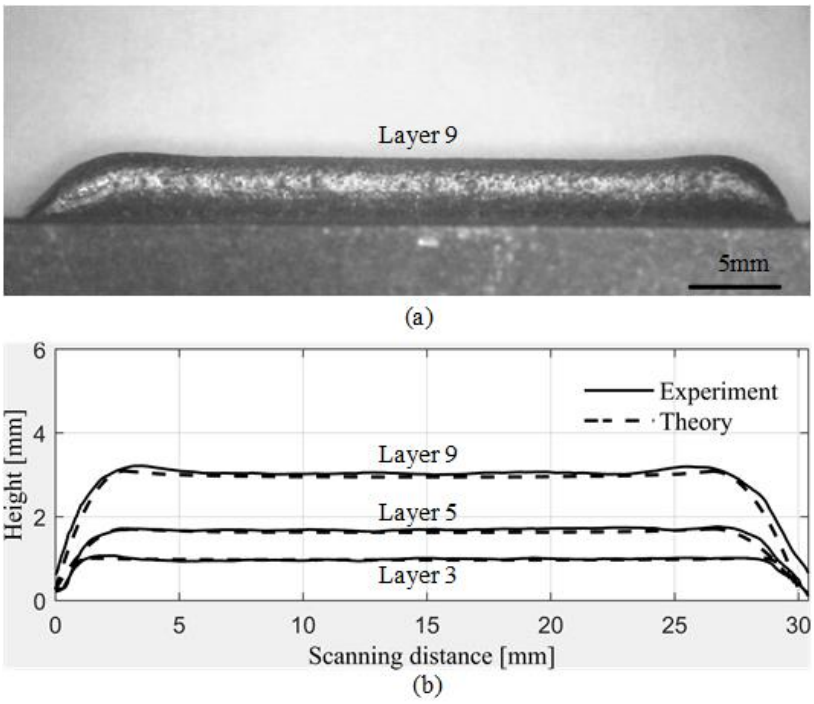

Figure 5-13. Dynamic clad height along the track length of the multi-layer thin wall structure. (a) Side view, (b) Measured and predicted clad height. Laser power 650 W, scanning speed 3 mm/s, powder feed rate 2 g/min, track length 30 mm, layer thickness 0.31 mm and nozzle height 8 mm.

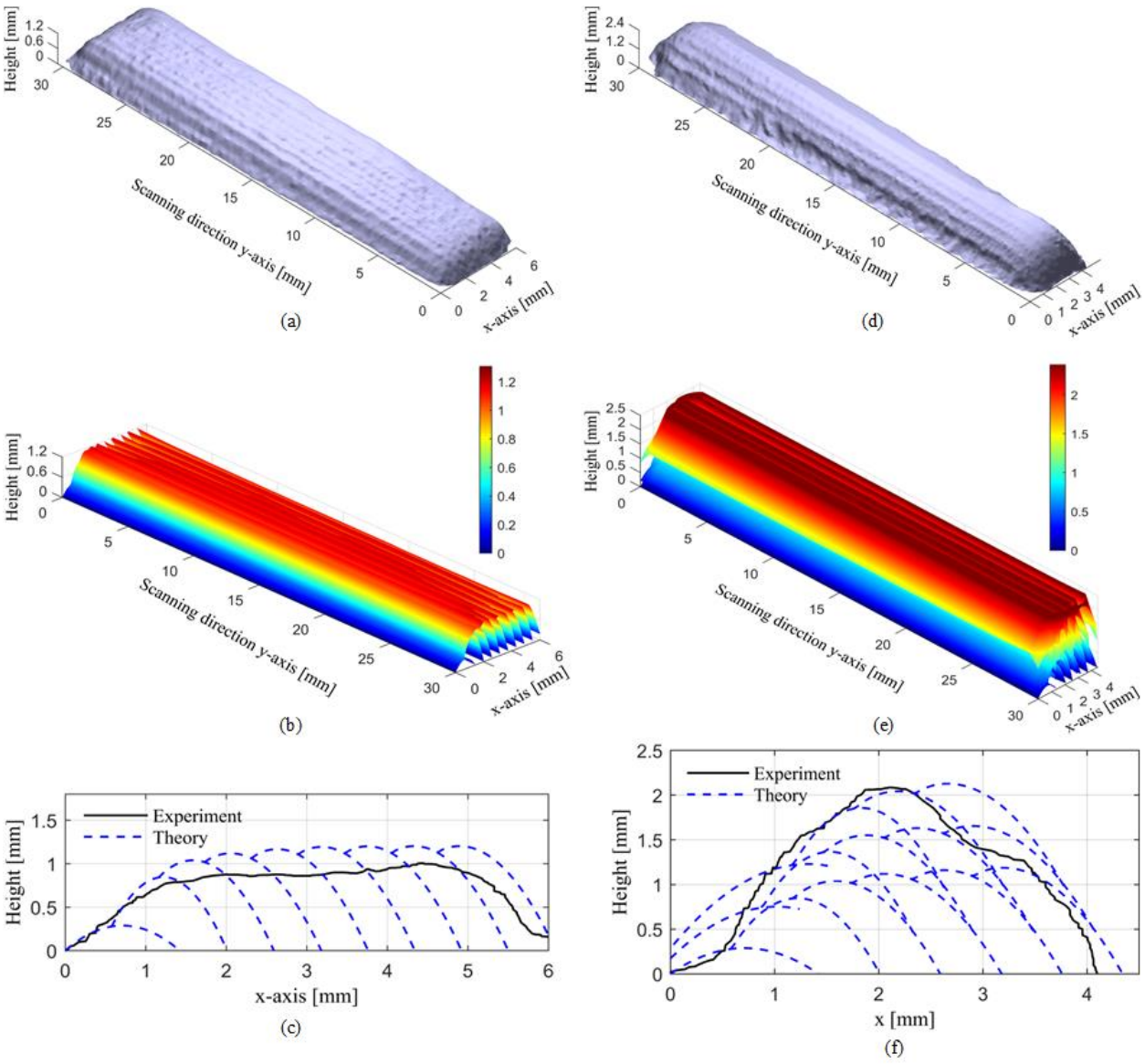

Figure 5-14. Measured and predicted 3D profiles and the associated transverse cross-section contours of the multi-track/layer builds. (a) Measured 3D, (b) predicted 3D and (c) the transverse cross-section (at y=15 mm) contours for one-layer and nine-track patch structure build, hatch space 0.58 mm with 58.6% overlapping. (d) Measured 3D, (e) predicted 3D and (f) the transverse cross-section (at y=15 mm) contours for three-layer and six-track patch structure build. Layer thickness 0.31 mm, laser power 650 W, track length 30 mm, scanning speed 3 mm/s, powder feed rate 2 g/min and nozzle height 8 mm.

Figure 5-14 shows the measured and predicted 3D profile and the associated transverse cross-section contours of the multi-track/layer builds, in which the build 3D profiles were simulated based on the built dynamic multi-track\layer profile model. Here has to be pointed out that the

scanning pattern for both Figure 5-13 and Figure 5-14 all follow the parallel scanning path as shown in Figure 5-2.

As observed, the predicted dynamic height in Figure 5-14 (b) and (e) match well with the measured results in Figure 5-14 (a) and (d), respectively. It is interesting to notice the realistic top surface waviness shown in Figure 5-14 (b) and (e), which indicates that the built dynamic model may be used for final surface waviness prediction. Figure 5-14 (c) and (f) depict the transverse cross-section contours at the half-track length plane (y=15 mm). The theory predicted contours are shown with the blue lines where each blue line describes one prior track contour and their accumulating combination was used to represent the final contour of the multi-layer/track builds. As seen, the theoretical calculated contours have a comparably larger height than that of the experiment measurements, which may be attributed to the ignorance of the heat convection and radiation in the theory model that induced a larger melt pool as well as a higher deposition rate. The thermal field will increase significantly due to the heat accumulation effect in the multi-layer/track deposition, which may lead to a more pronounced convection and radiation at the high level of temperature field condition. In addition, the evaporation effect is neglected in the built model, which may not be so dominant in the low level thermal field situation, but is expected to play a more important role at the high level temperature case and lead to a considerable mass loss and a lower clad height.

5.4.3. Sensitivity analysis

The sensitivity analysis was conducted by varying the values of process parameters and material properties and investigating their effect on the clad height. Table 5-3 shows the mean values and the corresponding values with variation of −10% and +10% for each parameter. The clad height was calculated with position located in the half-track length transverse cross-section, and only one parameter was modified with keeping the other parameters equal to the mean values in each single calculation.

As shown in Figure 5-15 (a) and (b), the effects of the process parameters and material properties on the clad height show similar patterns for both the single-track and multi-layer thin-wall builds. It can be seen that the powder feed rate has the largest positive effect on the clad height, followed by the laser absorptivity and laser power, whereas the process speed has the largest

negative effect on the clad height, followed by the powder density and thermal conductivity. Therefore, choosing proper process parameter values for a specific powder material will be crucial for the clad height control.

Table 5-3. Process parameters and material properties for sensitivity analysis

Parameter	-10%	Mean	10%
Laser power, [W]	585	650	715
Process speed, [mm/s]	2.7	3	3.3
Powder feed rate, [g/min]	1.8	2	2.2
Laser absorptivity	0.54	0.6	0.66
Density, $[kg/m^3]$	6707.25	7452.5	8197.75
Thermal conductivity, $[W/(m \cdot K)]$	51.75	57.50	63.25
Specific energy,$[J/(Kg \cdot K)]$	571.24	634.71	698.18

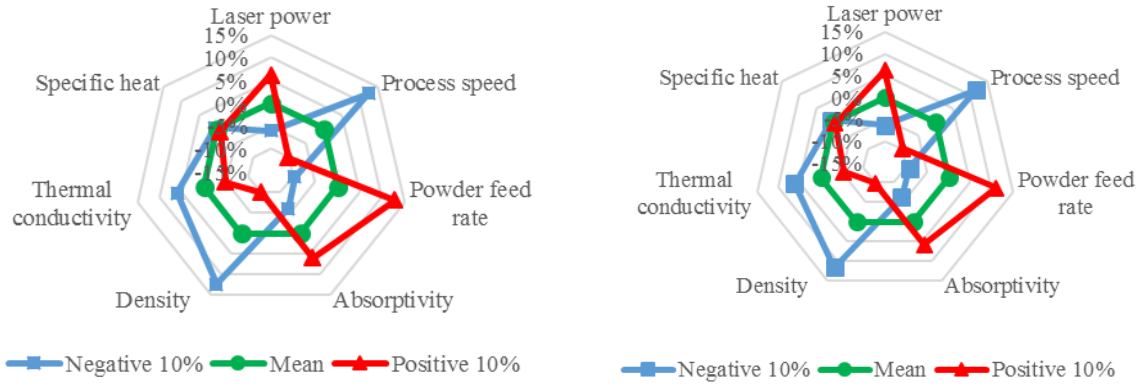

(a) (b)

Figure 5-15. Sensitivity analysis of process parameters and material properties effect on the clad height. (a) Single-track, (b) Nine-layer thin-wall structure.

5.5. Summary

In the LPF-AM process, the heat accumulation and the melt pool bead spreading clearly play important roles in the thermal field distribution and final clad dimension during the multi-layer multi-track deposition. Both the thermal field and the clad dimension are essential factors for the final fabricated part's mechanical property and integrity. This chapter built a physics-based

process model, in which the residual heat and melt pool bead spreading were incorporated into the model for temperature field calculation and the final clad geometry prediction. Experimental validation of single-track deposition shows a high level of agreement at different levels of specific energy and powder feed rate. Multi-track/layer experiments demonstrate that the model can accurately predict the dynamic height as well as the simple patch structure 3D profile. The discrepancies between the experimental and model predicted results may be caused by the deviation of the powder feeding, ignorance of the heat convection and the unavoidable oxidation during the process. Sensitivity analysis shows that the process parameters as well as the powder material properties play important roles in the final clad dimension.

The simulations of the thermal field and the as-built deposits' geometry were run on a HP® computer with Intel® Core™ i7-6700 CPU (3.4GHz). The calculation code was programmed by Matlab® R2017b with a built adaptive quadrature algorithm. The integral calculation tolerance is set as $TOL_{Int} = 10^{-3}$ and the drop out temperature rise tolerance is set as $TOL_{dT} = 10^{-3}K$.

For a track length of 30 mm, the simulation for the transient temperature of the moving point or a fixed point in an 80 layers thin-wall structure or an 80 tracks patch (single-layer and multi-track) took 0.2 s, the simulation for the thermal history of a moving or a fixed point in an 80 layers thin-wall structure or an 80 tracks patch (single-layer and multi-track) took 36 s. The simulation for the dynamic height or 3D profile of the designed nine-layers thin-wall structure took 12 s, the simulation for the dynamic 3D profile of the designed nine-tracks and single-layer patch took 90 s, the simulation time for the dynamic 3D profile of the designed six-tracks and three-layers patch took 150 s.

Chapter 6. Comprehensive Analytical Model of the LPB-AM Process*

6.1. Introduction

The LPB-AM process involves a large number of process parameters, i.e., laser power, laser beam size, scanning speed, layer thickness, stripe width, stripe overlap and hatch space. Improper parameter setting may lead to a variety of defects [152], i.e., lack of fusion, porosity and severe thermal stress. Those defects can deteriorate the fabrication quality and induce severe distortion in the final parts. In addition, keeping the optimized scanning parameters over the complete manufacturing process of LPB-AM may not guarantee a defect-free fabrication due to the process perturbations (e.g., local geometry variation, heat accumulation and disturbances in the work environment). Kruth *et al.* [153] observed warped contours and dross formation in the fabrication process of LPB-AM with fixed optimized parameters. Those defects were attributed to a large alternation of local geometrical features that greatly changes local heat conduction. Steuben *et al.* [62] showed common disturbances in the multi-track scanning of LPB-AM under fixed process parameters. The common disturbances are attributed to excess heat accumulation, inducing non-uniform melt pools and excessive voids in the deposits. Moreover, the defects formed in the LPB-AM process significantly increase unnecessary post-processing costs for the fabricated parts [154].

Process related defects can be identified with repeated experiments and may be eliminated by processing optimization. By contrast, the effect of process perturbations may be negated by real-time process adjustments with feedback control only [20]. Researchers have demonstrated a great potential to achieve in-situ feedback control of the LPB-AM process by using advanced on-line monitoring systems (e.g. melt pool radiation intensity [12], track dimension [155], layer roughness [156]) with high sampling rate. These monitoring systems are summarized in the recent review work of Grasso and Colosimo [157].

---

* A similar version of this chapter will be submitted as:

Huang Yuze, Hamed Asgari, Zhang Zhidong, Mohammad Ansari, Mir Behrad Khamesee, Ehsan Toyserkani. Process Modeling and Optimization of Laser Powder-bed Fusion Additive Manufacturing: Formulation, Verification and Multi-Objective Optimization.

Considering the issues discussed above, a time-efficient process model of LPB-AM is highly needed for optimizing the process parameters, providing the parameter perturbations and stabilizing the controller in the feedback control of the LPB-AM process. To date, unfortunately, there is a limited number of high efficiency computational models with the ability of providing online thermal or dimensional features of the LPB-AM process in a sufficient reaction time. Jason *et al.* [20] argued that the model calculation time should be faster than the sampling frequency (10 kHz) in the in-situ model-based feedback control of LPB-AM, which is around $100\ \mu s$ for the calculation rate.

Moreover, few of the above-mentioned effective approximation models have considered different melting regimes of the LPB-AM process, which are accompanied by various physics phenomena. According to Gunenthiram *et al*. [158], the LPB-AM process can be subdivided into four differentiable regimes (shown in Figure 6-1) depending upon the process parameters: unstable balling regime; stable heat conduction regime; stable keyhole regime (moderate vaporization with stable keyhole) and unstable humping (periodic formation of humps and valleys) regime with severe vaporization. The balling regime has been reported to be due to the lack of melting, whereas the humping regime is attributed to the lateral surface tension that is induced by the severe vapor recoil pressure and provokes the periodic melt pool shrinkage [159]. Furthermore, it was reported by Jingjing *et al.* [108] that the mechanical and microstructural properties of LPB-AM fabricated parts depended highly on the melting mode. The microstructure of the Ti-6Al-4V samples consisted of acicular α' phase and a typical hierarchical structure of martensite under conduction mode, while α' and α lamellae were the main constituent phases in keyhole regime. The experimental study of Ting *et al.* [109] showed that the fabricated AL7050 samples were characterized with varying surface morphology, defects and microstructure under different melting modes. Therefore, the melting regime, as a key factor, should be taken into consideration in the LPB-AM process model development.

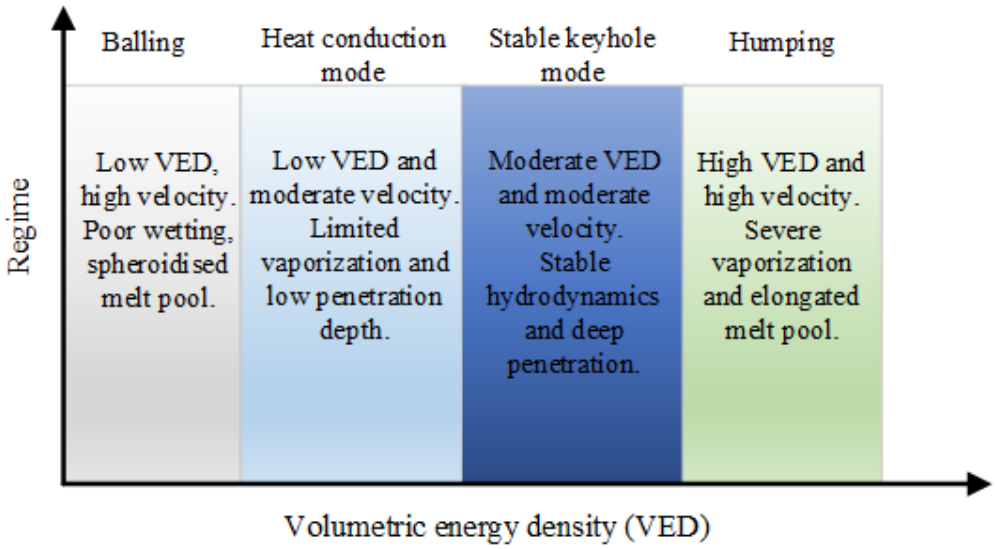

Figure 6-1. Melting regimes of the LPB-AM process under the varying volumetric energy density

Trapp *et al.* [160] reported that thresholds for different melting modes cannot be simply defined as the peak temperature of the melt pool (e.g., boiling temperature for keyhole mode). The complex physical phenomena such as surface wetting, evaporation and hydrodynamic flows should also be considered for the model based thresholds. Instead of the complex multi-physics modeling, King *et al.* [161] experimentally measured that the threshold for the keyhole mode was $\Delta H/h_e \approx (30 \pm 4)$ for steel materials in a single-track scanning. This was successfully verified in the mesoscopic numerical modeling of LPB-AM by Khairallah *et al*. [162]. Therefore, to simply the model, this research follows their experimental method to measure the thresholds for the transition mode at the first step.

As the photons that compose the laser beam penetrate deeply into the powder bed and repetitive reflection and absorption take place between the particles, the classical ray tracing method [162] has been widely used to simulate the laser energy transition in LPB-AM process. Nevertheless, in the ray tracing method, each single particle constitutes a separate geometry that induces a large calculation cost. Instead of the ray tracing method, the laser beam energy may be represented by a volumetric heat source as suggested by Smith *et al.* [163] and Hussein *et al.* [164]. Therefore, in the present chapter, a volumetric heat source with a dynamic penetration depth under different melting regimes is innovatively proposed and utilized. Under the heat conduction regime, the penetration depth is calculated from Lambert-beer law, whereas in the keyhole case, the melt pool depth is calculated based on analytical model of the keyhole depth.

Additionally, in the LPB-AM process, the laser beam will heat and melt the randomly packed powder bed with a quite different thermophysical properties compared to that of the bulk material. Khairallah and Anderson [165] found that the thermophysical properties of the powder bed may significantly affect the melt pool stability and thermal distribution. To reduce the computational cost while keeping a high fidelity of the model, they suggested to use the homogeneous models together with incorporating the effective thermophysical properties of the fine scale powder bed. Moreover, Denlinger *et al.* [166] reported that the magnitude of the calculated temperature field could be overestimated by 30 % if neglecting the powder bed property. By contrast, the error of prediction accuracy can be reduced to 11% by using an effective thermal model of the powder bed.

Inspired by the above excellent research works, in this chapter, a time-efficient comprehensive analytical model is built with grasping enough physics fidelity to be useful in the LPB-AM process optimization and control. In the unstable balling and humping regimes, bead-shaped surface and large undercuts may be induced, which deteriorate the deposited layer surface and decrease the quality of the fabricated parts. These unstable regimes can be avoided at the parameter setting stage by identifying an appropriate process window. Therefore, in this chapter, the model mainly considers the stable melting modes of the LPB-AM: the heat conduction, the transition and the stable keyhole modes. The powder bed is treated as a homogeneous medium with effective thermophysical properties derived from the randomly packed fine scale powder bed. Single-track and multi-layer multi-track scanning experiments with stainless steel (SS) 17-4 PH powders are then conducted to validate the model.

6.2. Model description

The major processing parameters of LPB-AM are laser power P_L, laser beam diameter d_l, scanning path, scanning speed v, stripe width w_s, hatch space h_s and layer thickness h_t,as shown in Figure 6-2. These operating parameters along with the powder bed properties should be studied together to build the physics-based LPB-AM process model.

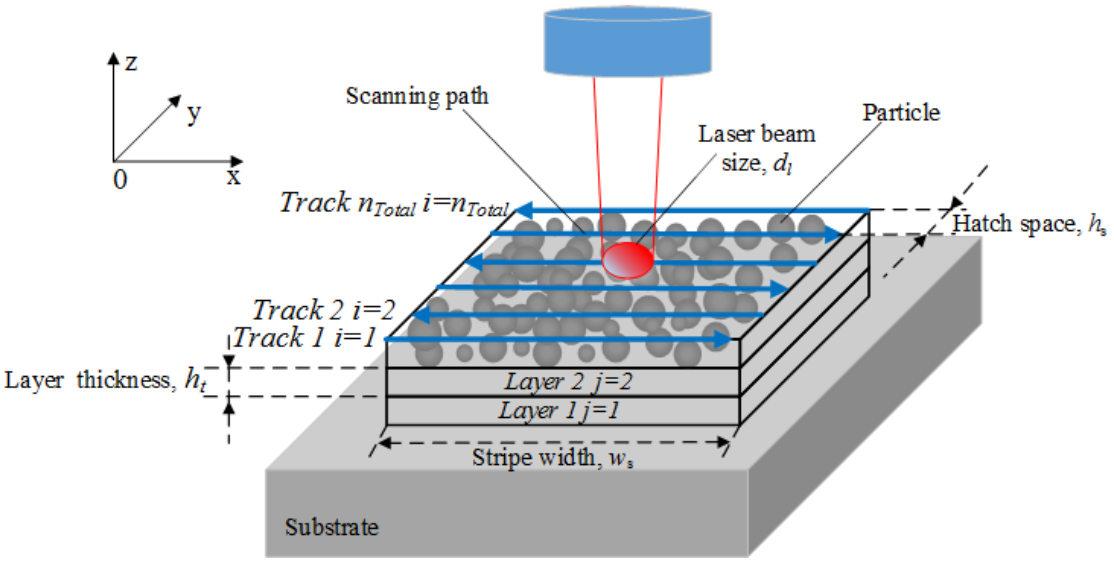

Figure 6-2. LPB-AM major operating parameters with the typical bi-directional zig-zag scanning pattern

6.2.1. Powder bed properties

The powder bed is treated as a homogeneous medium with effective thermophysical properties derived from the randomly packed fine scale powder bed. The stochastic powder bed is generated by following the random packing rain model, which was elaborated in the references [167,168]. The particle size distribution is simulated with the measured data that are described in the following Section 6.3. Accordingly, the packing porosity φ of the powder bed can be calculated as,

$$\varphi = \frac{V_B - \sum_{i=1}^{N}\left(4\pi r_{pi}^3/3\right)}{V_B} \tag{6-1}$$

where V_B is the powder bed volume, r_{pi} the i_{th} particle radius and N is the total particle number within the volume V_B.

Considering the porous nature of the powder bed, the effective powder bed density at temperature T can be approximated by the weighted aggregate density of the powder and gas mixture [169]:

$$\rho(T) = (1-\varphi)\rho_{powder}(T) + \varphi\rho_{gas} \tag{6-2}$$

where ρ, ρ_{powder} and ρ_{gas} are the density of the powder bed, bulk powder material and the argon gas, respectively.

Similarly, the heat capacity of the powder bed at temperature T can be calculated by the weighted volumetric capacity of the bulk and gas mixture [169]:

$$\rho(T)c(T) = (1-\varphi)\rho_{powder}(T)c_{powder}(T) + \varphi\rho_{gas}c_{gas} \quad (6\text{-}3)$$

where c, c_{powder} and c_{gas} are the specific heat of the powder bed, bulk powder material and the argon gas, respectively.

As the values of density and heat capacity of the argon gas are relatively small with respect to those of the bulk metallic material, the gas property may not be taken into account in the above Equations (6-2), (6-3). Subsequently, the temperature-independent powder bed density $\bar{\rho}$ and heat capacity $\bar{c}$ can be calculated based on Equations (6-2), (6-3) as:

$$\bar{\rho} = (1-\varphi)\bar{\rho}_{powder} \quad (6\text{-}4)$$

and

$$\bar{c} = \bar{c}_{powder} \quad (6\text{-}5)$$

where the $\bar{\rho}_{powder}$ and $\bar{c}_{powder}$ are the temperature averaged density (averaged over the temperature range shown in Table 6-1) and heat capacity of the powder material, respectively.

Multiple studies [170,171] have shown that the thermal conductivity of the powder bed k stays at a significantly low value ($< 0.2\ W/mk$) for the powder solidus state ($T < T_M$) but increases rapidly at the melting temperature T_M. Ali *et al.* [172] reported that the value of k ($T < T_M$) may be around 1% of the bulk powder material (k_{powder}) value. Therefore, the temperature-independent thermal conductivity of the powder bed $\bar{k}$ can be approximated as:

$$\bar{k} = k_{powder}(T_M) \quad (6\text{-}6)$$

Previous study by Alexander *et al.* [173] also reported that the thermal conductivity could be considered at the melting point where most of the energy was deposited.

6.2.2. Volumetric heat source

The heat source profile of the laser beam with TEM_{00} mode is characterized with a Gaussian distribution in the transverse plane. This was verified in several research works [45,162] and showed a good agreement with experimental results. For the heat source profile over the vertical

plane, which describes the laser beam penetration into the porous powder bed with scattering and absorption, is not yet fully understood [174]. To simplify the heat source modeling, a similar Gaussian distribution is utilized to represent the heat source profile in the vertical direction. Meanwhile, a dynamic penetration depth d_p is incorporated into the heat source model to describe the effective heat source dimension in the vertical direction under different melting regimes.

In the heat conduction regime, the penetration depth d_p of the heat source can be calculated as the depth that the laser intensity falls to $1/e \approx 0.37$ of the initial density by following the Lambert-Beer law:

$$\begin{cases} I_0 exp(-\beta_e d_p) = I_0 exp(-1), & if\ d_p < h_c \\ d_p = h_c, & if\ d_p \geq h_c \end{cases} \tag{6-7}$$

where β_e is the optical extinction coefficient of a porous metallic powder bed. It should be noticed that when the penetration depth d_p is larger than the layer thickness in the heat conduction mode, the layer thickness is used to represent the penetration depth. The optical extinction coefficient β_e is expressed by Gusarov *et al.* [46,175] as:

$$\beta_e = \frac{3(1-\varphi)}{2\varphi D} \tag{6-8}$$

where D is the averaged particle diameter.

In the keyhole mode, the penetration depth is expressed by the keyhole depth [176]:

$$d_p = \frac{\beta P_L}{2\pi \bar{k} T_B} ln\left(\frac{r_k + \bar{\alpha}/v}{r_k}\right) \tag{6-9}$$

where T_B is the boiling temperature, β the laser absorptivity, r_k the keyhole radius and $\bar{\alpha} = \bar{k}/\bar{\rho}\bar{c}$ is the effective thermal diffusivity of the powder bed. The keyhole radius is approximated by the half of the laser beam radius $r_k = r_l/2$, where $r_l = d_l/2$ is the laser beam radius. For steel materials, the boiling temperature is considered to be around 3273 K [161].

In the transition mode that occurs between the heat conduction and keyhole regimes, the averaged depth of heat conduction and keyhole regimes is used. Therefore, the penetration depth of the heat source is presented as:

$$d_p = \begin{cases} 1/\beta_e\,, & Conduction\ mode \\ \left[\dfrac{\beta P}{2\pi \bar{k} T_B} ln\left(\dfrac{r_k + \bar{\alpha}/v}{r_k}\right) + \dfrac{1}{\beta_e}\right]/2\,, & Transition\ mode \\ \dfrac{\beta P}{2\pi \bar{k} T_B} ln\left(\dfrac{r_k + \bar{\alpha}/v}{r_k}\right), & Keyhole\ mode \end{cases} \tag{6-10}$$

Moreover, the volumetric heat source can be expressed as:

$$q(x,y,z) = \frac{6\sqrt{3}\beta P_L}{r_l^2 d_p \pi \sqrt{\pi}} \exp\left[-\frac{3(x^2+y^2)}{r_l^2} - \frac{3z^2}{d_p^2}\right] \tag{6-11}$$

which is similar to the Goldak's ellipsoidal 3D heat source [177] while a dynamic heat source penetration depth is applied here. In addition, based on in-situ absorptivity measurements of the stainless steel powders as reported by Trapp *et al.* [160], the absorptivity values vary greatly under the different melting regimes in the LPB-AM process. It was found that the absorptivity was kept roughly around 0.5 at the heat conduction regime and increased to around 0.6 at the early stage of keyhole regime. Therefore, different absorptivity values of 0.5, 0.55 and 0.6 are assumed for the heat conduction mode, transition mode and stable keyhole mode, respectively.

The threshold for the mode transitions in single-track scanning is identified by the normalized enthalpy $\Delta H/h_s$ as reported in [161]:

$$\frac{\Delta H}{h_e} = \frac{6^{3/4}\beta P_L}{h_s\sqrt{\pi \alpha_{powder}(T_M) v r^3}}, \qquad h_e = \rho_{powder}(T_M)\cdot c_{powder}(T_M)\cdot T_M \tag{6-12}$$

where ΔH is the absorbed energy density, h_e the melting enthalpy and $\alpha_{powder}(T_M) = k_{powder}(T_M)/\rho_{powder}(T_M)c_{powder}(T_M)$ is the thermal diffusivity of the powder material at the melting temperature. The coefficient $6^{3/4}$ in Equation (6-12) is used to establish consistency in the calculation of ΔH with that of prior works [161,173] based on the built heat source.

In the multi-track scanning, the accumulated heat may enhance the absorbed energy density by an increment $\Delta H'$:

$$\Delta H' = \rho_{powder}(T_M)\cdot c_{powder}(T_M)\cdot (T_{AI} - T_0) \tag{6-13}$$

where T_{AI} is the dynamic initial temperature determined by the accumulated heat and is given by Equation (6-17) in Section 6.2.3.

Correspondingly, the threshold of normalized enthalpy in the multi-track scanning may be reduced compared to that of single-track scanning due to the accumulated heat. The decrement of the normalized enthalpy threshold may be expressed as:

$$\frac{\Delta H'}{h_e} = \frac{\rho_{powder}(T_M) \cdot c_{powder}(T_M) \cdot \left(T_{AI,n} - T_0\right)}{h_e} \tag{6-14}$$

However, as the temperature increment $(T_{AI} - T_0)$ induced by heat accumulation is less than the melting temperature $(T_{AI} - T_0) < T_M$, the decrement $\Delta H'/h_e$ should be small ($\Delta H'/h_e < 1$).

6.2.3. Thermal modeling

As described in Section 6.2.1, the properties of the stochastic packed powder bed may be homogenized by the temperature-independent effective thermophysical properties. Therefore, based on Equations (2-3) and (2-4) of thermal conduction, the transient temperature rise for the proposed volumetric heat source (Section 6.2.2) over the semi-infinite homogeneous powder bed can be calculated as:

$$\begin{aligned}\Delta T(X,t) = 2 \cdot \frac{1}{2} \cdot \frac{1}{\bar{\rho}\bar{c}} \cdot \frac{6\sqrt{3}\beta P_L}{r_l^2 d_p \pi \sqrt{\pi}} \int_{\tau=0}^{\tau=t} d\tau \int_{-\infty}^{+\infty} dx' \int_{-\infty}^{+\infty} dy' \int_{-\infty}^{+\infty} dz' \\ \exp\left[-\frac{3\left(x'^2 + y'^2\right)}{r_l^2} - \frac{3z'^2}{d_p^2}\right] \cdot \left[\frac{1}{4\pi\bar{\alpha}(t-\tau)}\right]^{3/2} \\ \cdot exp\left[-\frac{(x - v_x\tau - x')^2 + \left(y - v_y\tau - y'\right)^2 + (z - z')^2}{4\bar{\alpha}(t-\tau)}\right]\end{aligned} \tag{6-15}$$

Equation (6-15) can be further simplified as:

$$\begin{aligned}\Delta T(X,t) = \frac{6\sqrt{3}\beta P_L}{\bar{\rho}\bar{c}\pi\sqrt{\pi}} \int_{\tau=0}^{\tau=t} \frac{1}{12\bar{\alpha}(t-\tau) + r_l^2} \cdot \frac{1}{\sqrt{12\bar{\alpha}(t-\tau) + d_p^2}} \cdot \\ exp\left\{-\frac{3[(x - v_x\tau)^2 + y^2]}{12\bar{\alpha}(t-\tau) + r_l^2} - \frac{3z^2}{12\bar{\alpha}(t-\tau) + d_p^2}\right\} d\tau\end{aligned} \tag{6-16}$$

The above solution of Equation (6-16) is similar to the hemispherical heat source solution of Nguyen *et al.* [178] by setting the dimension of the heat source in z-axis as the dynamic penetration depth d_p. However, here the top boundary of Ω $(z = 0)$ is set as $-k\frac{\partial T(X,t)}{\partial z} = 0$. In other words, it is assumed that there is no heat transfer across the surface $z = 0$. Therefore, all

the laser power will flow into the region $z \leq 0$ and the temperature rise should be doubled as shown in Equation (6-15).

In the LPB-AM process, the inter-layer recoating time is roughly $12\,s$ [179], which is significantly larger than the laser spot irradiation time. Roberts *et al.* [180] found that the temperature of the previously deposited layers almost reached the ambient temperature due to the ample time for heat dissipation before the following layers were deposited. Therefore, the accumulated heat between the inter-layers are ignored in the present research. However, for the multi-track scanning, Luis *et al.* [88] argued that the melt pool size of the following tracks would be increased due to the accumulation of heat. To consider the heat accumulation effect in the multi-track scanning, an adaptive initial temperature T_{AI} is incorporated into the model based on the Equation (5-2). Thereafter, the transient temperature $T_n(X,t)$ of the interest point X=(x, y, z) for nth track at time moment t can be computed as:

$$\begin{cases} T_n(X,t) = \left[T_{AI,i}(X, t-t_i^s) + \Delta T_i(X, t-t_i^s)\right] \middle| i = n\,, n > 1 \\ T_{AI,n}(X, t-t_i^s) = \sum_{i=1}^{i=n-1} \{\Delta T_i(X', t-t_i^s) | X' = [x, y-(n-i)h_s, z]\} + T_0 \\ \Delta T_i(X, t-t_i^s) = \dfrac{6\sqrt{3}\beta P_L}{\bar{\rho}\bar{c}\pi\sqrt{\pi}} \int_{\tau=0}^{\tau=t-t_i^s} \dfrac{1}{12\bar{\alpha}(t-\tau)+r_l^2} \cdot \dfrac{1}{\sqrt{12\bar{\alpha}(t-\tau)+d_p^2}} \cdot \\ \qquad exp\left\{-\dfrac{3[(x-v_i\tau)^2+y^2]}{12\bar{\alpha}(t-\tau)+r_l^2} - \dfrac{3z^2}{12\bar{\alpha}(t-\tau)+d_p^2}\right\} d\tau \end{cases} \tag{6-17}$$

where i denotes the scanning track index, T_0 is the ambient temperature. t_i^s and v_i are the deposition starting time and laser scanning speed of the ith track, respectively.

Considering the high cooling rate in the LPB-AM process, the transient temperature value $T_{AI,S} = \Delta T(X, r_l/v) + T_0$ at the time moment $t = r_l/v$, when the laser beam passes one beam radius, is set as the saturation value for the adaptive initial temperature T_{AI} (T).

In addition, ignoring the melt pool dynamics may result in unrealistic predictions of melt pool temperature values and melt pool size. However, the prevailing Computational Fluid Dynamic(CFD) modeling is extremely computationally expensive. To simply the model while keeping reasonable accuracy, the thermocapillary convection (Marangoni flow) effect on the thermal field is compensated by enlarging the thermal conductivity as [67],

$$\bar{k}^* = \mu_M k_{powder}(T_M) \tag{6-18}$$

where $\mu_M = 3.5$ is the correction coefficient.

Moreover, it has been shown that the radiative and convective heat losses are insignificant compared to the heat conduction [180]. Therefore, the heat loss induced by convection and radiation are not included in the present model.

6.2.4. Melt pool and track dimensional modeling

As the heated particles are fully melt by the laser beam in the LPB-AM process, the pores between the particles in the powder bed will be largely removed and forms a liquid melt pool, the formed melt pool will then cool down, solidify and finally reach the ambient temperature as shown in Figure 6-3. The associated shrinkage occurs in the process may be summarized as three stages [181]: stage I, powder layer to liquid metal; stage II, liquid metal to solidified metal at melting temperature; stage III, solidified metal cools to ambient temperature. Dai and Shaw [182] reported that there was quite small changes in the temperature distribution of the melt pool with and without considering the volume shrinkage. Therefore, the melt pool dimensions (e.g., width w_m, and depth d_m) may be estimated with the solid-liquid interface boundary by solving the thermal field solution of Equation (6-17) as illustrated in the Figure 6-14 of Section 6.4.

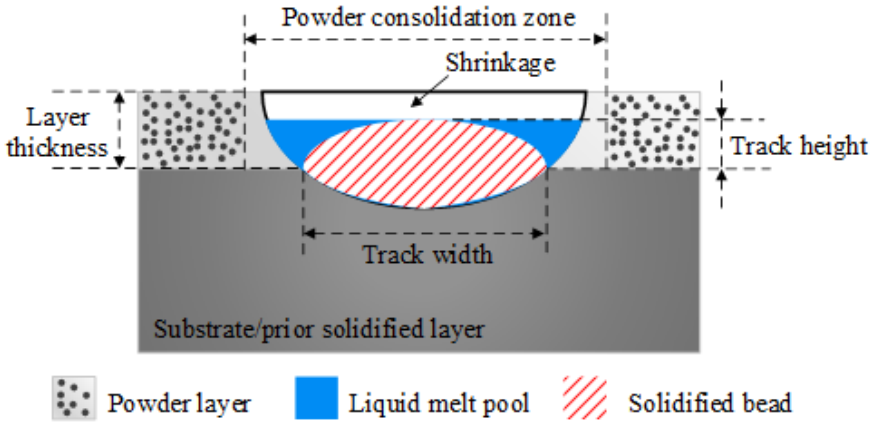

Figure 6-3. Schematic of the typical transverse cross-section of the single-track with considering the shrinkage.

Paul *et al.* [183] found that the volume shrinkage mainly occurred in the building direction (track height direction) at stage I and stage II. They reported that the volume shrinkage ratio was

equivalent to the initial powder bed porosity φ. Therefore, it is reasonable to assume that the shrinkage only takes effect in the building direction by a shrinkage ratio of powder bed porosity φ at the stage I and stage II. By contrast, an insignificant volume change can be assumed in the building direction at stage III. Subsequently, the final track height H at ambient temperature may be calculated based on the mass conservation as:

$$H = (1 - \varphi)h_t \tag{6-19}$$

The final track length L and track width W at ambient temperature can be approximated as,

$$\frac{L(T_M) - L}{L(T_M)} = \frac{W(T_M) - W}{W(T_M)} = \alpha_L(T_M - T_0) \tag{6-20}$$

where $L(T_M)$ and $W(T_M)$ are the solidified track length and track width at the melting temperature in stage II, respectively. α_L is the linear thermal expansion coefficient. Based on the above assumption in the shrinkage stage I and stage II, the $L(T_M)$ can be estimated with the initial scanning vector length L_0 and the $W(T_m)$ can be approximated by the liquid melt pool width w_m.

Thereafter, under the stable heat conduction and stable keyhole melting regime, the single-track dimension may be approximated by the parabolic function as,

$$f(x, y) = \frac{-4H}{W^2} y^2 + H \tag{6-21}$$

Since the track width W is derived from the melt pool width w_m, which is calculated based on the transient thermal field $T(X, t)$, the track width W is a function of position $x = vt$.

In the multi-track scanning, the overlapping tracks are formed continuously with a distance of the hatch space h_s. It is known that a relatively large hatch space (larger than the track width) may result in poor interlayer overlapping and a discontinuous structure. However, it was also reported that a consecutive reduction in the height of the deposited tracks might be induced through substrate denudation when the hatch space was equal to or less than the track width [184]. Therefore, the hatch space and the substrate denudation effect should be jointly considered in the geometric modeling of the multi-track structures. Based on the recursive overlapping profile model (derived in Section 5.2.2), the dimension of the track is approximated by the parabolic function in the present chapter.

6.3. Materials and experimental procedure

6.3.1. Powder material

Gas atomized stainless steel (SS) 17-4 PH powder (EOS GmbH, München, Germany) was utilized in this research. The morphology of the powder particles was investigated using a Zeiss LEO FE-SEM 1530 scanning electron microscope (SEM) as shown in Figure 6-4 (a). It can be seen that most particles exhibit a spherical or near spherical morphology while other particles with irregular-shaped morphology can also be identified. The particle size distribution was determined by the CAMSIZER X2 (Retsch Technology, Haan, Germany) and is shown in Figure 6-4 (b). It is seen that the particle size distribution can be fitted by a Gaussian distribution with mean value of 48 μm and standard deviation of 12 μm. The temperature dependent thermophysical properties of the SS 17-4 PH powder material are tabulated in Table 6-1.

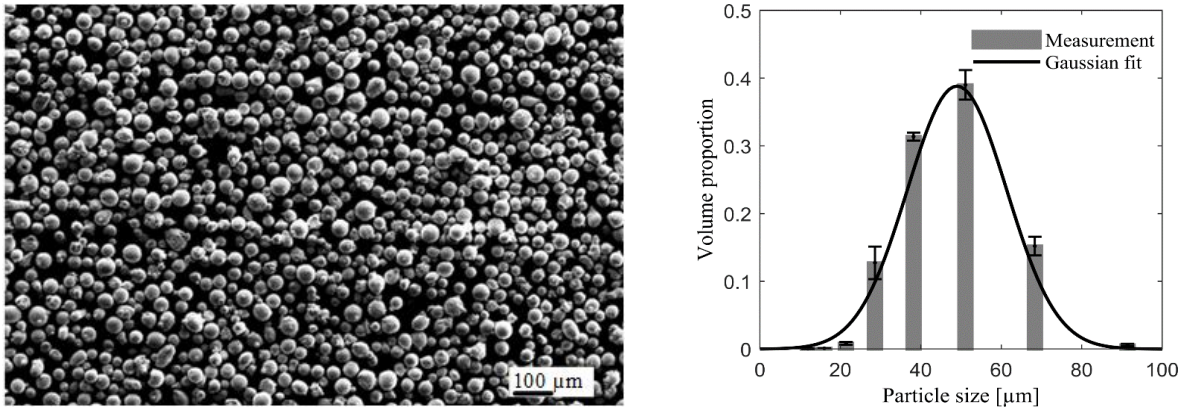

(a) (b)

Figure 6-4. SS 17-4 PH powder characteristics (a) Powder morphology (b) Particle size distribution with Gaussian fit

Table 6-1. SS 17-4PH powder thermal-physical parameters [185,186].

Melting temperature T_m [K]	Density $\rho\ [kg/m^3]$	Thermal conductivity $k\ [W/(m \cdot K)]$	Specific heat $c\ [J/(kg \cdot K)]$
1693	7800(300K)-7250 (1693K)	11.5(373K)-31.5(1673K)	426(473K)-833(1693K)

6.3.2. Experimental processing

Experiments were carried out on the EOS M290 additive manufacturing machine under the argon atmosphere. The machine unitizes a continuous wave ytterbium (YB) fiber laser with

TEM_{00} mode and a maximum power of 400 W. The internal chamber was preheated to a fixed temperature of 353 K to minimize residual stress and reduce defects in the fabricated samples.

To validate the built model, both single-track and multi-layer multi-track samples were fabricated. The single-tracks were directly built on a mild carbon steel substrate (dimension of $250\,mm \times 250\,mm \times 50\,mm$) with a track length of 20 mm, whereas the multi-layer multi-track samples were fabricated by following a 90° inter-layer rotation scanning strategy (shown in Figure 6-5) with a supporting structure of 5 mm thickness. As can be seen from Figure 6-5, the parallel stripes run across the whole length of each layer by following the zig-zag scanning pattern. Here has to be noticed that the track width (3.05 mm) is the sum of the stripe width (3 mm) and stripe overlap (50 µm). The major processing parameters are listed in Table 6-2.

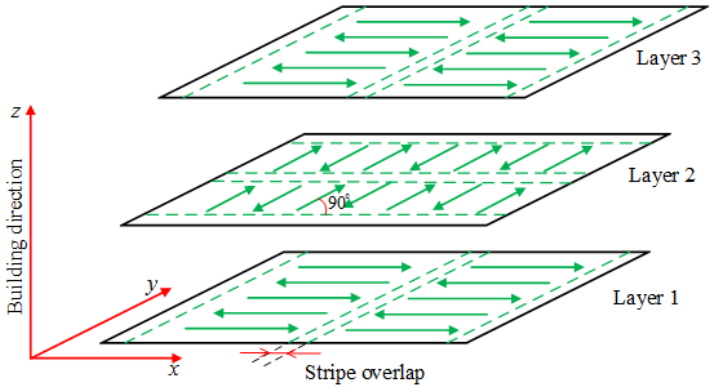

Figure 6-5. Schematic of the rotated scanning strategy in the LPB-AM process. The stripes (green arrow solid-line) rotate counterclockwise by 90° in the following each new layer compared to the previous ones.

Table 6-2. Processing parameters for SS 17-4 PH powder in the selective laser melting process

Parameters	Values	Parameters	Values
Scanning speed, [mm/min]	600~1300	Correction factor, μ_M	3.5
Laser power, [W]	170~220	Ambient temperature, [K]	353
Hatch space, [µm]	100	Thermal expansion coefficient	14×10^{-6} $[m/mK]$ [55]
Laser beam diameter, [µm]	100	Laser absorptivity	0.5, 0.6
Stripe width, [mm]	3	Single-track length, [mm]	20
Stripe overlap, [µm]	50	Layer thickness, [µm]	20, 40

The single-track samples were cross-sectioned in the middle-track length plane and etched with 5% Nital solution after grinding and polishing. For the multi-track multi-layer samples, the side face,

i.e. the face parallel to the building direction, was ground and polished using conventional metallography methods. The mirror-like surface of these samples was then etched using a solution of 75% hydrochloric acid and 25% nitric acid. The melt pool dimensions of all samples were measured by Olympus optical microscope (OM) and laser microscope VK-X250K. The measured melt pool data of single-track samples were published in the references [187,188]

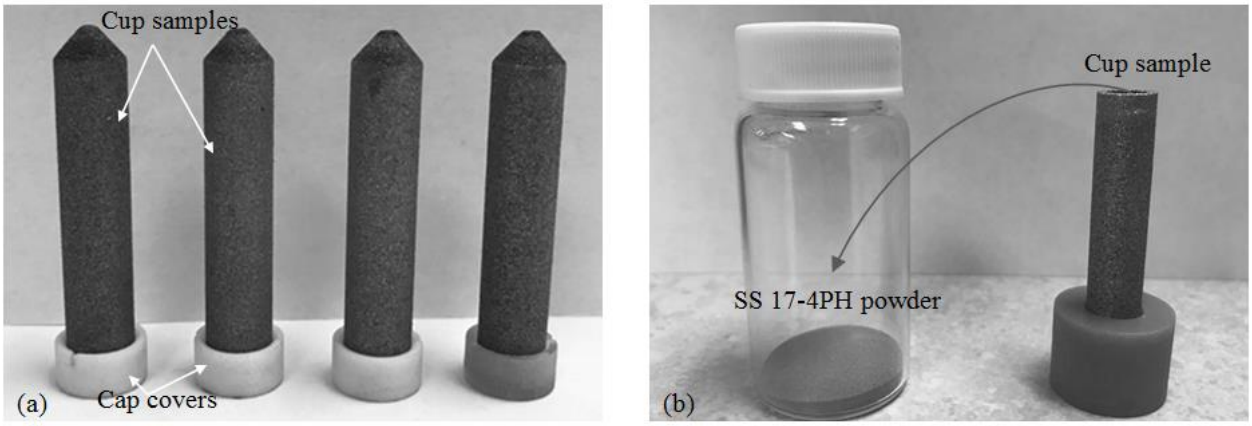

Figure 6-6. Powder bed porosity measurement. (a) Images of the fabricated hollow cylindrical cup artifact (Bottom up). (b) Powder mass measurement.

Four hollow cup artifacts (Figure 6-6 (a)) were fabricated at different powder bed locations. Thereafter, the porosity of the powder bed was indirectly measured through geometry and mass measurements of the printed hollow cup artifacts (shown in Figure 6-6 (b)) according to the methods elaborated in reference [189]. The dimensional features of the hollow cups, diameter D_{cup} and height H_{cup}, were measured by a digital caliper. The mass of the cups, filled with powder (M_1) and no powder (M_2), were measured by the standard scale (Sartorius Secura 225D, Göttingen, Germany). The powder bed porosity was then calculated based on the measured data from each cup artifact as:

$$\varphi = 1 - \frac{4(M_1 - M_2)/\pi D_{cup}^2 H_{cup}}{\rho_P} \tag{6-22}$$

The final powder bed porosity were averaged based on the cup artifacts measurement data.

6.4. Results and discussion

6.4.1. Powder bed porosity

Figure 6-7 shows the simulated 3D profile of the powder bed according to the stochastic packing rain model, as described in Section 6.2.1. The particle size distribution follows the fitted Gaussian distribution based on the measurements, as illustrated in Section 6.3. Particles with different sizes together with voids among the powder bed particles can be seen in Figure 6-7. It should be noted that the position and the exact size of the individual particles may vary from run to run. Due to this randomness, three runs with same volume ($500\ \mu m \times 300\ \mu m \times 200\ \mu m$) were conducted to predict the porosity level of the powder bed. The measured (experimental) and simulated (predicted) values of the powder bed porosity level are listed in Table 6-3. A good agreement (3.1% error percentage) is observed between the two sets of results.

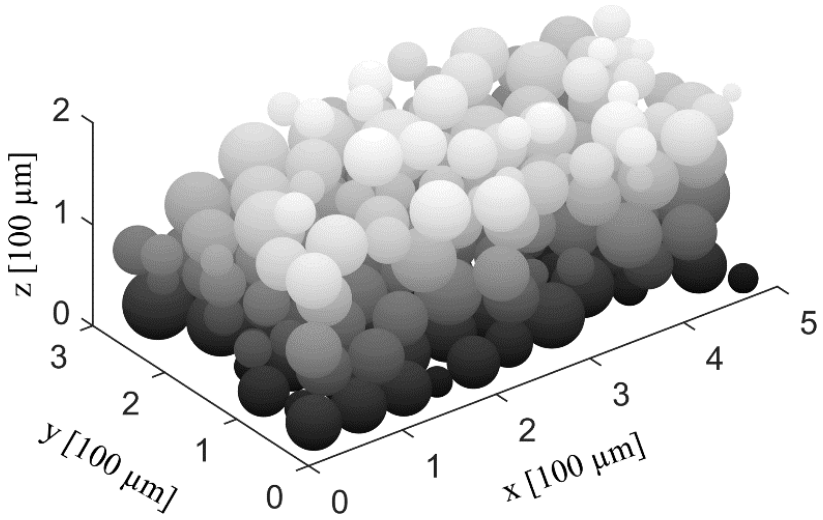

Figure 6-7. Simulated 3D profile of the stochastic packing SS 17-4PH powder bed. The size distribution of the particles were modeled with Gaussian distribution as measured in Section 6.3.1 (average particle diameter 48 µm, standard deviation 12 µm).

Table 6-3. Measured and simulated powder bed porosity with SS 17-4PH particle

SS 17-4 PH	Measured porosity	Predicted porosity	Difference (%)
	0.486 ± 0.02	0.501 ± 0.04	3.1%

6.4.2. Utility of the normalized enthalpy to set the melting mode thresholds

Figure 6-8 depicts the melt pool geometry variation with respect to the normalized enthalpy. The parameter values for the calculation of normalized enthalpy are given in Table 6-4. As seen from Figure 6-8, the melt pool depth is smaller than the melt pool half-width at a relatively low normalized enthalpy (e.g., 22.36). This is a typical melt pool shape under the heat conduction mode. With an increase in the normalized enthalpy, the melt pool depth increases significantly and the melting regime changes to the transition mode and keyhole mode, sequentially. Generally, the keyhole regime can be identified from the melt pool shape that the depth is larger than the half-width [161].

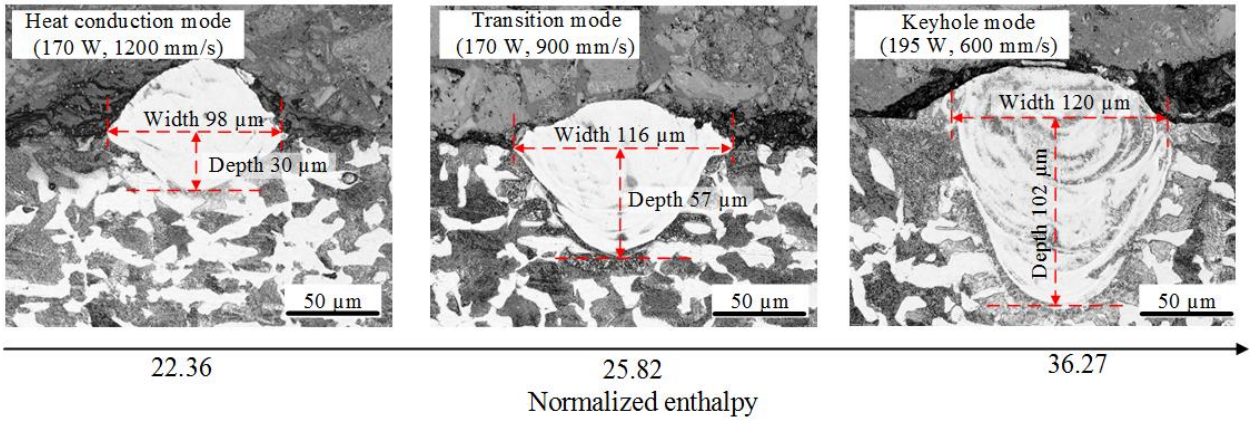

Figure 6-8. Transverse cross-section profile of single-track under varying normalized enthalpy. 40 µm layer thickness.

Table 6-4. Parameter values for normalized enthalpy calculation

SS 17-4 PH	Absorptivity	Laser beam radius [µm]	Melting enthalpy [J/m^3]	Thermal diffusivity (T=T$_M$) [m^2/s]
	0.55	50	1.02×10^{10}	5.216×10^{-6}

However, once the normalized enthalpy reaches a very high value (e.g., 40.93, as shown in Figure 6-9 (c)), an unstable keyhole/humping melting mode with a super large melt pool depth is observed. In addition, the unstable humping features with periodic humps and valleys can be clearly noticed in Figure 6-9 (a, b) at this high normalized enthalpy case. According to the prior study of Gunenthiram *et al* [158,159], the formation of the unstable keyhole/humping mode may

be attributed to the severe metal vaporization at the high normalized enthalpy case, which induces the strong lateral surface tension and provokes the periodic melt pool shrinkage.

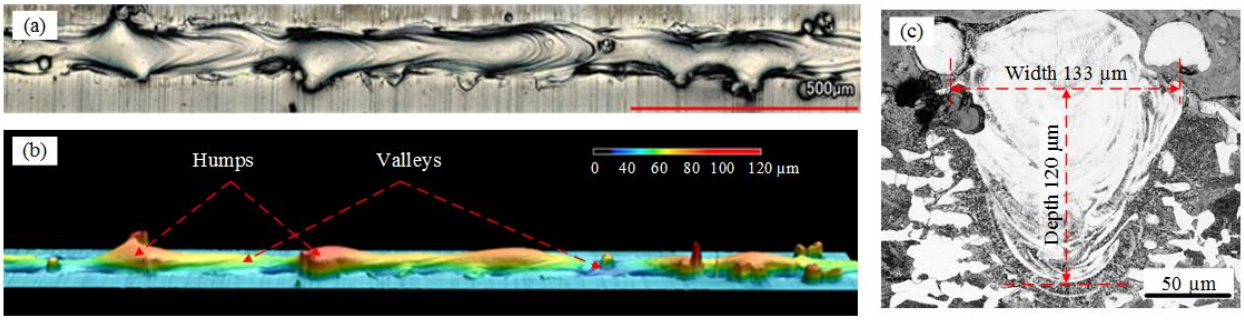

Figure 6-9. Top view of the single-track (a), the associated 3D track height profile (b) and (c) transverse cross-section under normalized enthalpy (40.93). Laser powder 220W, scanning speed 600 mm/s, layer thickness 40 µm.

Figure 6-10 (a-f) shows the variations of the measured melt pool depth over the laser power, scanning speed and normalized enthalpy under different layer thicknesses of the single-track experiments. It is observed that the variation in the melt pool depth shows irregular patterns over the varying laser power (Figure 6-10 a, b) or scanning speed (Figure 6-10 c, d). By contrast, the melt pool depth collapses to a single line in the plot of melt pool depth vs. normalized enthalpy as shown in Figure 6-10 (e, f). This is consistent with the results reported by prior references [161,173].

Furthermore, as it is seen in Figure 6-10 (e, f), the melting regime changes gradually from the heat conduction to the keyhole mode (depicted by the variations of the circle symbols from vacant to solid) with an increase of the normalized enthalpy, which agrees well with the melt pool cross-section observations shown in Figure 6-8. As can be seen, the melting regime (mode) is heat conduction when the normalized enthalpy is smaller than 24. A transition region from heat conduction to keyhole mode is seen over the range of $24\sim28$. Once the normalized enthalpy exceeds the value of 28, a full keyhole melting mode is obtained. Therefore, the thresholds for the melting regime transiting from conduction to transition mode and changing from transition mode to keyhole mode may be identified with the normalized enthalpies of $\Delta H/h_s = 24$ and $\Delta H/h_s = 28$, respectively. The observed keyhole mode threshold of $\Delta H/h_s = 28$ is also consistent with the reported value of $\Delta H/h_s \approx (30 \pm 4)$ [161] for single-track fabrication of steel powder material in the LPB-AM process.

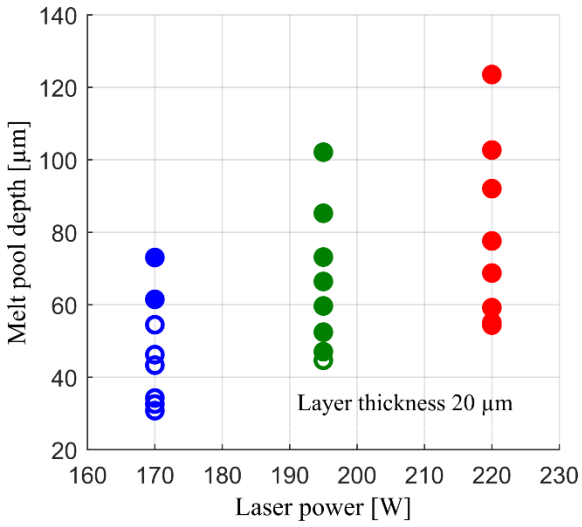
Melt pool depth [µm]
Laser power [W]
Layer thickness 20 µm

(a)

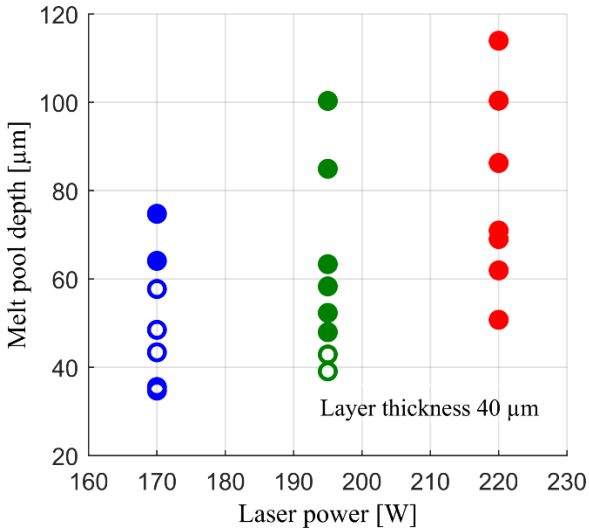
Melt pool depth [µm]
Laser power [W]
Layer thickness 40 µm

(b)

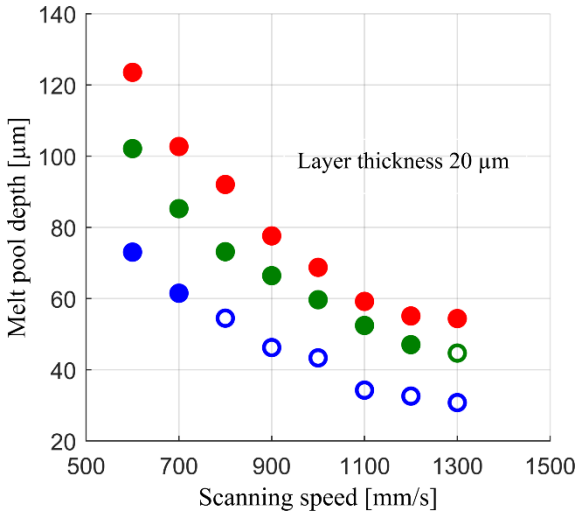
Melt pool depth [µm]
Scanning speed [mm/s]
Layer thickness 20 µm

(c)

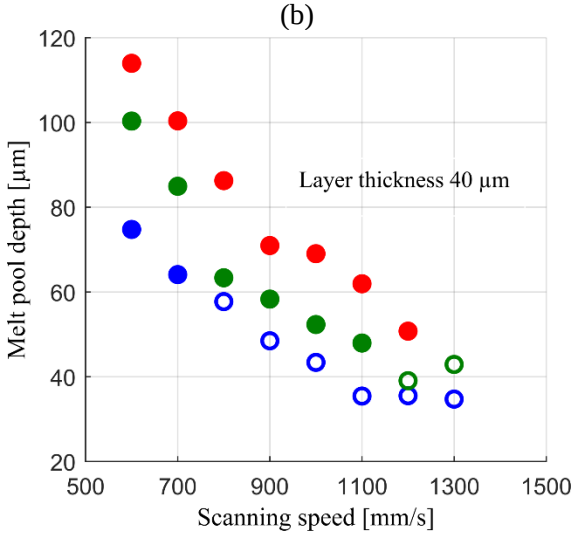
Melt pool depth [µm]
Scanning speed [mm/s]
Layer thickness 40 µm

(d)

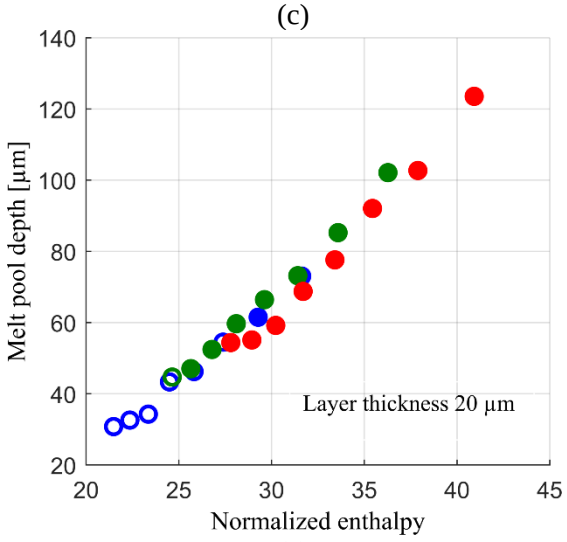
Melt pool depth [µm]
Normalized enthalpy
Layer thickness 20 µm

(e)

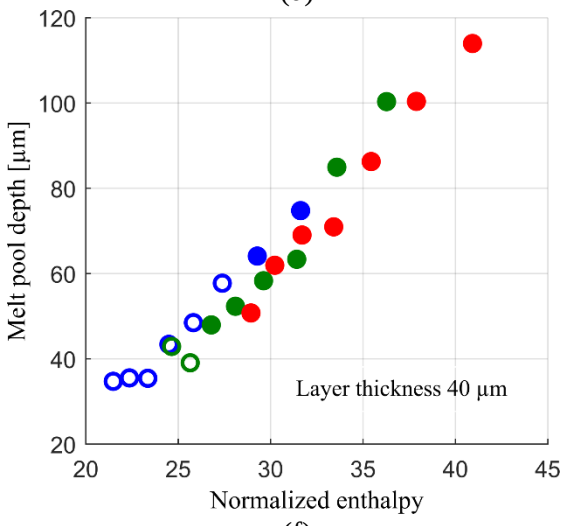
Melt pool depth [µm]
Normalized enthalpy
Layer thickness 40 µm

(f)

Figure 6-10. Single-track melt pool depth vs. (a), (b) laser power, (c), (d) scanning speed and (e), (f) normalized enthalpy under different layer thicknesses (20 μm and 40 μm) in the LPB-AM process. Different laser power values of 170 W, 195 W, 220 W are tagged with blue, green and red color symbols, respectively. The solid and the vacant circle symbols indicate keyhole and conduction melting mode, respectively. The standard deviation of the melt pool depth is within $0.7\sim9\ \mu m$.

Similarly, the thresholds for the melting regimes in multi-track fabrication may also be identified by the normalized enthalpy based on the melt pool dimensional features. The accumulated heat associated with the scanning pattern in the multi-track scanning may induce two different types of melt pools with distinct dimensions at the ends of the scanning track, as shown in Figure 6-11 (a), which was also reported by Luis *et al.* [88]. By contrast, in the mid-track-length zones, the melt pools become more uniform as observed in Figure 6-11 (b).

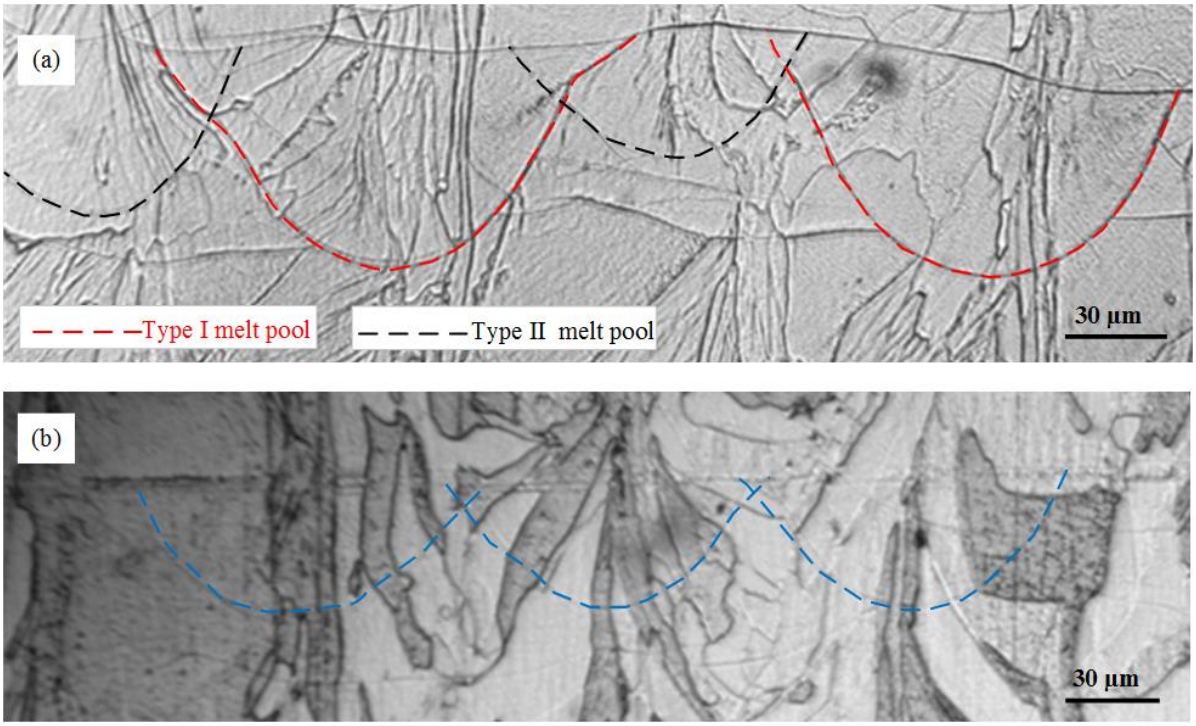

Figure 6-11. Melt pools observed in the transverse cross-section of the multi-track multi-layer samples. (a) Two distinct types of melt pool observed near the ends of the scanning track. The Type I melt pool is marked with red color. Type II melt pool is marked with black color. (b)Nearly uniform melt pools observed in the half-track-length cross-section. Laser power 175 W, scanning speed 700 mm/s for (a) and 900 mm/s for (b), hatch space 100 μm, stripe width 3 mm, stripe overlap 50 μm.

Figure 6-12 illustrates the formation pattern of the two types of the melt pools (Figure 6-11) under zig-zag scanning pattern. It can be seen that Type I melt pool (large-size melt pool) forms

when the heat reloading of the following track is exerted immediately after the prior track scanning (e.g., from A to B shown in Figure 6-12). The Type II melt pool (small-size melt pool), however, forms when the accumulated heat of the prior heat reloading is almost dissipated after scanning of a whole track length (e.g. from B to C shown in Figure 6-12). Therefore, these two types of melt pool depths were measured separately to determine the thresholds for the melting regimes in the multi-track fabrication.

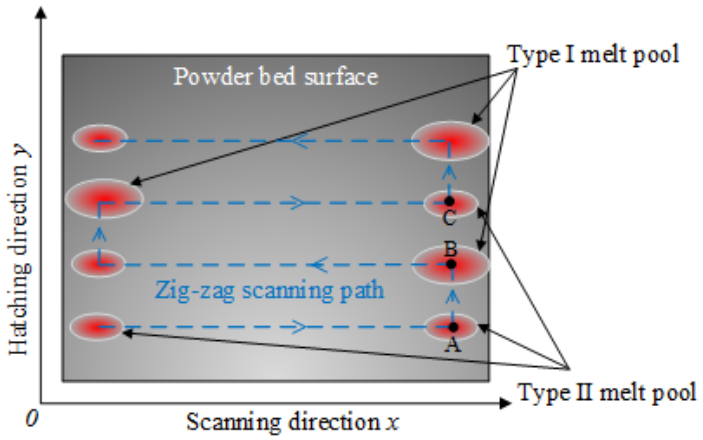

Figure 6-12. Schematic of the formation of the two types of melt pools.

As shown in Figure 6-13 (a, b), the threshold of the keyhole melting mode for these two types of melt pools can be identified through a roughly similar normalized enthalpy of $\Delta H/h_e \approx 31$. In fact, this similar threshold indicates that the heat accumulation effect on the melting regime is insignificant. This is consistent with the small variation of normalized enthalpy ($\Delta H'/h_e < 1$) induced by heat accumulation, as illustrated in Section 6.2.2. In addition, it is found that the threshold of normalized enthalpy for the keyhole mode in multi-track scanning is larger than that of the single-track scanning, opposing with the model derived in Section 6.2.2. This conflicting finding may be explained by the lager thermal conductivity under the multi-track scanning compared with that in the single-track scanning. The increased thermal conductivity is caused by the solidification occurs in the neighboring scans, changing from porous powder bed to solidified metal tracks.

To achieve a uniform threshold of normalized enthalpy for both single-track and multi-track scanning, the effective thermal conductivity under multi-track scanning was multiplied by a coefficient of $(31/28)^2$. Thereafter, under the multi-track scanning case, the thresholds for the melting regime changing from conduction to transition mode and switching from transition mode

to keyhole mode can be identified with the normalized scaling enthalpy values of 24 and 28, respectively.

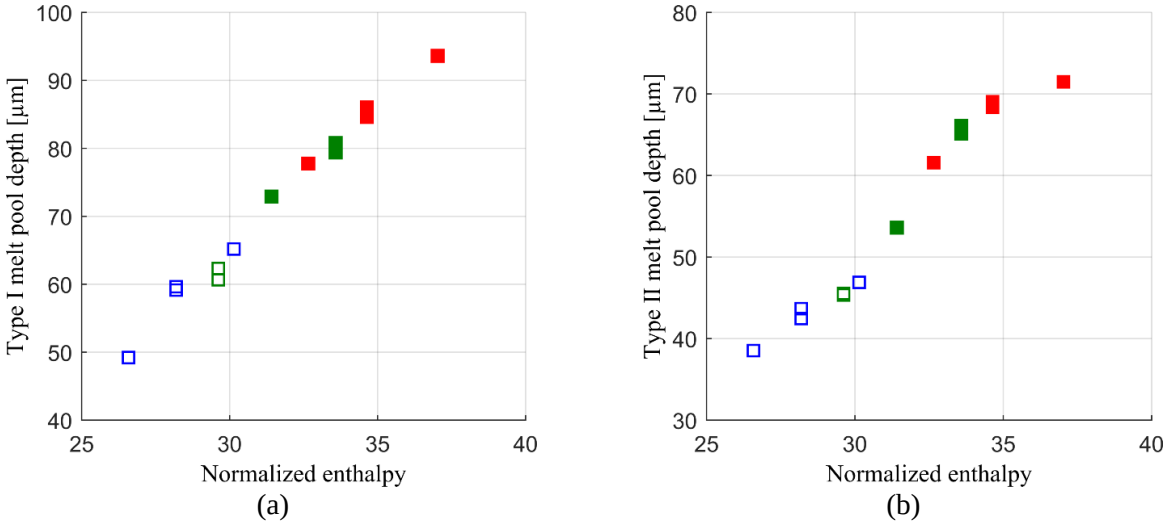

Figure 6-13. Melt pool depth vs. normalized enthalpy of multi-track multi-layer samples. (a) Type I melt pool. (b) Type II melt pool. The solid and the vacant symbols indicate keyhole and conduction mode melting, respectively. Different laser power values of 170 W, 195 W, 220 W are tagged with blue, green and red color symbols, respectively. Layer thickness 40 μm.

6.4.3. Thermal field simulation

In the LPB-AM process, the thermal distribution determines the formation and sustainability of the melt pool, which further affects the quality of the single-track and final product. However, the cooling rate during the LPB-AM process is very high (typically around $10^6\ K/s$), which increases the difficulty to measure the real-time thermal evolution during the process. In the present research, based on the thermal model presented in Section 6.2, the transient temperature field in the LPB-AM process were time-efficiently calculated in the Matlab® R2017b by a HP® computer with Intel® CoreTM i7-6700 CPU (3.4GHz). It was found that the calculation time for the thermal solution of single point is around 1.2 ms with a tolerance of $10^{-3}K$.

Figure 6-14 shows the transient temperature distribution of the melt pool in the single-track scanning. As seen, the melt pool boundary can be identified by the liquid-solid isotherm in both the transverse plane (Figure 6-14 (a)) and longitudinal plane (Figure 6-14 (b)). Accordingly, the dimensional features of the melt pool (melt pool w_m, melt pool depth d_m) can be indexed.

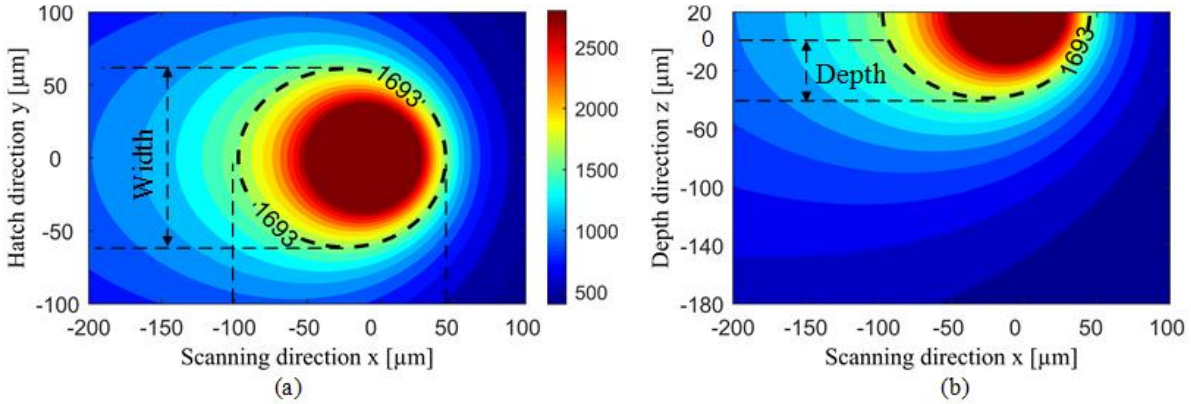

Figure 6-14. Simulated melt pool temperature distribution at the time moment (t = L/2*v*, half-track length location). (a) xy plane (powder bed surface plane), (b) xz plane (longitudinal cross-section). Laser power 170 W, scanning speed 1000 mm/s, layer thickness 20 μm, track length L=20 mm. The melt pool boundary is indicated by the black dashed line (T=1693 K).

Figure 6-15 presents the calculated initial temperature variation over the stripe width in multi-track scanning. It can be observed that the initial temperature increases slightly with the addition of the track numbers, which is resulted from the increased heat accumulation under a longer scanning time. Moreover, the maximum initial temperatures tend to appear at the end of each track. This may lead to an alternative variation of the melt pool size, as shown in Figure 6-12.

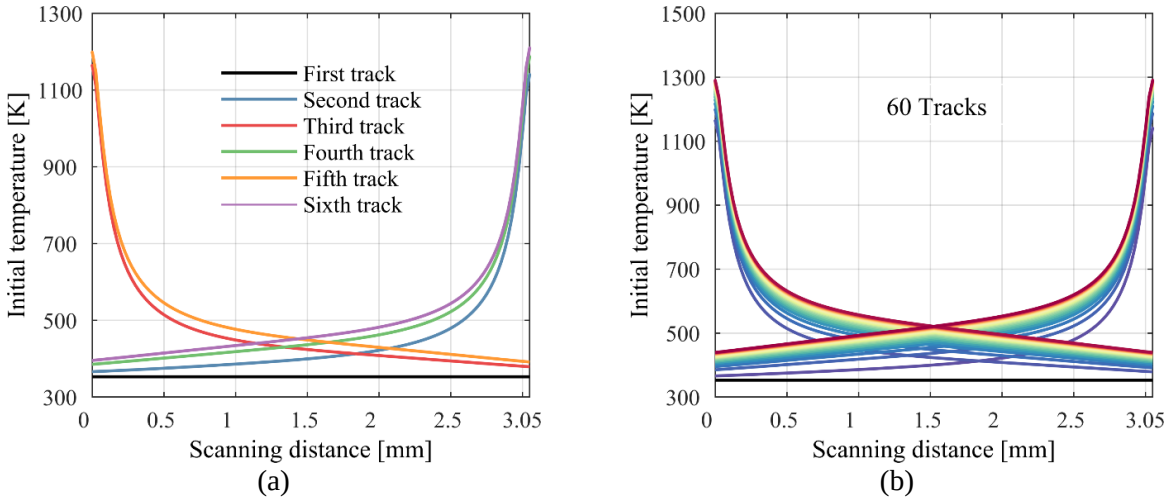

Figure 6-15. Predicted initial temperature of the multi-track scanning in the LPB-AM process. (a) 6 tracks, (b) 60 tracks. Laser power 215 W, scanning speed 900 mm/s, hatch space 100 μm, stripe width 3 mm, stripe overlap 50 μm.

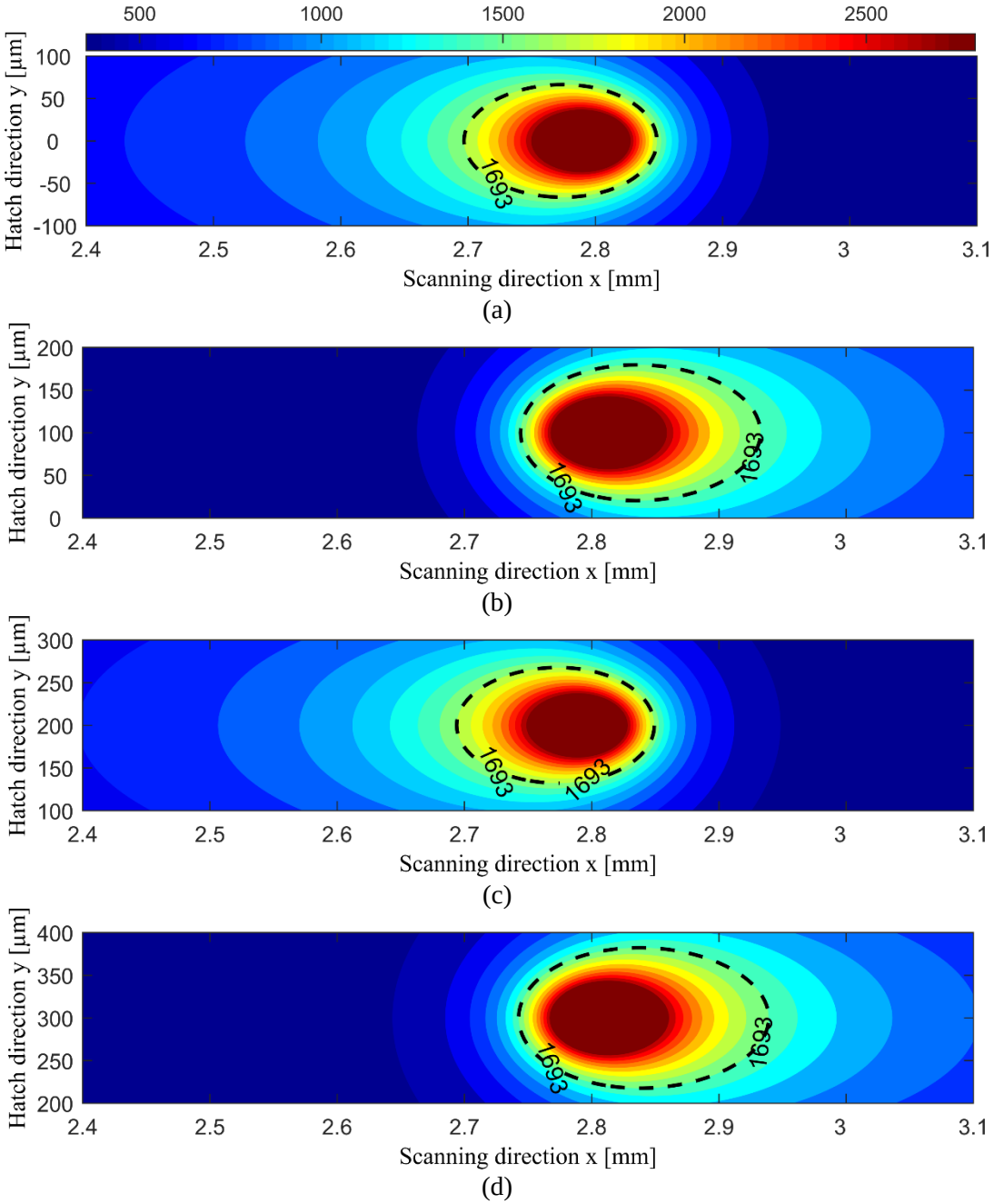

Figure 6-16. Transient temperature distribution of the melt pool top surface near the track ending zones following the zig-zag scanning pattern. (a) First track, x=2.8, y=0, t=3.11 ms. (b) Second track, x=2.8, y=100 μm, t=3.67 ms. (c) Third track, x=2.8,y=200 μm t=9.89 ms. (c) Fourth track, x=2.8,y=200 μm t=10.44 ms. Laser power 215 W, scanning speed 900 mm/s, hatch space 100 μm, stripe width 3 mm, stripe overlap 50 μm, layer thickness 40 μm.

Figure 6-16 further shows the transient temperature evolution of the track ending zones on the powder bed surface in the multi-track scanning The melt pool boundary is defined by the liquid-

solid isotherm. It is seen that the melt pool size changes with the scanning path. For instance, the melt pool size is reduced for the third track ($t = 9.89\ ms$) compared to that of the second track ($t = 3.67\ ms$). However, after completing the third scanning, the melt pool size is enlarged again during the fourth scanning ($t = 10.44\ ms$). These predicted phenomena are consistent with the numerical simulations of Luis *et al.* [88].

6.4.4. Melt pool dimensional verification

In the LPB-AM process, the melt pool evolution plays a key role in defect formation, interlayer bonding, grain growth, dimensional accuracy and surface finish [190]. However, the size of the melt pool is typically small (roughly around $50{\sim}200\ \mu m$ in diameter). Due to the dearth of the characterization tools, it is difficult to conduct the in-situ measurements of the melt pool size in the LPB-AM process, particularly for real-time melt pool depth measurement. However, the in-situ melt pool size can be calculated based on the built model with the predicted thermal field. Here the melt pool dimension at the middle track length cross-section plane is further compared to the experimental measurements under the single-track and multi-track scanning cases of LPB-AM.

Figure 6-17 shows the comparative results of the calculated melt pool dimension and corresponding measurements for samples fabricated with different laser powers and various scanning speeds under different layer thickness. As it is seen in Figure 6-17 (a-d), the measured depth and width of the melt pool both decrease gradually with an increase in the laser scanning speed. This may be ascribed to the fact that deposited energy is reduced per unit time when scanning speed is increased. In addition, a high level of accuracy can be observed in predicted melt pool depth and width compared to the experimental measurements under the steady melting regime, with a maximum of 14% error for width prediction and 15% error for depth calculation. However, the measured melt pool depth becomes much larger than the calculated ones under the unsteady keyhole mode (e.g. $v = 600\ mm/s$, $P = 220\ W$ with normalized enthalpy value of 40.93). In the unsteady keyhole regimes, the Marangoni flow induced by the strong temperature gradient may increase the melt pool depth [162]. Moreover, the strong recoil pressure induced by the severe evaporation under the high normalized enthalpy case may further deepen the melt pool. These factors may explain why the predicted melt pool depth is lower than that of the experimental measurement.

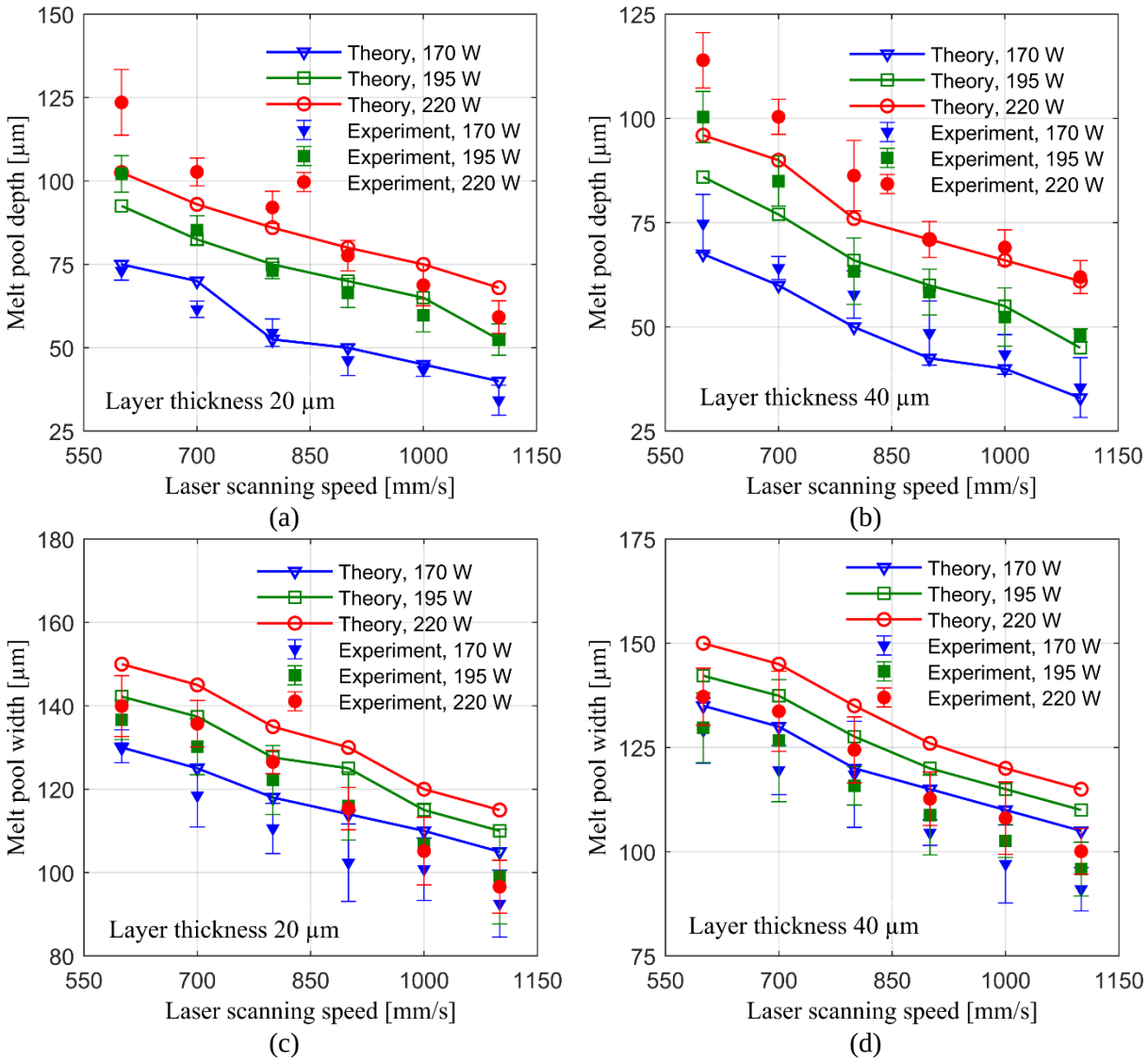

Figure 6-17. Melt pool dimension verification of single-track under varying scanning speeds, laser power and layer thickness. (a), (b) melt pool depth. (c), (d) melt pool width. The melt pool dimension was measured at the transverse cross-section of half-track length. Track length 20 mm.

Figure 6-18 presents the melt pool dimensions under the multi-track scanning with varying normalized scaling enthalpy. It is noticed that the measured melt pool dimension increases significantly with an increase in the normalized scaling enthalpy, which is consistent with the experimental results reported by King *et al*. [161]. In addition, the melt pool width tends to reach a steady value in the high normalized enthalpy case. It should be mentioned that the final etching surface is not kept constant, which is roughly varied from 100 μm to 300 μm from the side surface of the cuboid samples. Therefore, the averaged melt pool dimensions at the different

scanning distance from the side surface (ranging from 100 μm to 300 μm) were utilized as the model prediction results.

As can be seen, most of the predicted values of the melt pool depth and width fall within the error bar of the corresponding experimental measurements, leading to a maximum error difference of 12 % for melt pool width and 11 % for melt pool depth. Discrepancies between the experiments and modelling results could have been induced by ignoring the severe recoil pressure and the drastic thermos-capillary convection flows in the built model.

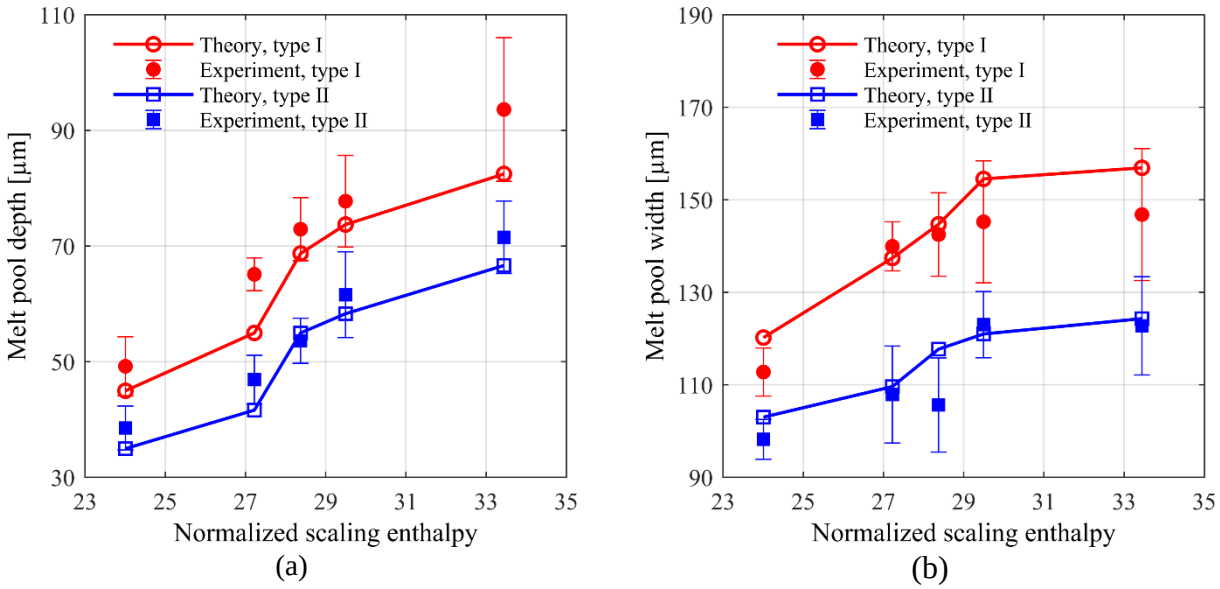

Figure 6-18. Melt pool dimension verification of multi-track multi-layer scanning samples under varying normalized scaling enthalpy. (a) Melt pool depth. (b) Melt pool width. Hatch space 100 μm, stripe width 3 mm, stripe overlap 50 μm, layer thickness 40 μm. The melt pool dimension was measured at the etching surface that varied from 100~300 μm from the side surface of the cuboid samples.

6.4.5. Track dimension verification

In the LPB-AM process, the components are fabricated in a layer-by-layer way. Therefore, the dimension and morphology of each formed layer play a significant role in determining the finish of the final fabricated parts. Using the model described in Section 6.2.4, the geometrical dimension of the single-track and multi-track scanning samples can be predicted, as shown in Figure 6-19 and Figure 6-20, respectively. It should be noted here that the track height profiles in the transverse cross-section were averaged based on the measurements at the middle-track length zone with a total number of 100 lines by a 2 μm interval.

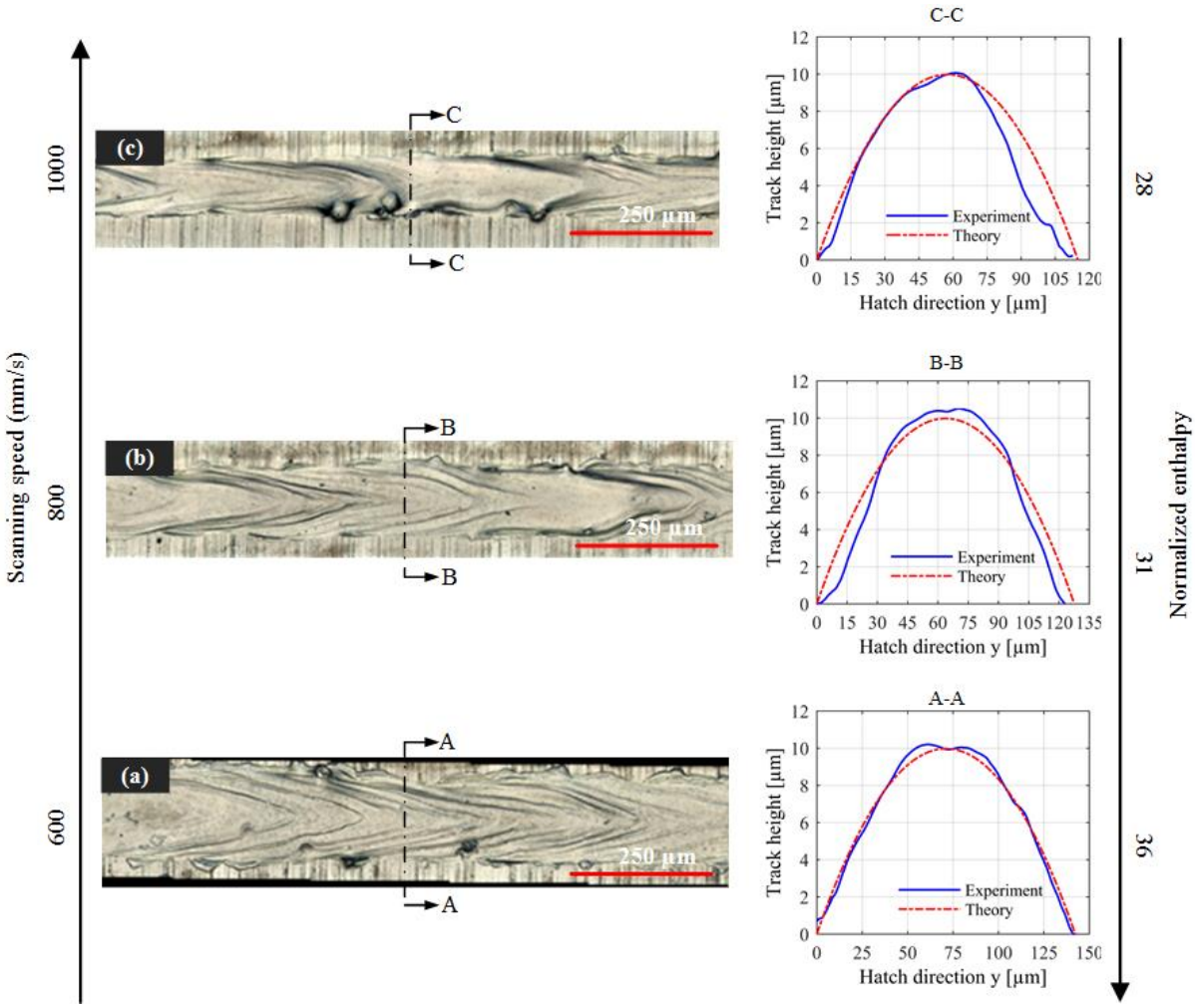

Figure 6-19. Top surface morphology and the corresponding transverse cross-section of single-track under different scanning speeds and normalized enthalpy. (a) 600 mm/s. (b) 800 mm/s. (c) 1000 mm/s. Laser power 195 W, layer thickness 20 µm, track length 20 mm

As illustrated in Figure 6-19, the predicted cross-sectional profiles of the single-track fit well with the measurements. It can be clearly seen that the track width increases gradually with an increase in the normalized enthalpy and decreases with an increase in the scanning speed. However, the track height keeps a relatively steady value under the single-track scanning, which mainly depends on the layer thickness.

Figure 6-20 presents the variation of the cross-sectional profiles in the multi-track scanning under a zig-zag scanning pattern. As it is seen in Figure 6-20 (a, b), the dimension of the first track is comparably narrower and wider than that of the following tracks in the width and height direction, respectively. This could be attributed to the substrate denudation effect [184]. During

denudation process, the powder particles are attracted from the two sides for the first track but mainly one side for the following tracks. As a result, possible interaction between the laser beam and substrate may take place in the following track. To consider the substrate denudation effect in the model calculations, the height of the first track was doubled while the heights of following tracks were halved. As can be seen in Figure 6-20 (b), predicted profile of the multi-track by the model agrees well with the experimental measurements. In addition, to avoid the non-uniform distribution of height induced by the substrate denudation, a proper scanning strategy should be applied for multi-track scanning in the LPB-AM process.

Moreover, as seen in Figs. 21 and 22, discrepancies exist between the predicted and measured profiles of track height. The prediction errors may be resulted from ignoring of the complicated wetting physics during the LPB-AM process. In addition, the inevitable oxidation may also influence the contact angle of the liquid melt pool, which may subsequently change the track height profile.

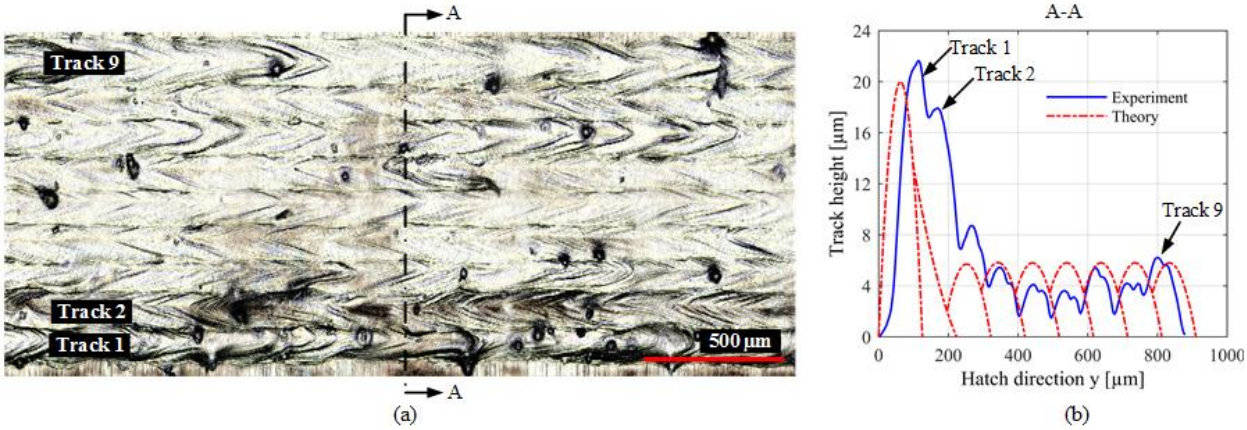

Figure 6-20. Top surface morphology (a) and the transverse cross-section (b) of single-layer nine-track sample under the zig-zag scanning pattern. Laser power 195 W, scanning speed 800 mm/s, hatch space 100 µm, layer thickness 20 µm, track length 20 mm.

6.5. Summary

A time-efficient comprehensive model with grasping enough physics fidelity of the LPB-AM process was built in this chapter. The transient temperature field and the dimension of the in-situ melt pool and final solidified track profile were solved from the built model. This can be used for process optimization and the design of model-based controller to achieve higher dimensional fabrication accuracy. Experiments with SS 17-4PH powder were conducted to verify the model.

It was found that the predicted results show a high accuracy compared to the experimental measurements for both the single-track and multi-track scanning samples.

The thermal field simulation in this research was run on a HP® computer with Intel® CoreTM i7-6700 CPU (3.4GHz). The calculation code was programmed by Matlab® R2017b. It was found that the calculation time for a single point is around 1.2 ms with a tolerance of $10^{-3}K$, confirming the high potential of the current research to be used for process optimization and in-situ process control.

Chapter 7. Application I: Rapid prediction of the Real-time Thermal Characteristics, Solidification Parameters and Microstructure in LPF-AM*

7.1. Introduction

The localized thermal characteristics, solidification parameters and the corresponding microstructure depend highly on the process parameters in the LPF-AM process. However, undesirable and inconsistent microstructure may potentially be induced due to the environmental disturbances or improper setting of process parameters. In addition, the characterization and validation of geometrical, microstructural and mechanical properties of as-built parts are driven primarily by offline post-processing analysis, which is time-consuming and expensive [191]. So far, a variety of process parameters have been linked to geometrical features through online/inline control strategies to improve dimensional accuracies (e.g., melt pool dimension [82], clad height [192] and clad geometry [70]). However, it should be noted the strategies that solely arrive at a high geometrical accuracy may not be sufficient if microstructure and mechanical properties of the fabricated parts are not desirable.

A large number of research studies have showed that the microstructural and mechanical properties of the LPF-AM fabricated parts are mainly governed by the real-time thermal characteristics of melt pool and the corresponding solidification parameters (thermal gradient (G) and solidification rate (R)). Additionally, the in-situ thermal characteristics and the associated solidification parameters depend highly on the process parameters. Akbari and Kovacevic [193] found that the smaller inter-layer dwell time can decrease the cooling rate ($G \times R$), leading to a coarser grain size and lower ultimate tensile strength. Farshidianfar et al. [144] reported that the size of the solidification structure and the associated solidification mode can be defined by the in-situ cooling rate, which is affected by the laser scanning speed, laser power and powder feed rate. Wang et al. [194] demonstrated that a lower linear heat input (laser power/scanning speed)

* A similar version of this chapter was submitted for publication as:

Huang Yuze, Mohammad Ansari, Hamed Asgari, Mohammad Hossein Farshidianfar, Dyuti Sarker, Mir Behrad Khamesee, Ehsan Toyserkani. Rapid Prediction of Real-time Thermal Characteristics, Solidification Parameters and Microstructure in Laser Directed Energy Deposition (Powder-fed Additive Manufacturing).Journal of Materials Processing Technology. 2019

is corresponding to a smaller-size melt pool, larger thermal gradient and higher cooling rate, therefore, resulting in higher yield strength, larger ultimate tensile strength and higher ductility compared to those of higher linear heat input. Furthermore, in the recent review work of Sames et al. [47] for metallic material additive manufacturing, it was stated that the control of microstructural and mechanical properties could be achieved through the manipulation of local solidification parameters. Moreover, Collins et al. [195] summarized the recent microstructural control work in metallic additive manufacturing and highlighted the key interdependencies among the processing parameters, composition and the resulting microstructure. They reported that the spatial-temporal solidification parameters could be estimated from the localized thermal behavior, which can be further controlled by varying processing parameters. Therefore, linking the process parameters to the real-time thermal characteristics and solidification parameters is highly required for developing on-line process control systems to manufacture parts with expected microstructural features and reliable mechanical properties in the LPF-AM process.

Numerous research studies have been done to establish the correlation between thermal characteristics, solidification parameters and process parameters for the microstructural and mechanical properties control and optimization. Lia et al. [196] measured the real-time thermal cycles in the LPF-AM process and calculated the corresponding G, R and $G \times R$ to evaluate the microstructural evolution. They showed that the process variables could be associated with the solidification parameters that govern the final microstructure. Using fitted relationships of the cooling rate and the secondary dendritic arm spacing (SDAS, SDAS is a common length scale for cellular/dendritic microstructure), the size of the microstructure can be predicted. However, the directly measured thermal data can only be used to represent thermal characteristics of the specific local zone. It has been argued that LPF-AM is a highly localized solidification process, in which the thermal behavior of each discrete location could differ significantly from that of the other positions [195].

Numerical modeling of the spatial-temporal thermal behavior is a possible alternative to the direct experimental measurement. Gockel et al. [197] proposed an integrated approach to control the microstructure in the single-track deposition, which was later extended to thin-wall structure [198]. The solidification parameters were derived from the numerical thermal model through Finite Element Method (FEM). Subsequently, the microstructure was predicted using the

solidification map of the specific material. Finally, the indirect microstructure control was achieved by relating the predicted microstructure to the derived melt pool dimensional map. Knapp et al. [191] built a digital twin of a single-layer deposition in LPF-AM. The spatialized transient temperature, cooling rate and solidification parameters were extracted from a numerical heat transfer and fluid flow model for a given set of process parameters. Accordingly, the SDAS and the hardness were predicted based on the analytical relationships. In addition, their experimental results showed that the SDAS in the LPF-AM process could be calculated by the well-known Kurz-Fisher (KF) model [199] with a high accuracy. Nevertheless, the FEM-based numerical models are computationally expensive and cannot be directly used for online control.

Since the direct experimental measurement and the FEM-based numerical modeling methods both have their limitations for a rapid estimation and online control of the thermal characteristics and microstructure, the time-efficient analytical thermal model could be considered as a potential choice. Bontha et al. [200] built thermal process maps to estimate the solidification microstructure based on both analytical and numerical thermal models in thin-wall structure deposition, which was also extended to bulky 3D structures [201]. Temperature-independent material properties were assumed in the analytical model, while the temperature-dependent properties and latent heat were considered in the numerical model. They found that the predicted solidification parameters from the FEM-based numerical solution and the quasi-steady-state analytical Rosenthal solution are in a reasonable agreement with each other for both the small-scale (LPF-AM) and large-scale (higher power) deposition processes. Liang et al. [202] developed a theoretical primary dendrite arm spacing (PDAS) model in terms of the process parameters and extended that to process-microstructure maps for microstructure control [203]. In their study, the solidification parameters were numerically solved from the analytical quasi-steady-state Rosenthal equation. The calculated G and R were then related to the microstructural characteristics and were verified by the experimental results. However, the above quasi-steady-state Rosenthal solution only shows the thermal characteristics at the time $t \to \infty$, which may not be accurate to represent the time-varying thermal characteristics in the LPF-AM process. Consequently, these models may not be applicable for real-time microstructural control.

This chapter aims to link the process parameters to the transient localized thermal characteristics and solidification parameters for rapid prediction of the solidification microstructure induced by

using the process model built in Chapter 5. The real-time thermal characteristics and the solidification parameters are extracted from a 3D analytical thermal model based on the process parameters. Subsequently, the calculated solidification parameters are combined with the substructure scale solutions for microstructural prediction. The structure scale solutions are handled by fitting the predicted solidification parameters with the measured PDAS and SDAS based on the well-known KF model [199]. Validation experiments are conducted by depositing stainless steel 316L (SS 316L) and Inconel 625 at different laser scanning speeds. The predicted real-time melt pool peak temperatures at different scanning speeds and various energy densities of SS 316L deposition are compared with the corresponding experimental results presented in the previous work [144]. The variations in the solidification scale and mode over the SS 316L and Inconel 625 deposits are also analyzed.

7.2. Theory

The transient temperature field solution in the LPF-AM process is elaborated in Section 5.2.1. After solving the transient thermal field, the cooling rate $\dot{T}$ for any interest point $X = (x, y, z)$ may be derived as,

$$\dot{T} = \partial T(X, \mathrm{t})/\partial t \tag{7-1}$$

The temperature gradient G on the solidification front can also be derived from the temperature solution as,

$$G = \sqrt{\left[\frac{\partial T(X, \mathrm{t})}{\partial x}\right]^2 + \left[\frac{\partial T(X, \mathrm{t})}{\partial y}\right]^2 + \left[\frac{\partial T(X, \mathrm{t})}{\partial z}\right]^2} \tag{7-2}$$

In the LPF-AM process, the laser beam moves continuously and the solidification front keeps pace with the advancing laser source as shown in Figure 7-1. As the local solidification front moves along the maximum temperature gradient, which is normal to the solid-liquid front and opposite to the local predominant heat flow direction *Q*, the solidification rate *R* may be calculated by [204],

$$R = v\cos\theta \tag{7-3}$$

where θ is the angle that between the local solid-liquid front normal and the laser scanning direction. Since θ is nearly 90° at the bottom part of the melt pool and approach 0° at the top

region, the solidification rate will reach the minimum at the bottom region and approach the maximum at the top part.

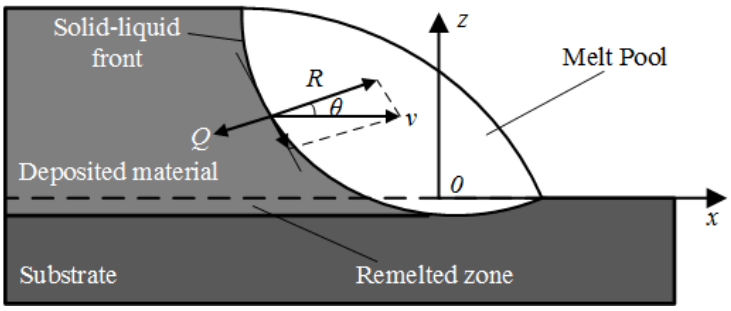

Figure 7-1. Schematic diagram of the solidification front in the longitudinal centerline cross-section (y=0) of the single-track deposition. Laser scanning speed *v*, solidification rate *R* and local predominant heat flow *Q*.

The angle θ may be derived based on the thermal solution in the longitudinal centerline cross-section as [205],

$$cos\theta = \frac{\partial T(X,\mathrm{t})/\partial x}{\sqrt{[\partial T(X,\mathrm{t})/\partial x]^2 + [\partial T(X,\mathrm{t})/\partial z]^2}} \tag{7-4}$$

It has to be noted that there is no temperature gradient in the transverse direction ($\partial T(X,\mathrm{t})/\partial y$) at the longitudinal centerline cross-section. From Equations (7-3) and (7-4), the solidification rate in the longitudinal centerline cross-section may be derived as,

$$R = \frac{\partial T(X,\mathrm{t})/\partial t}{\sqrt{[\partial T(X,\mathrm{t})/\partial x]^2 + [\partial T(X,\mathrm{t})/\partial z]^2}} \tag{7-5}$$

Similarly, for the spatial point $X = (x, y, z)$ in the Cartesian coordinate system, $cos\theta$ can be calculated as $cos\theta = [\partial T(X,\mathrm{t})/\partial x]/\sqrt{[\partial T(X,\mathrm{t})/\partial x]^2 + [\partial T(X,\mathrm{t})/\partial z]^2 + [\partial T(X,\mathrm{t})/\partial z]^2}$ and the corresponding solidification rate can be expressed as $R = \dot{T}/G$.

The dendrite arm spacing (DAS) λ has been established based on the solidification parameters (*G* and *R*) by the well-tested Kurz and Fishers' model [199],

$$\lambda = AG^{-n}R^{-m} \tag{7-6}$$

where *A*, *n*, and *m* are material-dependent parameters. The DAS provides a useful approach to establish the precise effect of solidification conditions on microstructure. Especially, the SDAS can be calculated by setting $n = m$ based on Equation (7-6).

7.3. Materials and procedure

In this research, SS 316L powder (Praxair Surface Technologies, PA, USA), -325 mesh, was deposited on the sandblasted AISI 1030 medium carbon steel substrate by an in-house developed LPF-AM apparatus. With the same apparatus, Inconel 625 powder (Carpenter, Pennsylvania, USA) in the size range of 45-125 µm was deposited on the sandblasted Inconel 625 plates. The LPF-AM apparatus was composed by a continuous 1.1 KW IPG photonics fiber laser system, a Sulzer Metco powder feeder and a Fadal CNC machine. The morphology of powder particles was studied using a Zeiss LEO FE-SEM 1530 scanning electron microscope (SEM). SEM images of the powder particles (SS 316L and Inconel 625) are shown in Figure 7-2. As seen, in both powders (Figure 7-2 (a) and (b)), most of the particles possess a spherical morphology while a few powder particles with other morphologies, e.g. irregular or satellite-like, can also be identified. The thermo-physical properties of the SS 316L and Inconel 625 powders are assumed to be temperature independent and the associated thermal parameters (shown in Table 7-1) were averaged over the temperature range. The fiber laser absorptivity was chosen as 0.4 [206] and 0.35 [120] for SS 316L and Inconel 625, respectively.

Experiments were done to test the developed relations with single-layer deposition. The process parameters used in the present research are listed in Table 7-2. To study the microstructural features using optical and scanning electron microscopy, the samples were cross-sectioned at the middle track length, mounted and polished using conventional metallography methods, followed by etching. The SS 316L and the Inconel 625 samples were etched by Marble's reagent (10 g $CuSO_4$ in 50 mL HCl and 50 mL H_2O) and reagent (10 mL glycerol, 50 mL HCl and 10 mL HNO_3), respectively. The DAS was measured in three different height locations of the deposits as illustrated in Figure 7-2 (c): the bottom region that is close to the fusion boundary (around 1/8h); the middle region that is equidistant from the bottom and top edges (1/2h); and the top region located at around the deposit top (around 7/8h). The DAS of the SS 316L deposits were measured based on the Hilliard single-circle procedure followed by the ASTM standard [207], while the DAS of the Inconel 625 deposit were measured individually by the Digimizer$^{@}$ software with hundreds of measurements and then averaged. The melt pool real-time temperature data of SS 316L deposition were used from the previous work [144]. The calculation of the real-

time thermal and solidification characteristics were conducted in the Matlab® R2017b by a HP® computer with Intel® Core™ i7-6700 CPU (3.4GHz).

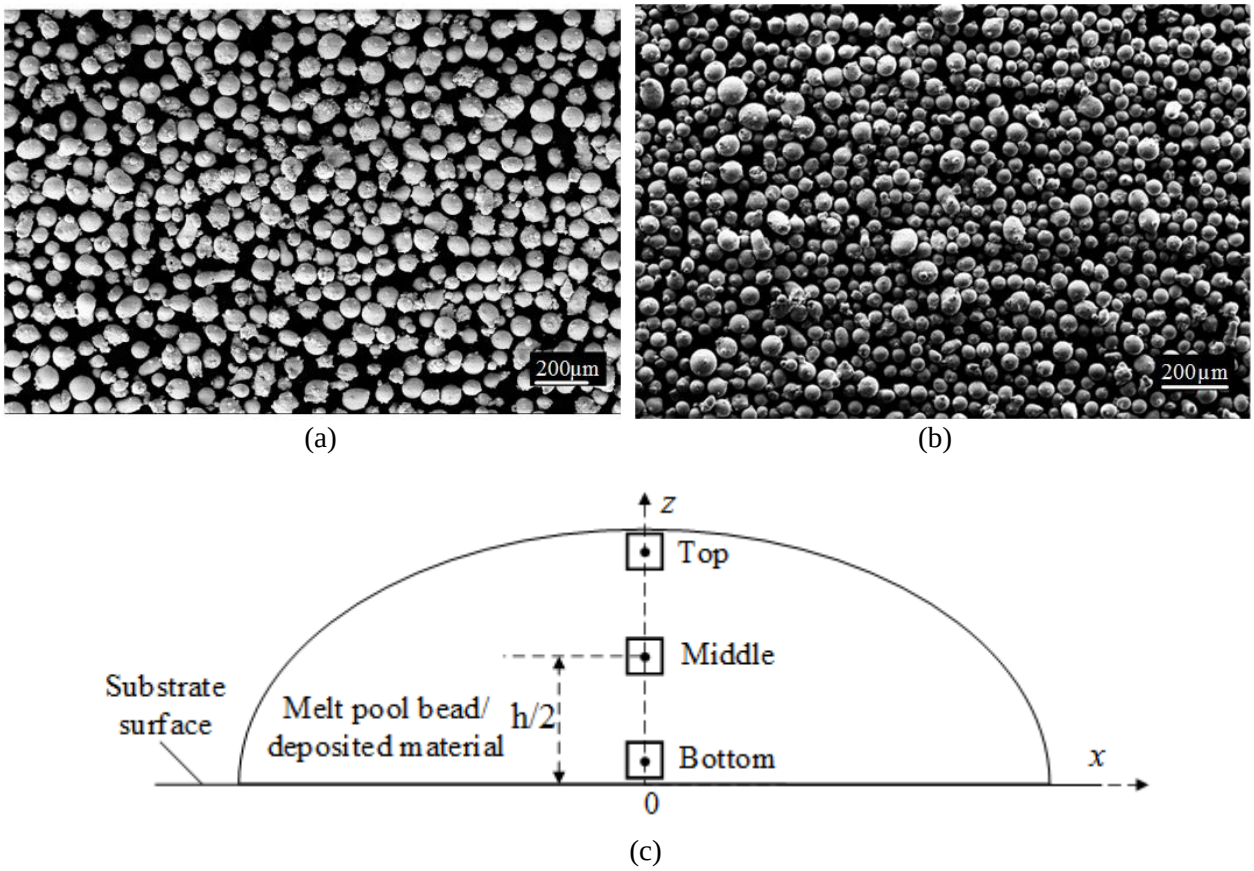

Figure 7-2. SEM images of the powder particles (a) SS 316L, (b) Inconel 625 and (c) schematic diagram showing the three different locations in the transverse cross-section of the bead/deposit for solidification parameter prediction and microstructure verification.

Table 7-1. Particle thermal-physical properties. The SS 316L thermal-physical properties were obtained from references [165,208]. Inconel 625 properties were obtained from reference [209].

	Solidus T_s, Liquidus T_l and Melting T_m temperature [K]	Density $\rho\ [Kg/m^3]$	Thermal conductivity $k\ [W/(m \cdot K)]$	Specific heat $c_p\ [J/(Kg \cdot K)]$
SS 316 L	1680, 1720,1700	7900 (300K)-7430 (1700K)	13.96 (300K)-35.95 (1700K)	434 (300K)-965 (1700K)
Inconel 625	1563,1623, 1593	8440	9.8 (300K) -25.6 (1273K)	410 (300K) -670 (1363K)

Table 7-2. Process parameters for SS 316L and Inconel 625 depositions

Process parameters	SS 316L	Inconel 625
Scanning speed, [mm/min]	25, 50, 100, 200	180, 270, 360
Laser power, [W]	700, 917	1000
Powder feed rate [g/min]	4	7
Laser beam diameter, [mm]	2.5	1.8
Nozzle angle,	55°	60°
Nozzle height, [mm]	10	7
Correction factor, μ_M	2.5	2.5
Ambient temperature, [K]	300	300
Brewster effect coefficient, a_w	0.0196	0.0196
Laser absorptivity	0.4	0.35
Carrying gas feed rate, [dL/min]	3.5	2.5
Track length, [mm]	30	30
Powder stream divergence angle	8.3	8.4

7.4. Results and discussion

7.4.1. Real-time temperature evolution

Figure 7-3 shows that the model predicted results are in a good agreement with the experimental measurements of the real-time melt pool peak temperature under different laser scanning speeds and various energy densities (P_L/vD). As seen in Figure 7-3 (a), the melt pool peak temperature decreases significantly with an increase in the laser scanning speed. This is because the energy density declines with the increase in the scanning speed, leading to a smaller amount of laser energy were added into the melt pool at per unit time. To further verify the effect of energy density on the peak temperature, the laser power and scanning speed were varied simultaneously to obtain the two different energy densities as shown in Figure 7-3 (b). As seen, a higher peak temperature is achieved with a larger energy density. Slight mismatches are also observed between the measured data and the model predictions, which may be ascribed to error/noise sources in the temperature measurement during deposition as well as the simplifying assumptions made for the thermal model.

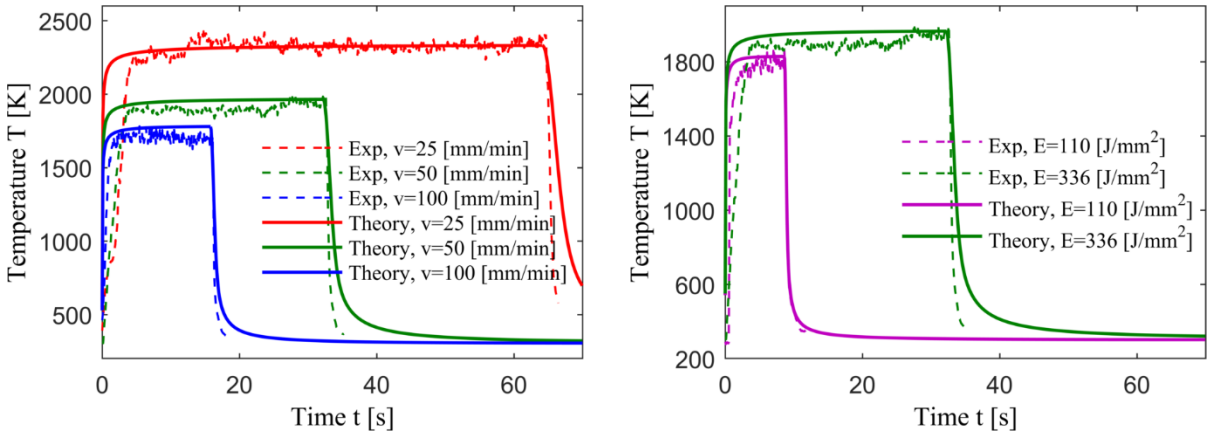

Figure 7-3. Real-time melt pool top surface peak temperature of SS 316L deposition under following conditions. (a) Different laser scanning speeds (laser power 700W) and (b) different energy densities (E=110 J/mm^2 with laser power 917W, scanning speed 200 mm/min; E=336 J/mm^2 with laser power 700W, scanning speed 50 mm/min). Powder feed rate 4g/min. The real-time melt pool peak temperature was adopted from a previous work [144].

The agreement between the calculated real-time melt pool peak temperature and the corresponding experimental measurements may provide sufficient confidence in using the thermal model to link the process parameters to the in-situ thermal characteristics. The melt pool peak temperature map was plotted as a function of laser power and scanning speed as shown in Figure 7-4. As seen, the maximum temperature occurs at the largest laser power and minimum scanning speed. However, the peak temperature has to be chosen in a way that the maximum temperature is higher than the melting temperature (1700 K) but lower than the boiling temperature (3200 K [175]) in the process window for effective deposition. The developed melt pool peak temperature map illustrated in Figure 7-4 can be effectively useful to optimize the process parameters to achieve an effective deposition.

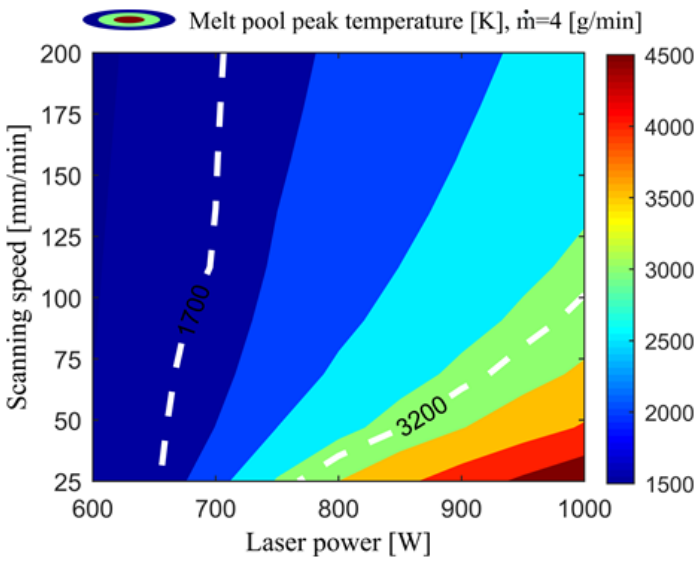

Figure 7-4. Melt pool peak temperature map for SS 316L single-track deposition. The peak temperature was calculated at the transient time moment ($t=L/2v$, track length L=30 mm). The melting temperature (1700 K) and boiling temperature (3200 K) of SS 316L are marked with white dash lines.

In LPF-AM, each location on the scanning route experiences a dynamic thermal cycle because the temperature rises up as the laser beam gets closer and then cools down when the laser passes away. In addition, the energy of the laser beam typically has a non-uniform distribution (e.g., Gaussian distribution), giving rise to an inconsistent temperature distribution within the melt pool. Therefore, the measured real-time top surface temperature of the melt pool shown in Figure 7-3 may not be accurate enough to estimate the local thermal characteristics of different zones within the melt pool area, particularly for the zones beneath the melt pool surface.

The local thermal history of the SS 316L deposition at different depth locations (Figure 7-2 (c)) of the melt pool bead are shown in Figure 7-5. It is evident from Figure 7-5 that a higher cooling rate and a larger peak temperature can be reached at the top location than that of the bottom location at the same scanning speed. This is in a good agreement with both the experimental result reported by Du et al. [210] and the numerical simulation founding from Gan et al. [211]. Moreover, the instantaneous heating/cooling rates are inversely proportional to the scanning speed for both bottom and top locations of the melt pool bead. Figure 7-5 (b) shows the local thermal cycles in the single-layer deposition. It is observed that both top and bottom locations will experience a thermal cycle with the motion of the laser beam along the track path. In this

situation, the temperature of the top and bottom locations increases instantly from the low ambient value to a high magnitude (e.g., T_s ,T_l) and then decreases over the time.

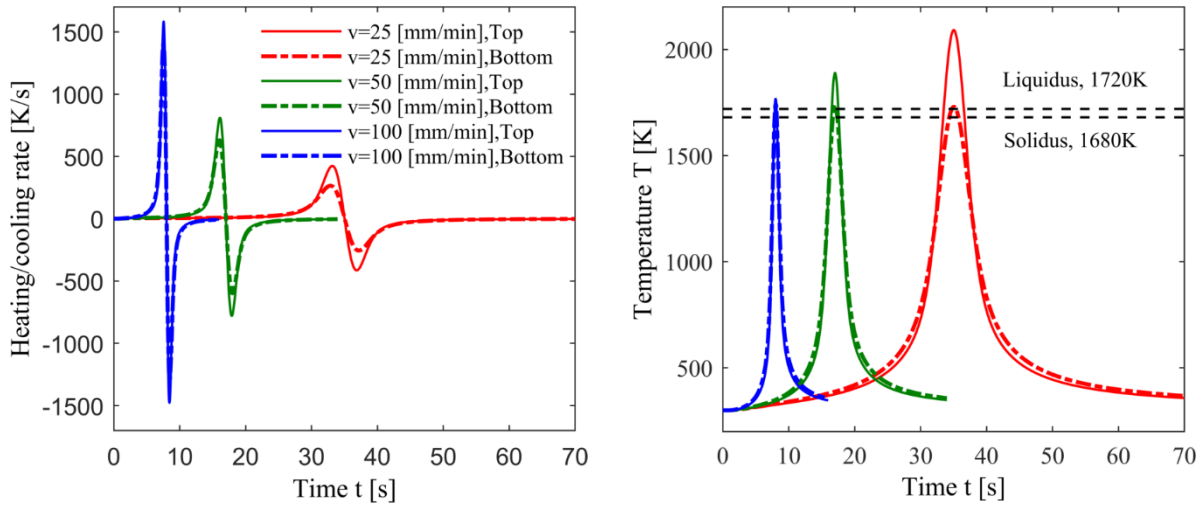

Figure 7-5. Real-time local thermal profiles at different clad height locations during single-layer SS 316L deposition. (a) Heating/cooling rate. (b) Temperature cycles. Laser power 700 W, powder feed rate 4 g/min. The liquidus and solidus temperatures of SS 316L are marked with black dash lines.

7.4.2. Solidification characteristics

Temperature gradient (G) and solidification rate (R) are the two main parameters effecting the solidification microstructure. The effect may be illustrated by the solidification map as presented in Figure 7-6. The solidification map is constructed by G and R in the combination forms with $G \times R$ (cooling rate) and G/R, where the G/R ratio governs the solidification mode while their product ($G \times R$) controls the scale of the solidification microstructure [212]. As seen in Figure 7-6, the solidification mode may transform from planar to cellular, columnar dendritic and equiaxed dendritic as the G/R ratio decreases. Additionally, a higher value of $G \times R$ will induce a finer substructure and consequently, may improve the mechanical properties of the fabricated parts (e.g., the yield stress [213]).

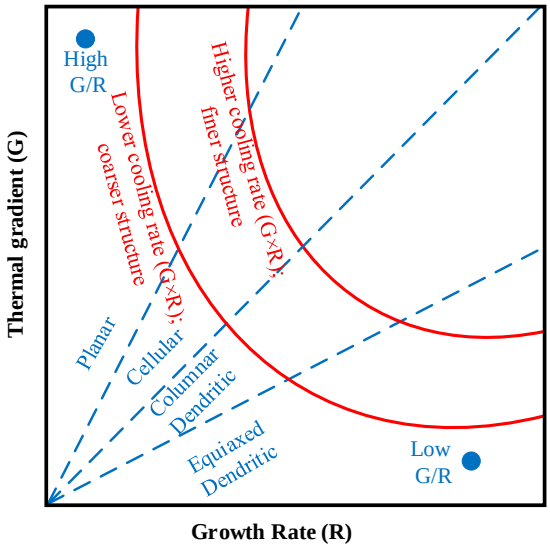

Figure 7-6. Effect of G and R on the mode and scale of solidification microstructure. Adopted from reference [214].

Previous papers [200,201,215] have shown that *G*, *R* and their associated combinations, i.e. *G*×*R* and *G*/*R*, vary significantly throughout the melt pool bead depth. As a result, the microstructure may be graded over the deposit height. However, measuring the *G* and *R* over the melt pool bead depth during the process remains extremely challenging due to the small-scale localized melting nature and the high solidification rate. The *G* and *R* can be calculated based on the Equations (7-2) and (7-3). Then a comparison of simulated *G*×*R* and *G*/*R* is performed for different locations along the melt pool bead depth, respectively. The transient cooling rate and the thermal gradient of the solidification front are both calculated at the time moment ($t = t_{T_s}$) of the last solidus temperature.

The calculated results of *G*×*R* and *G*/*R* for different depth locations of SS 316L and Inconel 625 melt pool beads are shown in Figure 7-7 (a-b) and Figure 7-7 (c-d), respectively. Here has to be noticed that the three melt pool bead depth locations corresponding to the three deposit height locations as illustrated in Figure 7-2 (c). As seen from Figure 7-7, with keeping all parameters constant but increasing the scanning speed, the cooling rates (*G*×*R*) increase significantly for all three locations, while *G*/*R* ratios decrease. Moreover, the cooling rate (*G*×*R*) increases from the bottom toward the top of the melt pool bead. By contrast, the *G*/*R* value decreases from the bottom location to the top region. The above simulated results are consistent with the previously reported experimental results, in which cooling rate (*G*×*R*) decreases and *G*/*R* ratio increases

with an increase in bead depth [210,211] or with a decrease in scanning speed [216,217]. The simulated cooling rates shown in Figure 7-7 are in the range of $10^2 \sim 10^3$ K /s for both SS 316L and Inconel 625 depositions. Other studies have also reported that the cooling rates for SS 316L [218,219] and Inconel 625 [196] depositions by LPF-AM are in the range of $10^2 \sim 10^4$ K /s.

The microstructure evolution in SS 316L and Inconel 625 deposits may be directly estimated from the predicted solidification parameters (Figure 7-7) with reference to the general solidification map (Figure 7-6). According to the calculated solidification parameters shown in Figure 7-7, it can be concluded that the microstructure gradually become finer from the bottom to the top of the deposits due to the variation of cooling rate ($G \times R$). Furthermore, from Figure 7-7 it is seen that the calculated *G/R* ratios for SS 316L and Inconel 625 deposits are in the range of 900 ~ 6000 Ks /mm^2 and 500 ~ 1000 Ks/mm^2, respectively. Kurz and Fisher [220] defined the threshold for planar solidification as $G/R = \Delta T_l/D$, where $\Delta T_l = T_l - T_s$ is the solidification temperature interval and *D* is the diffusion coefficient within the liquid phase. In some previous research works, the $\Delta T_l/D$ values for SS 316L and nickel-based alloys have been reported as 50000 Ks /mm^2 [221] and 7000 Ks /mm^2 [222], respectively. These values far exceed the predicted G/R values (shown in Figure 7-7). Consequently, it can be concluded that planar solidification will not occur for both SS 316L and Inconel 625 deposits. The predicted *G/R* value (shown in Figure 7-7 (b)) for SS 316L are also larger than that of reported for equiaxed solidification (*G/R*=10 Ks /mm^2 [223]). Therefore, columnar or cellular structure may be observed in the SS 316L deposits. In comparison to the columnar-to-equiaxed transition (CET) curve of Inconel 625 reported by Hu et al. [224], the estimated *G/R* values (shown in Figure 7-7 (d)) for Inconel 625 fall in the specific *G/R* window of equiaxed and columnar dendritic substructure. Accordingly, transition from columnar dendritic to equiaxed dendritic may occur in the Inconel 625 deposits.

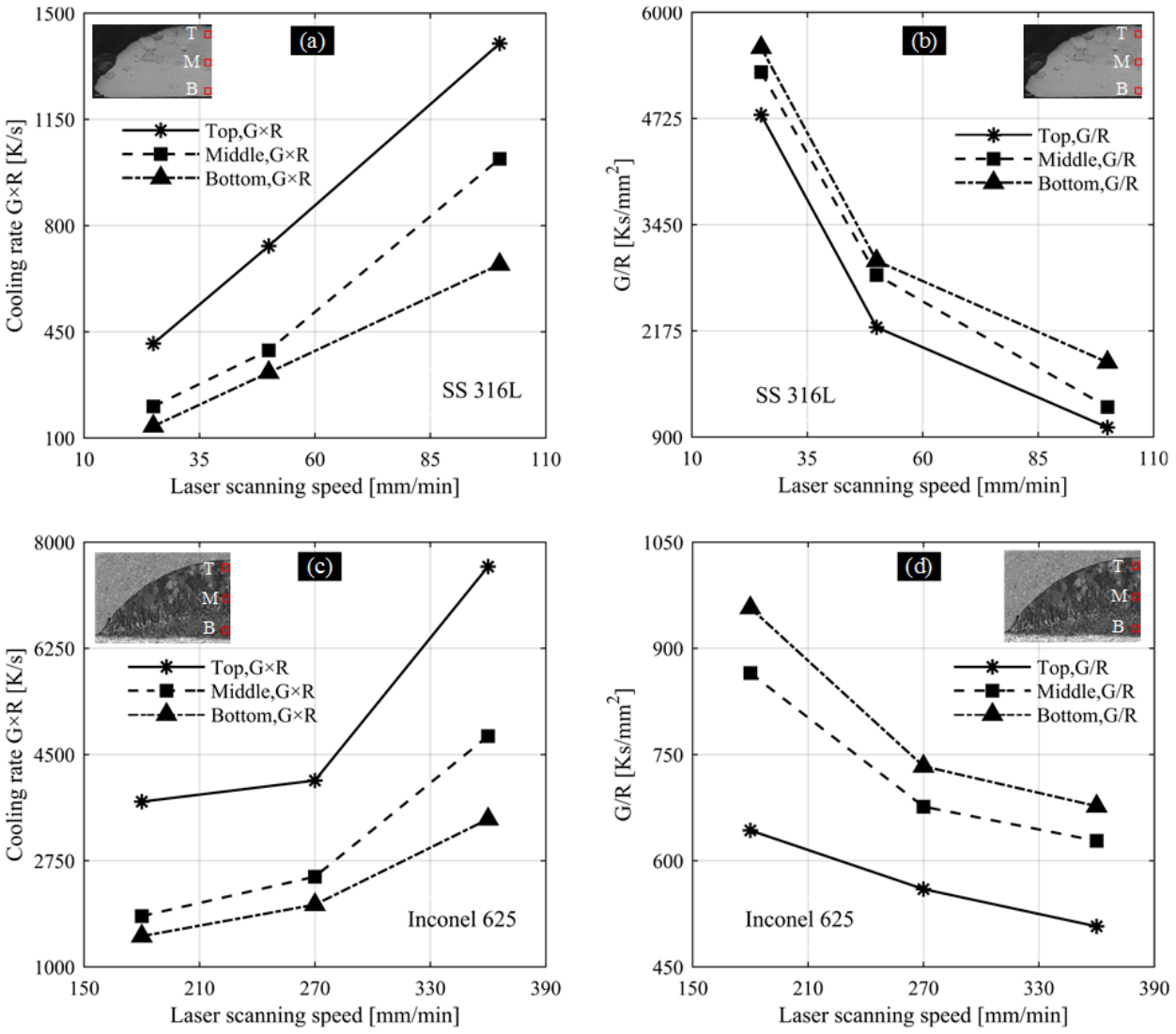

Figure 7-7. Predicted in-situ solidification characteristics at different melt pool bead depth locations versus the laser scanning speed for the transient time moment $t=L/2v$. (a) (c) and (b) (d) are the cooling rate G×R and G/R ratio for SS 316L and Inconel 625, respectively. 700 W laser power and 4g/min powder feed rate were used for SS 316L simulation, and 1000 W laser power and 7 g/min powder feed rate were used for Inconel 625 simulation. Track length L=30 mm. The three different height locations in the final deposit were marked with red blocks to represent the corresponding depth locations in the melt pool bead. T, M and B represents the top, middle and bottom positions, respectively.

To validate the predicted solidification parameters, the transverse cross-section micrographs of the SS 316L and Inconel 625 deposits were investigated in the bottom, middle and top regions (illustrated in Figure 7-2 (c)) of deposits and the results were shown in Figure 7-8 and Figure 7-9, respectively. Figure 7-8 shows the microstructure of the SS 316L deposits under various laser

scanning speeds. As seen, all samples exhibit a typical cellular microstructure in the transverse cross-section, which agrees with the predictions presented in the above paragraph. In addition, the PDAS shrinks dramatically as the laser scanning speed increases. This may be attributed to the fact that a larger cooling rate ($G \times R$) will be induced by a higher scanning speed, resulting in a finer microstructure as illustrated in the solidification map (Figure 7-6). In addition, it is noticed that a coarser cellular structure is prevalent at the bottom zone of the deposit and the PDAS decreases towards the top zone (shown in Figure 7-8). This kind of trend has also been found in the studies conducted by Yadroitsev et al.[225] with SS 316L powder and Gan et al. [211] with Co-based alloy powder. The above observed microstructural variations (Figure 7-8) are consistent with the calculated solidification parameters (Figure 7-7) and the associated predicted microstructural evolutions that were discussed in the above paragraph.

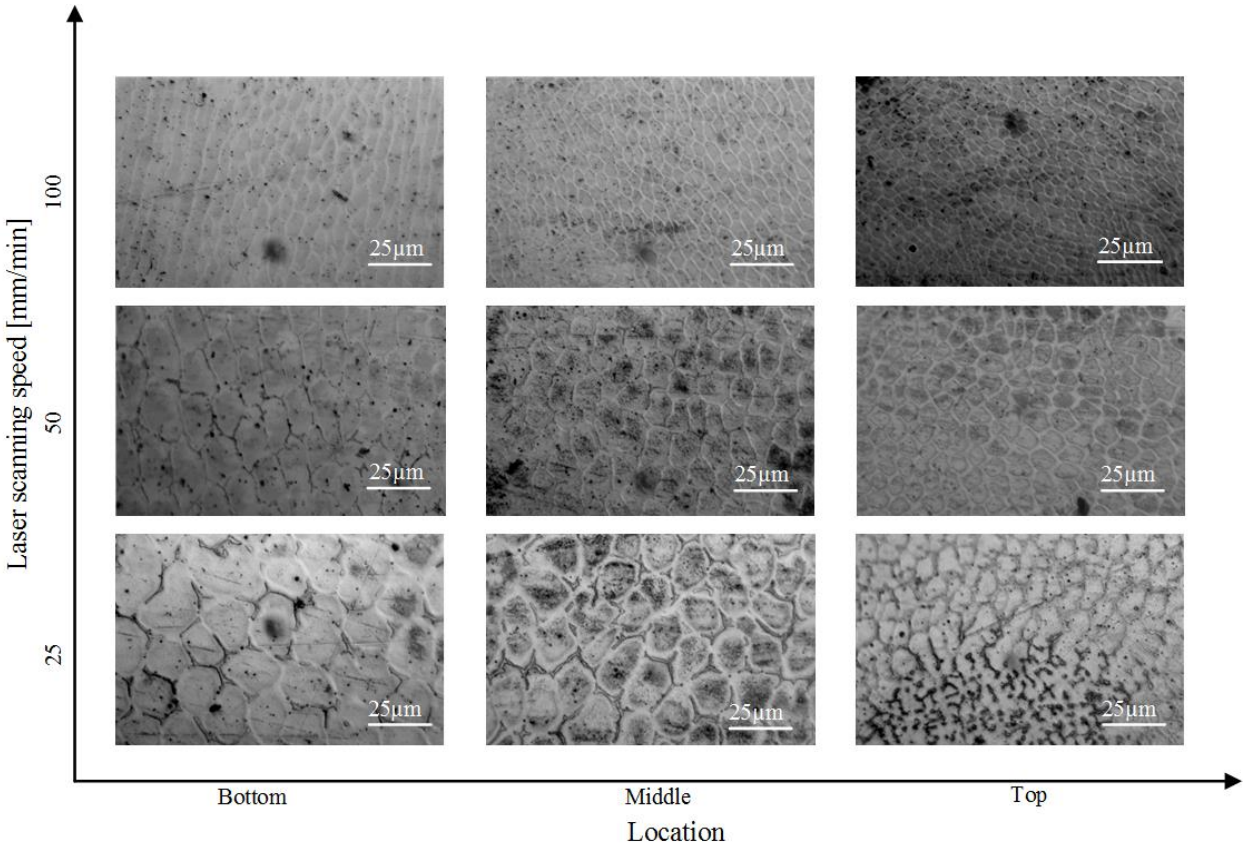

Figure 7-8. High magnification images of the SS 316L samples at different height locations of the deposits in the half-track length cross-section under different scanning speeds. Laser power 700 W, powder feed rate 4 g/min and track length 30 mm.

Figure 7-9 shows the microstructure of the Inconel 625 deposits in the transverse cross-section under different laser scanning speeds. Figure 7-9 (a) presents the microstructure profiles of the entire deposit at low magnification and Figure 7-9 (b) displays the microstructure profiles along the centerline of the deposit height at high magnification. It is evident that, for the regions with increasing distance to the substrate surface (from the bottom to the top regions of the deposits), different microstructures show up with decreasing size. Columnar-dendritic substructure without secondary dendrites is predominantly distributed near the bottom zones of the deposits, which is consistent with the experimental observations reported in references [224,226]. These relatively large columnar dendrites (PDAS of 8 ~ 12μm) are observed in all the samples under the three different scanning speeds (180, 270, 360 mm/min). The area right above the substrate belongs to the initial stage of solidification and is resistant to the etchant reagent. Thus, those zones located right above the substrate do not show a clear substructure. Columnar-dendritic substructure with classical secondary dendrites (SDAS of 3.6 ~ 5μm) were observed in the middle region of the deposit. In addition, the transition of substructure from columnar dendrite to finer equiaxed dendrite (SDAS of 3 ~ 4μm) is noticed at the top region. Similar solidification microstructure evolution was also observed in the research work done by Xu et al. [227] for Inconel 625 deposition by LPF-AM.

The microstructural evolution presented in Figure 7-9 is consistent with the above microstructure predictions that are derived from the calculated solidification parameters (shown in Figure 7-7). At the melt pool bead bottom region, the solidification rate ($R = vcos\theta$) is quite small since the normal of the local solidification front is nearly perpendicular to the laser travelling direction ($\theta \approx 90^{\circ}$), resulting in a relatively large *G/R* value as shown in Figure 7-7 (d). Therefore, the typical columnar dendrites formed and no secondary dendrites grew near the bottom region. With an increase in distance from the substrate surface, the *G/R* value decreases (shown in Figure 7-7 d) due to the rapid growing solidification rate. This results in the gradual transition of the solidification mode from columnar dendritic to equiaxed dendritic. Meanwhile, the solidification front becomes less stable at a reduced *G*/*R* ratio, which in turn, promotes the growth of the secondary dendrites. Furthermore, the substructure scale decreased with an increase in the scanning speed as well as an increase in distance from the substrate surface, which is attributed to the highly increased cooling rate ($G \times R$) as depicted in Figure 7-7 (c).

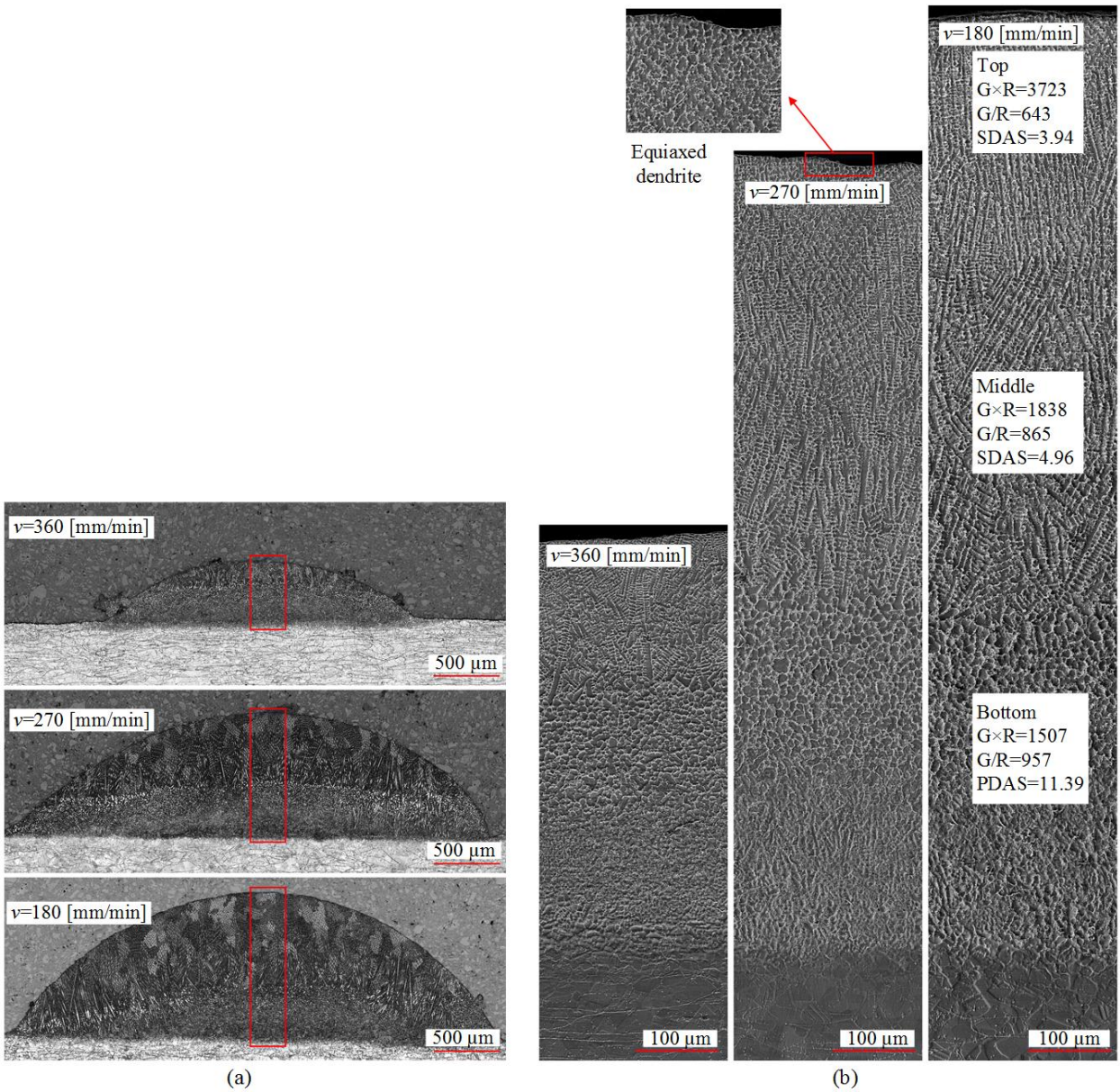

Figure 7-9. SEM images of Inconel 625 samples in the half-track length cross-section at different scanning speeds. (a) Low magnification view (b) High magnification view along the clad height for the marked out area in (a) by red rectangles. The calculated $G\times R$ (K/s), G/R (Ks/mm^2) and the measured DAS (µm) for 180 mm/min scanning speed deposition were labeled in (b) for different height locations.

To quantitatively analyze the scale of solidification microstructure in the LPF-AM process, the DAS values were measured for different height locations of the deposits (illustrated in Figure 7-2 (c)) under various scanning speeds, where the results are presented in Figure 7-10. Considering the fact that the secondary dendrites are not prominent in all regions of the SS 316L deposits (Figure 7-8), the PDAS is used to represent the microstructure length scale. From Figure 7-10 (a),

it can be clearly seen that the PDAS of the SS 316L shrinks from approximately 16 μm to 5.5 μm throughout the deposit when the scanning speed increases. These results are in agreement with the experimental PDAS values (6 ~12 μm) measured by Tan et al. [218] for the SS 316L deposits. Figure 7-10 (b) shows that with an increase of scanning speed, the SDAS and PDAS of Inconel 625 decreases from 5 μm to 3 μm and 11 μm to 9 μm, respectively. Similar SDAS and PDAS results (SDAS 3.5 μm and PDAS 10 μm) were reported by Marchese et al. [228] for Inconel 625 samples deposited by LPF-AM.

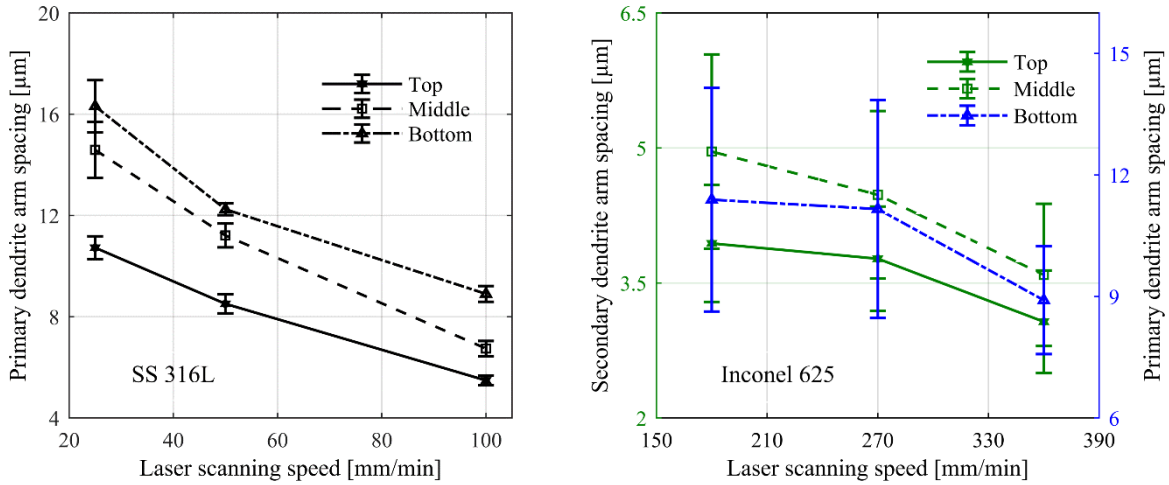

Figure 7-10. Variation of the microstructure scale in dependence on the location and laser scanning speed. (a) PDAS for top, middle and bottom locations of the SS 316L deposit (b) SDAS for middle and top location of Inconel 625 deposit and PDAS for bottom location of Inconel 625 deposit.

The measured PDAS and SDAS values were related to the calculated solidification parameters (G and R) based on the well-tested Kurz and Fishers' model (Equation (7-6)). The material-dependent coefficients A, n, and m were determined by using a least squares fit procedure. For the SS 316L powder material, the exponents were set as n=m=1/3 based on the previous study [229]. Subsequently, the constant A can be determined as A=80.37 with a coefficient of determination r^2=0.94. Similarly, The SDAS of the Inconel 625 can be fitted with the calculated G×R values by setting the exponents as n=m=1/3, and the constant A was then finalized as A=60.64 with r^2=0.99. For the PDAS prediction of Inconel 625, the exponent values n=1/2 and m=1/4 have been proved to be reasonably accurate for nickel-based superalloys in the laser additive manufacturing process [202,230]. Therefore, the constant A was determined as

A=428.44 with r^2=0.944. The fitted microstructure scale solutions and the measured PDAS and SDAS average values are shown in Figure 7-11.

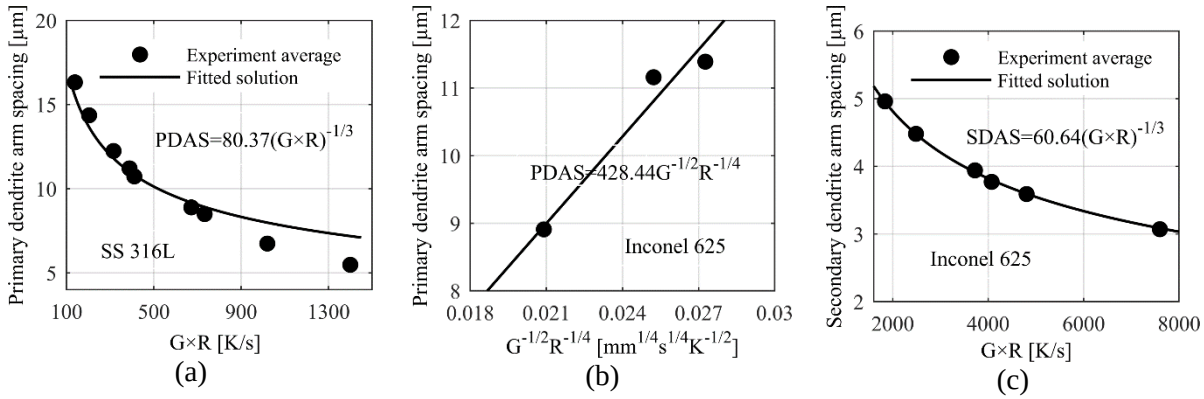

Figure 7-11. Experiment measured PDAS (a), (b) and SDAS (c) averaged values and the fitted microstructure scale solutions in a function of thermal gradient and solidification rate.

According to the built microstructure scale relationships shown in Figure 7-11, the microstructure scale of the in-situ LPF-AM deposition may be predicted and viewed with respect to the primary process parameters. Figure 7-12 shows the derived PDAS map for the top zone of the SS 316L bead with respect to the laser power and scanning speed at the transient time moment $t=L/2v$. The PDAS values were calculated by combining the predicted solidification parameters with the fitted substructure scale solutions. As seen, the PDAS gradually grows with an increase in the laser power. This might be related to the fact that the higher laser power lowers the cooling rate, resulting in a coarser microstructure. More interestingly, it is observed that the PDAS has a higher variation rate over the scanning speed compared to that of the laser power. The experiment conducted by Muvvala et al. [231] showed that the cooling rate was more sensitive to the scanning speed in comparison to the laser power, which may justify the above PDAS variation rate observation. Moreover, it is observed that the finer microstructure may be achieved at the process parameter combination of higher scanning speeds with lower laser powers. However, the parameter combination should be kept within the temperature threshold window (shown in Figure 7-4) of the melt pool for an effective deposition.

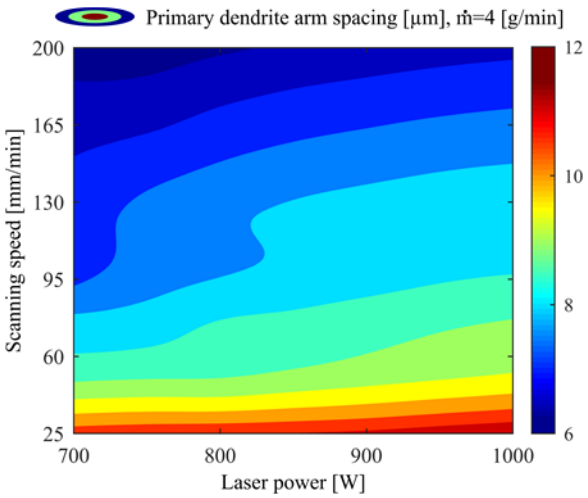

Figure 7-12. PDAS map in dependence on the laser power and scanning speed for the top zone of SS 316L bead at the transient time moment (t=*L/2v*) with a cellular dendritic morphology.

7.5. Summary

In this chapter, by utilizing the built process model of LPF-AM as elaborated in Chapter 5, the real-time localized transient thermal characteristics (temperature, cooling rate) and solidification parameters (thermal gradient and solidification rate) were linked to the process parameters for rapid prediction of the solidification microstructure in the LPF-AM process. Single-layer tracks of SS 316L and Inconel 625 were deposited at different laser scanning speeds to evaluate the above mentioned relations. It was found that the model predicted results are in good consistent with the experimental results. The DAS is more sensitive to scanning speed than laser power. Moreover, the finer microstructure could be achieved at the process parameter combination of higher scanning speed with lower laser power. However, to fulfill an effective deposition, the parameter combinations should be kept within the melt pool temperature threshold window. The cooling rate ($G \times R$) increases from the bottom to the top location of the deposits, leading to the finer microstructure at the top zone for both the SS 316L and Inconel deposits. On the contrary, the G/R value decreases from the bottom location to the top location of the deposit, resulting in the gradual transition of the solidification mode for Inconel 625 deposits.

The calculation time for the localized-transient cooling rate ($G \times R$) and G/R ratio are around 4 ms with a tolerance of 10^{-3} in this study, confirming the potential of this work to be used for in-situ prediction of thermal and solidification characteristics as well as the real-time microstructural control. It should be mentioned that the calculation time may be considerably reduced with more

advanced code optimization algorithms (e.g., switching from Matlab to a compiled programming language such as C++).

Chapter 8. Application II: Rapid Prediction of Thermal Cycle and Layer-wise Hardness for Stainless Steel 316L Thin-Wall Structure in LPF-AM*

8.1. Introduction

In the LPF-AM process, the complicated thermal cycles strongly depend on the processing parameters [3,194]. Improper parameter setting changes the thermal cycle history and may cause defects, i.e. pores, inclusions and cracks, that deteriorate the mechanical property of the as-built parts. In addition, the multi-layer deposition of LPF-AM is not a simple successive solidification, the accumulated heat from the prior layers can also change the heating and cooling rate of the following deposited layers. The process parameters should be adjusted for each layer to keep a steady deposition and preserve a uniform mechanical property [232]. Furthermore, due to the dearth of characterization tools, the in-situ thermal measurements are available only for the top surface locations where a thermal or photodiode imaging system is focused. Therefore, fast prediction of the thermal cycles and the corresponding mechanical property is urgently required for process parameter optimization and online control, to avoid common defects and ultimately achieve the desirable mechanical properties.

Previous works on thermal cycle prediction of LPF-AM mainly utilize the Finite-Element Method (FEM) or Finite-difference method (FDM) to solve the built heat transfer models. They couple the thermal solutions with the mechanical and kinetic models to estimate the associated microstructural and mechanical properties. Costa et al. [233] built an FEM based thermo-kinetic model to investigate the substrate-size and interlayer-dwell-time effects on the thermal cycles, microstructure and the hardness distribution in the multilayer deposition of AISI 420 tool steel by LPF-AM. In their study, the final hardness of the deposit was predicted by the weighted average hardness of individual phases during the process. Zheng et al. [204,234] calculated the thermal cycle solutions from the thermal model built by the FDM and validated the predicted

* A similar version of this chapter will be submitted for publication as:
Huang Yuze, Mohammad Ansari, Hamed Asgari, Mir Behrad Khamesee, Ehsan Toyserkani. Rapid Prediction of Thermal Cycle and Layer-wise Hardness for Austenitic Stainless Steel 316L Thin-Wall Structure in Laser Directed Energy Deposition (Powder-fed Additive Manufacturing).

cooling rate by using the established relations of secondary dendrite arm spacing (SDAS) in the multi-layer deposition of SS 316L in LPF-AM. The micro-hardness variation in deposit thickness was also estimated based on the Hall-Petch equation. Manvatkar et al. [229] developed an FEM-based heat conduction model to compute the thermal cycles in the thin-wall structure deposition of 316L by LPF-AM. The computed layer-wise cooling rates were then used to predict the SDAS along the deposit's heights, and the corresponding layer-wise hardness distribution was estimated by the Hall-Petch function. They found that the layer-wise SDAS and hardness were under-predicted and over-predicted, respectively. Later, in their extended study [235], they incorporated the heat convection and fluid flow into the thermal model and showed that the difference between the predicted and measured results in cooling rate and SDAS were significantly reduced. The above successful FEM- or FDM-based thermal models can provide estimations of the localized thermal cycles in LPF-AM with great accuracy, but the calculation time is high, and the models cannot be used for in-situ process control.

Analytical thermal models have also been conducted to predict the thermal cycles and the associated microstructural and mechanical properties in LPF-AM. Bontha et al. [200] predicted the thermal cycles and the associated solidification microstructure based on the quasi-steady-state Rosenthal solution in the thin wall structure deposition of LPF-AM. They also compared the quasi-steady-state solution with a nonlinear FEM-based thermal solution that considered the temperature-dependent thermal properties, finding that the Rosenthal solution provided a reasonable estimation for the solidification microstructure in the thin-wall Ti–6Al–4V deposition. However, Andrew et al. [236] argued that the quasi-steady-state Rosenthal solution is insufficient for predicting the cooling rate in thin-wall deposition. They compared the computed cooling rate from the quasi-steady-state Rosenthal solution with the experimental measurements, under various processing parameters in the multi-layer deposition of Fe-Co-1.5V, and found large differences for all cases. In a recent study by Jianyi et al [137], the quasi-steady-state Rosenthal solution was expanded to a transient analytical thermal solution, where the effects of the accumulation heat, the substrate thickness and the built-structure geometry on the thermal cycles were considered. The predicted thermal cycles were validated by the in-situ temperature measurements in the thin-wall Ti-6AL-4V depositions of LPF-AM, and showed a maximum error rate of 27%. The relatively large prediction error here may be induced by ignoring the

feeding powder flow, a fact verified in the research of Yaojian et al. [203], in which the feeding powder strongly influences the thermal fields and the associated microstructure in LPF-AM.

This chapter aims to develop an integrated approach to predicting the localized thermal cycles and layer-based hardness by using the model built in Chapter 5. Special attention is paid to thin-wall structure deposition with SS 316L powder. SS 316L has high corrosion and oxidation resistance and has been widely used with additive manufacturing for broad applications in marine, medical and nuclear industries [237]. Hardness is one of the most-common metrics for the mechanical properties of parts fabricated by LPF-AM, and can typically be measured in a fast and inexpensive way. In addition, the measured hardness data can provide insights into other properties (e.g., yield strength, wear resistance) [238].

8.2. Theory

In multi-layer thin-wall structure deposition, shown in Figure 8-1, the laser starts at time t^s and follows the scanning pattern along the *x*-axis. The built coordinate (*x*, *y*, *z*) is moving together with the laser, and the origin is set as the laser beam center.

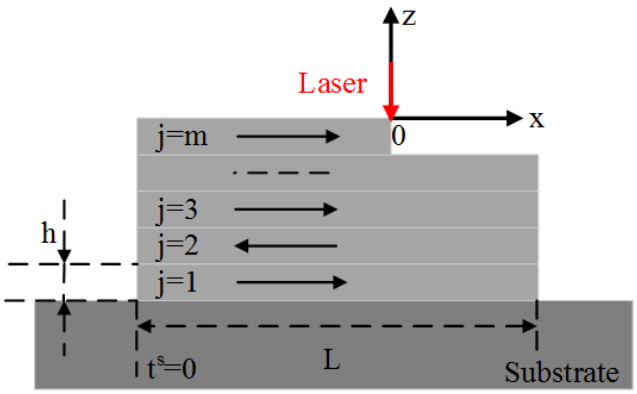

Figure 8-1. Schematic diagram for multi-layer thin wall structure deposition.

Based on the model built in Chapter 5, the cooling rate $\dot{T}$ for $X = (x, y, z)$ of the mth layer at time moment t can be derived as,

$$\dot{T} = \partial T_m(X, \mathrm{t})/\partial t \tag{8-1}$$

The length scale of the solidification microstructure in SS 316L deposits can be represented by dendritic arm spacing (DAS) [204,229]. With the transient cooling rate solution (Equation 8-1), the DAS can be predicted based on the well-tested Kurz and Fisher model [199],

$$\mathrm{DAS} = A\dot{T}^{-B} \tag{8-2}$$

where A and B are material-dependent parameters.

As the previous study [238] argued, no secondary phases or other solid-state transformations happen in austenitic steels, the strength and hardness mainly depend on the solidification scale and the chemical composition. Therefore, the yield strength σ_y may be estimated based on the well-known Hall-Petch relation as [239],

$$\sigma_y = \sigma_0 + k_y\left(d_g\right)^{-1/2} \tag{8-3}$$

where σ_0 and k_y are material constants and d_g is the average grain size.

As the austenitic SS 316L deposited by LPF-AM typically exhibit a fine substructure with primary cells and columnar dendrites, researchers [204,229] have suggested that the grain size d_g shown in Equation (8-3) should be replaced by the finer DAS for strength and hardness prediction. Consequently, the yield strength σ_y should be computed as $\sigma_y = \sigma_0 + k_y(DAS)^{-1/2}$. Then the Vickers hardness (H_V) of the deposits may be predicted as [240],

$$H_V = 3\sigma_y(0.1)^{2-m} \tag{8-4}$$

where m=2.25 is the Meyer exponent of steels [229].

8.3. Materials and experimental procedure

In this study, SS 316L powder (North American Höganäs, NY, USA) in the size range of 45-120 µm was deposited on the sandblasted AISI 1018 steel substrate by the robotic laser powder-fed DMD®-IC106 (DM3D Technology, MI, USA) system. The DMD®-IC106 system (shown in Figure 8-2) includes a disk laser with the maximum power of 2 KW and wavelength 1030 nm and a dual powder feeder that is used to feed the metallic powder through a coaxial nozzle. The laser absorptivity was chosen as 0.4 for SS 316L, which is in line with the reported values in published works [175,206]. The thermo-physical properties of the SS 316L powder are shown in Table 7-1, Chapter 7.

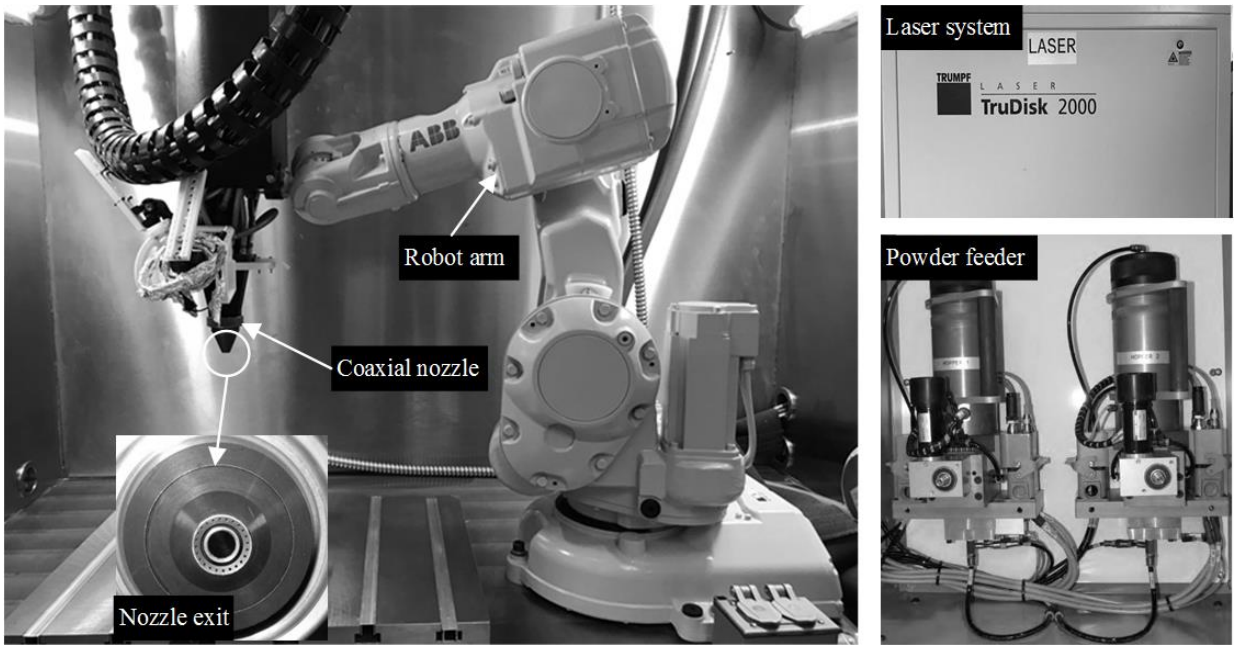

Figure 8-2. Coaxial robot-based LPF-AM equipment

Experiments were conducted for thin-wall structure deposits (shown in Figure 8-3 (a-c)) by following the scanning pattern as illustrated in Figure 8-1. The process parameters are listed in Table 8-1. The samples were cross-sectioned, mounted, polished and etched. All the deposited structures were sectioned at the mid-track length to measure the layer-based micro-hardness and investigate the microstructure by optical and scanning electron microscopy. The micro-hardness were measured at three adjacent midpoints in the length and width directions for each layer as illustrated in Figure 8-3 (c) by the Wilson 402MVD Vickers hardness tester, where a load of 300 gf and a dwelling time of 30 s were set for hardness testing. The associated dendrite arm spacing were measured at the same locations (as illustrated in Figure 8-3 (c)) based on the Hilliard single-circle procedure followed by the ASTM standard [207]. The constants of A and n are taken as 80 and 0.33 [204], respectively. The coefficients, σ_0 and k_y were set as 150.8 and 575 MPA $(\mu m)^{0.5}$ [241], respectively. The calculation of the thermal cycles in this study were conducted in the Matlab® R2017b by a HP® computer with Intel® CoreTM i7-6700 CPU (3.4GHz).

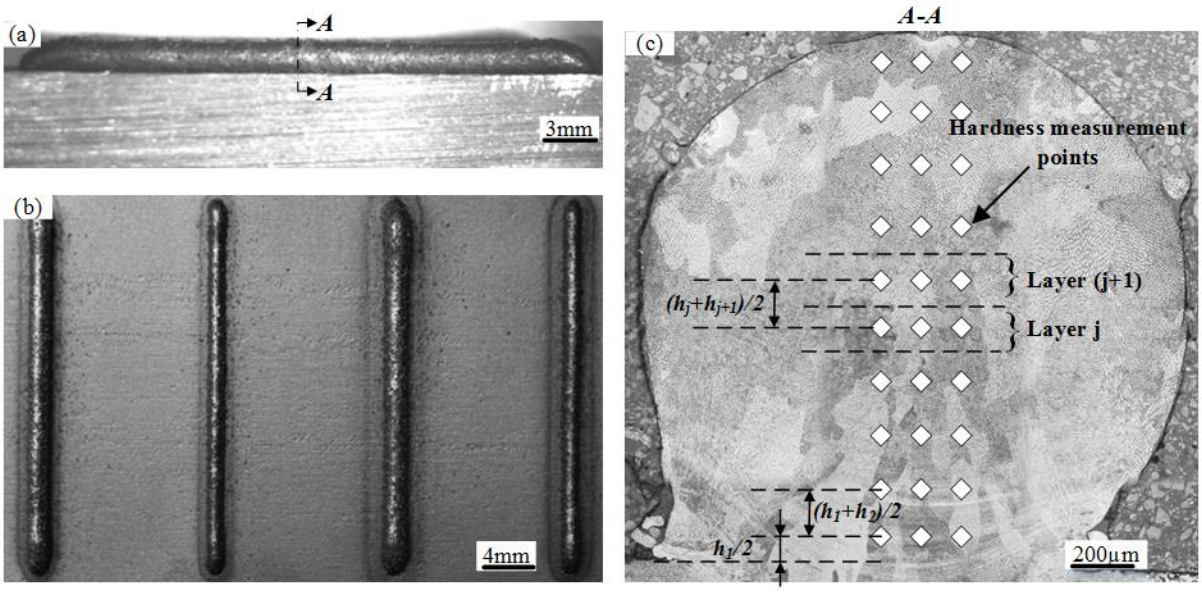

Figure 8-3. SS 316L multi-layers thin-wall deposits (a) Side view, (b) Top view and (c) Mid-length cross-section with locations of hardness indents..

Table 8-1. Process parameters for SS 316L deposition by coaxial LPF-AM

Parameters	Values	Parameters	Values
Scanning speed, [mm/min]	250, 500	Correction factor, μ_M	2.5
Laser power, [W]	600	Ambient temperature, [K]	300
Powder feed rate [g/min]	8.5	Brewster effect coefficient, a_w	0.0196
Laser beam diameter, [mm]	1.4	Laser absorptivity	0.4
Nozzle height, [mm]	20	Track length, [mm]	30
Layer thickness, [mm]	0.2	Powder stream radius, [mm]	4

8.4. Results and discussion

Figure 8-4 shows the calculated temperature variation of the points located at the mid-track length and top surface of different layers in thin-wall structure deposition using LPF-AM. Each cycle peak represents the new heat loading that occurs with each additional layer. As seen in Figure 8-4 (a), the temperature rises immediately as the laser approaches and rapidly as the laser moves away. At the end of the prior layer's deposition, a new layer arrives, and reheats all the prior layers, leading to a rapid thermal cycle revolution.

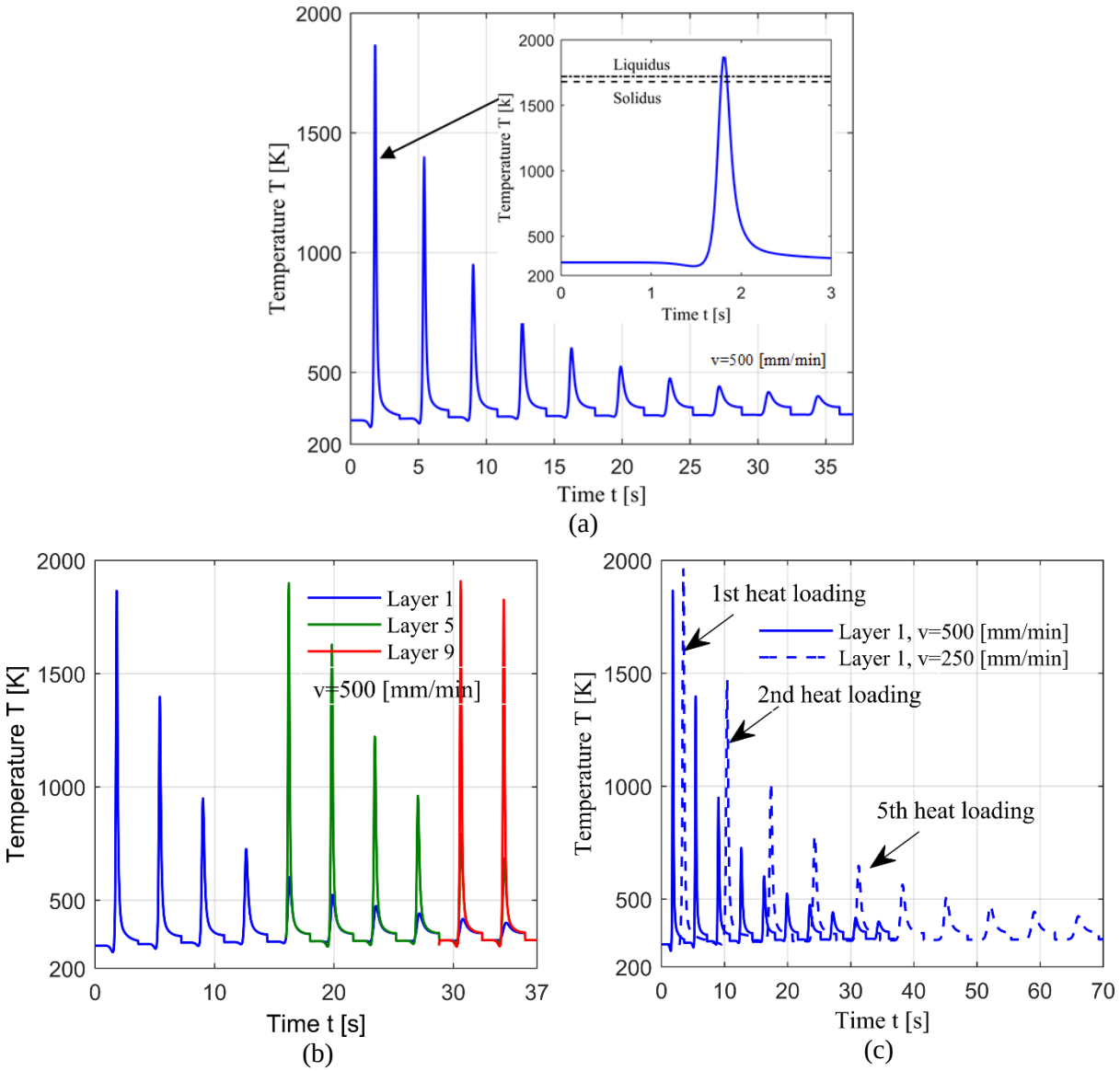

Figure 8-4. Thermal cycles of the points located mid-track length and on the top surface of the (a) first layer, (b) alternate layers 1, 5 and 9 and (c) first layers under different scanning speeds in a ten layers thin-wall deposition of SS 316L by LPF-AM.

In addition, the initial temperature of each following layer increases with an increase in the numbers of deposition layers. This finding may be attributed to the heat accumulation during multi-layer deposition, and has also been reported by previous research [204]. The accumulated heat amount is affected by the processing parameters (e.g., laser power, scanning speed). Similarly, the accumulated heat will also increase the peak temperatures of the following layers, shown in Figure 8-4 (b), where layer 9 has a higher peak temperature than layer 5 or layer 1. As observed from Figure 8-4 (c), the peak temperature of each thermal cycle decreases with an

increase of the laser scanning speed because a smaller amount of laser energy is deposited per unit time under a higher scanning speed. Therefore, the complicated thermal cycle revolution in multi-layer deposition can be predicted by the model built in this research.

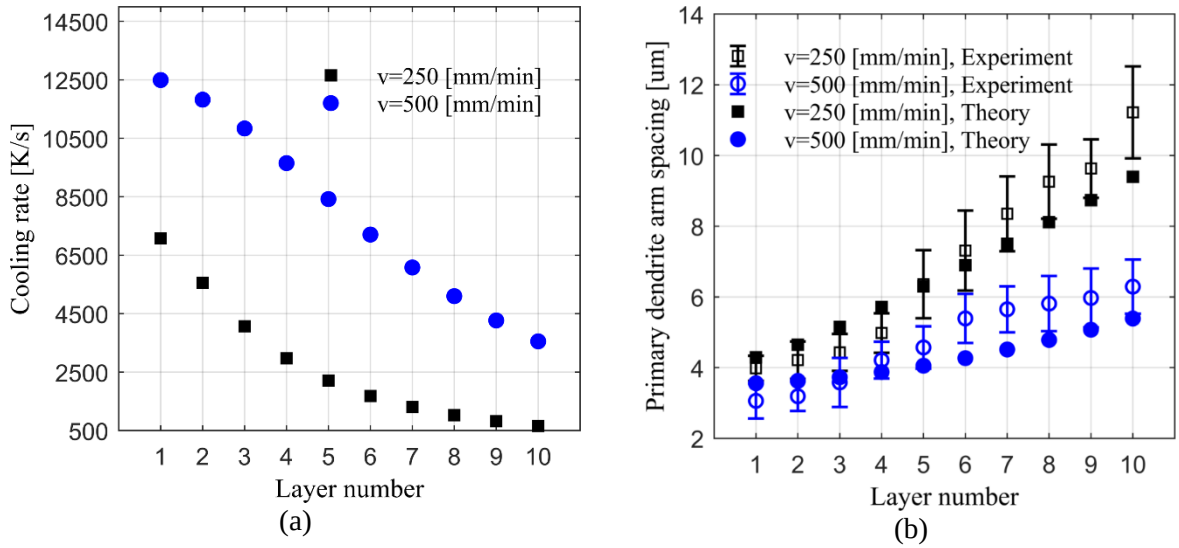

Figure 8-5. Layer-based cooling rate (a) and (b) primary dendrite arm spacing variations with the layer numbers in ten-layer thin-wall structure deposited by LPF-AM.

Subsequently, the cooling rates in the multi-layer deposition were calculated based on the thermal cycle solutions. The layer-based cooling rate was calculated for the locations (Figure 8-3 (c)) used to measure the layer hardness at the time moment ($t = t_{TS}$) of the last solidus temperature for each layer. Moreover, to compensate for the decreasing heat transfer rate of the following layers due to heat accumulation, the layer-based cooling rates were calculated with an increase of heat loading distance. The increased heat loading distance is assumed to be equal to the thickness of the built deposits. As can be seen in Figure 8-5 (a), the predicted layer-based cooling rate declines with an increase of deposition layer numbers, probably caused by the increase of the accumulated heat, which lowers the heat transfer rate in the upper layers. In the multi-layer deposition of the LPF-AM process, as the number of deposited layers increases, the heat transfer is mainly directed through the previously deposited hot layers, rather than the cold substrate, leading to a lower cooling rate. In addition, it can be clearly observed from Figure 8-5 (a) that the cooling rate increases dramatically with an increase of the scanning speed, being consistent with the experimental results in reference [144].

Figure 8-6 further verifies the prediction results as depicted in Figure 8-5 and shows a finer microstructure at the bottom layer than that at the top layer. As seen, the solidification microstructure are primary cells without secondary dendrites, agreeing with the experimental observations in the previous research [204,229].

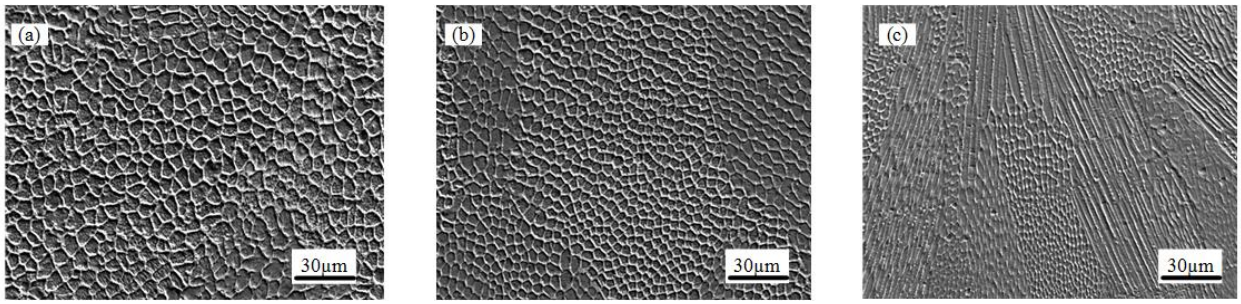

Figure 8-6. SS 316L solidification microstructure in the mid-track length cross-section of (a) top, (b) middle, and (c) bottom layer of ten-layer thin-wall deposit. Scanning speed 250 [mm/min].

As all the SS 316L deposits exhibit a typical cellular microstructure without secondary dendrites as shown in Figure 8-6, the primary dendrite arm spacing (PDAS) was used to represent the solidification microstructure length scale. As can be observed from Figure 8-5 (b), the predicted PDAS agrees well with the experimental measurement for each layer. The PDAS grows with an increase of the layer numbers while shrinks with an increase of the laser scanning speed. The reason may be explained by the fact that the increased residual heat in the upper layers lowers the cooling rate while the increased scanning speed enlarges the cooling rate as shown in Figure 8-5 (a). Accordingly, a higher cooling rate induces a finer solidification microstructure or vise versa [214]. Additionally, the predicted PDAS is gently larger than the associated experiment measurement at the lower layers and is smaller than the measurements at the upper layers. The slight overestimation for the PDAS at the lower layers may be attributed to the ignorance of the rapid heat sink effect of the substrate in the built analytical thermal model. The underestimation of the PDAS at the upper layers may be caused by the over-prediction of the cooling rate. In the built thermal model, the thermal conductivity of the materials are assumed to be temperature-independent, leading to a lower heat conduction rate at the high temperature case. In addition, the heat convention in the melt pool reduces the cooling rate [235], and the heat convection effect is not considered in the thermal model.

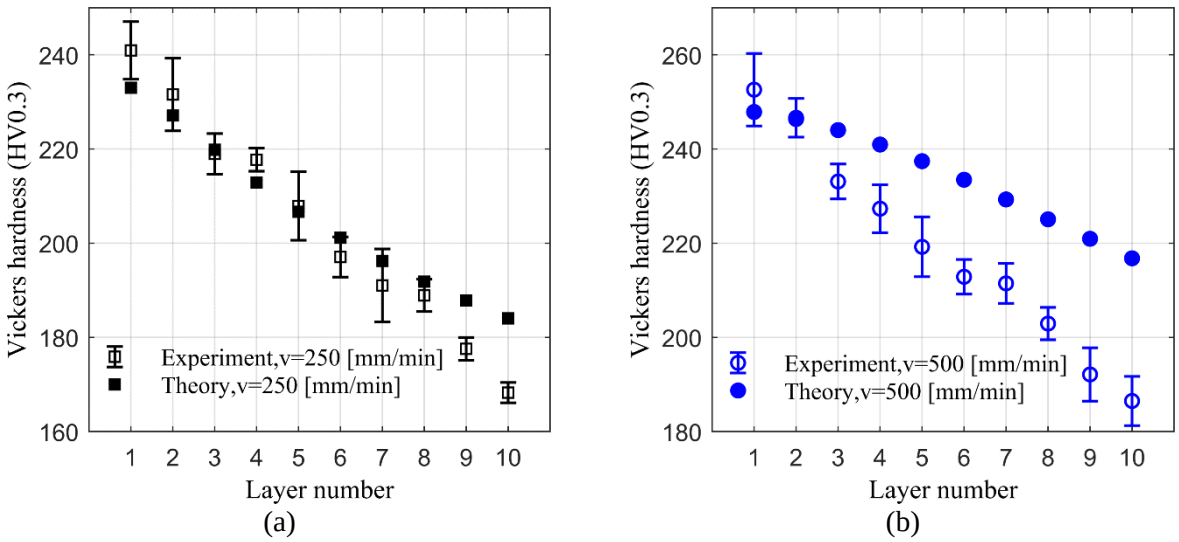

Figure 8-7. Micro-hardness variation with the deposited layer numbers in a ten-layer thin-wall structure SS 316L deposit under (a) 250 [mm/min] scanning speed, (b) 500 [mm/min] scanning speed.

Figure 8-7 shows the predicted and measured micro-hardness for each layer in a ten-layer thin-wall structure deposited by LPF-AM. It can be clearly seen that the calculated micro-hardness is consistent with the experimental measurement under different scanning speeds. For both the lower scanning speed case (Figure 8-7 (a)) and higher scanning speed case (Figure 8-7 (b)), the layer-based micro-hardness decreases with an increase of layer numbers because the accumulated heat increases with the deposition time as the layer number increases. In addition, the heat transfer is directly transferred through the heated deposition layers rather than the substrate. Therefore, the hardness tends to be lower at the upper layers compared to that of the higher layers. Moreover, the calculated micro-hardness is gently smaller than the experimental values at the initial layers and become larger than the experimental results at the upper layers. These differences may be induced by the imprecise cooling rate prediction as discussed above. Another error source for those differences might be the ignorance of the residual stress in the yield strength calculation by Equations (8-3) and (8-4).

8.5. Summary

The localized thermal cycles of multi-layer thin-wall structure deposited by LPF-AM were predicted with the model built in Chapter 5. Subsequently, the layer-based cooling rate and micro-hardness were calculated based on the Kurz and Fisher model and the Hall-Petch relation, respectively. Ten-layer thin-wall SS 316L deposition experiments were conducted under

different laser scanning speeds, and the associated layer-based PDAS and micro-hardness were measured to verify the model.

Below are the summarized findings.

(1) The predicted PDAS matched well with the experimental measurements, verifying the accuracy of the cooling rate calculated by the thermal model. The calculated PDAS was slightly larger than the experimental values at the lower layers and become smaller than the associated measured results at the upper layers. This finding is attributed to the underestimation of the cooling rate at the initial layers with ignoring the rapid heat sink effect of the substrate.

(2) The measured micro-hardness decreases with an increase of the layer numbers because the increasing heat accumulation and the distance from the substrate lower the heat transfer rate, leading to a decreased cooling rate in the upper layers with consequent lower micro-hardness.

(3) The calculated layer-based micro-hardness agreed fairly with the experimental measurements. The calculated micro-hardness values were larger than the experimental values at the upper layers under different scanning speeds, with a maximum prediction error of ~16.2%. The difference is mainly caused by the imprecise cooling rate prediction that occurs with assuming the temperature-independent thermal conductivity and ignoring the heat convection in the melt pool.

(4) The calculation time for the localized cooling rate and layer-based micro-hardness are around $4\,ms$, confirming the potential of this work to be used for in-situ model-based feedback control in the LPF-AM process.

Chapter 9. Application III: Multi-objective Optimization of LPB-AM*

9.1. Introduction

Currently, owing to the dearth of characterization tools, it is extremely hard to measure the in-situ subsurface features (e.g., melt pool depth, subsurface temperature) in the LPB-AM process. The major challenges have been discussed in Section 2.2.2. By utilizing the time-efficient process model of LPB-AM as built in Chapter 6, the real-time localized fabrication characteristics can be predicted with an adequate accuracy. However, the built process model is insufficient for quality prediction (e.g., density, roughness) of the final built parts due to the effect of the unforeseen stochastic physical phenomena (e.g., denudation, spatter) that are difficult to be mathematically modeled.

Therefore, in this chapter, the developed process model was utilized to predict the in-situ build rate in the LPB-AM process. Meanwhile, empirical models were built to predict the density and the surface roughness of the as-built parts by using response surface regression with a Box-Behnken design. Subsequently, the built process model and empirical model were integrated to simultaneously optimize the density, surface roughness and the in-situ build rate by using a multi-objective genetic optimization algorithm.

9.2. Materials and experimental procedure

The same stainless steel (SS) 17-4 PH powder as listed in Section 6.3.1 was utilized to run the experiments on the EOS M290 additive manufacturing machine. 3D cuboid samples ($6\,mm \times 6\,mm \times 40\,mm$) with multi-layer multi-track scanning were fabricated as shown in Figure 9-1. Same scanning pattern as illustrated in Figure 6-5 was applied for the 3D cuboid samples fabrication with stripe width (3 mm) and stripe overlap (50 μm).

---

* A similar version of this chapter will be submitted for publication as:
Huang Yuze, Hamed Asgari, Zhang Zhidong, Mohammad Ansari, Mir Behrad Khamesee, Ehsan Toyserkani. Process Modeling and Optimization of Laser Powder-bed Fusion Additive Manufacturing: Formulation, Verification and Multi-Objective Optimization.

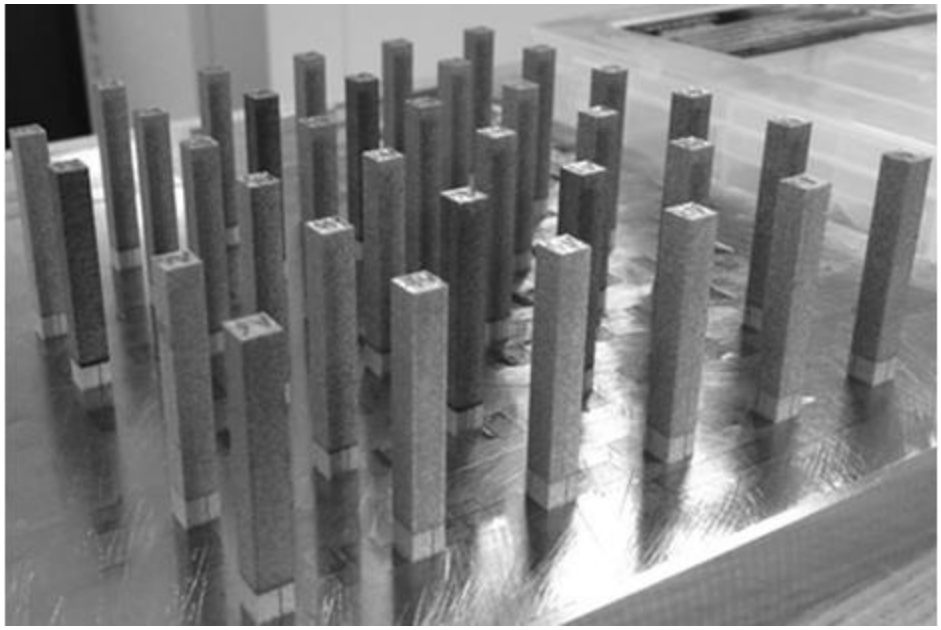

Figure 9-1. Images of the LPB-AM printed cuboid samples

9.2.1. Design of experiments (DOE)

The Design-Expert® Software Version 11 (Stat-Ease Inc., Minneapolis, USA) was employed to plan the multi-layer multi-track scanning experiments using the response surface methodology (RSM) [242] with a Box-Behnken design [243]. Three different levels of laser power, scanning speed and hatch space were selected for the Box-Behnken design with five center points, as presented in Table 9-1. These parameter levels were selected with a scaling normalized enthalpy range $(24{\sim}33)$ to keep a stable melting regime based on the single-track results. The layer thickness was fixed at $40\ \mu m$. Subsequently, a quadratic regression model and a two-factor interaction (2FI) regression model were built for relative density and the surface roughness by using response surface regression, respectively. In addition, analysis of variance (ANOVA) was used to identify the significant parameters and their associated significant interactions.

Table 9-1. Processing parameters for the Box-Behnken design and the associated measured surface roughness and relative density.

Run	Laser power [W]	Scanning speed [mm/min]	Hatch space [µm]	Roughness, Sa [µm]	Relative density, ρ_r [%]
1	175	700	100	8.800	95.8
2	175	800	110	16.200	96.3
3	215	900	100	10.850	99.2
4	195	800	100	10.185	98.5
5	195	800	100	10.075	98.8
6	195	700	90	7.025	97.5
7	195	900	90	11.873	97.2
8	195	900	110	14.155	96.4
9	215	800	90	9.090	99.9
10	215	700	100	8.610	97.9
11	195	800	100	11.290	98.6
12	175	900	100	14.015	95.6
13	195	700	110	8.270	95.4
14	195	800	100	9.745	98.6
15	175	800	90	8.215	98.0
16	195	800	100	8.580	98.4
17	215	800	110	8.250	99.1

9.2.2. Sample characterization

The density of the as-built cuboid samples were measured according to the ASTM B311-17 standard method [244]. In addition, the porosity of the cuboid samples were also checked by X-ray computed tomography (XCT) technique using a ZEISS Xradia 520 Versa 3D X-ray microscope at a resolution (voxel size) of 13 µm.

As can be seen in Figure 9-2 (a, b), the as-built samples by LPB-AM have a significant anisotropic surface topography. Therefore, instead of using the two-dimensional center-line average roughness R_a, the three-dimension (3D) surface roughness S_a were utilized to represent the surface finish. The top surface roughness of the cuboid samples was measured by a laser microscope VK-X250K (Keyence, Itasca, USA). For each sample, three different areas with dimensions of $500\ \mu m \times 700\ \mu m$ were scanned for surface roughness (S_a) measurement. The averaged measurement results of sample density and top surface roughness are utilized to build the empirical model and were listed in Table 9-1.

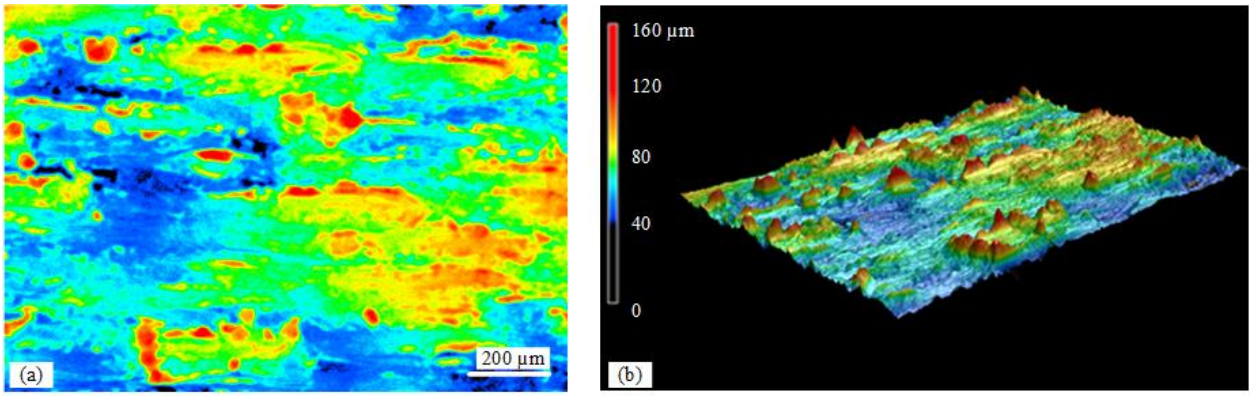

Figure 9-2. Top surface image of the cuboid sample with anisotropic surface topography. (a) 2D image. (b) 3D image. Laser power 175 W, scanning speed 700 mm/s, layer thickness 40 µm, hatch space 100 µm.

9.3. Multi-Objective Optimization

The real-time build rate B_R may be defined as the volume of effective solidification of the powder material per second (mm^3/s),

$$B_R = v \times w_p \times d_p \tag{9-1}$$

For the in-situ melt pool dimensions (melt pool width w_p, melt pool depth d_p) in the multi-track and multi-layer scanning, as listed in Equation (9-1), the averaged values of first five tracks at the middle-stripe width position are applied. This could be calculated based on the built analytical model in Chapter 6.

The density and the top surface roughness of the final part were empirically modeled by using response surface regression with a Box-Behnken design. The associated ANOVA results for the relative density and surface roughness are presented in Tables D-1 and D-2 (Appendix G),

respectively. In the ANOVA results, the capital letters A, B and C represent laser power, scanning speed and hatch distance, respectively. As seen from Tables D-1 and D-2, the Model F-values are relatively large that imply the both built models are significant. In particular, the chance of occurrence for these large F-values caused by noise is only 0.01%. In addition, the Lack of Fit F-values are relatively small that indicate the Lack of Fit are not significant compared to the pure error in both built models. The predicted values of R^2 are in reasonable agreement with the associated adjusted values of R^2, with a difference less than 0.2 for the both built models. The large values of adequacy precisions (larger than 4) show desirable adequate signals for both the built models.

Moreover, based on the calculated P-values (the model terms are significant when P-values are less than 0.05 (95% confidence level)), it can be derived that the significant parameters and their associated interactions are A, B, C, AB, BC, B^2, C^2 and A, B, C, AC for the relative density and surface roughness, respectively. According to the computed F-values, the predominant factor for relative density is laser power (A), followed by the square of scanning speed (B^2), hatch space (C), interaction of laser power and scanning speed (AB), square of hatch space (C^2), interaction of scanning speed and hatch space (BC) and scanning speed (B). By contrast, the most influential factor for the surface roughness is scanning speed (B), followed by the interaction of laser power and hatch space (AC), hatch space (C) and laser power (A).

Correspondingly, the final regression equations for the relative density and surface roughness are expressed as:

$$\begin{aligned}\rho_r = {} & 0.400344 - 0.00308P + 0.00184v + 2.22849h_s + 1.92392 \times 10^{-6}Pv \\ & + 0.010096Ph_s + 0.003155vh_s + 3.02637 \times 10^{-6}P^2 \\ & - 1.56774 \times 10^{-6}v^2 - 37.03461h_s^2\end{aligned} \tag{9-2}$$

and

$$\begin{aligned}S_a = {} & -260.83171 + 1.33544P + 0.069247v + 2076.53125h_s \\ & - 0.000372Pv - 11.03125Ph_s + 0.26vh_s\end{aligned} \tag{9-3}$$

respectively. It should be emphasized that the achieved empirical models for relative density and surface roughness are only valid within the investigated stable melting regimes. In other words,

the unstable balling and humping regions are not considered as those unstable regimes could be easily tailored based on the normalized enthalpy values in the experimental design stage.

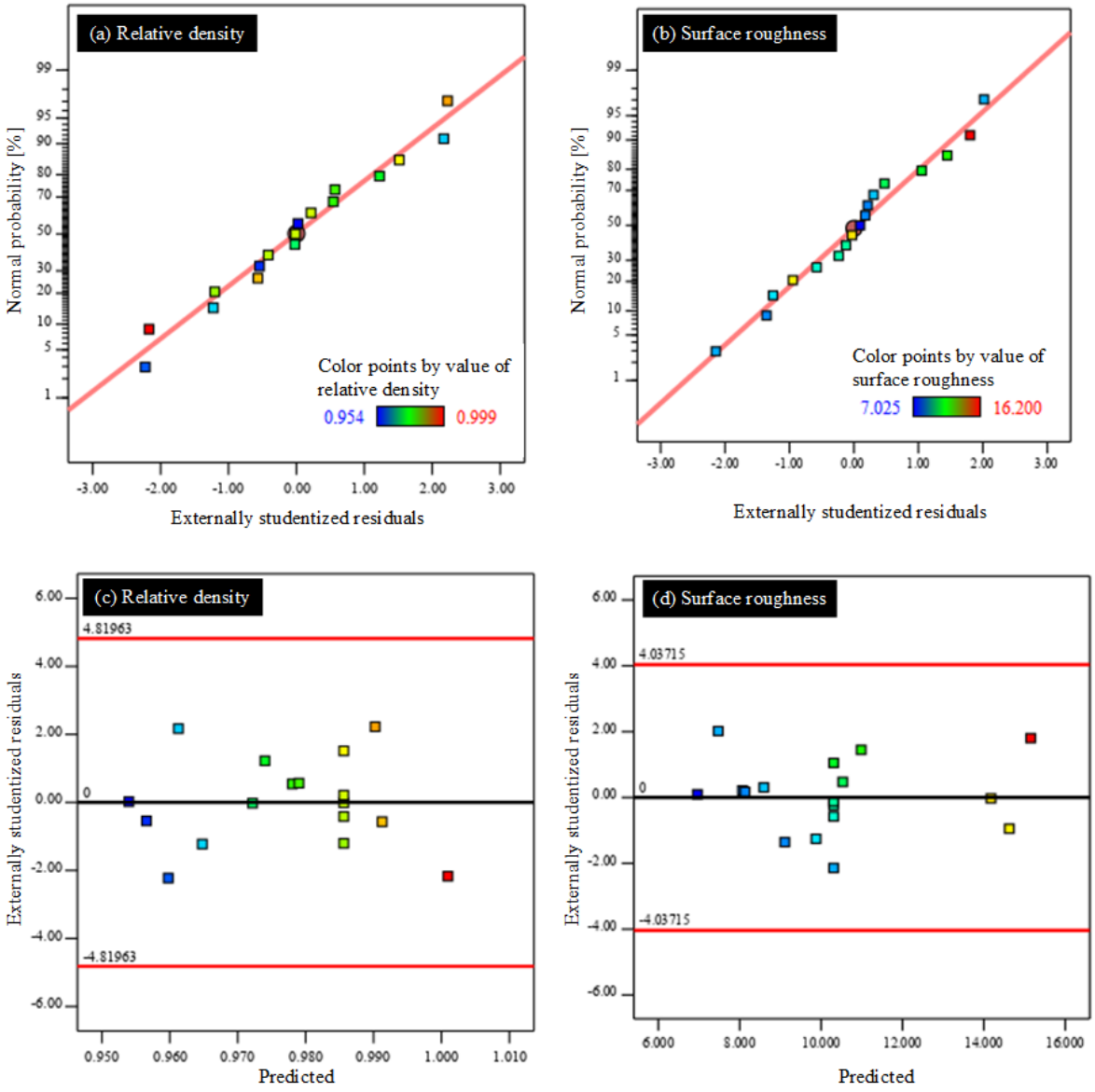

Figure 9-3. Diagnostics plots for externally studentized residuals. Normal probability plot for (a) relative density (b) surface roughness. Residuals versus the predicted response values for (c) relative density (d) surface roughness.

To check the adequacy of the built empirical models, the studentized residuals were calculated and analyzed. As shown in Figure 9-3 (a) and (b), the normal probability plot of the residuals follows a straight line for both of the relative density and surface roughness models, indicating the residuals of both models follow the normal distribution. In addition, Figure 9-3 (b) and (d)

show the plot of residuals over the ascending predicted response values for the relative density and roughness, respectively. As seen, the plots are random scatters that indicates the size of residuals are independent of the size of the predicted values. This further confirms the constant variance assumption are valid in the built models.

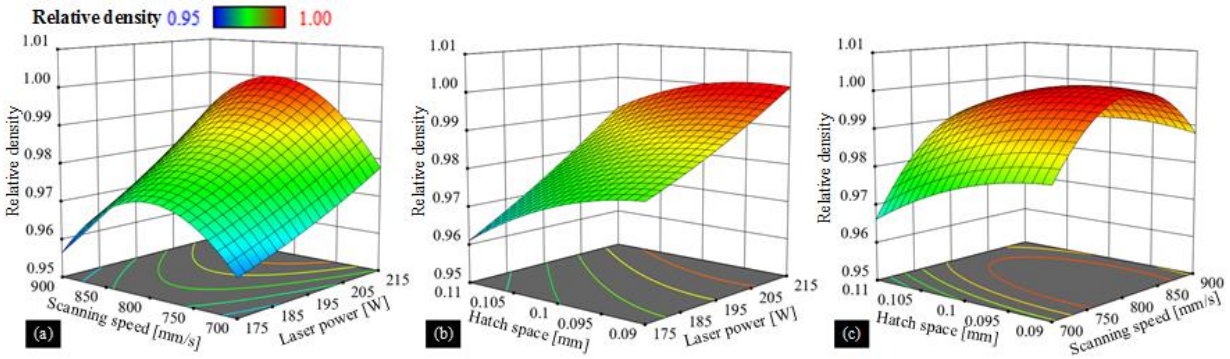

Figure 9-4. Three dimensional surface plots for relative density. (a) Hatch space 0.1 [mm]. (b) Scanning speed 800 [mm/s]. (c) Laser power 215 [W].

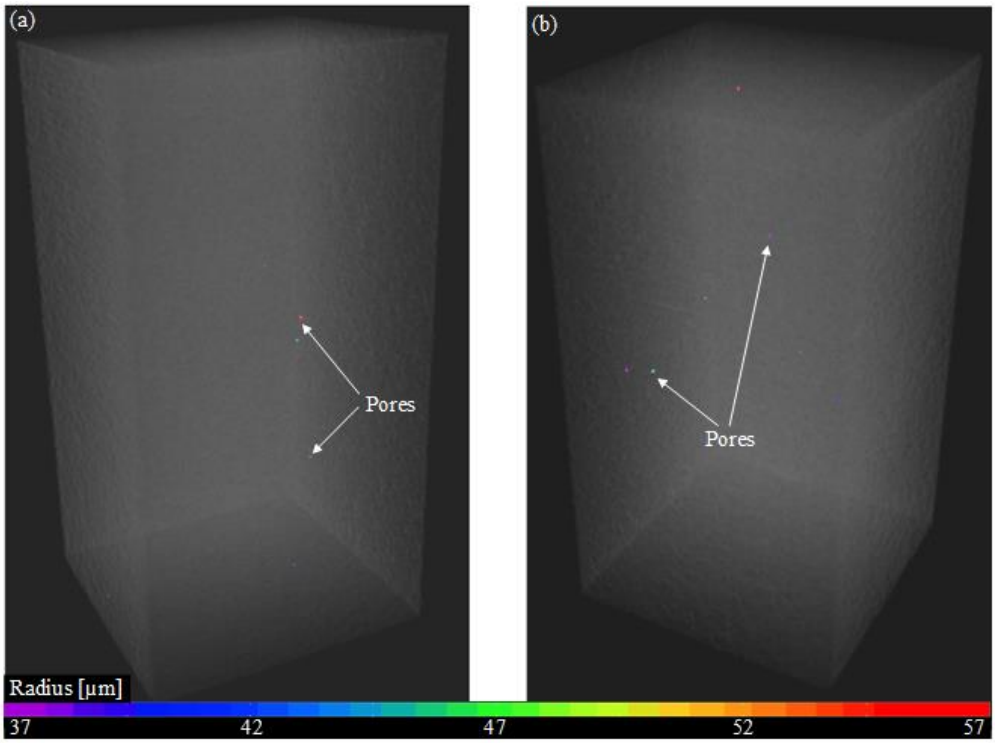

Figure 9-5. 3D visualization of the porosities in the fabricated cuboid samples. (a) Laser power 215 W, scanning speed 800 mm/s, hatch space 0.09 mm, normalized scaling enthalpy 31.28. (b) Laser power 215 W, scanning speed 900 mm/s, hatch space 0.1 mm. normalized scaling enthalpy 29.49. The pores are labeled by the radius of the spheres shown in the 3D images.

Figure 9-4 (a-c) show the 3D response surface plots for the relative density. It can be observed that the relative density of the fabricated cuboid sample varies with a non-linear combinations of the laser power, scanning speed and hatch space. This phenomenon was also reported by Luis *et al.* [88] in the Inconel 625 powder material fabrication by LPB-AM. In addition, it can be found that the large values of relative densities are obtained at the combinations of high laser power, large scanning speed and small hatch space. This conclusion is further verified by the CT scanning results, as shown in the Figure 9-5. As observed, very limited pores can be detected in the samples under the above combinations.

Moreover, with keeping a high laser power (215 W) and a small hatch space (0.09 mm), as shown in Figure 9-4 (c), the relative density increases at first then decreases with the increase in the scanning speed. The variation pattern of the density may be related to the change of the normalized enthalpy, which is initially at a quite large value under the relatively low scanning speed. This may lead to severe evaporation and recoil pressure, resulting in destabilization of the melt flow and increase in porosity level [245]. With increasing in scanning speed, the normalized enthalpy decreases and a melting regime with high stability is achieved. However, when the scanning speed increases to a relatively high value, the normalized enthalpy reaches a low level and the melt pool size significantly decreases, as shown in Figure 6-17 and Figure 6-18. This may result in low bonding and small overlapping rate among the neighboring scanning vectors, which in turn, encourages the formation of pores or voids between tracks/layers [162]. Similar trends for the variation of the normalized enthalpy were also reported by King *et al.* [161] and Khairallah *et al.* [162] in the LPB-AM process. They concluded that the unstable melting regime would be achieved when the normalized enthalpy was too high or too low compared to the threshold of the keyhole regime under a medium normalized enthalpy. To be more specific, insufficient melting is induced under the too low normalized enthalpy case. However, pores or voids are generated under the too high normalized enthalpy case.

Figure 9-6 (a-c) show the 3D response surface plots for the top surface roughness. The non-linear relationships are obviously noticeable for the interaction effect of laser power and hatch space on the surface roughness. The interaction effects, however, for both the laser power-scanning speed and scanning speed-hatch space are almost linear. Figure 9-6 (a) depicts that the surface roughness increases significantly with an increase in the scanning speed but decreases gently

with the increase in the laser power. According to the research conducted by Mumtaz and Hopkinson [246], lower scanning speed leaves more time for the melt pool to be flattened by the resultant force of gravity, surface curvature and external shear force before completion of solidification process. Therefore, the top surface roughness is subsequently reduced under low scanning speed. In addition, increasing the laser power under stable keyhole regime may enhance the recoil pressure. This can further flatten the melt pool and increase the top surface quality, as reported by Mahmoud *et al.* [247]. As observed in the Figure 9-6 (a) and (b), smaller hatch space induces lower surface roughness. This is consistent with the previous observation of Mahmoud *et al.* [247], in which decreasing the hatch space was shown to improve the overlap between the neighboring tracks and boost the wettability of the melt pool, resulting in better surface quality. Moreover, it can be seen in Figure 9-6 (b) that the effect of laser power on the surface roughness becomes more considerable under large hatch space, which may be explained by the same neighboring track connection theory due to the hatch space.

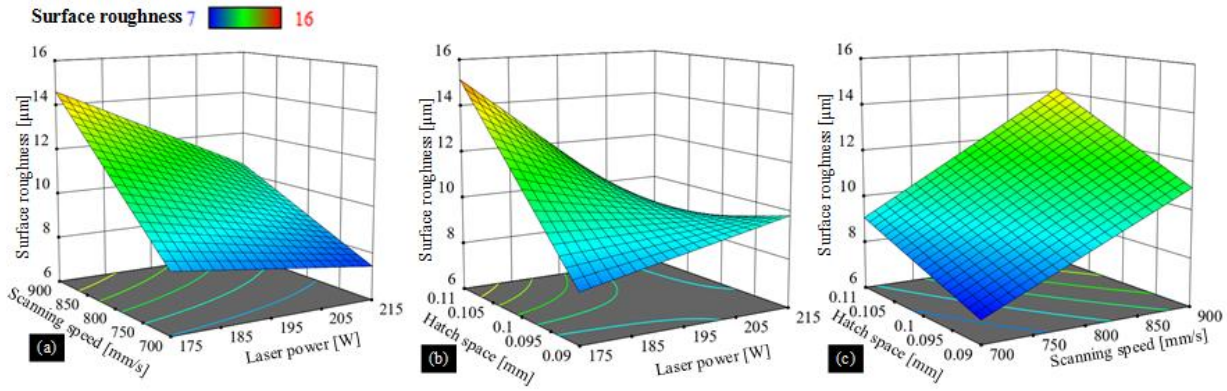

Figure 9-6. Three dimensional surface plots for top surface roughness. (a) Hatch space 0.1 [mm]. (b) Scanning speed 800 [mm/s]. (c) Laser power 195 [W].

High relative density is achieved at a specific normalized enthalpy under the combinations of high laser power, relatively large scanning speed and small hatch space. However, the low surface roughness is obtained under the small scanning speed. Moreover, the maximum real-time build rate is reached at the largest normalized scaling enthalpy with highest melt pool dimension (depth and width), as shown in Figure 6-18. These objectives are conflicting with each other and the selection of the optimized process parameters cannot be easily performed with only fulfilling one objective. Therefore, a multi-objective optimization is conducted to simultaneously optimize these objects. This is done by integrating the physically-based analytical model (solution for the

in-situ build rate) and the statistically-driven empirical models (surface regression models of relative density and surface roughness) under the steady melting regimes with the following parameter constrains:

$$Minimize\{-\rho_r\ (P, v, h_s), S_a\ (P, v, h_s), -B_R\ (P, v, h_s)\ \};$$

$$175 \le P \le 215\ \text{W};\ 700 \le v \le 900 \frac{mm}{s};\qquad (9\text{-}4)$$

$$90 \le h_s \le 110\ \mu m;\ w_s = 3\ mm;\ h_t = 40\ \mu m$$

The multi-objective optimization is solved by using the gamultiobj function in Matlab based on the controlled genetic algorithm (a variant of Non-dominated Sorting Genetic Algorithm-II [248]) to find the minima of the multi-functions defined in Equation (9-4). The solver parameters of the gamultiobj function are listed in Table E-1, Appendix H.

Figure 9-7 (a) and Figure 9-7 (b, c, d) present a set of optimal solutions in the 3D Pareto front with regarding to the objectives, namely maximum density, minimum surface roughness and maximum build rate, and corresponding decision variables, i.e. processing parameters, respectively. It can be seen in Figure 9-7 (a) that some solutions which achieve the small surface roughness objective may result in low build rate and small density. Depending on the objective priority, the optimized parameter solution set can be chosen based on Figure 9-7 (b, c, d). As observed, the maximum density and build rate can be achieved at a combination of parameters with high laser power, medium scanning speed and medium hatch space. By contrast, the minimum surface roughness may be obtained by a combination of low scanning speed, small laser power and small hatch space.

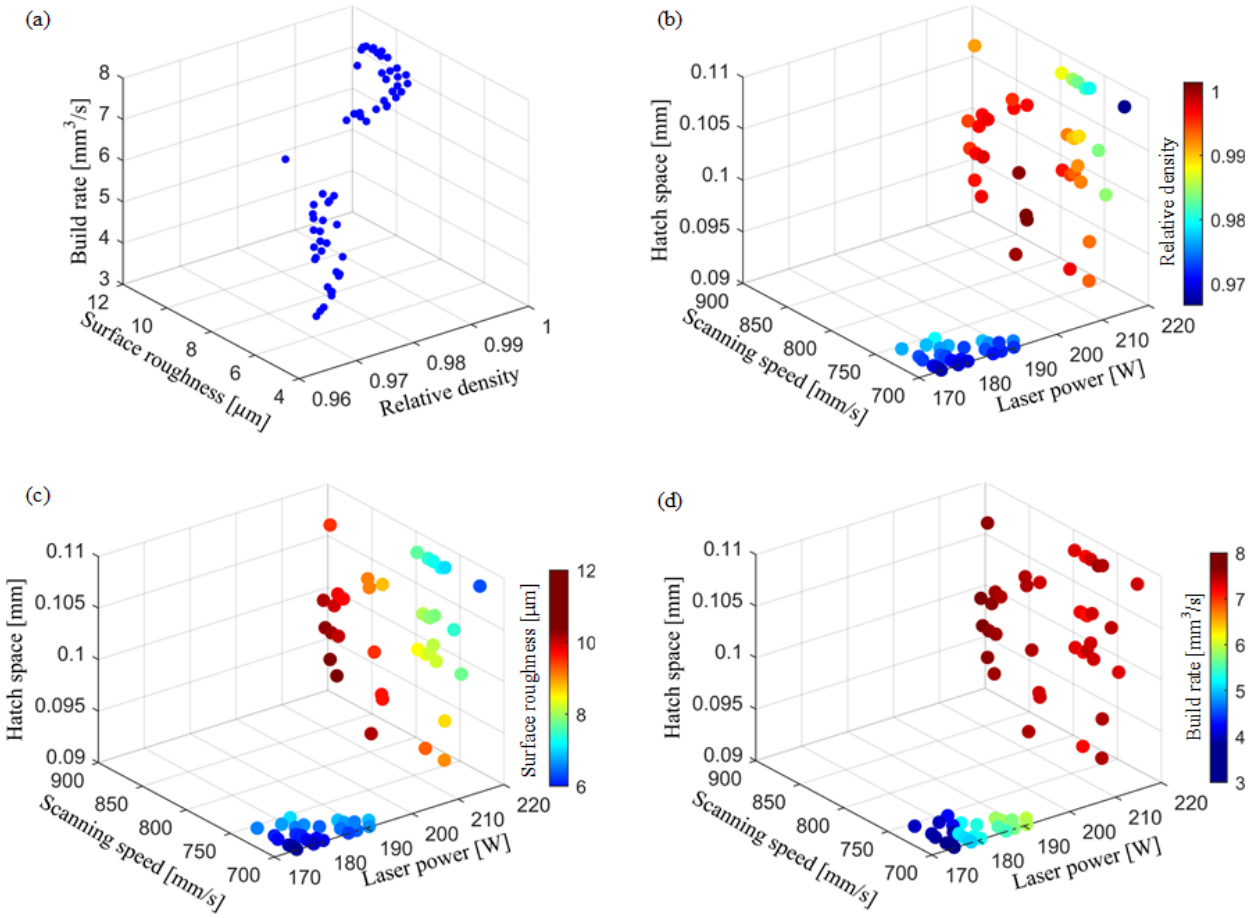

Figure 9-7. Multi-objective optimization solutions for maximum density, minimum surface roughness and maximum build rate. (a) 3D Pareto front with the objective items. (b) 3D Pareto front with the decision variables mapping by relative density. (c) 3D Pareto front with the decision variables mapping by surface roughness. (d) 3D Pareto front with the decision variables mapping by build rate.

9.4. Summary

Reducing the building time while maintaining the fabrication quality is vital to broaden the industrial application of LPB-AM. By utilizing the time-efficient process model as built in Chapter 6, this chapter achieves the simultaneously optimization for minimizing surface roughness, maximizing the part's density and maximizing the real-time build rate.

The multi-objective optimization shows that the maximum density and build rate can be achieved at a parameters combination of high laser power, medium scanning speed and medium hatch space. By contrast, the minimum surface roughness can be obtained under the parameters combination with low scanning speed, small laser power and small hatch space. In addition, the

optimized parameter solution set can be chosen based on the built 3D Pareto fronts depending on the objective priority.

Chapter 10. Conclusions and Future Work

The major objective of this thesis has been to develop time-efficient, simple yet reasonably accurate process models for both LPF-AM and LPB-AM. The models were expected to incorporate the most critical physics in the process, be capable of time-efficient process optimization, and potentially be employable for in-situ process control. Another goal was to explore a non-contact magnetic focusing approach to concentrating the diverging particles in the LPF-AM process. To this end, accelerated models for both LPF-AM and LPB-AM were built. In addition, a magnetic concentration approach was explored with three innovative configurations, all theoretically tested. This chapter summarizes the overall conclusions and findings in the thesis, and accordingly, proposes possible future-research directions.

10.1. Summary of Conclusions and Findings

Time-efficient process models of both LPF-AM and LPB-AM were built by a comprehensive analytical approach in the thesis. In the process modeling of LPF-AM, most of the relevant physics were considered: the interaction physics of the laser beam, powder stream and substrate, the wetting behavior of the liquid melt pool, the accumulated heat in the deposition process and the dynamic overlapping profile of the multi-track scanning were considered. Correspondingly, a heat and mass coupling comprehensive model of the LPF-AM process was achieved. The built model was verified experimentally with both a metal alloy material of Inconel 625 and pure iron under a wide range of process parameters. The model was also applied to predict the localized-transient thermal, sub-structural and mechanical features of the as-built deposits. Similarly, for the process modeling of LPB-AM, the critical physics i.e., the randomly packed powder bed, heat source penetration, melting regime, heat accumulation and volume shrinkage were taken into consideration. Experiments with metallic SS 17-4PH powder validated the built model. Furthermore, the model was employed for a multi-objective optimization of the LPB-AM process.

A novel magnetic concentration approach was proposed with three innovative configurations for the concentration design, namely, the doublet-Halbach-PMQs, doublet- EMQs and linear-Halbach-PM. These different designs were theoretically tested with the built mathematical model. A linear-Halbach-PM setup was fabricated with Neodymium magnets N52 to build a strong

permanent magnet source. Experiments were also conducted with large-sized pure aluminum particles under the built linear-Halbach-PM setup.

According to the built models and the associated experimental results, major conclusions and findings can be summarized as:

1. A new module that analytically couples the laser heat flux and the powder mass flow was developed for LPF-AM. Important physics i.e., the attenuated laser intensity distribution, the heated powder spatial distribution and the melt pool 3D shape with its boundary variation were taken into consideration. Experimental depositions of Inconel 625 powder prove the high accuracy of the built module in clad geometry prediction (a maximum percentage difference of ~6.2% for clad width, ~7.8% for clad height).

2. A powder catchment module of LPF-AM was built considering the variation of 3D melt pool shape and powder stream spatial distribution. Experimental depositions of Inconel 625 show a prediction error of less than ~6.8%.

3. A novel magnetic concentration approach was explored for non-ferrous metallic particle focusing in the gas-powder stream of LPF-AM with various configurations. A one-pole linear-Halbach-PM array was fabricated with Neodymium magnets N52 to test the proposed PM-configuration. The other proposed configurations were theoretically tested. It was found that the proposed doublet-EMQs concentration with high frequency may be capable of concentrating particles with a radius $r_p \geq 150\,\mu m$. Whilst this study did not confirm the concentration effect for the realistic powder stream, it did partially substantiate the focusing effect of the proposed approach for single particle focusing.

4. With the built laser heat flux and powder mass flow coupled module, a comprehensive fast model of the LPF-AM process was developed. The single-track experimental measurements (clad height, clad width, dilution and wetting angle) show that the prediction error of the built model is less than ~14%. The multi-track multi-layer measurements also indicate that the model can perform high-accuracy dimension prediction of the built features.

5. Among the LPF-AM critical process parameters (i.e., laser power, scanning speed, powder feed rate, laser absorptivity, density, thermal conductivity and specific energy), the powder feed rate was found to have the largest positive effect on the clad height based on the sensitivity analysis, followed by laser absorptivity and laser power. By contrast, the process speed was found to have the largest negative effect on the clad height.

6. The built comprehensive model of LPF-AM was successfully used for the real-time thermal characteristics, solidification parameters, and the corresponding microstructure prediction. The calculated real-time peak temperatures of the melt pool matched well with the experimental results under the SS 316L powder deposition. The predicted microstructure variations were in good agreement with the experimental observations for both SS 316L and Inconel 625 deposits at different locations of the deposited tracks made at various scanning speeds. When the developed model was applied for layer-wise hardness prediction, the calculated micro-hardness corresponded well with the experimental results, with a maximum prediction error of 16.2%.

7. The porosity of a randomly packed powder bed in the LPB-AM process can be calculated from the built stochastic rain model with high accuracy. The predicted powder bed porosity was consistent with the experimental measurements with a 3.1% error percentage.

8. Under both single-track and multi-track scanning of SS 17-4PH powder in the LPB-AM process, the thresholds for the melting regime transitions from the heat conduction mode to the transition mode and the transition mode to the keyhole mode can be identified with the normalized enthalpies $\Delta H/h_s = 24$ and $\Delta H/h_s = 28$, respectively. Furthermore, the heat accumulation effect on the melting mode was insignificant during multi-track scanning.

9. A time-efficient process model of LPB-AM was developed by a comprehensive analytical approach. Experiments with SS17-4PH powder were conducted to verify the model. Under single-track scanning, the predicted melt pool dimensions show a high accuracy compared to the experimental measurements under a steady melting regime, with a maximum ~14% error for width prediction and ~15% error for depth calculation. Under multi-track scanning, most

of the predicted dimensions fall within the error bar of the corresponding experimental measurements, leading to a maximum error difference of ~12 % for melt pool width and ~11 % for melt pool depth.

10. The developed model of LPB-AM was successfully used for multi-objective optimization when combined with the part-scale density and surface roughness empirical models under the genetic optimization algorithm. The largest contribution here is that the optimized parameter solution set was provided with built 3D Pareto fronts. Accordingly, a variant optimized parameter set could be chosen based on the objective priority in the LPB-AM process.

11. The simulations were run on a HP® computer with an Intel® CoreTM i7-6700 CPU (3.4GHz). The calculation code was programmed by Matlab® R2017b. The integral calculation tolerance was set to $TOL_{Int} = 10^{-3}$ and the drop out temperature rise tolerance was set as $TOL_{dT} = 10^{-3}\ K$. The calculation time for the localized-transient characteristics in LPF-AM was around 4 ms, whereas the calculation time for the thermal solution of single point in LPB-AM was around 1.2 ms. These rapid computational rates of the built models are at least three times faster than those of the conventional models, confirming the capability of the built models for fast process optimization. Notwithstanding that the calculation rate of the built LPB-AM model has not fulfilled the response pace requirement (0.1 ms [20] for LPB-AM) in the in-situ thermal feedback control, this work offers valuable insights into fast and high-fidelity process modeling. Moreover, the calculation rate of the built models may be significantly improved through advanced programming language or high-performance computers.

10.2. Future Work

A natural progression of this work is to realize the utilization of the built models in online feedback control of LPF-AM and LPB-AM. Considerably more work (e.g., temperature-dependent thermo-physical properties, arbitrary-shaped domains simulation) will need to be done to fulfill this implementation. In addition, studies need to be carried out on advanced magnetic source, particle interactions, and dynamic profiles of the powder stream to expand and validate the realistic application of the proposed magnetic concentration generator.

10.2.1. Modeling of LPF-AM and LPB-AM

1. The assumption of the temperature-independent thermo-physical properties of powder materials is one of the major error sources in process modeling of both LPF-AM and LPB-AM. Instead of using averaged thermo-physical properties, temperature-varying thermo-physical properties should be incorporated into the built models to increase the fidelity of the built models.

2. Although the built models (Chapter 5 and Chapter 6) in this thesis have been extended from single-track to multi-track multi-layer simulations, they are limited to orthogonal domain simulation. As a result, model enhancement for arbitrary-shaped domains simulation is highly needed.

3. The computation time for the built accelerated model of LPB-AM (Chapter 6) does not currently fulfill the requirement for short response time of thermal feedback control system in the LPB-AM process. Further model acceleration with advanced programming language (C++) or techniques (e.g., paralleling coding) should be conducted.

4. The built models have been experimentally verified through lateral, coaxial LPF-AM deposition systems and EOS LPB-AM systems with various powder materials; those include alloy materials of Inconel 625, SS 316L, SS 17-4PH and pure iron material. More diverse AM systems should be employed for further model verification. Likewise, model verification should be sought under a larger number of powder materials.

5. While the calculation rate of the built LPF-AM model fulfills the response pace requirement ($100\ ms$ [19] for LPF-AM) of the thermal feedback control systems in LPF-AM, the built model is limited for single-material deposition only. Fast process modeling of LPF-AM with multi-material deposition for functionally graded materials (FGM) parts would be a fruitful area for further work.

10.2.2. Magnetic concentration generator for particle concentration

1. Although the theoretical calculations show that the proposed doublet- EMQs concentration generator is capable of focusing small-sized particles, magnetic sources with extremely high frequency are required. This high field frequency demand is truly challengeable for the conventional electromagnetic source. As a result, new magnetic sources (e.g., superconducting magnet) with high field frequency are urgently needed for further exploration.

2. The research of the thesis only theoretically tested the concentration effect for the spherical-shaped particles. More broadly, research is also needed to test particles with other irregular shapes.

3. Further research needs to be conducted on particle interaction effect (e.g., particle collision) and drag force effect to achieve the simulation of the powder stream dynamic profile with a higher accuracy.

4. The present research is applicable for electrical conducting metallic particles only. To expand the application of the proposed concentration generator for non-conducting particles, the charged particle technique should be explored and incorporated into the proposed concentration generator.

Letter of Copyright Permission

Home | Account Info | Help

Title:	A comprehensive analytical model for laser powder-fed additive manufacturing
Author:	Yuze Huang,Mir Behrad Khamesee,Ehsan Toyserkani
Publication:	Additive Manufacturing
Publisher:	Elsevier
Date:	October 2016

Logged in as:
Yuze Huang
Account #:
3001402902
LOGOUT

Please note that, as the author of this Elsevier article, you retain the right to include it in a thesis or dissertation, provided it is not published commercially. Permission is not required, but please ensure that you reference the journal as the original source. For more information on this and on your other retained rights, please visit: https://www.elsevier.com/about/our-business/policies/copyright#Author-rights

BACK | CLOSE WINDOW

SPRINGER NATURE LICENSE TERMS AND CONDITIONS

Feb 11, 2019

This Agreement between Yuze Huang ("You") and Springer Nature ("Springer Nature") consists of your license details and the terms and conditions provided by Springer Nature and Copyright Clearance Center.

License Number	4525911154054
License date	Feb 11, 2019
Licensed Content Publisher	Springer Nature
Licensed Content Publication	Springer eBook
Licensed Content Title	Direct Laser Cladding , Current Status and Future Scope of Application
Licensed Content Author	A. Weisheit, A. Gasser, G. Backes et al
Licensed Content Date	Jan 1, 2013
Type of Use	Thesis/Dissertation
Requestor type	academic/university or research institute
Format	print and electronic
Portion	figures/tables/illustrations
Number of figures/tables/illustrations	1
Will you be translating?	no
Circulation/distribution	501 to 1000
Author of this Springer Nature content	no
Title	Accelerated Modeling of Laser Powder- Bed/Fed Additive Manufacturing Processes and the Associated Magnetic Focusing Module
Institution name	n/a
Expected presentation date	Apr 2019
Portions	Fig. 5.22 Additive manufacturing of blades on a shaft
Requestor Location	Yuze Huang 200 University Ave W, Waterloo Canada Waterloo, ON N2L3G1 Canada Attn: Yuze Huang
Billing Type	Invoice
Billing Address	Yuze Huang 200 University Ave W, Waterloo Canada Waterloo, ON N2L3G1 Canada Attn: Yuze Huang
Total	0.00 CAD

ELSEVIER LICENSE
TERMS AND CONDITIONS

Feb 12, 2019

This Agreement between Yuze Huang ("You") and Elsevier ("Elsevier") consists of your license details and the terms and conditions provided by Elsevier and Copyright Clearance Center.

License Number	4526841282981
License date	Feb 12, 2019
Licensed Content Publisher	Elsevier
Licensed Content Publication	Elsevier Books
Licensed Content Title	Laser Additive Manufacturing
Licensed Content Author	M. Munsch
Licensed Content Date	Jan 1, 2017
Licensed Content Pages	22
Start Page	399
End Page	420
Type of Use	reuse in a thesis/dissertation
Intended publisher of new work	other
Portion	figures/tables/illustrations
Number of figures/tables/illustrations	1
Format	both print and electronic
Are you the author of this Elsevier chapter?	No
Will you be translating?	No
Original figure numbers	Figure 15.5 Laser additively manufactured custom-made partial hip replacement.
Title of your thesis/dissertation	Accelerated Modeling of Laser Powder- Bed/Fed Additive Manufacturing Processes and the Associated Magnetic Focusing Module
Expected completion date	Apr 2019
Estimated size (number of pages)	200
Requestor Location	Yuze Huang 200 University Ave W, Waterloo Canada Waterloo, ON N2L3G1 Canada Attn: Yuze Huang
Publisher Tax ID	GB 494 6272 12
Total	0.00 USD
Terms and Conditions	

References

[1] J. Waller, B. Parker, K. Hodges, E. Burke, Nondestructive evaluation of additive manufacturing state-of-the-discipline report, 2014.

[2] S. Das, Physical Aspects of Process Control in Selective Laser Sintering of Metals, Adv. Eng. Mater. 5 (2003) 701–711. doi:10.1002/adem.200310099.

[3] T. DebRoy, H.L. Wei, J.S. Zuback, T. Mukherjee, J.W. Elmer, J.O. Milewski, A.M. Beese, A. Wilson-Heid, A. De, W. Zhang, Additive manufacturing of metallic components – Process, structure and properties, Prog. Mater. Sci. 92 (2018) 112–224. doi:10.1016/j.pmatsci.2017.10.001.

[4] ASTM International, Standard Terminology for Additive Manufacturing Technologies (F2792-12a), 2015.

[5] Roland Berger Strategy Consultants, Additive manufacturing 2013 A game changer for the manufacturing industry?, 2013. https://www.rolandberger.com/en/Publications/Additive-manufacturing-2013.html (accessed February 9, 2019).

[6] A.J. Pinkerton, Advances in the modeling of laser direct metal deposition, J. Laser Appl. 27 (2015) S15001. doi:10.2351/1.4815992.

[7] G. Tapia, A. Elwany, A Review on Process Monitoring and Control in Metal-Based Additive Manufacturing, J. Manuf. Sci. Eng. 136 (2014) 060801. doi:10.1115/1.4028540.

[8] S.A.M. Tofail, E.P. Koumoulos, A. Bandyopadhyay, S. Bose, L. O'Donoghue, C. Charitidis, Additive manufacturing: Scientific and technological challenges, market uptake and opportunities, Mater. Today. (2017). doi:10.1016/j.mattod.2017.07.001.

[9] M. Ma, Z. Wang, D. Wang, X. Zeng, Control of shape and performance for direct laser fabrication of precision large-scale metal parts with 316L Stainless Steel, Opt. Laser Technol. 45 (2013). doi:10.1016/j.optlastec.2012.07.002.

[10] H. Shipley, D. McDonnell, M. Culleton, R. Lupoi, G. O'Donnell, D. Trimble, Optimisation of process parameters to address fundamental challenges during selective laser melting of Ti-6Al-4V: A review, Int. J. Mach. Tools Manuf. (2018). doi:10.1016/j.ijmachtools.2018.01.003.

[11] E. Toyserkani, A. Khajepour, S.S. Corbin, Laser cladding, CRC press, 2004. doi:10.1201/9781420039177.

[12] S. Clijsters, T. Craeghs, S. Buls, K. Kempen, J.-P. Kruth, In situ quality control of the selective laser melting process using a high-speed, real-time melt pool monitoring system, Int. J. Adv. Manuf. Technol. 75 (2014) 1089–1101. doi:10.1007/s00170-014-6214-8.

[13] H.-K.K. Lee, Effects of the cladding parameters on the deposition efficiency in pulsed Nd:YAG laser cladding, J. Mater. Process. Technol. 202 (2008) 321–327. doi:10.1016/j.jmatprotec.2007.09.024.

[14] M.F.S. John E. Brockmann, John R. Torczynski, Ronald C. Dykhuizen, Richard A. Neiser, J.E. Brockmann, J.R. Torczynski, R.C. Dykhuizen, R.A. Neiser, M.F. Smith, Aerodynamic beam generator for large particles, U.S. Patent 6,348,687, 2002.

[15] X. Chen, Modelling of directed energy deposition processes, Missouri University of Science and Technology, 2014. http://scholarsmine.mst.edu/masters_theses/7259/ (accessed February 7, 2019).

[16] P. Peyre, P. Aubry, R. Fabbro, R. Neveu, A. Longuet, Analytical and numerical modelling of the direct metal deposition laser process, J. Phys. D. Appl. Phys. 41 (2008) 025403. doi:10.1088/0022-3727/41/2/025403.

[17] R. Forslund, A. Snis, S. Larsson, Analytical solution for heat conduction due to a moving Gaussian heat flux with piecewise constant parameters, Appl. Math. Model. 66 (2019) 227–240. doi:10.1016/j.apm.2018.09.018.

[18] S. Mohanty, J. Hattel, Cellular scanning strategy for selective laser melting: Capturing thermal trends with a low-fidelity, pseudo-analytical model, Math. Probl. Eng. 2014 (2014) 1–14. doi:10.1155/2014/715058.

[19] P. Aggarangsi, J.L. Beuth, D.D. Gill, Transient Changes in Melt Pool Size in Laser Additive Manufacturing Processes, Proc. 15th Solid Free. Fabr. Symp. (2004) 163–174. http://edge.rit.edu/content/P10551/public/SFF/SFF 2004 Proceedings/SFF Papers 2004/16-Beuth.pdf (accessed February 7, 2019).

[20] J. Fox, F. Lopez, B. Lane, H. Yeung, S. Grantham, On the Requirements for Model-Based Thermal Control of Melt Pool Geometry in Laser Powder Bed Fusion Additive Manufacturing, in: Mater. Sci. Technol. Conf. Exhib. 2016, MS T 2016, 2016: pp. 133–140.

[21] M. Alimardani, E. Toyserkani, J.P. Huissoon, C.P. Paul, On the delamination and crack formation in a thin wall fabricated using laser solid freeform fabrication process: An experimental–numerical investigation, Opt. Lasers Eng. 47 (2009) 1160–1168. doi:10.1016/J.OPTLASENG.2009.06.010.

[22] Y.. Pei, J.T.. De Hosson, Functionally graded materials produced by laser cladding, Acta Mater. 48 (2000) 2617–2624. doi:10.1016/S1359-6454(00)00065-3.

[23] R.M. Mahamood, E.T. Akinlabi, Laser metal deposition of functionally graded Ti6Al4V/TiC, Mater. Des. 84 (2015) 402–410. doi:10.1016/J.MATDES.2015.06.135.

[24] J. Mazumder, H. Qi, Fabrication of 3-D components by laser aided direct metal deposition, in: Crit. Rev. Ind. Lasers Appl., 2005: pp. 38–59. doi:10.1117/12.601652.

[25] K. Feng, Y. Chen, P. Deng, Y. Li, H. Zhao, F. Lu, R. Li, J. Huang, Z. Li, Journal of Materials Processing Technology Improved high-temperature hardness and wear resistance of Inconel 625 coatings fabricated by laser cladding, J. Mater. Process. Tech. 243 (2017) 82–91. doi:10.1016/j.jmatprotec.2016.12.001.

[26] R. Vilar, A. Almeida, Repair and manufacturing of single crystal Ni-based superalloys components by laser powder deposition—A review, J. Laser Appl. 27 (2015) S17004. doi:10.2351/1.4862697.

[27] R. Schafrik, D. Ward, J.R. Groh, Application of Alloy 718 in GE Aircraft Engines: Past, Present and Next Five Years, in: Superalloys 718, 625, 706 Var. Deriv., 2001: pp. 1–11. doi:10.7449/2001/Superalloys_2001_1_11.

[28] P. Marks, 3D printing takes off with the world's first printed plane, (2011). https://www.sciencedirect.com/science/article/pii/S0262407911618174 (accessed

February 11, 2019).

[29] A. Singh, A. Ramakrishnan, G.P. Dinda, Direct laser metal deposition of eutectic Al-Si alloy for automotive applications, in: Miner. Met. Mater. Ser., 2017: pp. 71–80. doi:10.1007/978-3-319-51493-2_8.

[30] S. Lathabai, Additive Manufacturing of Aluminium-Based Alloys and Composites, in: Fundam. Alum. Metall., Woodhead Publishing, 2018: pp. 47–92. doi:10.1016/B978-0-08-102063-0.00002-3.

[31] L.E. Murr, S.M. Gaytan, F. Medina, H. Lopez, Next-generation biomedical implants using additive manufacturing of complex , cellular, Phil. Trans. R. Soc. A. 368 (2010) 1999–2032. doi:10.1098/rsta.2010.0010.

[32] J.D. Majumdar, I. Manna, Direct Laser Cladding , Current Status and Future, in: 2012: p. 513. doi:10.1007/978-3-642-28359-8.

[33] S.M. Thompson, L. Bian, N. Shamsaei, A. Yadollahi, Scott M. Thompson, Linkan Bian, Nima Shamsaei, Aref Yadollahi, An overview of Direct Laser Deposition for additive manufacturing; Part I: Transport phenomena, modeling and diagnostics, Addit. Manuf. 8 (2015) 36–62. doi:10.1016/j.addma.2015.07.001.

[34] Y. Huang, M.B.M.B.M. Khamesee, E. Toyserkani, A comprehensive analytical model for laser powder-fed additive manufacturing, Addit. Manuf. 12 (2016) 90–99. doi:10.1016/j.addma.2016.07.001.

[35] H. Gedda, J. Powell, G. Wahlström, W.-B.B. Li, H. Engström, C. Magnusson, G. Wahlstrom, W.-B.B. Li, H. Engstrom, C. Magnusson, Energy redistribution during CO2 laser cladding, J. Laser Appl. 14 (2002) 78–82. doi:10.2351/1.1471565.

[36] J. Mazumder, D. Dutta, N. Kikuchi, A. Ghosh, Closed loop direct metal deposition: art to part, Opt. Lasers Eng. 34 (2000) 397–414. doi:10.1016/S0143-8166(00)00072-5.

[37] K.P. Karunakaran, S. Suryakumar, V. Pushpa, S. Akula, Low cost integration of additive and subtractive processes for hybrid layered manufacturing, Robot. Comput. Integr. Manuf. 26 (2010) 490–499. doi:10.1016/J.RCIM.2010.03.008.

[38] L. Tang, R.G. Landers, Melt Pool Temperature Control for Laser Metal Deposition Processes—Part II: Layer-to-Layer Temperature Control, J. Manuf. Sci. Eng. 132 (2010) 011011. doi:10.1115/1.4000883.

[39] S.J. Wolff, S. Lin, E.J. Faierson, W.K. Liu, G.J. Wagner, J. Cao, A framework to link localized cooling and properties of directed energy deposition (DED)-processed Ti-6Al-4V, Acta Mater. 132 (2017) 106–117. doi:10.1016/j.actamat.2017.04.027.

[40] N. Shamsaei, A. Yadollahi, L. Bian, S.M. Thompson, An overview of Direct Laser Deposition for additive manufacturing; Part II: Mechanical behavior, process parameter optimization and control, Addit. Manuf. 8 (2015) 12–35. doi:10.1016/j.addma.2015.07.002.

[41] P. Muller, P. Mognol, J.Y. Hascoet, Modeling and control of a direct laser powder deposition process for Functionally Graded Materials (FGM) parts manufacturing, J. Mater. Process. Technol. 213 (2013) 685–692. doi:10.1016/j.jmatprotec.2012.11.020.

[42] S. Ocylok, A. Weisheit, I. Kelbassa, Functionally graded multi-layers by laser cladding for

increased wear and corrosion protection, in: Phys. Procedia, Elsevier, 2010: pp. 359–367. doi:10.1016/j.phpro.2010.08.157.

[43] M.M.M. Francois, A. Sun, W.W.E. King, N.J. Henson, D. Tourret, C.A. Bronkhorst, N.N. Carlson, C.K. Newman, T. Haut, J. Bakosi, J.W. Gibbs, V. Livescu, S.A. Vander Wiel, A.J. Clarke, M.W. Schraad, T. Blacker, H. Lim, T. Rodgers, S. Owen, F. Abdeljawad, J. Madison, A.T. Anderson, J.-L. Fattebert, R.M. Ferencz, N.E. Hodge, S.A. Khairallah, O. Walton, Modeling of additive manufacturing processes for metals: Challenges and opportunities, Curr. Opin. Solid State Mater. Sci. 21 (2017) 198–206. doi:10.1016/j.cossms.2016.12.001.

[44] T.G. Spears, S.A. Gold, In-process sensing in selective laser melting (SLM) additive manufacturing, Integr. Mater. Manuf. Innov. 5 (2016) 2. doi:10.1186/s40192-016-0045-4.

[45] M. Markl, C. Körner, Multiscale Modeling of Powder Bed–Based Additive Manufacturing, Annu. Rev. Mater. Res. 46 (2016) 93–123. doi:10.1146/annurev-matsci-070115-032158.

[46] A. V. Gusarov, J.P. Kruth, Modelling of radiation transfer in metallic powders at laser treatment, Int. J. Heat Mass Transf. 48 (2005) 3423–3434. doi:10.1016/j.ijheatmasstransfer.2005.01.044.

[47] W.J.W. Sames, F.A.F. List, S. Pannala, R.R.R. Dehoff, S.S. Babu, The metallurgy and processing science of metal additive manufacturing, Int. Mater. Rev. 61 (2016) 315–360. doi:10.1080/09506608.2015.1116649.

[48] C. Qiu, M. Al Kindi, A.S. Aladawi, I. Al Hatmi, A comprehensive study on microstructure and tensile behaviour of a selectively laser melted stainless steel, Sci. Rep. 8 (2018). doi:10.1038/s41598-018-26136-7.

[49] M. Munsch, Laser additive manufacturing of customized prosthetics and implants for biomedical applications, in: Laser Addit. Manuf. Mater. Des. Technol. Appl., 2016: pp. 399–420. doi:10.1016/B978-0-08-100433-3.00015-4.

[50] C.Y.C. Yap, C.K. Chua, Z.L. Dong, Z.H. Liu, D.Q. Zhang, L.E. Loh, S.L. Sing, Review of selective laser melting: Materials and applications, 2015. doi:10.1063/1.4935926.

[51] J.P. Kruth, B. Vandenbroucke, J. Van Vaerenbergh, I. Naert, Digital manufacturing of biocompatible metal frameworks for complex dental prostheses by means of SLS/SLM, in: Virtual Model. Rapid Manuf. Adv. Res. VIRTUAL RAPID Prototyp., 2005: pp. 139–145.

[52] M. Wehmoller, P. Warnke, C. Zilian, H. Eufinger, CARS: Computer Assisted Radiology and Surgery, 2005.

[53] I. Yadroitsev, P. Bertrand, B. Laget, I. Smurov, Application of laser assisted technologies for fabrication of functionally graded coatings and objects for the International Thermonuclear Experimental Reactor components, J. Nucl. Mater. 362 (2007) 189–196. doi:10.1016/J.JNUCMAT.2007.01.078.

[54] A. du Plessis, I. Yadroitsava, I. Yadroitsev, Ti6Al4V lightweight lattice structures manufactured by laser powder bed fusion for load-bearing applications, Opt. Laser Technol. 108 (2018) 521–528. doi:10.1016/J.OPTLASTEC.2018.07.050.

[55] E.J.R. Parteli, T. Pöschel, Particle-based simulation of powder application in additive manufacturing, Powder Technol. 288 (2016) 96–102. doi:10.1016/j.powtec.2015.10.035.

[56] F. Medina, Reducing metal alloy powder costs for use in powder bed fusion additive manufacturing: Improving the economics for production, The University of Texas, 2013. doi:AAI3611283.

[57] J.A. Slotwinski, E.J. Garboczi, Metrology Needs for Metal Additive Manufacturing Powders, JOM. 67 (2015) 538–543. doi:10.1007/s11837-014-1290-7.

[58] M. Barclift, S. Joshi, T. Simpson, C. Dickman, Cost Modeling and Depreciation for Reused Powder Feedstocks in Powder Bed Fusion Additive Manufacturing, Proceeding 27th Annu. Int. Solid Free. Fabr. Symp. (2016) 2007–2028. doi:10.7748/nr.2.2.13.s3.

[59] W.E. King, A.T. Anderson, R.M. Ferencz, N.E. Hodge, C. Kamath, S.A. Khairallah, A.M. Rubenchik, Laser powder bed fusion additive manufacturing of metals; physics, computational, and materials challenges, Appl. Phys. Rev. 2 (2015) 041304. doi:10.1063/1.4937809.

[60] P. Mishra, T. Ilar, F. Brueckner, A. Kaplan, Energy efficiency contributions and losses during selective laser melting, J. Laser Appl. 30 (2018) 032304. doi:10.2351/1.5040603.

[61] M. Binder, C. Anstaett, M. Horn, F. Herzer, G. Schlick, C. Seidel, J. Schilp, G. Reinhart, Potentials and challenges of multi-material processing by laser-based powder bed fusion, in: Solid Free. Fabr. 2018 Proc. 29th Annu. Int., 2018: pp. 376–387.

[62] J.C. Steuben, A.J. Birnbaum, A.P. Iliopoulos, J.G. Michopoulos, Enriched Analytical Solutions for Additive Manufacturing Modeling and Simulation, Addit. Manuf. (2018) 1–11. doi:10.1016/j.addma.2018.10.017.

[63] I. Tabernero, a. Lamikiz, E. Ukar, L.N. López de Lacalle, C. Angulo, G. Urbikain, Numerical simulation and experimental validation of powder flux distribution in coaxial laser cladding, J. Mater. Process. Technol. 210 (2010) 2125–2134. doi:10.1016/j.jmatprotec.2010.07.036.

[64] S.Y. Wen, Y.C. Shin, J.Y. Murthy, P.E. Sojka, Modeling of coaxial powder flow for the laser direct deposition process, Int. J. Heat Mass Transf. 52 (2009) 5867–5877. doi:10.1016/j.ijheatmasstransfer.2009.07.018.

[65] Y. Lee, M. Nordin, S. Babu, D. Farson, Influence of Fluid Convection on Weld Pool Formation in Laser Cladding, Weld. J. 93 (2014) 292s-300s.

[66] E. Toyserkani, A. Khajepour, S. Corbin, Three-dimensional finite element modeling of laser cladding by powder injection: Effects of powder feedrate and travel speed on the process, J. Laser Appl. 15 (2003) 153. doi:10.2351/1.1585087.

[67] E. Toyserkani, A. Khajepour, S. Corbin, 3-D finite element modeling of laser cladding by powder injection: Effects of laser pulse shaping on the process, Opt. Lasers Eng. 41 (2004) 849–867. doi:10.1016/S0143-8166(03)00063-0.

[68] X. He, J. Mazumder, Transport phenomena during direct metal deposition, J. Appl. Phys. 101 (2007) 053113. doi:10.1063/1.2710780.

[69] M. Alimardani, E. Toyserkani, J.P. Huissoon, A 3D dynamic numerical approach for temperature and thermal stress distributions in multilayer laser solid freeform fabrication process, Opt. Lasers Eng. 45 (2007) 1115–1130. doi:10.1016/j.optlaseng.2007.06.010.

[70] A. Fathi, A. Khajepour, M. Durali, E. Toyserkani, Geometry Control of the Deposited

Layer in a Nonplanar Laser Cladding Process Using a Variable Structure Controller, J. Manuf. Sci. Eng. 130 (2008) 031003. doi:10.1115/1.2823085.

[71] L. Song, V. Bagavath-Singh, B. Dutta, J. Mazumder, Control of melt pool temperature and deposition height during direct metal deposition process, Int. J. Adv. Manuf. Technol. 58 (2012) 247–256. doi:10.1007/s00170-011-3395-2.

[72] Y. Jin, S. Joe Qin, Q. Huang, Offline Predictive Control of Out-of-Plane Shape Deformation for Additive Manufacturing, J. Manuf. Sci. Eng. 138 (2016) 121005. doi:10.1115/1.4033444.

[73] Q. Huang, H. Nouri, K. Xu, Y. Chen, S. Sosina, T. Dasgupta, Statistical Predictive Modeling and Compensation of Geometric Deviations of Three-Dimensional Printed Products, J. Manuf. Sci. Eng. 136 (2014) 061008. doi:10.1115/1.4028510.

[74] H. Qi, J. Mazumder, H. Ki, Numerical simulation of heat transfer and fluid flow in coaxial laser cladding process for direct metal deposition, J. Appl. Phys. 100 (2006) 024903. doi:10.1063/1.2209807.

[75] M. Picasso, C.F. Marsden, J.D. Wagniere, A. Frenk, M. Rappaz, A simple but realistic model for laser cladding, Metall. Mater. Trans. B. 25 (1994) 281–291. doi:10.1007/BF02665211.

[76] A. Fathi, E. Toyserkani, A. Khajepour, M. Durali, Prediction of melt pool depth and dilution in laser powder deposition, J. Phys. D. Appl. Phys. 39 (2006) 2613–2623. doi:10.1088/0022-3727/39/12/022.

[77] S. Zhou, X. Dai, H. Zheng, Analytical modeling and experimental investigation of laser induction hybrid rapid cladding for Ni-based WC composite coatings, Opt. Laser Technol. 43 (2011) 613–621. doi:10.1016/j.optlastec.2010.09.001.

[78] X. Gong, Y. Zhang, M. Liu, Powder transport model for laser cladding by lateral powder feeding: I. Powder flow field with cylindrical distribution, Int. J. Adv. Manuf. Technol. 67 (2012) 2501–2509. doi:10.1007/s00170-012-4667-1.

[79] A.F.H. Kaplan, G. Groboth, Process Analysis of Laser Beam Cladding, J. Manuf. Sci. Eng. 123 (2001) 609. doi:10.1115/1.1344899.

[80] C. Doumanidis, Y.-M. Kwak, Geometry Modeling and Control by Infrared and Laser Sensing in Thermal Manufacturing with Material Deposition, J. Manuf. Sci. Eng. 123 (2001) 45. doi:10.1115/1.1344898.

[81] H. Tan, J. Chen, F. Zhang, X. Lin, W. Huang, Estimation of laser solid forming process based on temperature measurement, Opt. Laser Technol. 42 (2010) 47–54. doi:10.1016/j.optlastec.2009.04.016.

[82] Q. Wang, J. Li, M. Gouge, A.R. Nassar, P. (Pan) Michaleris, E.W. Reutzel, Physics-Based Multivariable Modeling and Feedback Linearization Control of Melt-Pool Geometry and Temperature in Directed Energy Deposition, J. Manuf. Sci. Eng. 139 (2016) 021013. doi:10.1115/1.4034304.

[83] J. Li, Q. Wang, P. (Pan) Michaleris, E.W. Reutzel, A.R. Nassar, An Extended Lumped-Parameter Model of Melt–Pool Geometry to Predict Part Height for Directed Energy Deposition, J. Manuf. Sci. Eng. 139 (2017) 091016. doi:10.1115/1.4037235.

[84] R. Ganeriwala, T.I. Zohdi, Multiphysics modeling and simulation of selective laser sintering manufacturing processes, in: Procedia CIRP, Elsevier, 2014: pp. 299–304. doi:10.1016/j.procir.2014.03.015.

[85] K. Zeng, C. Teng, S. Xu, T. Sublette, N. Patil, D. Pala, B. Stucker, A Comparison of the Computational Speed of 3DSIM versus ANSYS Finite Element Analyses for Simulation of Thermal History in Metal Laser Sintering, Int. Solid Free. Fabr. Symp. (2014) 1205–1212.

[86] J. Risse, L. Papadakis, A. Loizou, J. Schrage, S. Bremen, A computational reduction model for appraising structural effects in selective laser melting manufacturing, Virtual Phys. Prototyp. 9 (2014) 17–25. doi:10.1080/17452759.2013.868005.

[87] H. Peng, M. Ghasri-Khouzani, S. Gong, R. Attardo, P. Ostiguy, B.A. Gatrell, J. Budzinski, C. Tomonto, J. Neidig, M.R. Shankar, R. Billo, D.B. Go, D. Hoelzle, Fast prediction of thermal distortion in metal powder bed fusion additive manufacturing: Part 1, a thermal circuit network model, Addit. Manuf. 22 (2018) 852–868. doi:10.1016/j.addma.2018.05.023.

[88] L.E. Criales, Y.M. Arısoy, B. Lane, S. Moylan, A. Donmez, T. Özel, Predictive modeling and optimization of multi-track processing for laser powder bed fusion of nickel alloy 625, Addit. Manuf. 13 (2017) 14–36. doi:10.1016/j.addma.2016.11.004.

[89] H. Park, … D.N. the 16th I.C. on, U. 2018, AI-Based Optimization of Process Parameters in Selective Laser Melting, in: Adv. Manuf. Technol. XXXII Proc. 16th Int. Conf. Manuf. Res. Inc. 33rd Natl. Conf. Manuf. Researc, Sweden, 2018: p. 119.

[90] L.N. Carter, K. Essa, M.M. Attallah, Optimisation of selective laser melting for a high temperature Ni-superalloy, Rapid Prototyp. J. 21 (2015) 423–432. doi:10.1108/RPJ-06-2013-0063.

[91] G. Tapia, S. Khairallah, M. Matthews, W.E. King, A. Elwany, Gaussian process-based surrogate modeling framework for process planning in laser powder-bed fusion additive manufacturing of 316L stainless steel, Int. J. Adv. Manuf. Technol. 94 (2018) 3591–3603. doi:10.1007/s00170-017-1045-z.

[92] C. Kamath, Data mining and statistical inference in selective laser melting, Int. J. Adv. Manuf. Technol. 86 (2016) 1659–1677. doi:10.1007/s00170-015-8289-2.

[93] Y. Yang, M.F.F.M. Knol, F. van Keulen, C. Ayas, A semi-analytical thermal modelling approach for selective laser melting, Addit. Manuf. 21 (2018) 284–297. doi:10.1016/j.addma.2018.03.002.

[94] W.W.M. Steen, J. Mazumder, Laser material processing, Springer Science & Business Media, 2010. doi:10.1016/0924-0136(93)90021-W.

[95] H.S. Carslow, J.C. Jaeger, J.E. Morral, Conduction of Heat in Solids, Second Edition, J. Eng. Mater. Technol. 108 (1986) 378. doi:10.1115/1.3225900.

[96] M.J. Anderson, R.S. Budwig, K.S. Line, J.G. Frankel, Use of acoustic radiation pressure to concentrate small particles in an air flow, Ultrasonics. (2002). http://ieeexplore.ieee.org/abstract/document/1193446/ (accessed April 22, 2017).

[97] R. Imani, E. Robert, Acoustic separation of submicron solid particles in air, Ultrasonics. (2015). http://www.sciencedirect.com/science/article/pii/S0041624X15001687 (accessed

April 22, 2017).

[98] A. Nacev, I.N. Weinberg, P.Y. Stepanov, S. Kupfer, L.O. Mair, M.G. Urdaneta, M. Shimoji, S.T. Fricke, B. Shapiro, Dynamic inversion enables external magnets to concentrate ferromagnetic rods to a central target, Nano Lett. 15 (2015) 359–364. doi:10.1021/nl503654t.

[99] Q.A. Pankhurst, N.K.T. Thanh, S.K. Jones, J. Dobson, Progress in applications of magnetic nanoparticles in biomedicine, J. Phys. D. Appl. Phys. 42 (2009) 224001. doi:10.1088/0022-3727/42/22/224001.

[100] A. Cieśla, Use of the high temperature superconductors (HTS) to the magnetic separation, Int. J. Appl. Electromagn. Mech. 25 (2007) 83–87.

[101] A. Belounis, R. Mehasni, M. Ouili, M.E. Latreche, Optimization of the capture element for an OGMS based on the 3D computation of the magnetic particle behavior, Int. J. Appl. Electromagn. Mech. 48 (2015) 387–397. doi:10.3233/JAE-140157.

[102] F. Settimo, P. Bevilacqua, P. Rem, Eddy current separation of fine non-ferrous particles from bulk streams, Phys. Sep. Sci. Eng. 13 (2004) 15–23. doi:10.1080/00207390410001710726.

[103] M. Lungu, P. Rem, Eddy-current separation of small nonferrous particles by a single-disk separator with permanent magnets, IEEE Trans. Magn. 39 (2003) 2062–2067. doi:10.1109/TMAG.2003.812724.

[104] V.I. Dyadin, V.Y.V. Kozhevnikov, A. V. Kozyrev, N.S. Sochugov, V.G. Podkovyrov, N.S. Sochugov, Pulsed electrodynamic separation of small conducting particles, Tech. Phys. Lett. 34 (2008) 91–93. doi:10.1134/S1063785008020016.

[105] N. Dholu, J.R. Nagel, D. Cohrs, R.K. Rajamani, Eddy current separation of nonferrous metals using a variable-frequency electromagnet, KONA Powder Part. J. 34 (2017) 241–247. doi:10.14356/kona.2017012.

[106] J.R. Nagel, Induced Eddy Currents in Simple Conductive Geometries: Mathematical Formalism Describes the Excitation of Electrical Eddy Currents in a Time-Varying Magnetic Field, IEEE Antennas Propag. Mag. 60 (2018) 81–88. doi:10.1109/MAP.2017.2774206.

[107] E. Schlömann, Separation of nonmagnetic metals from solid waste by permanent magnets. I. Theory, J. Appl. Phys. 46 (1975) 5012–5021. doi:10.1063/1.321491.

[108] J. Yang, J. Han, H. Yu, J. Yin, M. Gao, Z. Wang, X. Zeng, Role of molten pool mode on formability, microstructure and mechanical properties of selective laser melted Ti-6Al-4V alloy, Mater. Des. 110 (2016) 558–570. doi:10.1016/j.matdes.2016.08.036.

[109] T. Qi, H. Zhu, H. Zhang, J. Yin, L. Ke, X. Zeng, Selective laser melting of Al7050 powder: Melting mode transition and comparison of the characteristics between the keyhole and conduction mode, Mater. Des. 135 (2017) 257–266. doi:10.1016/j.matdes.2017.09.014.

[110] A.J. Pinkerton, An analytical model of beam attenuation and powder heating during coaxial laser direct metal deposition, J. Phys. D. Appl. Phys. 40 (2007) 7323–7334. doi:10.1088/0022-3727/40/23/012.

[111] J. Lin, Simple model of powder catchment in coaxial laser cladding, Opt. Laser Technol. 31 (1999) 233–238. doi:10.1016/S0030-3992(99)00046-8.

[112] A. Frenk, M. Vandyoussefi, J.-D. Wagnière, W. Kurz, A. Zryd, Analysis of the laser-cladding process for stellite on steel, Metall. Mater. Trans. B. 28 (1997) 501–508. doi:10.1007/s11663-997-0117-0.

[113] J. Lin, Concentration mode of the powder stream in coaxial laser cladding, Opt. Laser Technol. 31 (1999) 251–257. doi:10.1016/S0030-3992(99)00049-3.

[114] A.J. Pinkerton, L. Li, Modelling Powder Concentration Distribution From a Coaxial Deposition Nozzle for Laser-Based Rapid Tooling, J. Manuf. Sci. Eng. 126 (2004) 33. doi:10.1115/1.1643748.

[115] N. Yang, Concentration model based on movement model of powder flow in coaxial laser cladding, Opt. Laser Technol. 41 (2009) 94–98. doi:10.1016/j.optlastec.2008.03.008.

[116] G. Zhu, D. Li, A. Zhang, G. Pi, Y. Tang, The influence of laser and powder defocusing characteristics on the surface quality in laser direct metal deposition, Opt. Laser Technol. 44 (2012) 349–356. doi:10.1016/j.optlastec.2011.07.013.

[117] C. Bohren, D. Huffman, Absorption and scattering of light by small particles, 2008. doi:10.1002/9783527618156.

[118] A.J. Pinkerton, R. Moat, K. Shah, L. Li, M. Preuss, P.J. Withers, A verified model of laser direct metal deposition using an analytical enthalpy balance method, in: 26th Int. Congr. Appl. Lasers Electro-Optics, ICALEO 2007 - Congr. Proc., Laser Institute of America, 2007. http://eprints.lancs.ac.uk/59694/ (accessed July 24, 2018).

[119] INCONEL® nickel-chromium alloy 625 Physical and Mechanical Properties, Spec. Met. Corp. (2013).

[120] N. Ahmed, K.T. Voisey, D.G. McCartney, Investigation into the effect of beam shape on melt pool characteristics using analytical modelling, Opt. Lasers Eng. 48 (2010) 548–554. doi:10.1016/J.OPTLASENG.2009.12.013.

[121] Y.R. Smith, J.R. Nagel, R.K. Rajamani, Eddy current separation for recovery of non-ferrous metallic particles: A comprehensive review, Miner. Eng. 133 (2019) 149–159. doi:10.1016/j.mineng.2018.12.025.

[122] F. Yu, W. Chen, D. Zhang, The Research of Simulation on Eddy Current Separation Process Based on MATLAB and COMSOL, in: Procedia CIRP, Elsevier, 2016: pp. 520–523. doi:10.1016/j.procir.2016.10.102.

[123] JD Jackson, Classical Electrodynamics, Third Edit, John Wiley, New York, 1998.

[124] J.D. Ray, J.R. Nagel, D. Cohrs, R.K. Rajamani, Forces on Particles in Time-Varying Magnetic Fields, KONA Powder Part. J. 35 (2018) 251–257. doi:10.14356/kona.2018016.

[125] J.R. Nagel, An analytic model for eddy current separation, Miner. Eng. 127 (2018) 277–285. https://www.sciencedirect.com/science/article/pii/S0892687518303765 (accessed February 26, 2019).

[126] S. Elgwel, A., Harmer, S. W., Bowring, N. J., & Yin, Resolution of Multiple Concealed Threat Objects Using Electromagnetic Pulse Induction, Prog. Electromagn. Res. (2012) 55–68.

[127] F. Morrison, An introduction to fluid mechanics, Cambridge University Press, 2013.

[128] V. Saveliev, System and Method for Separating Electrically Conductive Particles, U.S. Patent 5,772,043, 1998.

[129] H. Naidu, Electrodynamic separation of metallic granules from mixed waste stream, The University of Utah, 2010.

[130] S.M. Wentworth, M.E. Baginski, D.L. Faircloth, S.M. Rao, L.S. Riggs, Calculating effective skin depth for thin conductive sheets, in: Antennas Propag. Soc. Int. Symp. 2006, IEEE, 2006: pp. 4845–4848. doi:10.1109/APS.2006.1711728.

[131] F. Marteau, A. Ghaith, P. N'Gotta, C. Benabderrahmane, M. Valléau, C. Kitegi, A. Loulergue, J. Vétéran, M. Sebdaoui, T. André, G. Le Bec, J. Chavanne, C. Vallerand, D. Oumbarek, O. Cosson, F. Forest, P. Jivkov, J.L. Lancelot, M.E. Couprie, Variable high gradient permanent magnet quadrupole (QUAPEVA), Appl. Phys. Lett. 111 (2017) 253503. doi:10.1063/1.4986856.

[132] S. Becker, M. Bussmann, S. Raith, M. Fuchs, R. Weingartner, P. Kunz, W. Lauth, U. Schramm, M. El Ghazaly, F. Grüner, H. Backe, D. Habs, Characterization and tuning of ultrahigh gradient permanent magnet quadrupoles, Phys. Rev. Spec. Top. - Accel. Beams. 12 (2009) 102801. doi:10.1103/PhysRevSTAB.12.102801.

[133] K. Halbach, Design of permanent multipole magnets with oriented rare earth cobalt material, Nucl. Instruments Methods. 169 (1980) 1–10. doi:10.1016/0029-554X(80)90094-4.

[134] J.K. Lim, P. Frigola, G. Travish, J.B. Rosenzweig, S.G. Anderson, W.J. Brown, J.S. Jacob, C.L. Robbins, A.M. Tremaine, Adjustable, short focal length permanent-magnet quadrupole based electron beam final focus system, Phys. Rev. Spec. Top. - Accel. Beams. 8 (2005) 1–17. doi:10.1103/PhysRevSTAB.8.072401.

[135] S. V Kulkarni, S.A. Khaparde, Transformer Engineering: Design and Practice, CRC press, 2004.

[136] C. Crowe, Multiphase flow handbook, CRC press, 2006.

[137] J. Li, Q. Wang, P. (Pan) Michaleris, An Analytical Computation of Temperature Field Evolved in Directed Energy Deposition, J. Manuf. Sci. Eng. 140 (2018) 101004. doi:10.1115/1.4040621.

[138] A.J. Pinkerton, L. Li, Modelling the geometry of a moving laser melt pool and deposition track via energy and mass balances, J. Phys. D. Appl. Phys. 37 (2004) 1885–1895. doi:10.1088/0022-3727/37/14/003.

[139] W. Perret, C. Schwenk, M. Rethmeier, Comparison of analytical and numerical welding temperature field calculation, Comput. Mater. Sci. 47 (2010) 1005–1015. doi:10.1016/J.COMMATSCI.2009.11.032.

[140] V. Ocelík, O. Nenadl, A. Palavra, J.T.M. De Hosson, On the geometry of coating layers formed by overlap, Surf. Coatings Technol. 242 (2014) 54–61. doi:10.1016/j.surfcoat.2014.01.018.

[141] S. Schiaffino, A.A. Sonin, Molten droplet deposition and solidification at low Weber numbers, Phys. Fluids. 9 (1997) 3172–3187. doi:10.1063/1.869434.

[142] D. Chatain, W.C. Carter, Spreading of metallic drops, Nat. Mater. 3 (2004) 843–845. doi:10.1038/nmat1275.

[143] D.W. Dietrich, Nonferrous Alloys and Special-Purpose Materials, in: ASM Handb. Vol 2, 1990: pp. 761–781.

[144] M.H.M. Farshidianfar, A. Khajepour, A.P.A.P. Gerlich, Effect of real-time cooling rate on microstructure in Laser Additive Manufacturing, J. Mater. Process. Technol. 231 (2016) 468–478. doi:10.1016/j.jmatprotec.2016.01.017.

[145] V. Manvatkar, A. De, T. DebRoy, Spatial variation of melt pool geometry, peak temperature and solidification parameters during laser assisted additive manufacturing process, Mater. Sci. Technol. 31 (2015) 924–930. doi:10.1179/1743284714Y.0000000701.

[146] H. Fayazfar, M. Salarian, A. Rogalsky, D. Sarker, P. Russo, V. Paserin, E. Toyserkani, A critical review of powder-based additive manufacturing of ferrous alloys: Process parameters, microstructure and mechanical properties, Mater. Des. 144 (2018) 98–128. doi:10.1016/j.matdes.2018.02.018.

[147] L. Zhu, Z.F. Xu, P. Liu, Y.F. Gu, Effect of processing parameters on microstructure of laser solid forming Inconel 718 superalloy, Opt. Laser Technol. 98 (2018) 409–415. doi:10.1016/j.optlastec.2017.08.027.

[148] Y.-F. Tao, J. Li, Y.-H. Lv, L.-F. Hu, Effect of heat treatment on residual stress and wear behaviors of the TiNi/Ti 2 Ni based laser cladding composite coatings, Opt. Laser Technol. 97 (2017) 379–389. doi:10.1016/j.optlastec.2017.07.029.

[149] J. Choi, Y. Chang, Characteristics of laser aided direct metal / material deposition process for tool steel, Mach. Tools Manuf. 45 (2005) 597–607. doi:10.1016/j.ijmachtools.2004.08.014.

[150] U. de Oliveira, V. Ocelík, J.T.M. De Hosson, Analysis of coaxial laser cladding processing conditions, Surf. Coatings Technol. 197 (2005) 127–136. doi:10.1016/j.surfcoat.2004.06.029.

[151] M.K. Alam, R.J. Urbanic, N. Nazemi, A. Edrisy, Predictive modeling and the effect of process parameters on the hardness and bead characteristics for laser-cladded stainless steel, Int. J. Adv. Manuf. Technol. 94 (2018) 397–413. doi:10.1007/s00170-017-0898-5.

[152] H.D. Carlton, A. Haboub, G.F. Gallegos, D.Y. Parkinson, A.A. MacDowell, Damage evolution and failure mechanisms in additively manufactured stainless steel, Mater. Sci. Eng. A. 651 (2016) 406–414. doi:10.1016/j.msea.2015.10.073.

[153] J. Kruth, P. Mercelis, J. Van Vaerenbergh, T. Craeghs, Feedback control of Selective Laser Melting, Proc. 3rd Int. Conf. Adv. Res. Virtual Rapid Prototyp. (2007) 1–7.

[154] V. Renken, L. Lübbert, H. Blom, A. von Freyberg, A. Fischer, Model assisted closed-loop control strategy for selective laser melting, Procedia CIRP. 74 (2018) 659–663. doi:10.1016/j.procir.2018.08.053.

[155] J.A. Kanko, A.P. Sibley, J.M. Fraser, In situ morphology-based defect detection of selective laser melting through inline coherent imaging, J. Mater. Process. Technol. 231 (2016) 488–500. doi:10.1016/j.jmatprotec.2015.12.024.

[156] P.J. DePond, G. Guss, S. Ly, N.P. Calta, D. Deane, S. Khairallah, M.J. Matthews, In situ

measurements of layer roughness during laser powder bed fusion additive manufacturing using low coherence scanning interferometry, Mater. Des. 154 (2018) 347–359. doi:10.1016/j.matdes.2018.05.050.

[157] M. Grasso, B.M. Colosimo, Process defects and in situ monitoring methods in metal powder bed fusion: A review, Meas. Sci. Technol. 28 (2017) 044005. doi:10.1088/1361-6501/aa5c4f.

[158] V. Gunenthiram, P. Peyre, M. Schneider, M. Dal, F. Coste, I. Koutiri, R. Fabbro, Experimental analysis of spatter generation and melt-pool behavior during the powder bed laser beam melting process, J. Mater. Process. Technol. 251 (2018) 376–386. doi:10.1016/j.jmatprotec.2017.08.012.

[159] V. Gunenthiram, P. Peyre, M. Schneider, M. Dal, F. Coste, R. Fabbro, Analysis of laser–melt pool–powder bed interaction during the selective laser melting of a stainless steel, J. Laser Appl. 29 (2017) 022303. doi:10.2351/1.4983259.

[160] J. Trapp, A.M. Rubenchik, G. Guss, M.J. Matthews, In situ absorptivity measurements of metallic powders during laser powder-bed fusion additive manufacturing, Appl. Mater. Today. 9 (2017) 341–349. doi:10.1016/j.apmt.2017.08.006.

[161] W.E. King, H.D. Barth, V.M. Castillo, G.F. Gallegos, J.W. Gibbs, D.E. Hahn, C. Kamath, A.M. Rubenchik, Observation of keyhole-mode laser melting in laser powder-bed fusion additive manufacturing, J. Mater. Process. Technol. 214 (2014) 2915–2925. doi:10.1016/j.jmatprotec.2014.06.005.

[162] S.A. Khairallah, A.T.A.A.T. Anderson, A.M. Rubenchik, W.W.E. King, Laser powder-bed fusion additive manufacturing: Physics of complex melt flow and formation mechanisms of pores, spatter, and denudation zones, Acta Mater. 108 (2016) 36–45. doi:10.1016/j.actamat.2016.02.014.

[163] J. Smith, W. Xiong, W. Yan, S. Lin, P. Cheng, O.L. Kafka, G.J. Wagner, J. Cao, W.K. Liu, Linking process, structure, property, and performance for metal-based additive manufacturing: computational approaches with experimental support, Comput. Mech. 57 (2016) 583–610. doi:10.1007/s00466-015-1240-4.

[164] A. Hussein, L. Hao, C. Yan, R. Everson, Finite element simulation of the temperature and stress fields in single layers built without-support in selective laser melting, Mater. Des. 52 (2013) 638–647. doi:10.1016/j.matdes.2013.05.070.

[165] S. a. Khairallah, A. Anderson, Mesoscopic simulation model of selective laser melting of stainless steel powder, J. Mater. Process. Technol. 214 (2014) 2627–2636. doi:10.1016/j.jmatprotec.2014.06.001.

[166] E.R. Denlinger, V. Jagdale, G. V. Srinivasan, T. El-Wardany, P. Michaleris, Thermal modeling of Inconel 718 processed with powder bed fusion and experimental validation using in situ measurements, Addit. Manuf. 11 (2016) 7–15. doi:10.1016/j.addma.2016.03.003.

[167] P. Meakin, R. Jullien, Restructuring effects in the rain model for random deposition, J. Phys. 48 (1987) 1651–1662. doi:10.1051/jphys:0198700480100165100.

[168] C. Körner, E. Attar, P. Heinl, Mesoscopic simulation of selective beam melting processes, J. Mater. Process. Technol. 211 (2011) 978–987.

doi:10.1016/J.JMATPROTEC.2010.12.016.

[169] D. Nield, A. Bejan, Convection in porous media, Fifth, Springer-Verlag, New York, 2016. doi:10.1007/978-3-319-49562-0.

[170] S.S. Sih, J.W. Barlow, The prediction of the emissivity and thermal conductivity of powder beds, Part. Sci. Technol. 22 (2004) 427–440. doi:10.1080/02726350490501682.

[171] M. Rombouts, L. Froyen, A. V. Gusarov, E.H. Bentefour, C. Glorieux, Photopyroelectric measurement of thermal conductivity of metallic powders, J. Appl. Phys. 97 (2005) 024905. doi:10.1063/1.1832740.

[172] A. Foroozmehr, M. Badrossamay, E. Foroozmehr, S. Golabi, Finite Element Simulation of Selective Laser Melting process considering Optical Penetration Depth of laser in powder bed, Mater. Des. 89 (2016) 255–263. doi:10.1016/J.MATDES.2015.10.002.

[173] A.M. Rubenchik, W.E. King, S.S. Wu, Scaling laws for the additive manufacturing, J. Mater. Process. Technol. 257 (2018) 234–243. doi:10.1016/J.JMATPROTEC.2018.02.034.

[174] G. Vastola, G. Zhang, Q.X. Pei, Y.W. Zhang, Modeling and control of remelting in high-energy beam additive manufacturing, Addit. Manuf. 7 (2015) 57–63. doi:10.1016/j.addma.2014.12.004.

[175] A. V. Gusarov, I. Yadroitsev, P. Bertrand, I. Smurov, Model of Radiation and Heat Transfer in Laser-Powder Interaction Zone at Selective Laser Melting, J. Heat Transfer. 131 (2009) 072101. doi:10.1115/1.3109245.

[176] G. Gladush, I. Smurov, Physics of laser materials processing: theory and experiment, Springer Science & Business Media, 2011.

[177] J. Goldak, A. Chakravarti, M. Bibby, A new finite element model for welding heat sources, Metall. Trans. B. 15 (1984) 299–305. doi:10.1007/BF02667333.

[178] N.T. Nguyen, A. Ohta, K. Matsuoka, N. Suzuki, Y. Maeda, Analytical Solutions for Transient Temperature of Semi-Infinite Body Subjected to 3-D Moving Heat Sources, Weld. Res. I (1999) 265–274. doi:10.1177/0883073813511301.

[179] H. Piili, A. Happonen, T. Väistö, V. Venkataramanan, J. Partanen, A. Salminen, Cost Estimation of Laser Additive Manufacturing of Stainless Steel, in: Phys. Procedia, Elsevier, 2015: pp. 388–396. doi:10.1016/j.phpro.2015.11.053.

[180] I.A.A. Roberts, C.J.J. Wang, R. Esterlein, M. Stanford, D.J.J. Mynors, A three-dimensional finite element analysis of the temperature field during laser melting of metal powders in additive layer manufacturing, Int. J. Mach. Tools Manuf. 49 (2009) 916–923. doi:10.1016/j.ijmachtools.2009.07.004.

[181] R. Paul, Modeling and Optimization of Powder Based Additive Manufacturing (AM) Processes, University of Cincinnati, 2013.

[182] K. Dai, L. Shaw, Finite element analysis of the effect of volume shrinkage during laser densification, Acta Mater. 53 (2005) 4743–4754. doi:10.1016/j.actamat.2005.06.014.

[183] R. Paul, S. Anand, F. Gerner, Effect of Thermal Deformation on Part Errors in Metal Powder Based Additive Manufacturing Processes, J. Manuf. Sci. Eng. 136 (2014) 031009. doi:10.1115/1.4026524.

[184] I. Yadroitsev, I. Smurov, Surface morphology in selective laser melting of metal powders,

in: Phys. Procedia, Elsevier, 2011: pp. 264–270. doi:10.1016/j.phpro.2011.03.034.

[185] A.S. Sabau, W.D. Porter, Alloy Shrinkage Factors for the Investment Casting of 17-4PH Stainless Steel Parts, Metall. Mater. Trans. B. 39 (2008) 317–330. doi:10.1007/s11663-007-9125-3.

[186] EOS IndustryLine, EOS Stainless Steel 17-4PH Powder, 2017.

[187] A.R. and Zhang, Z., Ali, U., Mahmoodkhani, Y., Huang, Y., Shahabad, S.I., Kasinathan, E. Toyserkani, Experimental and numerical investigation on the effect of layer thickness during laser powder-bed fusion of stainless steel 17-4PH, Int. J. Rapid Manuf. X (2019) xxx–xxx.

[188] Z. Zhang, Y. Huang, A. Rani Kasinathan, S. Imani Shahabad, U. Ali, Y. Mahmoodkhani, E. Toyserkani, 3-Dimensional heat transfer modeling for laser powder-bed fusion additive manufacturing with volumetric heat sources based on varied thermal conductivity and absorptivity, Opt. Laser Technol. 109 (2019) 297–312. doi:10.1016/j.optlastec.2018.08.012.

[189] A. Rogalsky, I. Rishmawi, L. Brock, M. Vlasea, Low cost irregular feed stock for laser powder bed fusion, J. Manuf. Process. 35 (2018) 446–456. doi:10.1016/j.jmapro.2018.08.032.

[190] L. Ladani, J. Romano, W. Brindley, S. Burlatsky, Effective liquid conductivity for improved simulation of thermal transport in laser beam melting powder bed technology, Addit. Manuf. 14 (2017) 13–23. doi:10.1016/j.addma.2016.12.004.

[191] G.L. Knapp, T. Mukherjee, J.S. Zuback, H.L. Wei, T.A. Palmer, A. De, T. DebRoy, Building blocks for a digital twin of additive manufacturing, Acta Mater. 135 (2017) 390–399. doi:10.1016/j.actamat.2017.06.039.

[192] E. Toyserkani, A. Khajepour, A mechatronics approach to laser powder deposition process, Mechatronics. 16 (2006) 631–641. doi:10.1016/J.MECHATRONICS.2006.05.002.

[193] M. Akbari, R. Kovacevic, An investigation on mechanical and microstructural properties of 316LSi parts fabricated by a robotized laser/wire direct metal deposition system, Addit. Manuf. 23 (2018) 487–497. doi:10.1016/J.ADDMA.2018.08.031.

[194] Z. Wang, T.A. Palmer, A.M. Beese, Effect of processing parameters on microstructure and tensile properties of austenitic stainless steel 304L made by directed energy deposition additive manufacturing, Acta Mater. 110 (2016) 226–235. doi:10.1016/j.actamat.2016.03.019.

[195] P.C. Collins, D.A. Brice, P. Samimi, I. Ghamarian, H.L. Fraser, Microstructural Control of Additively Manufactured Metallic Materials, Annu. Rev. Mater. Res. 46 (2016) 63–91. doi:10.1146/annurev-matsci-070115-031816.

[196] F. Lia, J.Z. Park, J.S. Keist, S. Joshi, R.P. Martukanitz, Thermal and microstructural analysis of laser-based directed energy deposition for Ti-6Al-4V and Inconel 625 deposits, Mater. Sci. Eng. A. 717 (2018) 1–10. doi:10.1016/j.msea.2018.01.060.

[197] J. Gockel, J. Beuth, K. Taminger, Integrated control of solidification microstructure and melt pool dimensions in electron beam wire feed additive manufacturing of ti-6al-4v, Addit. Manuf. 1 (2014) 119–126. doi:10.1016/j.addma.2014.09.004.

[198] J. Gockel, J. Fox, J. Beuth, R. Hafley, Integrated melt pool and microstructure control for Ti–6Al–4V thin wall additive manufacturing, Mater. Sci. Technol. 31 (2015) 912–916. doi:10.1179/1743284714Y.0000000704.

[199] W. Kurz, D.J. Fisher, Dendrite growth at the limit of stability: tip radius and spacing, Acta Metall. 29 (1981) 11–20. doi:10.1016/0001-6160(81)90082-1.

[200] S. Bontha, N.W. Klingbeil, P.A. Kobryn, H.L. Fraser, Thermal process maps for predicting solidification microstructure in laser fabrication of thin-wall structures, J. Mater. Process. Technol. 178 (2006) 135–142. doi:10.1016/j.jmatprotec.2006.03.155.

[201] S. Bontha, N.W. Klingbeil, P.A. Kobryn, H.L. Fraser, Effects of process variables and size-scale on solidification microstructure in beam-based fabrication of bulky 3D structures, Mater. Sci. Eng. A. 513–514 (2009) 311–318. doi:10.1016/J.MSEA.2009.02.019.

[202] Y.-J. Liang, A. Li, X. Cheng, X.-T. Pang, H.-M. Wang, Prediction of primary dendritic arm spacing during laser rapid directional solidification of single-crystal nickel-base superalloys, J. Alloys Compd. 688 (2016) 133–142. doi:10.1016/J.JALLCOM.2016.06.289.

[203] Y.J. Liang, X. Cheng, J. Li, H.M. Wang, Microstructural control during laser additive manufacturing of single-crystal nickel-base superalloys: New processing–microstructure maps involving powder feeding, Mater. Des. 130 (2017) 197–207. doi:10.1016/j.matdes.2017.05.066.

[204] B. Zheng, Y. Zhou, J.E.E. Smugeresky, J.M.M. Schoenung, E.J.J. Lavernia, Thermal Behavior and Microstructure Evolution during Laser Deposition with Laser-Engineered Net Shaping: Part II. Experimental Investigation and Discussion, Metall. Mater. Trans. A Phys. Metall. Mater. Sci. 39 (2008) 2237–2245. doi:10.1007/s11661-008-9566-6.

[205] H.L. Wei, J. Mazumder, T. DebRoy, Evolution of solidification texture during additive manufacturing, Sci. Rep. 5 (2015) 16446. doi:10.1038/srep16446.

[206] S. Wen, Y.C. Shin, Modeling of transport phenomena during the coaxial laser direct deposition process, J. Appl. Phys. 108 (2010) 044908. doi:10.1063/1.3474655.

[207] Astm Standard, E112-12:Standard Test Methods for Determining Average Grain Size, ASTM Int. E112-12 (2004) 1–27. doi:10.1520/E0112-12.1.4.

[208] S. Roy, M. Juha, M.S. Shephard, A.M. Maniatty, Heat transfer model and finite element formulation for simulation of selective laser melting, Comput. Mech. 62 (2018) 273–284. doi:10.1007/s00466-017-1496-y.

[209] Y.M. Arısoy, L.E. Criales, T. Özel, Modeling and simulation of thermal field and solidification in laser powder bed fusion of nickel alloy IN625, Opt. Laser Technol. 109 (2019) 278–292. doi:10.1016/j.optlastec.2018.08.016.

[210] L. Du, D. Gu, D. Dai, Q. Shi, C. Ma, M. Xia, Relation of thermal behavior and microstructure evolution during multi-track laser melting deposition of Ni-based material, Opt. Laser Technol. 108 (2018) 207–217. doi:10.1016/J.OPTLASTEC.2018.06.042.

[211] Z. Gan, G. Yu, X. He, S. Li, Numerical simulation of thermal behavior and multicomponent mass transfer in direct laser deposition of Co-base alloy on steel, Int. J. Heat Mass Transf. 104 (2017) 28–38. doi:10.1016/j.ijheatmasstransfer.2016.08.049.

[212] W. Kurz, B. Giovanola, R. Trivedi, THEORY OF MICROSTRUCTURAL DEVELOPMENT DURING RAPID SOLIDIFICATION, Acta Met. 34 (1986) 823–830. doi:10.1007/978-94-009-4456-5_24.

[213] N. Hansen, Hall–Petch relation and boundary strengthening, Scr. Mater. 51 (2004) 801–806. doi:10.1016/J.SCRIPTAMAT.2004.06.002.

[214] S. Kou, Welding Metallurgy, 2nd ed., 2002. doi:10.1002/0471434027.

[215] S. Cao, D. Gu, Q. Shi, Relation of microstructure, microhardness and underlying thermodynamics in molten pools of laser melting deposition processed TiC/Inconel 625 composites, J. Alloys Compd. 692 (2017) 758–769. doi:10.1016/j.jallcom.2016.09.098.

[216] H. Yin, S.D. Felicelli, Dendrite growth simulation during solidification in the LENS process, Acta Mater. 58 (2010) 1455–1465. doi:10.1016/J.ACTAMAT.2009.10.053.

[217] W. Ou, T. Mukherjee, G.L. Knapp, Y. Wei, T. DebRoy, Fusion zone geometries, cooling rates and solidification parameters during wire arc additive manufacturing, Int. J. Heat Mass Transf. 127 (2018) 1084–1094. doi:10.1016/j.ijheatmasstransfer.2018.08.111.

[218] W. Tan, S. Wen, N. Bailey, Y.C. Shin, Multiscale Modeling of Transport Phenomena and Dendritic Growth in Laser Cladding Processes, Metall. Mater. Trans. B. 42 (2011) 1306–1318. doi:10.1007/s11663-011-9545-y.

[219] W. Hofmeister, M. Griffith, M. Ensz, J. Smugeresky, Solidification in direct metal deposition by LENS processing, JOM. 53 (2001) 30–34. doi:10.1007/s11837-001-0066-z.

[220] W. Kurz, D. Fisher, Fundamentals of Solidification, 4th ed., CRC Press, 1998. doi:AR1RAAAAMAAJ.

[221] U. Scipioni Bertoli, B.E. MacDonald, J.M. Schoenung, Stability of cellular microstructure in laser powder bed fusion of 316L stainless steel, Mater. Sci. Eng. A. 739 (2019) 109–117. doi:10.1016/J.MSEA.2018.10.051.

[222] J.J. Blecher, T.A. Palmer, T. Debroy, Solidification map of a nickel-base alloy, in: Metall. Mater. Trans. A Phys. Metall. Mater. Sci., Springer US, 2014: pp. 2142–2151. doi:10.1007/s11661-013-2149-1.

[223] K. Zhang, S. Wang, W. Liu, X. Shang, Characterization of stainless steel parts by Laser Metal Deposition Shaping, Mater. Des. 55 (2014) 104–119. doi:10.1016/j.matdes.2013.09.006.

[224] Y.L. Hu, X. Lin, X.F. Lu, S.Y. Zhang, H.O. Yang, L. Wei, W.D. Huang, Evolution of solidification microstructure and dynamic recrystallisation of Inconel 625 during laser solid forming process, J. Mater. Sci. 53 (2018) 15650–15666. doi:10.1007/s10853-018-2701-x.

[225] I. Yadroitsev, P. Krakhmalev, I. Yadroitsava, S. Johansson, I. Smurov, Energy input effect on morphology and microstructure of selective laser melting single track from metallic powder, J. Mater. Process. Technol. 213 (2013) 606–613. doi:10.1016/j.jmatprotec.2012.11.014.

[226] G.P. Dinda, A.K. Dasgupta, J. Mazumder, Texture control during laser deposition of nickel-based superalloy, Scr. Mater. 67 (2012) 503–506. doi:10.1016/j.scriptamat.2012.06.014.

[227] X. Xu, G. Mi, L. Chen, L. Xiong, P. Jiang, X. Shao, C. Wang, Research on microstructures and properties of Inconel 625 coatings obtained by laser cladding with wire, J. Alloys Compd. 715 (2017) 362–373. doi:10.1016/J.JALLCOM.2017.04.252.

[228] G. Marchese, X. Garmendia Colera, F. Calignano, M. Lorusso, S. Biamino, P. Minetola, D. Manfredi, Characterization and Comparison of Inconel 625 Processed by Selective Laser Melting and Laser Metal Deposition, Adv. Eng. Mater. 19 (2017) 1600635. doi:10.1002/adem.201600635.

[229] V.D. Manvatkar, A.A. Gokhale, G. Jagan Reddy, A. Venkataramana, A. De, Estimation of melt pool dimensions, thermal cycle, and hardness distribution in the laser-engineered net shaping process of austenitic stainless steel, Metall. Mater. Trans. A Phys. Metall. Mater. Sci. 42 (2011) 4080–4087. doi:10.1007/s11661-011-0787-8.

[230] H.S. Whitesell, L. Li, R.A. Overfelt, Influence of solidification variables on the dendrite arm spacings of Ni-based superalloys, Metall. Mater. Trans. B Process Metall. Mater. Process. Sci. 31 (2000) 546–551. doi:10.1007/s11663-000-0162-4.

[231] G. Muvvala, D. Patra Karmakar, A.K. Nath, Online monitoring of thermo-cycles and its correlation with microstructure in laser cladding of nickel based super alloy, Opt. Lasers Eng. 88 (2017) 139–152. doi:10.1016/j.optlaseng.2016.08.005.

[232] L. Wang, S. Felicelli, Process Modeling in Laser Deposition of Multilayer SS410 Steel, J. Manuf. Sci. Eng. 129 (2007) 1028. doi:10.1115/1.2738962.

[233] L. Costa, R. Vilar, T. Reti, A.M. Deus, Rapid tooling by laser powder deposition : Process simulation using finite element analysis, Elsevier. 53 (2005) 3987–3999. doi:10.1016/J.ACTAMAT.2005.05.003.

[234] B. Zheng, Y. Zhou, J.E. Smugeresky, J.M. Schoenung, E.J. Lavernia, Thermal behavior and microstructural evolution during laser deposition with laser-engineered net shaping: Part I. Numerical calculations, Metall. Mater. Trans. A Phys. Metall. Mater. Sci. 39 (2008) 2228–2236. doi:10.1007/s11661-008-9557-7.

[235] V. Manvatkar, A. De, T. Debroy, Heat transfer and material flow during laser assisted multi-layer additive manufacturing, J. Appl. Phys. 116 (2014) 124905. doi:10.1063/1.4896751.

[236] A.B. Kustas, D.F. Susan, K.L. Johnson, S.R. Whetten, M.A. Rodriguez, D.J. Dagel, J.R. Michael, D.M. Keicher, N. Argibay, Characterization of the Fe-Co-1.5V soft ferromagnetic alloy processed by Laser Engineered Net Shaping (LENS), Addit. Manuf. 21 (2018) 41–52. doi:10.1016/j.addma.2018.02.006.

[237] M. Ghasri-Khouzani, H. Peng, R. Attardo, P. Ostiguy, J. Neidig, R. Billo, D. Hoelzle, M.R. Shankar, Direct metal laser-sintered stainless steel: comparison of microstructure and hardness between different planes, Int. J. Adv. Manuf. Technol. 95 (2018) 4031–4037. doi:10.1007/s00170-017-1528-y.

[238] J.S. Zuback, T. DebRoy, J.S. Zuback, T. DebRoy, The Hardness of Additively Manufactured Alloys, Materials (Basel). 11 (2018) 2070. doi:10.3390/ma11112070.

[239] W. Smith, J. Hashemi, Foundations of Materials Science and Engineering, 2009. doi:10.1016/j.jdent.2011.06.001.

[240] G. Dieter, Mechanical metallurgy, 3rd ed., McGraw Hill Book Co, 1998.

doi:10.1016/S0016-0032(62)91145-6.

[241] K.K. Singh, S. Sangal, G.S. Murty, Hall–Petch behaviour of 316L austenitic stainless steel at room temperature, Mater. Sci. Technol. 18 (2002) 165–172. doi:10.1179/026708301125000384.

[242] R.F. Gunst, R.H. Myers, D.C. Montgomery, Response Surface Methodology: Process and Product Optimization Using Designed Experiments, Technometrics. 38 (1996) 285. doi:10.2307/1270613.

[243] S.L.C. Ferreira, R.E. Bruns, H.S. Ferreira, G.D. Matos, J.M. David, G.C. Brandão, E.G.P. da Silva, L.A. Portugal, P.S. dos Reis, A.S. Souza, W.N.L. dos Santos, Box-Behnken design: An alternative for the optimization of analytical methods, Anal. Chim. Acta. 597 (2007) 179–186. doi:10.1016/J.ACA.2007.07.011.

[244] Standard Test Method for Density of Powder Metallurgy (PM) Materials Containing Less Than Two Percent Porosity 1, ASTM Int. West Conshohocken. 93 (2008) 1–5. doi:10.1520/B0311-13.2.

[245] C. Qiu, C. Panwisawas, M. Ward, H.C. Basoalto, J.W. Brooks, M.M. Attallah, On the role of melt flow into the surface structure and porosity development during selective laser melting, Acta Mater. 96 (2015) 72–79. doi:10.1016/j.actamat.2015.06.004.

[246] K. Mumtaz, N. Hopkinson, Top surface and side roughness of Inconel 625 parts processed using selective laser melting, Rapid Prototyp. J. 15 (2009) 96–103. doi:10.1108/13552540910943397.

[247] M. El-Sayed, M. Ghazy, Y. Yehia, K. Essa, Optimization of SLM Process Parameters for Ti6Al4V Medical Implants, Rapid Prototyp. J. (2018) RPJ-05-2018-0112. doi:10.1108/RPJ-05-2018-0112.

[248] K. Deb, A. Pratap, S. Agarwal, T. Meyarivan, A fast and elitist multiobjective genetic algorithm: NSGA-II, IEEE Trans. Evol. Comput. 6 (2002) 182–197. doi:10.1109/4235.996017.

[249] D.W. Green, R.H. Perry, Perry´s chemical engineers' handbook, 8th ed., McGraw Hill, New York, 2008.

Appendix A Powder Stream Effective Radius

The effective radius of powder stream is defined as one that reduced to $1/e^2$ of the peak concentration value in the stream center. The grey values of the images for the powder stream in transverse direction were measured by the ImageJ software, which shows a Gaussian distribution (as shown in Figure A-1). Then the effective radius of powder stream $r(z)$ at a distance z with the nozzle outlet can be measured in ImageJ. For simplification of the modeling, the powder stream is approximated with circular cone geometry. The effective radius of powder stream can be derived as,

$$r(z) = r_0 + z tan\theta \tag{A-1}$$

In which θ is the effective divergence angle, r_0 is the nozzle internal radius. Cold flow experiments were designed to measure the effective divergence angle with various settings of nozzle internal diameter, argon gas velocity and powder feed rate by a CCD camera (see Table A.1).

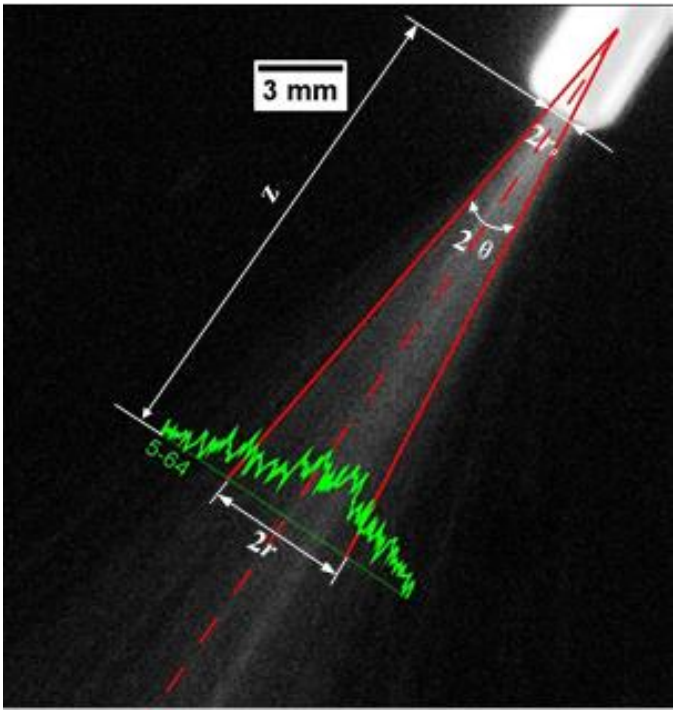

Figure A-1. Powder stream effective divergence angle measurement

Table A-1. Powder stream effective divergence angles

Powder feed rate (*g/min*)	Argon gas feed rate (*dL/min*)	r_0=0.35(mm)		r_0=0.7 (mm)		r_0=0.8(mm)	
		Divergence Angle (°)	Valid for (*mm*)	Divergence Angle (°)	Valid for (*mm*)	Divergence Angle (°)	Valid for (*mm*)
3	2.5	4.5±0.2	Z<18	5.8±0.2	Z<20	6.4±0.2	Z<24
3	3.5	4.7±0.2	Z<18	6.0 ±0.2	Z<20	6.8±0.2	Z<24
3	4.5	5.2±0.2	Z<17	6.4±0.2	Z<19	7.1±0.2	Z<23
5	2.5	5.7±0.2	Z<17	6.8±0.2	Z<18	7.6±0.2	Z<24
5	3.5	6.4±0.2	Z<17	8.0±0.2	Z<18	8.1±0.2	Z<22
5	4.5	6.6 ±0.2	Z<17	8.4±0.2	Z<18	8.5±0.2	Z<22
7	2.5	7.3±0.2	Z<16	8.6±0.2	Z<17	9.0 ±0.2	Z<21
7	3.5	7.7±0.2	Z<16	8.9±0.2	Z<17	9.5±0.2	Z<20
7	4.5	8.1±0.2	Z<16	9.3±0.2	Z<17	9.8±0.2	Z<20

Appendix B Effective Molten Pool Projection Area

To calculate the effective molten pool projection area, the molten pool top surface is approximated by the inclined surface S_1 that cuts through its highest point *E* and lowest point *A*. S_1 is projected to powder transverse planes S_2 and S_3 with the effective projection area A_{S_2} and A_{S_3} (shown in Figure B-1)

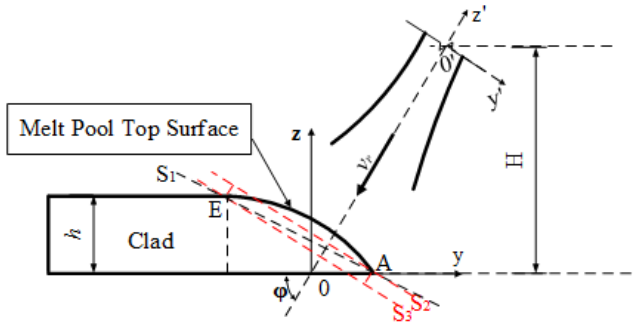

Figure B-1. Molten pool projection on powder transverse plane

Based on the 3D molten pool function built in Section 3.2.4, the molten pool projections on inclined surfaces S_2 and S_3 are approximated with the geometry of ellipses.

Projection area A_{S_2}:

$$\begin{cases} \dfrac{y'^2}{\iota_1^2}+\dfrac{x'^2}{w^2}=1, \mathrm{z}'=\mathrm{z}_{S_2}, \mathrm{y}'\in[-\iota_1,0], \mathrm{x}'\in\left[-\dfrac{w}{2},\dfrac{w}{2}\right] \\ \dfrac{y'^2}{\iota_2^2}+\dfrac{x'^2}{w^2}=1, \mathrm{z}'=\mathrm{z}_{S_2}, \mathrm{y}'\in[0,\iota_2], \mathrm{x}'\in\left[-\dfrac{w}{2},\dfrac{w}{2}\right] \end{cases} \tag{B-1}$$

Projection area A_{S_3}:

$$\begin{cases} \dfrac{y'^2}{\iota_1^2}+\dfrac{x'^2}{w^2}=1, \mathrm{z}'=\mathrm{z}_{S_3}, \mathrm{y}'\in[-\iota_1,0], \mathrm{x}'\in\left[-\dfrac{w}{2},\dfrac{w}{2}\right] \\ \dfrac{y'^2}{\iota_2^2}+\dfrac{x'^2}{w^2}=1, \mathrm{z}'=\mathrm{z}_{S_3}, \mathrm{y}'\in[0,\iota_2], \mathrm{x}'\in\left[-\dfrac{w}{2},\dfrac{w}{2}\right] \end{cases} \tag{B-2}$$

where l_1 and l_2 are the major semi-axis of the ellipse projection area A_{S_2} and A_{S_3}, respectively. w is the minor semi-axis, being equal to half of the melt pool projection width on substrate surface.

Appendix C Drag Force Calculation for Spherical Particles

As the transverse velocity component of the particle is nearly the same with that of the carrier gas in the blown-powder feeding process, the gas drag force in the transverse direction will be almost zero. Here only the radial drag force component was computed. The parameter data used for drag force calculation was listed in Table C-1.

Table C-1. Parameters for the drag force calculation

Particle radius	Relative velocity	Gas kinematic viscosity	Gas density	Drag force
$25\sim500\ \mu m$	$0.1\sim0.5\ m/s$	$1.48\times10^{-5}\ m^2/s$	$1.225\ Kg/m^3$	$0.02\sim0.2\ \mu N$

The Reynolds number of the particles is computed as,

$$R_e = \frac{2v_r R_p}{\vartheta} \tag{C-1}$$

where v_r is the relative velocity of the particle to the gas flow, ϑ the kinematic viscosity of gas flow. It was noticed that the Reynolds number in this research follows within the range of $0.1 \leq R_e \leq 1000$. Accordingly, the drag coefficient C_D can be calculated as [249],

$$C_D = \frac{24}{R_e}(1 + 0.14R_e^{0.7}) \tag{C-2}$$

Thereafter, the radial drag force component can be calculated as [127],

$$F_D = \frac{\pi}{2} C_D \rho v_r^2 R_p^2 \tag{C-3}$$

After solving the above Equations (C-1, C-2 and C-3), the radial drag force component was found to be in the range of $0.02\sim0.2\ \mu N$. Compared to the magnetic force that are capable for effective particle focusing ($\geq 10\ \mu N$) as shown in Figure 4-8 (c), the gas drag force on the particle can be ignored due to their relatively small magnitude, roughly $0.2\%\sim2\%$ of the effective magnetic force.

Appendix D Aluminum Particle Deflection Test

To investigate the concentration effect of the linear-Halbach-PM configuration, a simplified one pole linear-Halbach-PM array configuration (Figure D-1 (a)) was designed and fabricated with Neodymium magnets N52 (K & J Magnetics, Plumsteadville, USA). As shown in Figure D-1 (b), the height ratio between the N52 magnets and the mild steel was optimized by the parametric sweep module in COMSOL Multiphysics® software. As seen, the largest field intensity can be achieved with a height ratio of ~0.1. The 2D filed intensity distribution was shown in Figure D-1 (c) with the optimized height ratio setup.

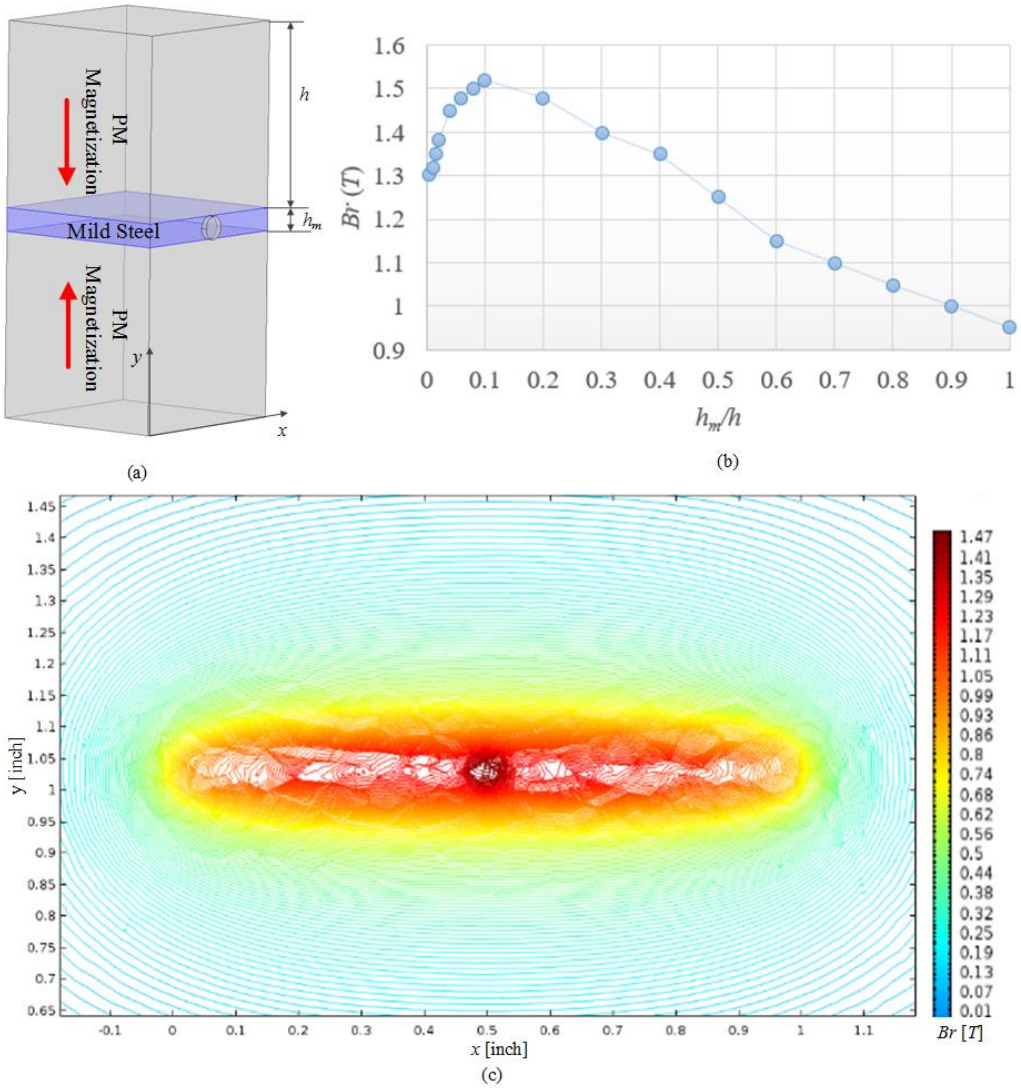

Figure D-1. Design optimization of the proposed one pole linear-Halbach-PM array. (a) Schematic 3D view. (b) Field intensity B_r sweep optimization. (c) Field intensity B_r 2D distribution.

The surface field intensity of the fabricated linear-Halbach-PM configuration was also measured by a LakeShore Model 410 Gauss meter, showing an averaged flux density of ~1.27 T. Pure aluminum particles (Alfa Aesar, Tewksbury, USA) were used in the experimental test and were sieved to the size range of $210 \sim 250\ \mu m$. The particle morphology was shown in Figure D-2 (b). As seen, most particles exhibit a near spherical morphology, whereas particles with irregular-shaped morphology can also be identified. The powder feeder purchased from Sulzer Metco was used to feed the particles passing through the designed one pole linear-Halbach-PM array with compressed argon gas.

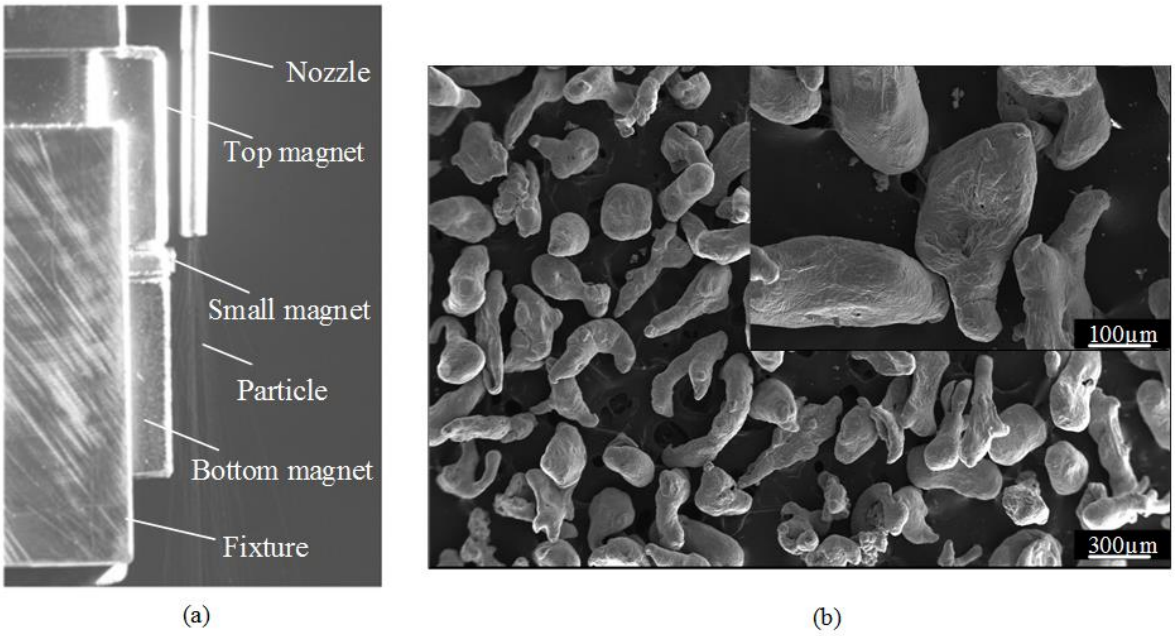

Figure D-2. (a) Experimental picture of the particle defection test under the fabricated one pole linear-Halbach-PM array and (b) aluminum particle morphology. The dimensions of N52 magnet block, middle mild steel block and small cylinder magnet were $25 \times 25 \times 25\ mm$, $25 \times 3 \times 25\ mm$ and $3\ mm$ diameter with $0.8\ mm$ thickness, respectively.

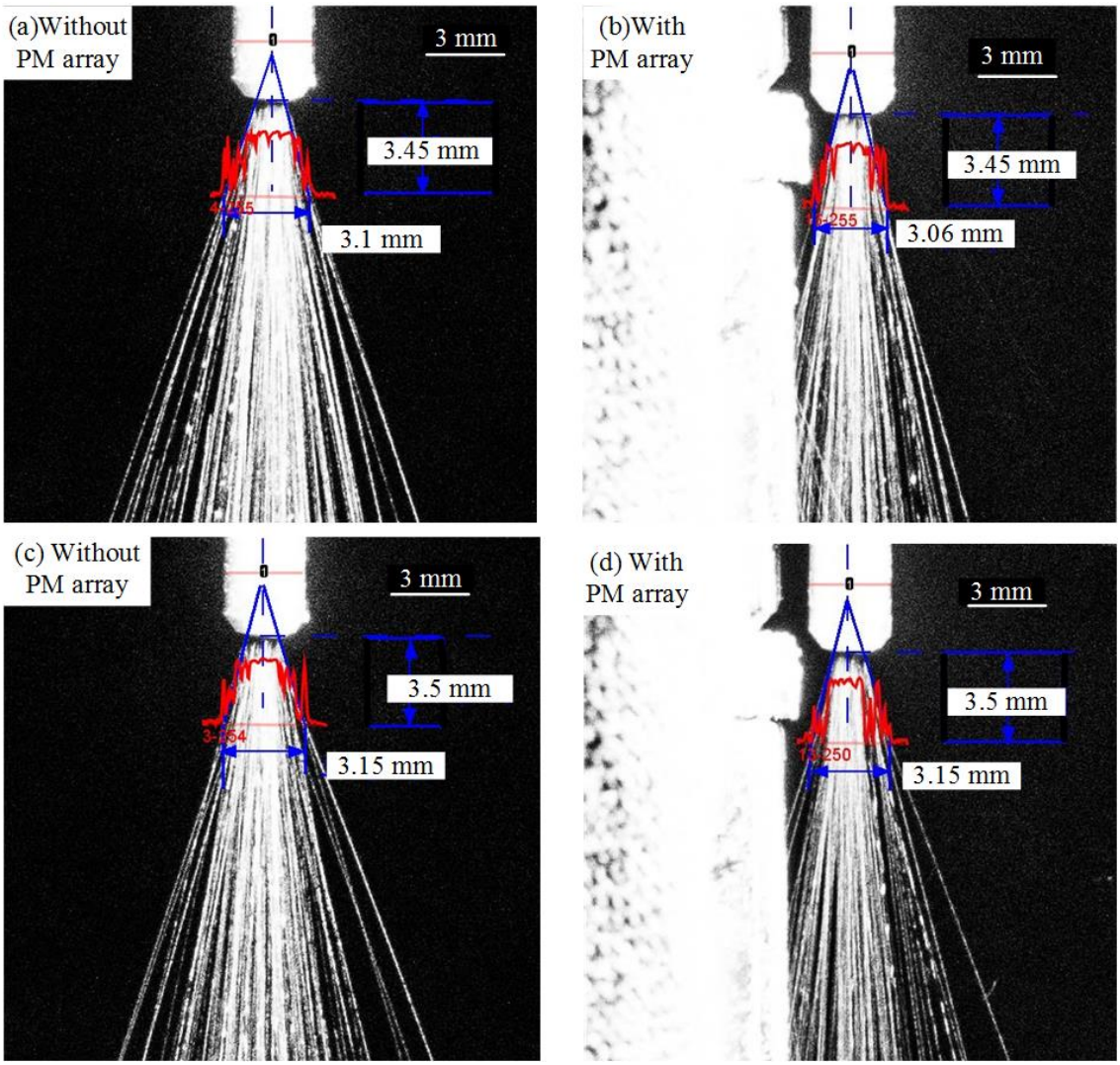

Figure D-3. Aluminum powder stream images. (a) Without PM array and (b) with PM array, the particle velocity is 2 m/s. (c) Without PM array and (d) with PM array, the particle velocity is 4 m/s.

Figure D-3 shows the powder stream images as the particle travelling with and without the fabricated one pole linear-Halbach-PM array. The images were taken by a Canon EOS 60D camera with a Penta-con 135 mm f/2.8 lens. Compared with the setup without PM array (Figure D-3 (a) and (c)), the powder streams still keep symmetrical and no deflection as the particles traveling though the PM array magnetic field (Figure D-3 (b) and (d)), which agrees with the derivation in Section 4.4 that the linear-Halbach-PM configuration is not capable for particle concentration.

Appendix E Magnetic Force Simulation

Magnetic forces on aluminum particles were simulated by an ANSYS Maxwell V16 software with a simplified one pole EM configuration. The transient eddy current density $\boldsymbol{J}$ in the particle/conductor is solved by,

$$\begin{cases} \nabla \times \frac{1}{\sigma} \nabla \times \boldsymbol{H} = -\frac{\partial \boldsymbol{B}}{\partial t} \\ \nabla \cdot \boldsymbol{B} = 0 \\ \nabla \cdot \left(\epsilon \nabla \frac{\partial \emptyset}{\partial t} \right) = \nabla \cdot (\sigma \nabla \emptyset) \\ \nabla \times \boldsymbol{H} = \boldsymbol{J} \end{cases} \quad \text{(E-1)}$$

where $\boldsymbol{H} = \boldsymbol{B}/\mu$ is the field strength, ϵ the absolute permittivity and $\emptyset$ is the electric potential. The boundary condition was set as $\boldsymbol{n} \cdot \boldsymbol{J} = 0$ ($\boldsymbol{n}$ is the normal vector) on the conductor surface. As seen in Figure E-1, the induced eddy currents show a non-uniform distribution over the whole particle when the particle travels through the designed one pole EM configuration.

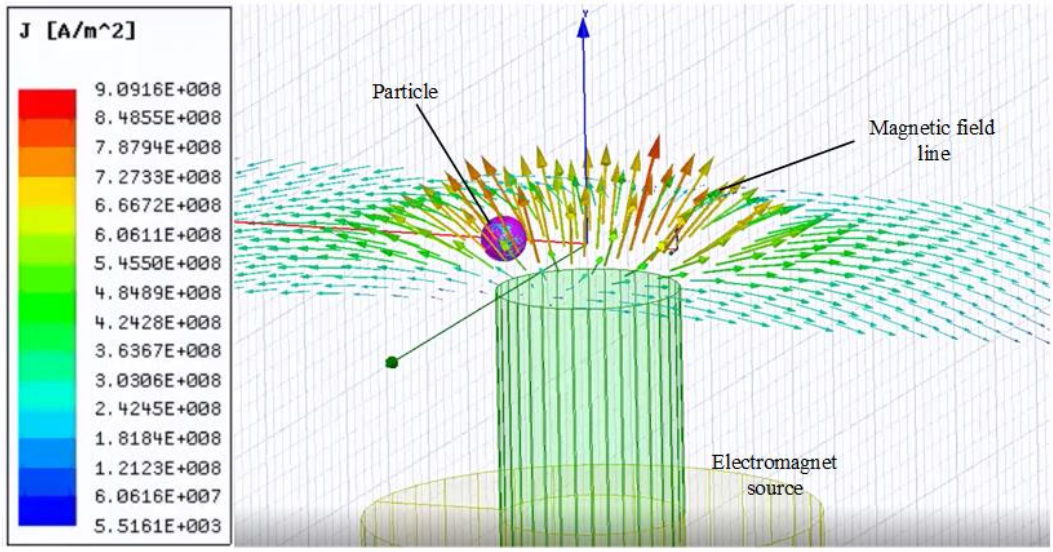

Figure E-1. Transient eddy current simulation for an aluminum particle travels though the one pole EM configuration. Particle radius $R_p = 300\ \mu m$, field frequency $f = 1\ MHz$.

Thereafter, the transient Lorentz force on the particle can be calculated by $\boldsymbol{F} = \int (\boldsymbol{J} \times \boldsymbol{B}) dV_p$. The averaged magnetic force for an aluminum particle of radius $R_p = 300\ \mu m$ was ~60 μN under the designed one pole EM concentration generator.

Appendix F Superposition of the Resultant Heat Source Solutions by Integration

The energy exchange for the resultant heat source may be considered as a local surface process on the $z = 0$ plane in the built moving coordinate as shown in Figure 5-2. Thus, the laser energy source and the equivalent powder stream energy source can be calculated as,

$$I(x,\mathrm{y}) = \frac{2\beta_w P_L}{\pi R_L^2} exp\left(-\frac{2(x^2+y^2)}{R_L^2}\right),\ R_L = \sqrt{R_{0L}^2 + 4\theta_L^2 z_0^2} \tag{F-1}$$

$$\begin{aligned} I_p(x,\mathrm{y}) &= \frac{2sin\varphi c_p \dot{m}(T_0 - T_m)}{\pi r_{avg}^2} exp\left[-\frac{2[x^2 + (ysin\varphi)^2]}{r_{avg}^2}\right] \\ r_{avg} &= \frac{r(-R_L) + r(R_L)}{2} = r_0 + Htan\theta/sin\varphi \end{aligned} \tag{F-2}$$

Thereafter, the 2D Gaussian heat source integral in Equation (5-6) can be simplified as,

$$\begin{aligned} &\int_{\xi=-\infty}^{\xi=\infty}\int_{\eta=-\infty}^{\eta=\infty} \frac{I(\xi,\eta)}{4\rho_p c_p[\pi\alpha_P(t-\tau)]^{3/2}} exp\left[-\frac{(x-\xi)^2 + (y - v\tau - \eta)^2 + \mathrm{z}^2}{4\alpha(t-\tau)}\right] d\xi d\eta \\ &= \int_{\xi=-\infty}^{\xi=\infty}\int_{\eta=-\infty}^{\eta=\infty} \frac{\beta_w P_L}{2\pi R_L^2 \rho_p c_p[\pi\alpha_P(t-\tau)]^{3/2}} exp\left[-\frac{(x-\xi)^2 + (y - v\tau - \eta)^2 + \mathrm{z}^2}{4\alpha(t-\tau)}\right. \\ &\qquad \left. -\frac{2\left(\xi^2+\eta^2\right)}{R_L^2}\right] d\xi d\eta \\ &= \frac{\beta_w P_L}{2\pi R_L^2 \rho_p c_p} \int_{\xi=-\infty}^{\xi=\infty}\int_{\eta=-\infty}^{\eta=\infty} \frac{1}{[\pi\alpha_P(t-\tau)]^{3/2}} exp\left\{-\left[\xi^2\left(\frac{2}{R_L^2} + \frac{1}{4\alpha(t-\tau)}\right) + \xi\left(\frac{-2x}{4\alpha(t-\tau)}\right)\right.\right. \\ &\qquad \left.\left. + \eta^2\left(\frac{2}{R_L^2} + \frac{1}{4\alpha(t-\tau)}\right) + \eta\left(\frac{-2(y-vt)}{4\alpha(t-\tau)}\right)\right] - \frac{x^2 + (y-vt)^2 + z^2}{4\alpha(t-\tau)}\right\} d\xi d\eta \\ &= \frac{2\,\beta_w P_L}{\rho_p c_p \pi\sqrt{\pi\alpha_P}} \frac{1/\sqrt{(t-\tau)}}{R_L^2 + 8\alpha_P(t-\tau)} exp\left[-\frac{2[x^2 + (y-v\tau)^2]}{R_L^2 + 8\alpha_P(t-\tau)} - \frac{z^2}{4\alpha_P(t-\tau)}\right] \end{aligned} \tag{F-3}$$

Similarly, the negative mass heat source integral in Equation (5-6) can be simplified as,

$$\begin{aligned} &\int_{\xi=-\infty}^{\xi=\infty}\int_{\eta=-\infty}^{\eta=\infty} \frac{I_p(\xi,\eta)}{4\rho_p c_p[\pi\alpha_P(t-\tau)]^{3/2}} exp\left[-\frac{(x-\xi)^2 + (y - v\tau - \eta)^2 + \mathrm{z}^2}{4\alpha(t-\tau)}\right] d\xi d\eta \\ &= \frac{2c_p\dot{m}(T_0 - T_m)}{\pi\rho_p c_p\sqrt{\pi\alpha_P}} \frac{1/\sqrt{(t-\tau)}}{r_{avg}^2 + 8\alpha_P(t-\tau)} exp\left[-\frac{2[x^2 + [(y-v\tau)/sin_\varphi]^2]}{r_{avg}^2 + 8\alpha_P(t-\tau)}\right. \\ &\qquad \left. -\frac{z^2}{4\alpha_P(t-\tau)}\right] \end{aligned} \tag{F-4}$$

Appendix G ANOVA Results

Table G-1. ANOVA for relative density with quadratic regression model

Source	Sum of Squares	df	Mean Square	F-value	p-value	
Model	0.003	9	0.0003	84.97	< 0.0001	significant
A-Laser power	0.0013	1	0.0013	343.61	< 0.0001	
B-Scanning speed	0	1	0	10.31	0.0148	
C-Hatch space	0.0004	1	0.0004	95.82	< 0.0001	
AB	0.0001	1	0.0001	15.08	0.006	
AC	0	1	0	4.15	0.081	
BC	0	1	0	10.14	0.0154	
A^2	6.17E-06	1	6.17E-06	1.57	0.2503	
B^2	0.001	1	0.001	263.53	< 0.0001	
C^2	0.0001	1	0.0001	14.71	0.0064	
Residual	0	7	3.93E-06			
Lack of Fit	0	3	5.45E-06	1.96	0.2625	not significant
Pure Error	0	4	2.79E-06			
Cor Total	0.003	16				
Std. Dev.	0.002		R^2	0.9909		
Mean	0.9771		Adjusted R^2	0.9793		
C.V. %	0.2028		Predicted R^2	0.9079		
			Adeq Precision	30.9087		

Table G-2. ANOVA for surface roughness with 2FI regression model

Source	Sum of Squares	df	Mean Square	F-value	p-value	
Model	91.13255625	6	15.18875938	16.18753	0.000127	significant
A-Laser power	13.5981125	1	13.5981125	14.49229	0.003447	
B-Scanning speed	41.33677813	1	41.33677813	44.05497	5.8E-05	
C-Hatch space	14.24445313	1	14.24445313	15.18113	0.002979	
AB	2.21265625	1	2.21265625	2.358154	0.155642	
AC	19.47015625	1	19.47015625	20.75046	0.00105	
BC	0.2704	1	0.2704	0.288181	0.603126	
Residual	9.382999632	10	0.938299963			
Lack of Fit	5.600749632	6	0.933458272	0.987199	0.530143	not significant
Pure Error	3.78225	4	0.9455625			
Cor Total	100.5155559	16				
Std. Dev.	0.968658848		R^2	0.906651		
Mean	10.30735294		Adjusted R^2	0.850642		
C.V. %	9.39774599		Predicted R^2	0.69327		
			Adeq Precision	13.17917		

Appendix H Parameters Setting for Gamultiobj Function Solver

Table H-1. Solver parameters of gamultiobj function for multi-objective optimization

Parameters	Value
Population size	200
Maximum generations	200
Constraint tolerance	1e-6
Crossover fraction	0.8
Elite count	50